DOCUMENTATION PAGE

Form Approved
OMB No. 0704-0188

AD-A221 182

1b. RESTRICTIVE MARKINGS

NONE

3. DISTRIBUTION / AVAILABILITY OF REPORT

APPROVED FOR PUBLIC RELEASE;
DISTRIBUTION UNLIMITED.

2b. DECLASSIFICATION / DOWNGRADING SCHEDULE

4. PERFORMING ORGANIZATION REPORT NUMBER(S)

5. MONITORING ORGANIZATION REPORT NUMBER(S)

AFIT/CI/CIA-90-007D

6a. NAME OF PERFORMING ORGANIZATION AFIT STUDENT AT Georgia Institute of Tech/Atlanta	**6b. OFFICE SYMBOL** *(If applicable)*	**7a. NAME OF MONITORING ORGANIZATION** AFIT/CIA

6c. ADDRESS (City, State, and ZIP Code)

7b. ADDRESS (City, State, and ZIP Code)

Wright-Patterson AFB OH 45433-6583

8a. NAME OF FUNDING / SPONSORING ORGANIZATION	**8b. OFFICE SYMBOL** *(If applicable)*	**9. PROCUREMENT INSTRUMENT IDENTIFICATION NUMBER**

8c. ADDRESS (City, State, and ZIP Code)

10. SOURCE OF FUNDING NUMBERS

PROGRAM ELEMENT NO.	PROJECT NO.	TASK NO.	WORK UNIT ACCESSION NO.

11. TITLE (Include Security Classification) (UNCLASSIFIED)

Models of Intracavity Frequency Doubled Lasers

12. PERSONAL AUTHOR(S)

Glenn E. James

13a. TYPE OF REPORT ~~THESIS/~~DISSERTATION	**13b. TIME COVERED** FROM _____ TO _____	**14. DATE OF REPORT (Year, Month, Day)** 1990	**15. PAGE COUNT** 314

16. SUPPLEMENTARY NOTATION APPROVED FOR PUBLIC RELEASE IAW AFR 190-1
ERNEST A. HAYGOOD, 1st Lt, USAF
Executive Officer, Civilian Institution Programs

17. COSATI CODES			**18. SUBJECT TERMS (Continue on reverse if necessary and identify by block number)**
FIELD	GROUP	SUB-GROUP	

19. ABSTRACT (Continue on reverse if necessary and identify by block number)

DTIC
ELECTE
APR 25 1990
B

BEST
AVAILABLE COPY

20. DISTRIBUTION / AVAILABILITY OF ABSTRACT ☒ UNCLASSIFIED/UNLIMITED ☐ SAME AS RPT. ☐ DTIC USERS	**21. ABSTRACT SECURITY CLASSIFICATION** UNCLASSIFIED
22a. NAME OF RESPONSIBLE INDIVIDUAL ERNEST A. HAYGOOD, 1st Lt, USAF	**22b. TELEPHONE (Include Area Code)** (513) 255-2259 **22c. OFFICE SYMBOL** AFIT/CI

MODELS OF INTRACAVITY FREQUENCY DOUBLED LASERS

A DISSERTATION
Presented to
The Academic Faculty

by

Glenn Edward James

In Partial Fulfillment
of the Requirements for the Degree
Doctor of Philosophy in Mathematics

Georgia Institute of Technology
March 1990

MODELS OF INTRACAVITY FREQUENCY DOUBLED LASERS

Capt. Glenn E. James, USAF
Ph.D., March 1990, 314 pages
Directed by Evans M. Harrell II, School of Mathematics,
Georgia Institute of Technology, Atlanta, GA 30332

In many laser applications, the frequency of light produced by the laser is doubled by a crystal with nonlinear optical properties. The presence of such a crystal inside a laser cavity can produce large, irregular fluctuations in the output intensity. This thesis examines nonlinear systems of ordinary differential equations for the longitudinal mode intensities (physical observables) and gains of intracavity doubled lasers. A new system of equations is derived which models the frequency doubling of a general class-B laser with any number of intracavity birefringent elements, and the relevant features of the cavity configuration are reduced to two parameters.

The complete range of behavior of the intensity output is characterized for one, two and three longitudinal modes in this general framework. A novel approach to the linearized stability analysis of the model leads to explicit stability criteria for the cavity parameters, and to several successful predictions of ways to stabilize the laser output. Several experimental laser configurations previously studied prove to be special cases of the general model; all the experimental results confirm the correspondence between the theory and experiment.

In the specific case of an intracavity doubled Nd:YAG laser, numerical results trace an intermittency route to chaos, with cross saturation as the control parameter. Samples of experimental output are closely matched by numerical integrations. The intracavity doubled Nd:YAG laser is found, in theory and experiment, to be a rich source of nonlinear dynamics.

T. Baer, "Large-Amplitude Fluctuations Due to Longitudinal Mode Coupling in Diode-Pumped Intracavity-Doubled Nd:YAG Lasers", J. Opt. Soc. Am. B3, 1175 (1986).

G.E. James, E.M. Harrell II, C. Bracikowski, Rajarshi Roy and K. Wiesenfeld, "On the Elimination of Chaos in an Intracavity Doubled Nd:YAG Laser", Opt. Lett., to be published (1990).

90 04 23 078

Availability Codes

Dist	Avail and/or Special
A-1	

MODELS OF INTRACAVITY
FREQUENCY DOUBLED LASERS

APPROVED:

Evans M. Harrell II

Evans M. Harrell II, Chairman

Rajarshi Roy

Rajarshi Roy

Luca Dieci

Luca Dieci

James V. Herod

James V. Herod

Kurt Wiesenfeld

Kurt W. .e..feld

Richard A. Duke

Richard A. Duke

MARCH 9, 1990

Date Approved by Chairman

I dedicate this work

to my brave and loving bride Patsy

to my bright and lively daughter Christine

to our beautiful baby, soon to arrive

ACKNOWLEDGMENTS

The collective "we" which appears in this thesis is no literary contraction, but a genuine sign of work I accomplished together with my research advisors, Evans Harrell and Rajarshi Roy, with Chris Bracikowski who assembled and conducted all the experiments, and with Kurt Wiesenfeld who helped simplify our analysis. I thank Luca Dieci for many helpful corrections to the thesis content and style.

I am very grateful to the Air Force Institute of Technology and the U.S. Air Force Academy Department of Mathematical Sciences for their sponsorship of my graduate studies. My deep appreciation also goes to James Herod, Gunther Meyer, and Richard Duke for coordinating my graduate program within the constraints of my Air Force assignment. I also acknowledge many useful discussions with Jack Hale and Konstantin Mischaikow on ordinary differential equations and bifurcations. I thank George Gray, Gautam Vemuri, John Thompson and Larry Fabiny for their patient instruction on details of lasers and optics. I recognize the experimental support we received from Tom Baer and Greg Kintz of Spectra Physics, in addition to helpful visits and discussions.

I acknowledge the useful information I learned from a Dynamical Systems class paper by K.-H. Kwek and the Ph.D. thesis of Keqin Gu (School of Mechanical Engineering). Their work is only referenced in Appendix C, but their papers and bibliographies pointed me toward important references on invariant measures.

My heartfelt thanks goes to my parents and my brother Doug for their many gifts and their enthusiastic support. Thanks, too, to Eleanor Thompson for letting me invade her copy shop.

And as the first are often recognized last -- thanks, God.

TABLE OF CONTENTS

LIST OF TABLES

LIST OF FIGURES

LIST OF FIGURES, continued

LIST OF FIGURES, continued

SUMMARY

In many laser applications, the frequency of light produced by the laser is doubled by a crystal with nonlinear optical properties. The presence of such a crystal inside a laser cavity can produce large, irregular fluctuations in the output intensity. This thesis examines nonlinear systems of ordinary differential equations for the longitudinal mode intensities (physical observables) and gains of intracavity doubled lasers. A new system of equations is derived which models the frequency doubling of a general class-B laser with any number of intracavity birefringent elements, and the relevant features of the cavity configuration are reduced to two parameters. General results are also presented on the possible polarization states of the output beam; these polarizations are explicitly included in a dynamical system for the first time. This analysis is also the first to include the possibility of birefringence in the gain medium.

The complete range of behavior of the intensity output is characterized for one, two and three longitudinal modes in this general framework. A novel approach to the linearized stability analysis of the model leads to explicit stability criteria for the cavity parameters, and to several successful predictions of ways to stabilize the laser output. Several experimental laser configurations previously studied prove to be special cases of the general model; all the experimental results confirm the correspondence between the theory and experiment. Extensive numerical integrations also display a wide range of dynamical behavior consistent with experimental observations.

In the specific case of an intracavity doubled Nd:YAG laser, numerical results trace an intermittency route to chaos, with cross saturation as the control parameter. Samples of experimental output are closely matched by numerical integrations. An additional set of rate equations are developed which display dynamics seen in experiments but not in previous

numerical results. Still another set of rate equations validates our approximation of the lasing transition in Nd:YAG as a two-level system. The intracavity doubled Nd:YAG laser is found, in theory and experiment, to be a rich source of nonlinear dynamics.

CHAPTER I

INTRODUCTION

In many laser applications, the frequency of light produced by the laser is doubled by a crystal with nonlinear optical properties. The presence of such a crystal inside a laser cavity can produce large, irregular fluctuations in the output intensity. This thesis examines nonlinear systems of ordinary differential equations for the intensities (physical observables) and gains in intracavity doubled lasers. We derive a new system of equations which models the frequency doubling of a general class-B laser with any number of intracavity birefringent elements, and the relevant features of the cavity configuration are reduced to two parameters.

While the numerical results we present are particular to the intracavity doubled Nd:YAG laser, our theory applies to a more general class of lasers. Our general results characterize the polarization states of the output beam, and for the first time these polarizations are explicitly included in the dynamical system which describes the doubled laser. This analysis is also the first to include the possibility of birefringence in the gain medium.

The complete range of behavior of the intensity output is characterized for one, two and three longitudinal modes in this general framework. A novel approach to the linearized stability analysis of the model leads to explicit stability criteria for the cavity parameters, and to several successful predictions of ways to stabilize the laser output. Several experimental laser configurations previously studied prove to be special cases of our

general model; all the experimental results confirm the correspondence between the theory and experiment. Extensive numerical integrations also display a wide range of dynamical behavior consistent with experimental observations.

This report is directed toward a broad audience which may have a strong background in physics or mathematics, but not necessarily both. Thus, the first chapter includes basic material on laser physics as well as dynamical systems and ordinary differential equations.

The previous rate equation model is studied in Chapter II. We analyze the stability of numerous steady state solutions, and we show how the stable and unstable manifolds of these points interact to give stable steady state, periodic, and chaotic behavior in the laser intensity output. In the specific case of an intracavity doubled Nd:YAG laser, numerical results trace an intermittency route to chaos, with cross saturation as the control parameter.

We develop the new model for intracavity doubled lasers in Chapter III. We derive and analyze the model in a very general framework, apply it to several specific laser configurations, and present the results of extensive numerical integrations. In addition to reproducing many qualitative features of experimental data, the numerical integrations closely match several specific examples of experimental output. Moreover, the analysis of our new equations predicts ways to eliminate the chaotic intensity fluctuations; these predictions have been verified in our experimental results.

The new model for intracavity doubling in Chapter III is referenced to the system of equations used by Baer. The basic template of equations is kept intact while we develop the new approach for specifically modeling the doubling process with arbitrary birefringent cavity elements. In Chapter IV we propose several variations on the basic template, where we develop new systems of equations from more fundamental physical principles. One new set of equations produces results which resemble intensity traces seen in laboratory

experiments but not yet predicted by any previous model. Still another set of rate equations confirms the two-level approximation for the lasing transition in the Nd:YAG laser. We conclude in Chapter V with suggestions for future research and a summary of our main results which highlight the utility of the intracavity doubled Nd:YAG laser for studying nonlinear dynamical phenomena.

Review of Laser Basics

A laser produces radiation with several characteristic features, one of which is that the emitted light can be nearly monochromatic, i.e. of a single frequency. Rather than construct a separate laser for each desired output frequency, we would like to be able to alter the configuration of a given laser in some simple way to produce light either within a range of frequencies, or at several specific frequencies. Tunable lasers, for example, have been designed which produce light within a range of frequencies. This thesis centers on lasers whose output frequency is changed by a crystal with nonlinear optical properties that doubles the frequency of incident light within a range of (crystal-dependent) wavelengths.

Frequency doubling can take place outside a laser cavity, simply by placing a nonlinear crystal in the path of the output beam. The beam which results is a combination of light at the input, or fundamental, frequency, and some small percentage of light at the doubled frequency. More efficient doubling can be achieved by intracavity doubling, i.e. by placing the doubling crystal inside the laser cavity, which takes advantage of the larger intracavity power. In a certain class of lasers, a serious experimental drawback to intracavity doubling is that the output beam intensity often displays large, irregular fluctuations in amplitude, fluctuations which may be undesirable for certain uses of the light at the doubled frequency.

This section reviews only the most fundamental concepts of lasers and optics necessary for understanding the basic dynamics of an intracavity frequency doubled laser. The following discussion is drawn from several standard texts which review these subjects in depth (Siegman, 1986; Sargent, et al., 1974; O'Shea, et al., 1978; Hecht and Zajac, 1979). We begin with a simple view of laser operation and work slowly toward an intuitive understanding of the differential equations which describe the relevant time-dependent variables in the laser.

Theoretically, any collection of identical particles (atoms, molecules, ions, etc.) which can be temporarily excited to an energy level above a ground state can be made to lase under suitable conditions. All we need at first (Fig. 1.1) is a source of input energy, the pump, to excite the active medium to the upper energy level E_1. An excited species will generally decay back to its ground state by one of two mechanisms: **spontaneous decay**, which is characterized by an upper state lifetime τ_f, or **stimulated emission**, where a passing photon with energy E_1-E_0 stimulates the excited particle and causes it to decay to its ground state, emitting a photon with the same energy. The frequency ω of these photons is determined by the relation E_1-E_0 = $\hbar\nu$, where $\hbar$ is Planck's constant (divided by 2π). The second photon generated by stimulated emission travels in the same direction and in phase with the incident photon; that is, the two photons propagate coherently. If we now place mirrors on either side of the source of excited particles (the **active medium**), some of the photons produced by spontaneous emission are reflected back into the excited population and generate a cascade of photons through stimulated emission. As long as there is sufficient pump energy to sustain a **population inversion** (more particles in the excited state than the ground state) the amplification by stimulated emission can continue indefinitely. The coherent beam of radiation produced by this process has a single frequency determined by the difference in energy levels of the active medium. A beam of
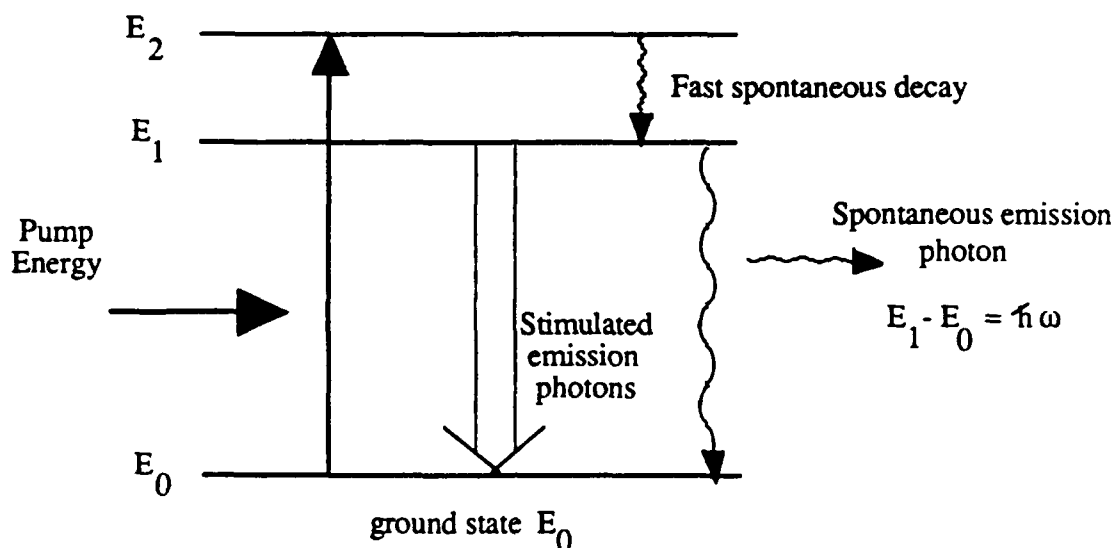
Fig. 1.1 Three-Level Lasing Scheme. Absorption of photons from the pump source excite the active medium; spontaneous and stimulated emission produce photons in the lasing transition.

light exits the cavity through the output mirror which is designed to transmit a small percentage of the incident light, while reflecting most of the light back into the cavity to sustain the lasing process.

The pump is an energy source that provides photons whose energy matches the absorptive energy transition, E_2-E_0. For the laser system we study in this thesis (Fig. 1.2), the pump is actually another laser, in fact an array of small semi-conductor lasers (called a **laser diode**); the active medium is a crystal of yttrium aluminum garnet, doped with neodymium ions, denoted Nd^{3+}:YAG. The system is commonly referred to as a **diode-pumped YAG laser**. The YAG laser is actually a four-level laser, shown in Fig. 1.3, where the pump transition is at one wavelength (near 810 nm), the spontaneous decay

INPUT
MIRROR

OUTPUT
MIRROR

HR 1064 nm
HR 532 nm

HR 1064 nm
HT 532 nm

LASER
DIODE
PUMP

Nd:YAG
CRYSTAL

KTP
CRYSTAL

QWP

ETALONS
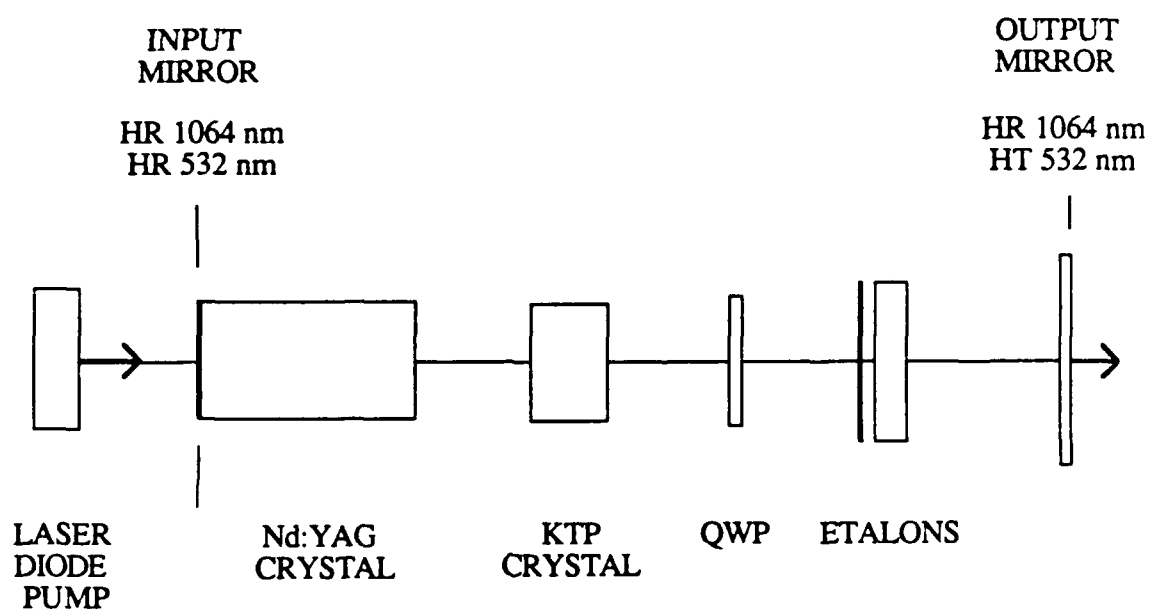
Fig. 1.2 General Cavity Configuration for the Intracavity Frequency Doubled
Nd:YAG Laser. The input mirror is highly reflective (HR) for both the
fundamental (1064 nm) and doubled (532 nm) intensities. The output
mirror reflects the fundamental frequency efficiently and is highly
transmissive (HT) for the green light. Some configurations include a
quarter wave plate (QWP) or etalons.

upper energy state E_3
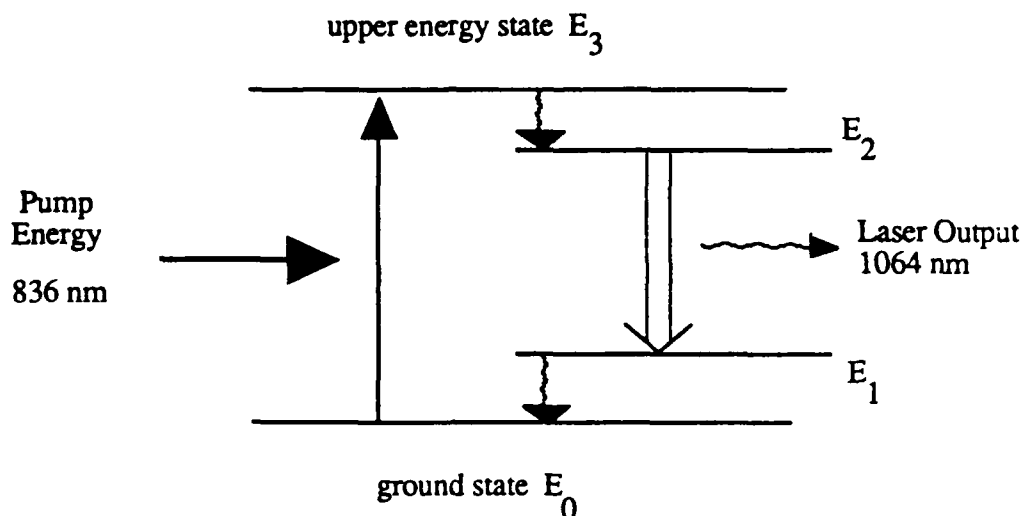
Fig. 1.3 Four-Level Lasing Transition in Nd:YAG. The fast spontaneous decay out of levels E_3 and E_1 allows a population inversion to be sustained between the middle two levels.

rates out of E_3 and E_1 are extremely fast, and lasing transition (and so the population inversion) is between energy levels E_2 and E_1, at a wavelength of 1064 nm (infrared). The propagation of light in the cavity can be described by complex electromagnetic waves which are solutions of Maxwell's equations with Dirichlet boundary conditions (amplitudes equal to zero) at the cavity mirrors. Thus, for a cavity of length L, we identify a single longitudinal **mode** as an electric field

$$E_j(z,t) = |E_j(t)| \sin \left(\frac{j\pi z}{L}\right) e^{-i(\Delta_j t + \varphi)} \qquad\qquad 1.1$$

whose spatial dependence is a sine function with a frequency restricted by the cavity length, and $\Delta_j = j\pi c/L$, where $c/2L$ is the spacing between allowed frequencies in the cavity. This **standing wave approximation** is valid for cavities like ours (Fig. 1.2) where the laser
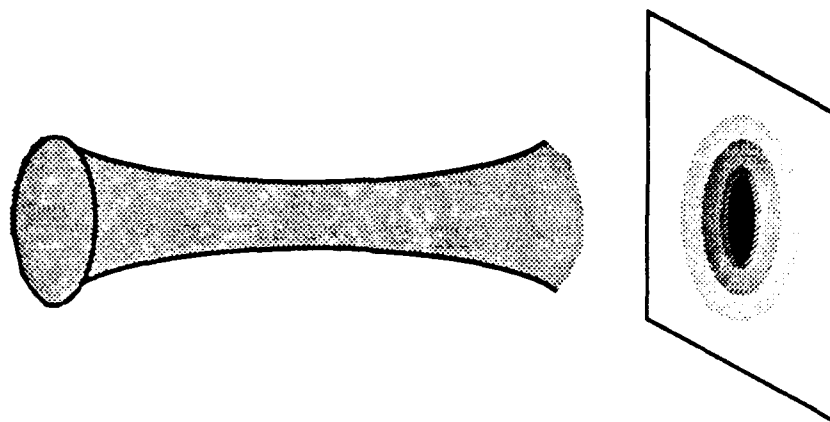
a. Convergent and Divergent Beam with
Gaussian Cross-Section
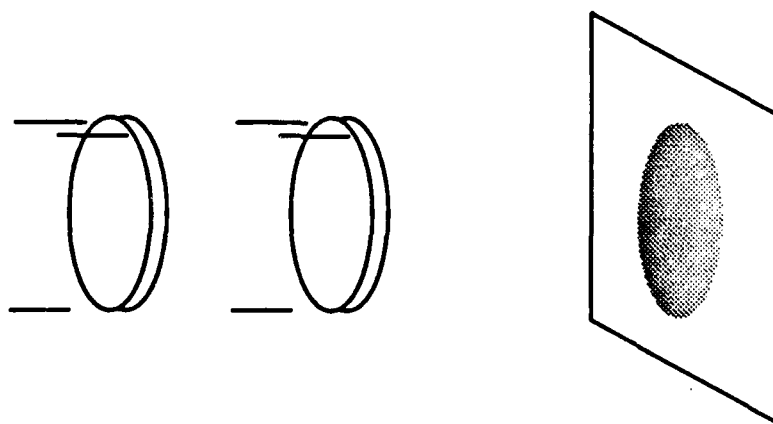
b. Plane Wave Approximation with
Uniform Cross-Section

Fig. 1.4 Comparison of Actual Beam Cross-Section with
Plane Wave Approximation.

beam reflects between two mirrors (as opposed to a ring laser where a beam can travel continuously in one direction). The intensity I_j of a longitudinal mode is simply the squared magnitude of its complex electric field: $I_j = |E_j|^2$. The cross-section of a laser beam is generally not uniform (Fig. 1.4), but we assume that the transverse modes do not affect the dynamics of the longitudinal modes; this is essentially a plane-wave approximation.

The laser's output intensity is the most directly observable physical quantity, so the relevant systems of ordinary differential equations which describe our laser include an equation for the intensity (or field) of each active longitudinal mode. The propagation of a longitudinal mode (i.e. a stream of photons) in the cavity serves to deplete the population in the upper excited energy state; we say this reduces the **gain** or the available gain for all the modes. In fact the net gain, G_j, of a particular mode is defined by the relative increase ($G_j > 1$) or decrease ($G_j < 1$) in the mode amplitude after one round trip through the cavity. The time evolution of the gain G_j depends on the population inversion (a larger inversion tends to strengthen the mode amplitude) and the losses experienced by the mode in a round trip (due to transmission through the output mirror and scattering by impurities in the air and in the optical cavity elements). Knowing the transmission percentage of the output mirror, we can calculate the approximate cavity losses for a given mode (see Appendix B).

The coupled ordinary differential equations that describe the time variations of intensity and gain for a single mode come from the optical Maxwell-Bloch equations (Siegman, 1986; McMackin, et al., 1988; Baer, 1986). These equations are referred to as rate equations because, while the sources of gain and loss only influence a given mode over a small portion of the complete round trip (or almost instantaneously as in the case of mirror transmission), these effects are represented as overall rates of gain or decay which apply uniformly over the length of the cavity. This is a common assumption and a well-established approach to laser dynamics. The Nd:YAG laser belongs to a much larger class

of lasers, class-B lasers (Arecchi, 1987), whose essential single-mode dynamics are contained in two coupled ordinary differential equations (see Appendix A for more details):

$$\tau_c \frac{dI}{dt} = I(G - \alpha) \qquad\qquad 1.2.a$$

$$\tau_f \frac{dG}{dt} = \gamma - G(1 + \beta I) \qquad\qquad 1.2.b$$

where τ_c is the cavity round trip time, τ_f is the upper state lifetime (or fluorescence time), α is the total cavity loss, γ is the pump strength, and β is a self-saturation parameter that gauges how strongly the intensity amplitude depletes the available gain. It is important to note that the time scales τ_c and τ_f for the YAG laser differ by five to six orders of magnitude, with τ_c on the order of nanoseconds and $\tau_f = 0.24$ msec. For reference, the phenomena studied in this thesis generally occur on a time scale of 1 μsec to 1 msec; for most of our discussions, 0.5 sec is an extremely long time, and 10^{14} Hz is a very high frequency.

There are an infinite number of candidate electric fields (1.1) that can oscillate in a given laser cavity; the gain profile of a cavity (Fig. 1.5) describes the cavity's gain (or loss) characteristics which select out certain modes to lase with different relative strengths. The relative losses experienced by different modes can arise from nonuniformity of optical elements in the cavity, beam misalignment, or intentionally through the use of etalons, glass plates inserted in the cavity to purposefully restrict the number of active modes. Another important influence on the relative mode strengths is the spatial overlap of modes in the active medium, where several longitudinal modes compete for the same (local) collection of excited particles (Fig. 1.6). For a single mode, there is no
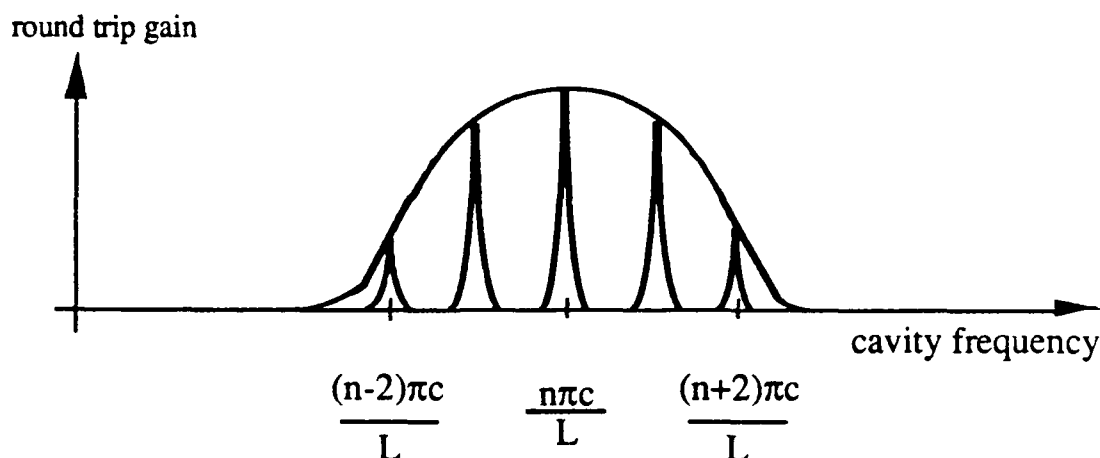
round trip gain

Fig. 1.5 Example of a Gain Profile for a Typical Laser Cavity.   Some frequencies
experience less gain during each round trip, as depicted by the gain profile.

problem; the mode amplitude varies in space sinusoidally, and wherever the intensity is

strong, the local population inversion is small (or zero). Similarly, the regions in the active

medium where the intensity is small have relatively large inversions. If a second mode tries

to lase (e.g., as we increase pump power above a certain threshold), it sees a nonuniform

population inversion along the length of the active medium; in the regions where both

intensities reach their relative maxima, the gain is quickly depleted and the two modes are

strongly coupled by their **cross-saturation**. This coupling plays an important role in

later discussions of multimode rate equations.

To this point, we have reviewed the basic operation of any laser. We now

introduce the concepts particular to frequency doubling. The first relevant property of an

optical element is its index of refraction, which describes the relative speed at which light

passes through the element. The index of refraction generally depends on the frequency

and incident angle of entering light. Many crystals, like mica and calcite, have

intensity   available gain
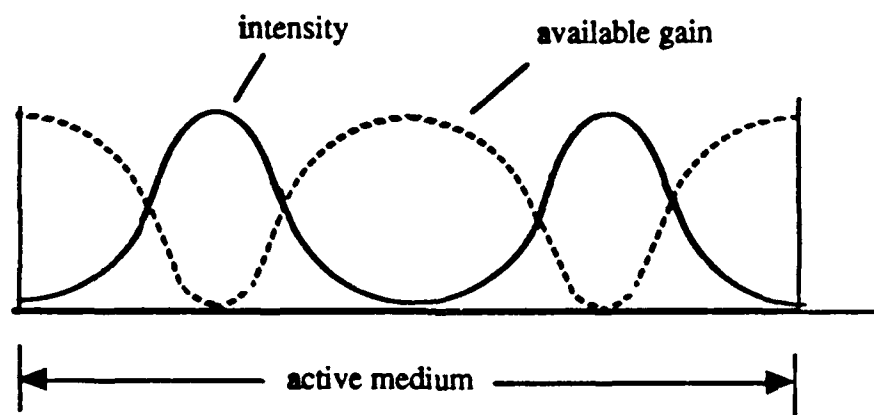
active medium

a. Intensity peaks deplete the available gain.
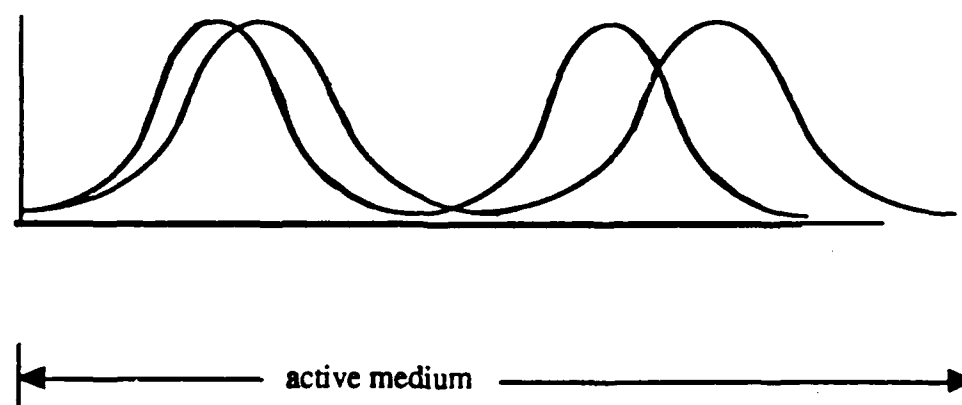
active medium

b. Strong coupling between two modes via spatial overlap

Fig. 1.6 Spatial Dependencies of Intensity and Gain in the Active Medium

more than one refractive index for different orientations of the electric field; a material with two principal indices of refraction n_j is called birefringent, and the directions associated with the two refractive indices are denoted the fast and slow axes (or extraordinary and ordinary axes), with the latter title referring to the smaller refractive index. For an electric field incident on a birefringent material, the field generally has components along both the fast and slow axes, so the birefringent element (with length l) introduces a relative phase delay $\delta = (n_1 - n_2)2\pi l/c$ between the two component directions. Special optically birefringent elements are designed to produce specific phase delays for electric fields of given frequencies. Later chapters, for example, illustrate the use of a quarter wave plate (QWP) which introduces a relative phase delay of $\pi/2$ in the two components of an electric field having a particular frequency.

The frequency doubling we consider in this thesis is accomplished by a birefringent potassium titanyl phosphate (KTP) crystal which converts a small percentage of input light at 1064 nm into green light at the doubled frequency, or halved wavelength 532 nm. The KTP crystal is cut at a particular length and orientation to make the doubling process as efficient as possible (Fan, et al., 1987; Ito, et al., 1975). When the intensity of a single longitudinal mode is (partially) converted to doubled light, we refer to the process as second harmonic generation (SHG); when two photons of different modes with similar frequencies combine to produce light at a frequency very close to that of the doubled frequency, we call the process sum-frequency generation. We refer to both processes as frequency doubling and make the distinction between SHG and sum-frequency generation when necessary.

An important feature of the doubling process is that the intensity of the doubled light is proportional to the squared intensity of the input light at the fundamental frequency. This is the motivation to place the doubling crystal inside the cavity, to take advantage of

the stronger intracavity fundamental intensity and increase the doubling efficiency. It also explains our interest in understanding and controlling the irregular intensity fluctuations that result from intracavity doubling.

We now return to Fig. 1.2 and describe our experimental setup in more detail. Our laser contains a 5 mm long Nd:YAG crystal pumped by a 10 element phase array laser diode. The diode laser beam is preconditioned by cylindrical lenses to focus to a small circular spot on the flat input face of the YAG rod. The input face of the YAG is coated with a mirror that allows the pump beam to enter the cavity, and reflects both the fundamental intensity (1064 nm) and the doubled intensity (532 nm) with high efficiency. A KTP crystal performs the intracavity doubling and is specially coated to minimize reflections at both wavelengths. The output mirror is highly reflective at the fundamental frequency, but is highly transmissive for the green light. Some cavity configurations we consider later include etalons to restrict the number of longitudinal modes in the cavity; other configurations include quarter wave plates to influence the propagation of different components of electric fields in the cavity.

The experimental pump strengths we consider are referenced to a threshold pump level at which the laser barely turns on. Our experiments include pump ranges from about 1.5 times threshold (intensity output is obscured by noise for any lower pumping) to 15 times threshold (an upper bound imposed by pump currents for the pumping laser). Samples of experimental output of total fundamental intensity (the total contribution of all longitudinal modes) are shown in Fig. 1.7. A wide range of behavior is observed, depending on the particular cavity configuration; the intensity traces shown here are for different values of input pump power. A realistic system of equations must also display this range of time-dependent behavior.

Pump Strength
(× threshold)

7.0

(d)

6.0

4.5

(c)

3.5

(b)   2.5

(a)   1.5
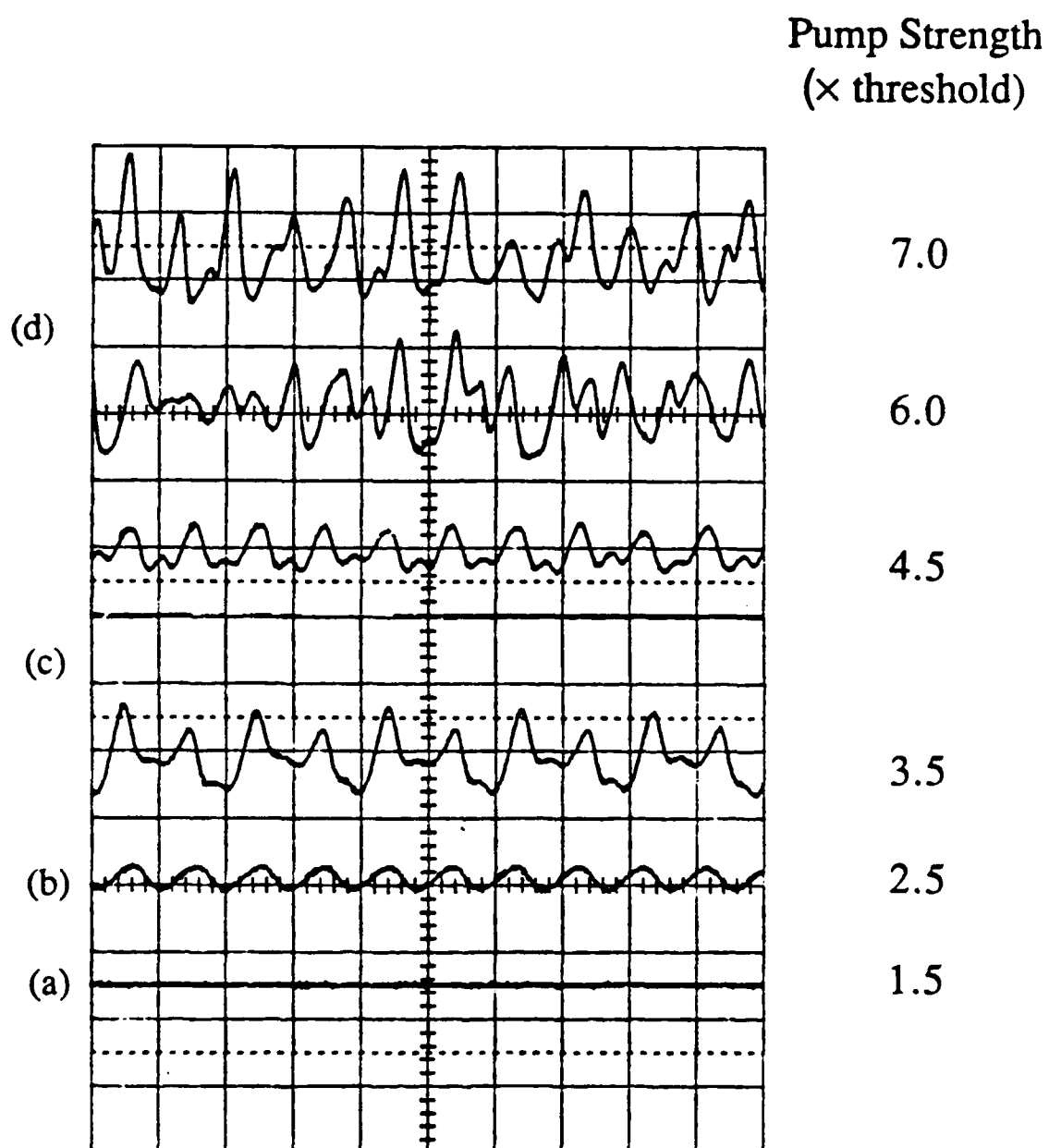
Fig. 1.7   Samples of Intensity Output from an Intracavity Doubled Nd:YAG Laser.
Changing the input pump power produces: (a) stable output, (b) periodic
output, (c) multiple-period output, (d) chaos.

There are, of course, other types of lasers which produce green light, so why should we trouble with the instabilities which seem to be inherent in intracavity doubling? The answer lies in recent improvements in the power and efficiency of diode lasers for use as pump sources for solid state gain media (Byer, et al., 1984; Fan and Byer, 1988; Chumbley, 1989; Lin, 1989; Perkins and Fahlen, 1987). Diode-pumped solid state lasers are compact, long-lived, and more efficient than other types of lasers which output light at comparable frequencies. The diode laser offers the advantage of stable pumping with little noise; the diode-pumped Nd:YAG has much greater frequency stability than the diode laser itself. There are countless applications for the green light produced by the frequency doubled YAG, with particular emphasis on color laser printing, in low-power applications (Fujii, 1986; Cook, 1988; Takashima, et al., 1987; Fitzpatric, et al., 1986). The growing interest in frequency doubled lasers highlights the importance of understanding the dynamics of the doubling process, so we can control the output instabilities which have restricted their use in some applications.

As a final note to this section, we highlight some vocabulary subtleties, to avoid confusion later in the thesis. The **fundamental** frequency in our laser is the frequency at which the Nd:YAG crystal lases, usually identified by the wavelength, 1064 nm. The **doubled** frequency is the output produced by the KTP doubling crystal; in our case this is at a wavelength of 532 nm. There are two different "frequency" domains we discuss in the thesis. The first is in the context used above where we address the frequency of electromagnetic field oscillations. This is distinct from the frequency content of intensity time histories which we examine later using Fast Fourier Transforms (FFT's) of numerical integrations and experimental data. Next we point out two kinds of **oscillations** found in our discussions. In one context, we say that a longitudinal mode is "active", or "lases", or "oscillates" in the laser cavity, interchangeably. In another context, we observe periodic or

irregular oscillations in the time traces of intensity output. Finally, we refer to **polarization** in two different ways. The first is an atomic polarization, a dipole moment due to a distribution of electric charge. This polarization is a key variable in the Maxwell-Bloch equations reviewed in Appendix A. The second polarization refers to the (not necessarily fixed) direction along which an electric field amplitude fluctuates. Thus, we can place polarizing filters in the path of the beam to measure intensity output in particular polarization directions. The interactions of polarized electric fields and birefringent materials is critical to the new model of intracavity doubling presented in Chapter III.

Basics of Dynamical Systems

This section briefly reviews the main tools of ordinary differential equations and dynamical systems which are used to study the systems of equations that arise in later chapters. We assume the reader is familiar with the technique of linearizing a system of equations in the neighborhood of a steady state point to discover some of its stability properties; we also assume a familiarity with different types of stability: center points, asymptotic stability, saddle points, etc. More details can be found in standard texts on ordinary differential equations and dynamical systems (e.g., Hale, 1969; Jordan and Smith, 1987; Guckenheimer, 1980).

We define a dynamical system using a differential equation which we write here in general form, for an N-dimensional vector x:

$$\frac{dx}{dt} = F(x,t) \qquad\qquad 1.3$$

where the right hand side of the equation is also vector-valued. (We recall that the Jacobian of F is the matrix formed by taking partial derivatives of F with respect to the components of x.) A dynamical system, then, is defined by a solution operator $\phi(x,t)$ which describes the time evolution of (1.3). The operator ϕ is defined on R^{N+1} (the N dimensions of x, plus time), is continuous with respect to initial conditions, and for any x in the domain of F, satisfies:

$$\phi(x,0) = x \qquad\qquad 1.4.a$$

$$\phi(x,t+s) = \phi(\phi(x,s),t) . \qquad\qquad 1.4.b$$

Property (1.4.b) simply states that the solution found by integrating (1.3) from 0 to (t+s), with initial condition x, is identical to the solution found by integrating from 0 to s with initial condition x, then using $\phi(x,s)$ as the initial condition for a subsequent integration from 0 to t (Fig. 1.8).

$$x = \phi(x,0)$$

$$\phi(x,s)$$

$$\phi(x,t+s)$$
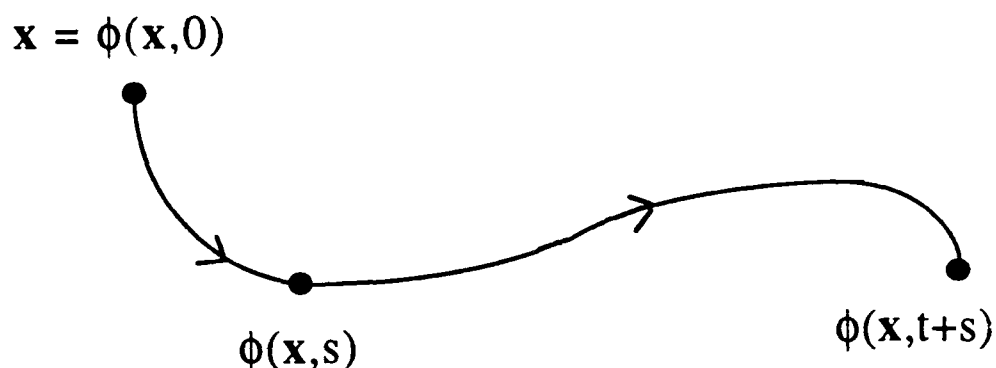
Fig. 1.8   Sketch of the Solution Operator ϕ.

Almost all the systems of equations we consider in this thesis are autonomous, i.e. **F** does not depend explicitly on time. For such equations, it is useful to construct phase diagrams like Fig. 1.9 for the system of equations in question. The N-dimensional phase space for (1.3) is defined by the N coordinates of **x**. The phase portrait usually includes the steady state points of (1.3), where **F** = 0, plus some general indication of the flow vectors (**F**(**x**)) elsewhere in the phase space. All the equations we consider have a right side **F** which is infinitely differentiable; this implies that the solution passing through every initial condition is unique.
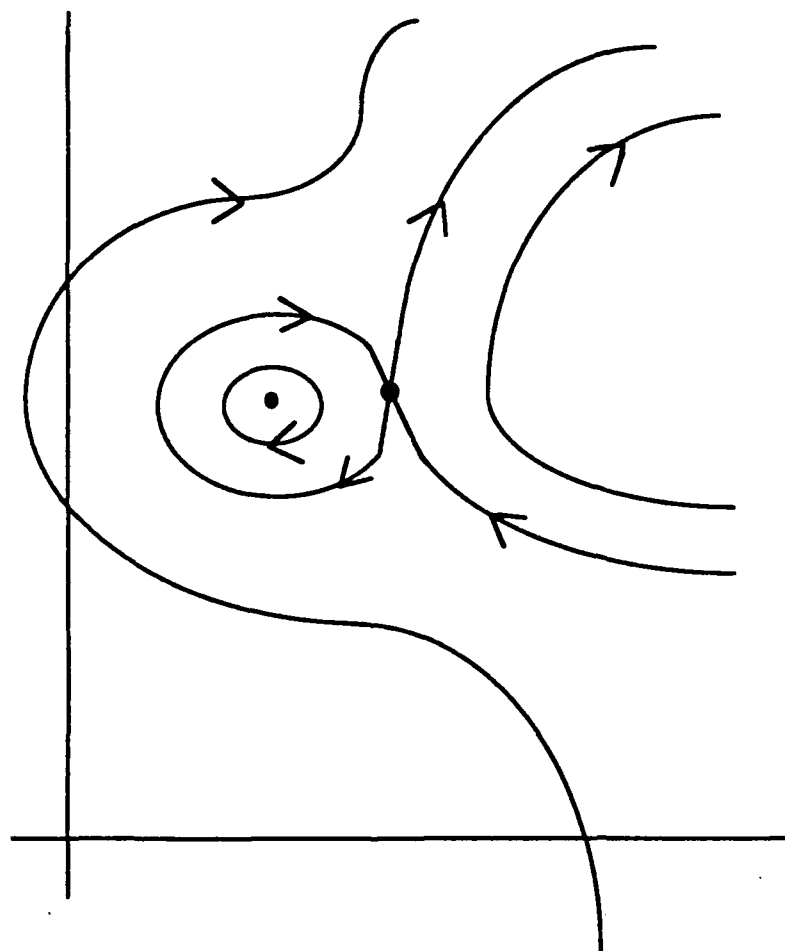
Fig. 1.9 Generic Phase Portrait. The sketch shows one center and one saddle point.

A phase sketch also indicates the type of stability of the steady state points as well as the structure of their stable and unstable manifolds. The stable manifold $W^s(x)$ of a point x where $F(x) = 0$, is the set of initial conditions whose solutions asymptotically approach x as $t \to +\infty$. Similarly, the unstable manifold $W^u(x)$ is the set of initial conditions whose solutions approach x as $t \to -\infty$. We sometimes refer to the solution passing through an initial condition as the trajectory of that point in phase space. A trajectory which does not asymptotically lead to a single point in phase space can have many other limiting behaviors: e.g., a periodic limit cycle, an unbounded trajectory, or a chaotic trajectory (to be defined shortly) which is bounded but aperiodic.

If our phase space is planar, and F is continuously differentiable, a classic theorem by Poincaré and Bendixson states that any bounded trajectory must approach either a single fixed point, a periodic limit cycle, or a homoclinic cycle (where one or more trajectories begin and end at a steady state point); this occurs because uniqueness of trajectories prevents them from crossing each other in the phase plane. If the phase space has three or more dimensions, however, there is extra room in the phase space for trajectories to pass around each other, so the restriction that trajectories can not cross no longer inhibits the limiting behavior of a trajectory (in most cases). Thus, for a bounded phase space with two dimensions, no chaotic solutions can exist. When the phase space has three or more dimensions, chaos can occur. Later in the thesis, this fact indicates the minimum number of differential equations needed in the model to produce chaotic output.

We use several other simple properties of (1.3) and its associated phase portrait to characterize the solutions of (1.3). For example, we can sometimes find a bounded region of phase space where all the flow vectors point into the interior of the set. A region like this is called an absorbing set; any trajectory which enters such a set must remain in it for all later times. We also get information about the flow from the trace of the Jacobian of F,

since the trace of a matrix equals the sum of its eigenvalues. If this trace is negative in a region of phase space, it indicates that the flow is locally dissipative. If a trajectory enters an absorbing set where the trace of the Jacobian is negative in the entire set, then the trajectory must asymptotically approach a stable steady state point in that set.

Another tool we use to study solutions to (1.3) is a Poincaré map. We define this map on a surface of N-1 dimensions called a **transversal,** which is chosen so that the flow is not tangent to the surface. For each point y on the transversal, the Poincaré map P(y) is defined as the point on the surface where the solution of (1.3) through y next passes through the transversal (Fig. 1.10). The properties of the Poincaré map give direct information about the flow in the complete phase space. A periodic orbit, for instance,
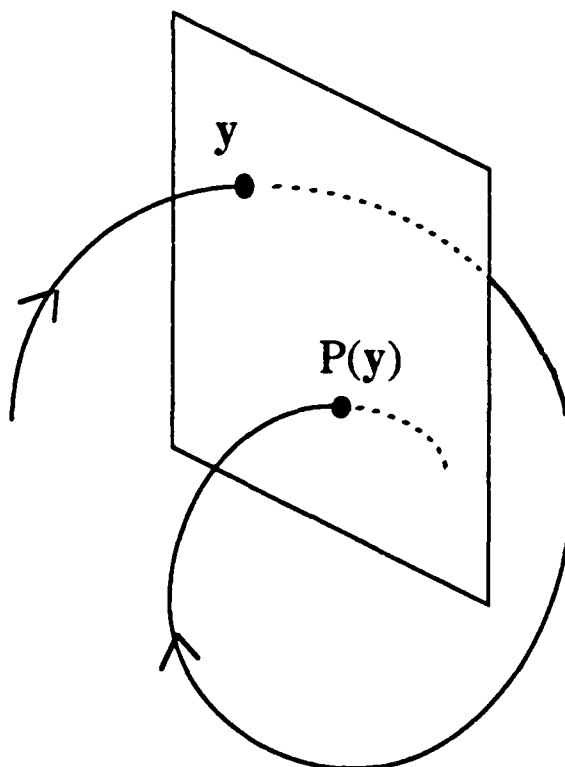
Fig. 1.10   Construction of a Poincaré Map.

crosses the transversal at the same point for all time, so points in a Poincaré map which tend toward a single fixed point indicate that the flow is converging to a periodic orbit. Similarly, toroidal flow in the phase space appears as a closed loop (or a countable number of fixed points) in the Poincaré map. The map inherits continuity from the continuity of F; we can linearize the Poincaré map about its fixed points and compute eigenvalues (Floquet exponents) of the linearized matrix to determine the stability properties of those fixed points. Some systems of equations can be integrated analytically to derive explicit expressions (or at least local approximations) for the Poincaré map on a given transversal. The equations we study in this thesis are sufficiently complicated to require numerical integration to approximate the Poincaré maps we use.

We now specify the conditions under which we identify a particular trajectory as chaotic. The first requirement is sensitivity to initial conditions (SIC). Recall that the solution operator is continuous as a function of initial conditions, but for trajectories which exhibit SIC, a small perturbation in the initial condition is amplified exponentially in increasing time, so that two trajectories which start out arbitrarily close to each other diverge exponentially in some finite time. The trajectories we identify as chaotic in Chapters II and III have this property. Chaotic solutions to our systems of equations also tend to "fill up" regions of a Poincaré map. That is, a periodic or quasiperiodic trajectory generates a point or a closed loop in the Poincaré map, while a chaotic trajectory generates a continuous distribution of points across a bounded (not necessarily connected) subset of the transversal (compare, for example, the maps in Fig. 3.17(j)). The aperiodic nature of a chaotic trajectory is further characterized by a broad FFT. A broad-banded spectrum can also be produced by a signal with substantial noise; however, a chaotic trajectory will also display SIC, while a noisy signal may not.

A route to chaos describes the changes in the character of the flow as a function of one or more parameters in **F**. A particular route to chaos is generally identified by the transfer of stability, or bifurcation, from one type of solution to another. An equilibrium point, for instance, may lose its stability as a parameter increases through some threshold value, such that the stable limiting behavior near that point is no longer a steady state but a periodic orbit. For an extensive study of bifurcation theory, see (Chow and Hale, 1982). One particular route to chaos we find in the equations studied in Chapter II is known as **intermittency**. In intermittent chaos, periods of laminar (apparently periodic) behavior are interrupted at irregular time intervals by turbulent (chaotic) flow. More details on the nature of intermittency in our problem are presented in the next chapter; a review of the fundamentals of intermittency appear in Appendix C, with extensive references.

CHAPTER II

THE BAER MODEL

Introduction

The first attempt to model the unstable multimode dynamics of a diode-pumped intracavity doubled Nd:YAG laser was documented by T. Baer of Spectra-Physics(Baer, 1986). He presented theory and experimental data that describe the time-dependent behavior of laser intensity as a function of the number of longitudinal modes oscillating in the cavity.

Recall that the frequencies and number of longitudinal modes are determined by the cavity length and by the cavity gain profile. By placing etalons (glass plates which affect the relative losses of different modes) in the cavity, Baer further controlled the number of active modes. With the laser restricted to single mode operation, he observed only stable steady state output. When two modes were allowed to oscillate, the total intensity output showed periodic pulses; the two modes took turns switching on and off. New intensity behavior was observed for three modes. For some cavity configurations, sequential pulsing was seen (numerically), similar to the output for two modes. In other cases, the total intensity for three active modes displayed large aperiodic fluctuations which did not damp out in time.

This section includes theoretical and numerical analyses of the model proposed by Baer. A linearized analysis for the multimode Baer equations was begun by P. Mandel and X.-G. Wu (Wu and Mandel, 1985; 1987). Their analysis focuses on the two-mode case,

with few restrictions on the parameters. The main result they report is that Hopf bifurcations (from equilibria to periodic solutions) only occur when two or more modes are oscillating; otherwise only steady bifurcations occur, from single-mode to two-mode solutions. They also report a linearized analysis of the N-mode equations in limits of certain parameter values.

The first unique element of our analysis is that we consider not only the stability characteristics of the steady state points, but also how the stable and unstable manifolds of these points interact (numerically) to produce different types of solutions. Throughout the thesis we examine global dynamics to see how various models compare to experiment when the laser does not operate in a stable steady state. We also present a novel technique for simplifying the linear stability analysis in a way that leads to more general criteria for steady state stability. Moreover, we believe our work to be the first which characterizes the observed aperiodic intensity fluctuations as chaotic dynamics; we provide numerical evidence of an intermittency route to chaos. Our study identifies the frequency doubled Nd:YAG laser as one of few experimental systems observed to date which demonstrate intermittent chaos in a strictly passive cavity configuration.

Single-Mode dynamics

Analysis

Prior to Baer's study, theoretical work had concentrated on equations which describe only a single mode in the laser (Smith, 1970; Kennedy and Barry, 1974). The differential equations model the time dependence of the single intensity I_1 and the associated gain G_1 (Baer, 1986):

$$\tau_c \frac{dI_1}{dt} = I_1 \left(G_1 - \alpha - \epsilon I_1 \right) \qquad\qquad 2.1.a$$

$$\tau_f \frac{dG_1}{dt} = \gamma - G_1 \left(1 + \beta_1 I_1 \right), \qquad\qquad 2.1.b$$

where τ_c is the time taken by a photon to make one round trip through the cavity; α represents all cavity losses exclusive of doubling losses; ϵ is a coupling coefficient which depends on the nonlinear optical properties of the KTP doubling crystal; τ_f is the fluorescence time (lifetime of the upper excited energy state); γ is the small-signal gain (due to the energy input by the pumping diode laser); β_1 is the saturation parameter which determines how strongly the intensity depletes the available gain. The parameter values used by Baer for the single-mode equations appear in Table 1.

Table 1. Parameter Values for the Single-Mode Baer Equations.
These are the parameter values used for the analyses
in this chapter, unless otherwise noted.

$\tau_c = 0.5 \times 10^{-9}$ sec   cavity round trip time

$\tau_f = 0.24 \times 10^{-3}$ sec   fluorescence time

$\alpha = 0.015$ cavity losses

$\epsilon = 5.0 \times 10^{-5}$ KTP coupling coefficient

$\gamma = 0.12$ pump parameter

$\beta_1 = 1.0$ self-saturation parameter

$l = 5.0$ cm   cavity length

We scale the intensity to be dimensionless, so all variables in (2.1) are non-negative and dimensionless, except for time variables. Recall that the gain G_1 is a measure of the net increase or decrease in intensity experienced during one round trip through the cavity. The cavity losses described by α are almost entirely due to transmission through the output mirror (see Fig 1.2). The doubling term $-\epsilon I_1^2$ represents the intensity losses due to second harmonic production through frequency doubling.

The relative magnitudes of various parameters govern much of the dynamics of (2.1). For any cavity length between 3 cm and 1 m, $\tau_f/\tau_c \approx 10^5$ (see Appendix B on parameter calculations), so I_1 fluctuates much faster than G_1. The tendency of I_1 to increase or decrease in (2.1.a) depends on how the current value of gain compares to the loss terms $(-\alpha - \epsilon I_1)$. As a physical constraint, the small signal gain γ must always exceed the loss α in order to sustain any lasing; this is confirmed analytically in the stability analysis below. Note that doubling losses are proportional to the squared intensity, while cavity losses are only proportional to I_1. Also notice that ϵ is several orders of magnitude smaller than α, so the frequency doubling process adds a small quadratic perturbation to the usual single-mode rate equations.

Equations 2.1 include another interesting detail. The intensity equation describes a single longitudinal mode which oscillates at the fundamental frequency; there is no differential equation for the new intensity at the doubled frequency. This is because we treat the doubling process strictly as a loss in the fundamental intensity, and because the higher frequency green light is almost entirely transmitted out of the cavity at the output mirror (see Fig 1.2). Thus we neglect the effect of small amounts of green light which are reflected back into the cavity.

We now give a complete study of the phase portrait and stability analysis for (2.1). This is fairly straightforward and provides a great deal of insight for the multimode dynamics which we treat in later sections. A local stability analysis and review of the single mode transient behavior was carried out in (Kennedy and Barry, 1974). Some of their eigenvalue analysis appears in the discussion which follows.

The region of interest in the two-dimensional phase plane is the first quadrant where intensity and gain are nonnegative observable quantities. There is actually a bounded rectangle U_1 which is an absorbing set, as long as ε is not zero (Fig. 2.1). (If $\varepsilon=0$, U_1 has no top boundary.) No trajectories can cross the bottom of the absorbing rectangle, since the flow along the G_1 axis converges to the point $G_1 = \gamma$. When $G_1 = 0$, along the I_1 axis, dG_1/dt is positive, so all the flow on this line must enter the rectangle. Similarly, the flow must enter the rectangle from the right, along the line $G_1 = \gamma$, since dG_1/dt is negative along that line. The top edge of the absorbing set is defined by any line $I_1 = $ constant, where the constant is greater than $\varepsilon/(\gamma - \alpha)$. This causes dI_1/dt to be negative, and flow must enter the rectangle from the top.

The sketch of the rest of the phase portrait begins with the identification of the equilibria and their stability analysis. The steady state solutions of (2.1) are found by setting the derivatives to zero, and solving for the following steady state values I_s and G_s:

$$G_s = \frac{\gamma}{(1 + \beta_1 I_s)}, \text{ with}$$

(a) $\quad I_s = 0$

(b) $\quad I_s = \left(\frac{\varepsilon + \alpha\beta_1}{2\varepsilon\beta_1}\right)\left(\sqrt{1 + \frac{4\varepsilon\beta_1(\gamma - \alpha)}{(\varepsilon + \alpha\beta_1)^2}} - 1\right)$

$\qquad\qquad\qquad\qquad\qquad\qquad\qquad\qquad\qquad 2.2$

(c) $\qquad I_s = \left(\dfrac{\varepsilon + \alpha \beta_1}{2\varepsilon \beta_1}\right)\left(-\sqrt{1 + \dfrac{4\varepsilon\beta_1(\gamma - \alpha)}{(\varepsilon + \alpha\beta_1)^2}} - 1\right)$

$\qquad\qquad\qquad\qquad\qquad\qquad\qquad\qquad\qquad\qquad\qquad$ 2.2, cont.

Both I_1 and G_1 are non-negative physical quantities, so the third equilibrium is not a feasible physical solution for any parameter values. The first solution, where the intensity is zero, represents a point where the laser is off. The second solution, with a non-zero intensity, is of most interest physically.

$\qquad$ The dynamics in the immediate neighborhood of an equilibrium is determined by linearizing the right side of (2.1). This Jacobian J_1, written here with the gain G_1 as the first coordinate, is:

$$\begin{bmatrix} -\dfrac{1}{\tau_f}(1 + \beta_1 I_s) & -\dfrac{1}{\tau_f}\beta_1 G_s \\[2mm] \dfrac{I_s}{\tau_c} & \dfrac{1}{\tau_c}(G_s - \alpha - 2\varepsilon I_s) \end{bmatrix} \qquad 2.3$$

where I_s and G_s are the steady state values of the intensity and gain. At the steady state point $G_s = \gamma$, $I_s = 0$ (2.2.a), the eigenvalues and eigenvectors of the Jacobian are:

$$\lambda_1 = -\dfrac{1}{\tau_f} \qquad v_1 = \begin{bmatrix} 1 \\ 0 \end{bmatrix}$$

$\qquad\qquad\qquad\qquad\qquad\qquad\qquad\qquad\qquad\qquad\qquad$ 2.4

$$\lambda_2 = \dfrac{\gamma - \alpha}{\tau_c} \qquad v_2 = \begin{bmatrix} -\dfrac{\beta_1 \gamma}{\tau_f} \\[3mm] \dfrac{\gamma - \alpha}{\tau_c} + \dfrac{1}{\tau_f} \end{bmatrix} .$$

The negative eigenvalue λ_1 indicates a trajectory approaching the equilibrium; its eigenvector points along the G_1 axis for all parameter values. The second eigenvalue depends somewhat on the parameter settings. If $\gamma < \alpha$, then λ_2 is negative and this equilibrium is stable. In fact, since the right boundary of U_1 is fixed at the line $G_1 = \gamma$, any value of γ less than α would prevent the gain from ever surpassing the losses, and this trivial equilibrium would be globally stable, i.e. the laser could never stay on. We also see from (2.2.b) that $\gamma = \alpha$ is a critical threshold above which the intensity may take on positive values. Thus, for the remainder of our analyses, we assume a value of γ greater than α. This renders λ_2 a positive eigenvalue which indicates a trajectory departing the neighborhood of the equilibrium; the eigenvector v_2 always points into the absorbing rectangle. These local flow characteristics are included in the phase diagram in Fig. 2.1.

When the Jacobian is evaluated at the internal equilibrium (2.2.b) the eigenvalues are:

$$\lambda_{1,2} = -\frac{1}{2}\left(\frac{\epsilon I_s}{\tau_c} + \frac{(1 + \beta_1 I_s)}{\tau_f}\right) \qquad 2.5$$

$$\pm \frac{1}{2}\sqrt{\frac{\epsilon^2 I_s^2}{\tau_c^2} + \frac{(1 + \beta_1 I_s)^2}{\tau_f^2} - \frac{2\epsilon I_s(1 + \beta_1 I_s) + 4\beta_1 G_s I_s}{\tau_c \tau_f}} \ .$$

The expression under the radical is dominated by the negative third term, so λ_1 and λ_2 are complex. These imaginary eigenvalues indicate locally spiralling trajectories, and the (always) negative real parts imply local convergence to the equilibrium.

The convergence to a stable equilibrium, as indicated by the linearization, is of course only a local property of the flow. While we have the existence of an absorbing set, which guarantees an attractor of some type in U_1, we can not immediately invoke a fixed

point theorem to prove global convergence to this equilibrium, because the flow is not dissipative everywhere in the region. (This is also the case in other well-known systems like the Van der Pol oscillator where global stability is difficult to prove analytically.) In particular, the shaded triangle of Fig. 2.1 is the region where the trace of the Jacobian, $\text{tr}(J_1)$, is positive, so the flow there is locally expansive. The hypotenuse of the triangle is the line where $\text{tr}(J_1) = 0$, i.e. there is no local dissipation or expansion. In the unshaded area, $\text{tr}(J_1)$ is negative, so the flow is dissipative, and any trajectory which remains in this region for all $t > t_0$ (for some reference time t_0) must converge to the equilibrium point. The two dimensional phase portrait can be sketched in some detail as seen in Fig. 2.1.

Numerical Results

Laboratory experiments where the laser operates in a single mode show only transient oscillations to a stable steady state; this fact supports the case for global convergence in the phase space analysis. Numerical integration of (2.1) also indicates global convergence: all numerical trajectories, for many initial conditions, converge to the nontrivial equilibrium (2.2.b).

In Fig. 2.2, we show intensity time traces obtained numerically. The intensity I_1 is plotted for different values of the parameter ε. For larger values of ε, i.e. stronger second harmonic conversion, the relaxation oscillations become completely damped out. The time scales of any oscillations are an important check for comparing numerical integrations to experimental data; such comparisons appear in later sections.
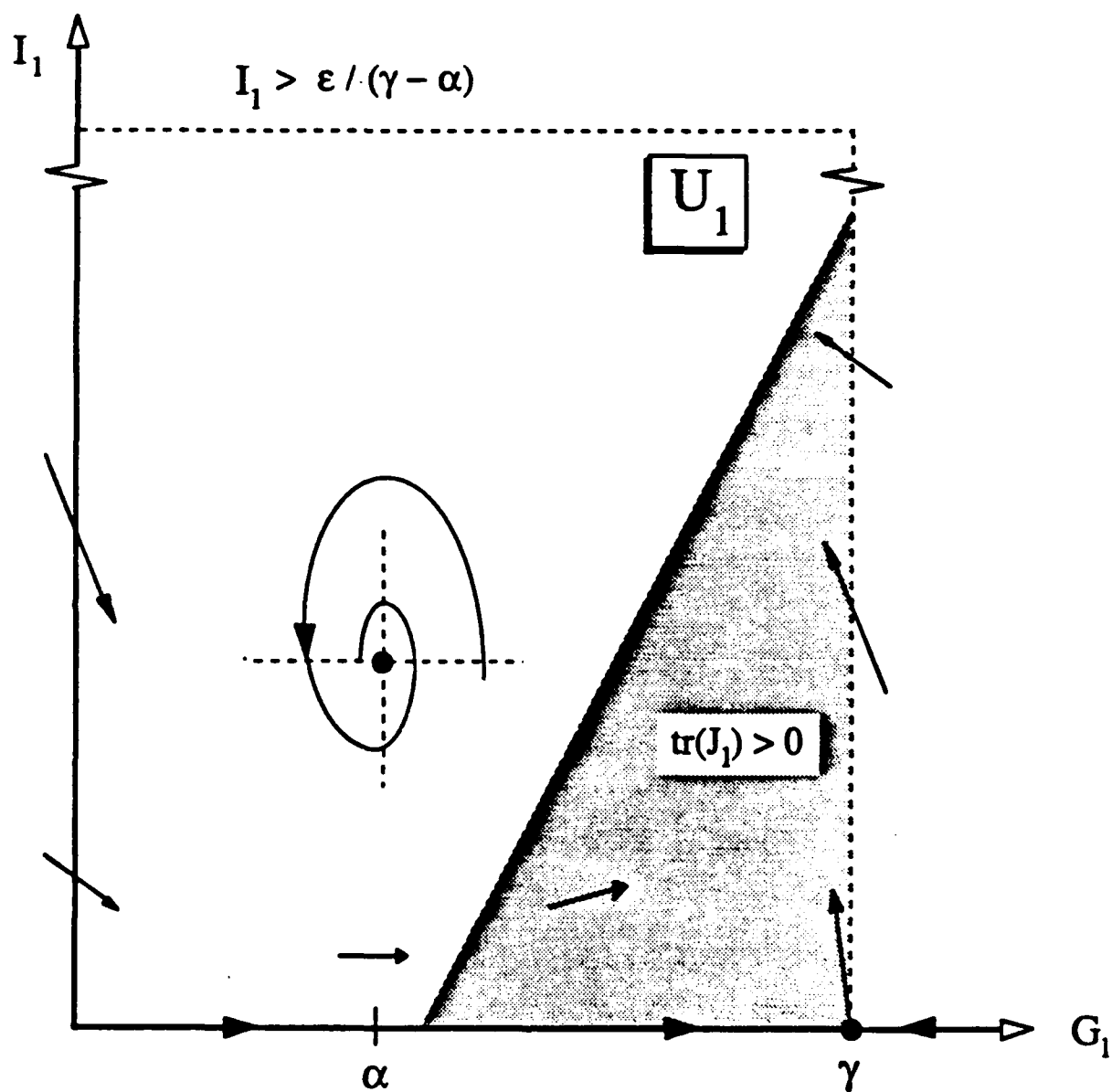
Fig. 2.1 Phase Portrait for the Single-Mode Baer Equations. The rectangle U_1 is an absorbing set.

The relative influence of the damping and the transient oscillations can be seen in a closer analysis of the eigenvalues in (2.5) (Kennedy and Barry, 1974). The real part of λ is the damping term, which depends on I_s, the steady state value of intensity:

$$Re(\lambda) = -\frac{1}{2}\left(\frac{\varepsilon}{\tau_c} I_s + \frac{\left(1 + \beta_1 I_s\right)}{\tau_f}\right).$$

2.6

Although I_s decreases with increasing ε (see (2.2.b)), the overall damping still increases for larger ε. This trend is highlighted in the plot of $Re(\lambda)$ in Fig. 2.3.

The oscillation frequency of trajectories which spiral in toward the steady state may be calculated from the imaginary part of λ. The magnitude of the negative term under the square root in (2.5) gives a good approximation for the frequency ω:

$$\omega \cong \left[\frac{2\varepsilon I_s\left(1 + \beta I_s\right) + 4\beta G_s I_s}{\tau_c \tau_f}\right]^{1/2}.$$

2.7

We notice that ε has a negligible influence on ω, while the damping term (2.6) is proportional to ε. This leads to an intersection of the curves in Fig. 2.3 at a critical value of ε, above which no oscillations away from the steady state are sustained. This is confirmed by the numerical time trace in Fig. 2.2(c), where ε is larger than the critical value, and the intensity asymptotically approaches steady state with no oscillations.
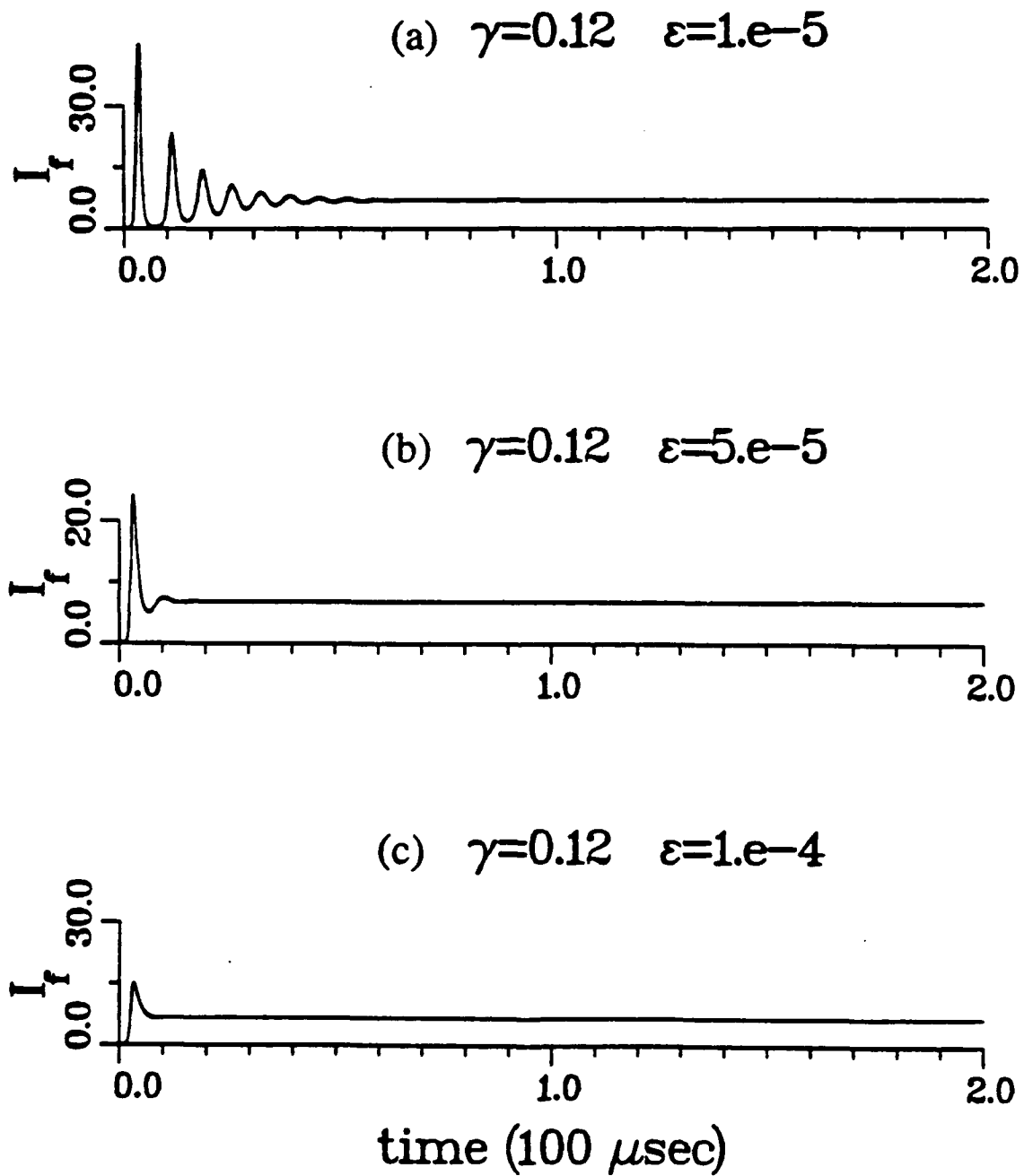
Fig. 2.2 Changes in Damping as a Function of ε.
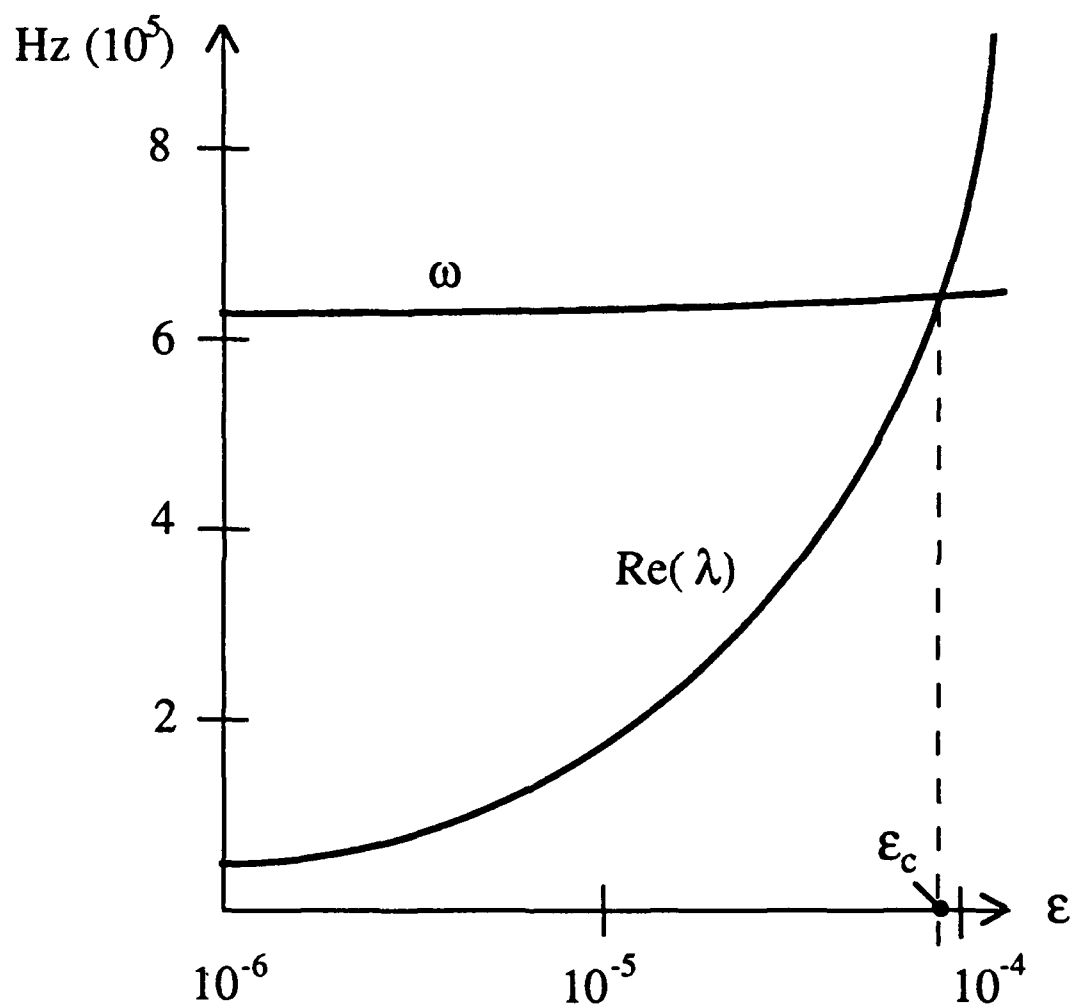
Fig. 2.3 Oscillation Frequency (ω) and Damping (Re(λ)) as Functions of ε.
For $\varepsilon > \varepsilon_c$ the damping suppresses all oscillations.

The transient oscillations shown in Fig. 2.2(b) correspond to spiralling trajectories in the associated phase space. For $\varepsilon = 5.0 \times 10^{-5}$, one sees in Fig. 2.4 that a trajectory, initiated near the unstable manifold of the trivial ($I_s = 0$) equilibrium, does not return to the expansive region of phase space. The existence of such an orbit, which spirals from the unstable manifold of (2.2.a) to the interior equilibrium (2.2.b), demonstrates global stability by the Poincaré-Bendixson theorem. This is true because any candidate periodic orbit would have to encircle the equilibrium and cross the spiral trajectory in finite time, violating the theorem.
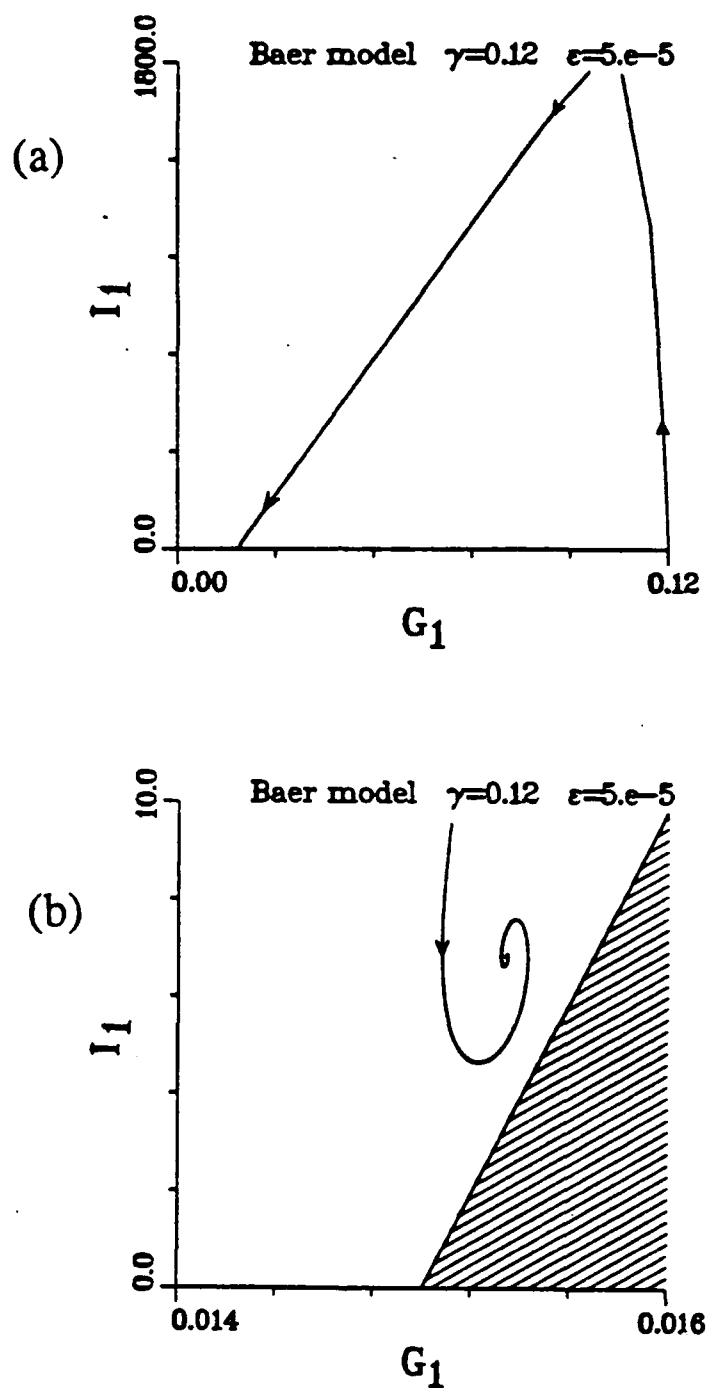
Fig. 2.4 Numerical Phase Portraits of the Single-Mode Baer Equations.
The intensity scale in (a) is enormous; the equilibrium point appears
close to the horizontal axis. (b) The trajectory does not return to the
shaded expansive region where $tr(J_1) > 0$.

Two-Mode Dynamics

Analysis

The study of the single-mode dynamics of an intracavity doubled laser is only a small step on the way to understanding the irregular intensity output observed by Baer. Ordinarily, one hopes to increase the laser output by allowing more than one longitudinal mode to lase; Baer hypothesized that some nonlinear coupling between modes was responsible for the large intensity fluctuations(Baer, 1986). A significant contribution of Baer's report was the generalization of the single-mode equations (2.1) to account for interactions between multiple longitudinal modes in the doubling process. To approach the multimode dynamics from the simplest point of view, we begin with an analysis of the two-mode case. The differential equations proposed by Baer (Baer, 1986) to model the intensities I_j and gains G_j of a doubled laser oscillating with two longitudinal modes are:

$$\tau_c \frac{dI_1}{dt} = I_1 \left(G_1 - \alpha_1 - \varepsilon I_1 - 2\varepsilon I_2 \right) \qquad 2.8.a$$

$$\tau_f \frac{dG_1}{dt} = G_1^0 - G_1 \left(1 + \beta_1 I_1 + \beta_{12} I_2 \right) \qquad 2.8.b$$

$$\tau_c \frac{dI_2}{dt} = I_2 \left(G_2 - \alpha_2 - \varepsilon I_2 - 2\varepsilon I_1 \right) \qquad 2.8.c$$

$$\tau_f \frac{dG_2}{dt} = G_2^0 - G_2 \left(1 + \beta_2 I_2 + \beta_{21} I_1 \right) . \qquad 2.8.d$$

These equations are almost identical to the single mode relations, with the following additional terms: (i) there is a separate small signal gain G_1^0 and G_2^0 for each mode; (ii) the cross saturation parameters β_{12} and β_{21} quantify how the two modes "compete" for the active medium (see discussion in Chapter I on spatial overlap); (iii) a new term also appears in the intensity equations to account for a different way of generating the new doubled frequency. The first doubling term, ϵI_1^2, describes losses in I_1 due to strict frequency doubling, or second harmonic generation (SHG), where two photons from the same longitudinal mode contribute to produce higher frequency light. The second doubling term, $2\epsilon I_1 I_2$, describes sum-frequency generation which also occurs in the doubling crystal. In the sum-frequency process, two different modes each contribute one photon to produce light at a frequency virtually indistinguishable from that made by SHG.

Baer justifies his choice of the factor 2, in the second doubling term, by noting that the sum-frequency output power is generally four times that produced by SHG (Shen,1984). If the subsequent loss in the fundamental intensities, due to sum-frequency generation, is shared equally, then the cross term $I_1 I_2$ appearing in each of the intensity equations should include a factor of 2. However, we have shown this to be true only in certain restrictive cases to be discussed in Chapter III (James, et al., 1990a). Nevertheless, it is still useful to retain Baer's hypothesis in the following analysis, to develop an intuition for the multimode dynamics of an intracavity doubled laser.

As in the single-mode case, the production of green light is treated as losses in the differential equations for the intensities which oscillate at the fundamental frequency. However, in the two-mode case, the total doubled intensity is now a sum of SHG contributions and sum-frequency generation. To compare the time histories of the total fundamental and doubled intensities (both measurable in the laboratory), the total doubled intensity I_d can be calculated by combining all the doubling loss terms:

$$I_d = \epsilon\, I_1^2 + \epsilon\, I_2^2 + 4\,\epsilon\, I_1\, I_2 \,. \qquad\qquad 2.9$$

The total fundamental intensity I_f is simply $I_1 + I_2$.

Similarly to what we found for the single-mode equations, the four-dimensional phase space for the two-mode case also has a bounded rectangular absorbing set, formed by the geometric cross product of the bounded rectangle U_1 for I_1 and G_1, and the rectangle U_2 for I_2 and G_2.

Steady State Analysis

In the two mode operation of the doubled $Nd:YAG$ laser, Baer observed only periodic pulsing of the two modes, and no stable steady state intensity was seen. Consistent with Baer's observations, we next show that all steady state points prove to be unstable for most

realistic parameter values.

Table 2. Parameter Values for the Two-Mode Baer Equations.

$\tau_c = 0.5 \times 10^{-9}$ sec	cavity round trip time
$\tau_f = 0.24 \times 10^{-3}$ sec	fluorescence time
$\alpha = \alpha_1 = \alpha_2 = 0.015$	cavity losses
$\epsilon = 5.0 \times 10^{-5}$	KTP coupling coefficient
$\gamma = G_1{}^o = G_2{}^o = 0.12$	pump parameter
$\beta_1 = \beta_2 = 1.0$	self-saturation
$\beta = \beta_{12} = \beta_{21} = 0.666$	cross-saturation

The linearization in its general form is, at best, cumbersome to study analytically. To simplify the analysis, we scale time $t_{new} = t/\tau_f$, define $\tau = \tau_c/\tau_f$, and choose symmetric mode-dependent parameters. That is, we let $\alpha_1 = \alpha_2 = \alpha$, $G_1^0 = G_2^0 = \gamma$, $\beta_1 = \beta_2 = 1$, and $\beta_{12} = \beta$. (The parameter values we use are close to those chosen by Baer; they are listed in Table 2.) In this case we get:

$$\tau \frac{dI_1}{dt} = I_1 (G_1 - \alpha - \varepsilon I_1 - 2 \varepsilon I_2) \qquad\qquad 2.10.a$$

$$\frac{dG_1}{dt} = \gamma - G_1 \left(1 + I_1 + \beta I_2 \right) \qquad\qquad 2.10.b$$

$$\tau \frac{dI_2}{dt} = I_2 (G_2 - \alpha - \varepsilon I_2 - 2 \varepsilon I_1) \qquad\qquad 2.10.c$$

$$\frac{dG_2}{dt} = \gamma - G_2 \left(1 + I_2 + \beta I_1 \right) . \qquad\qquad 2.10.d$$

We now examine four steady state points of these equations, characterized by whether the steady state intensities are on or off:

A. $I_1 > 0, I_2 > 0$.

B. $I_1 = 0, I_2 = 0$.

C. $I_1 > 0, I_2 = 0$.

D. $I_1 = 0, I_2 > 0$.

Case A. Here we have both intensities on, and because of the symmetric form of (2.10) we need to find an equilibrium point where both intensities have the same value I_s

and the gains are both equal to G_S. (See Appendix E for a discussion of the uniqueness of this point.) We solve for I_S and G_S in:

$$0 = G_s - \alpha - 3 \varepsilon I_s$$

$$0 = \gamma - G_s (1 + [1 + \beta] I_s) ,$$

2.11

and find that the explicit expressions for I_S and G_S are very similar to the single-mode solutions in (2.2.b). In particular,

$$I_s = \frac{\gamma - \alpha}{\alpha(1+\beta)} + O(\varepsilon) \quad \text{and} \quad G_s = \alpha + O(\varepsilon). \qquad 2.12$$

We now prove that we can constrain the parameters in order to guarantee stability of this equilibrium.

Proposition 2.1. If $\gamma > \alpha$ and

$$\varepsilon < \frac{1}{I_s} (1 + [1 + \beta]I_s) = \varepsilon_c$$

then the equilibrium point in (2.12) is asymptotically stable.

Proof. The stability of the equilibrium is determined from the eigenvalues of the Jacobian of (2.10) evaluated at the equilibrium:

$$\begin{bmatrix} \frac{1}{\tau}(G_s - \alpha - 2\,\epsilon\,[I_s + I_s]) & \frac{1}{\tau}I_s & -\frac{1}{\tau}2\,\epsilon\,I_s & 0 \\[2em] -G_s & -(I_s + \beta\,I_s + 1) & -\beta\,G_s & 0 \\[2em] -\frac{1}{\tau}2\,\epsilon\,I_s & 0 & \frac{1}{\tau}(G_s - \alpha - 2\,\epsilon\,[I_s + I_s]) & \frac{1}{\tau}I_s \\[2em] -\beta\,G_s & 0 & -G_s & -(I_s + \beta\,I_s + 1) \end{bmatrix}$$

$$\ldots\ 2.13$$

To calculate the eigenvalues of this matrix we first use a simple decoupling transformation. This technique was suggested to us by Kurt Wiesenfeld who identified some similarities between the matrix above and the linearization of systems of ordinary differential equations describing the dynamics of Josephson junction arrays (see, e.g. Aronson, et al. 1987). This technique also helps simplify many stability analyses in later sections.

For the two mode equations, we let

$$A = I_1 + I_2 \qquad\qquad B = G_1 + G_2$$
$$a = I_1 - I_2 \qquad\qquad b = G_1 - G_2 \qquad\qquad 2.14$$

and

$$f = 1 + (1+\beta)\,I_s,$$

where the outlined variables are small perturbations away from the steady state point. Then the transformed linearized system consists of two uncoupled pairs of equations:

$$\frac{d}{dt}\begin{bmatrix} A \\ B \end{bmatrix} = \begin{bmatrix} -\frac{3\varepsilon}{\tau}I_s & \frac{I_s}{\tau} \\ -(1+\beta)G_s & -f \end{bmatrix}\begin{bmatrix} A \\ B \end{bmatrix} \qquad 2.15.a$$

$$\frac{d}{dt}\begin{bmatrix} a \\ b \end{bmatrix} = \begin{bmatrix} \frac{\varepsilon}{\tau}I_s & \frac{I_s}{\tau} \\ -(1-\beta)G_s & -f \end{bmatrix}\begin{bmatrix} a \\ b \end{bmatrix} \qquad 2.15.b$$

Since the matrices in (2.13) and (2.15) are related by a similarity transformation, their eigenvalues are the same. Eigenvectors, if we want them, require a back transformation. The eigenvalues of (2.15.a) are:

$$\lambda_{1,2} = -\frac{1}{2}\left(f + \frac{\varepsilon I_s}{\tau}\right)$$

$$\pm \frac{1}{2}\sqrt{\left(f + \frac{\varepsilon I_s}{\tau}\right)^2 - 4\frac{I_s}{\tau}\left[(1+\beta)G_s + 3\varepsilon f\right]} \quad . \qquad 2.16$$

It is straightforward to show that these eigenvalues are complex. From (2.12) and the parameters in Table 1, we see that $I_s\varepsilon/\tau$ is of order 1. This also implies that $f = O(1)$, so in (2.16) the dominant term under the square root (with the factor of I_sG_s/τ) is negative. Since the real part of the eigenvalues is always negative, a two dimensional manifold of the phase space near this equilibrium resembles a stable spiral.

The eigenvalues of the second transformed matrix (2.15.b) are

$$\lambda_{1,2} = -\frac{1}{2}\left(f - \frac{\varepsilon I_s}{\tau}\right)$$

$$\pm \frac{1}{2}\sqrt{\left(f - \frac{\varepsilon I_s}{\tau}\right)^2 + 4\frac{I_s}{\tau}\left[\varepsilon f - (1 - \beta) G_s\right]} \ . \tag{2.17}$$

Reasoning as before, these eigenvalues are also complex, but the stability of the equilibrium now depends on the parameter values. In fact, stability now requires

$$\varepsilon < \frac{\tau}{I_s}(1 + [1 + \beta]I_s) \ . \tag{2.18}$$

$\square$

For the parameter values in Table 1, this condition is approximately $\varepsilon < 3.0 \times 10^{-6}$; note this condition is not satisfied by the ε value used by Baer.

The approximation for I_s which we noted earlier now takes on much more importance: $I_s \cong (\gamma - \alpha)/[\alpha(1+\beta)]$. Since we saw that α is the critical, or threshold, value for γ, this approximation for I_s represents how far above threshold the laser is being pumped. (In fact, in our integration programs, we simply define γ as $(1+p)\,\alpha$, where p is some percentage above threshold.) That means that the stability criterion in (2.18) relates steady state stability to the pump strength (I_s) and to the doubling efficiency (ε) in a very direct way. That is, a stronger pump implies that the equilibrium (with both intensities on, for this case) is unstable for a larger range of ε. This important relation between pump strength and stability will also appear in our analyses of systems with more modes.

So we see that for ε less than a critical value (which includes the case $\varepsilon = 0$), the eigenvalues in (2.17) have negative real parts and this equilibrium is asymptotically stable. As ε takes on larger values and fails the stability test in (2.18), the equilibrium acquires an
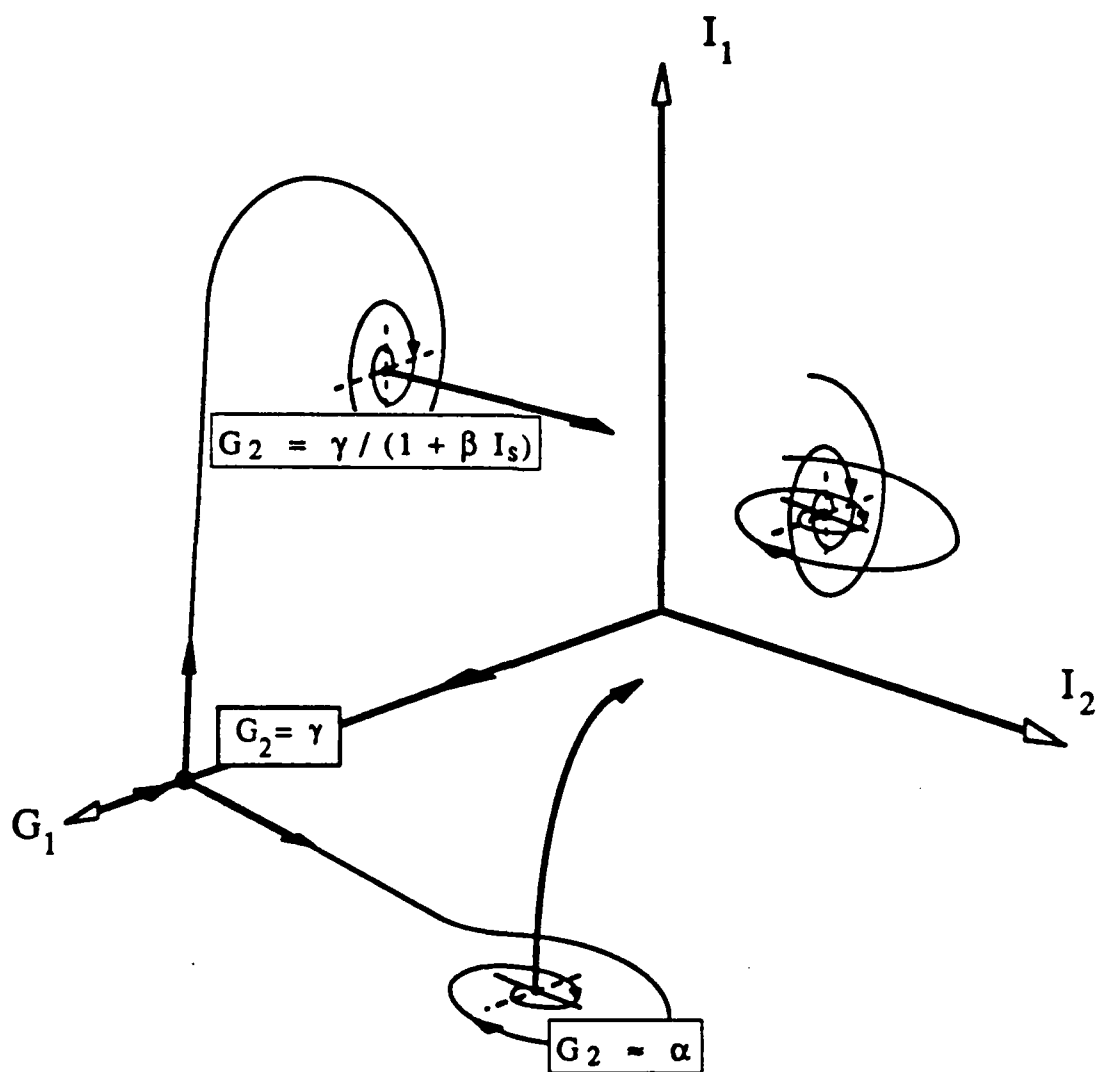
Fig. 2.5 Phase Portrait of the Two-Mode Baer Equations. The phase space
is actually four-dimensional; the appropriate values of G_2 in the fourth
dimension are noted near the steady state points. For small ε, only the
interior steady state point is completely stable.

unstable manifold of dimension 2. The resulting bifurcation is investigated in the next section. For now, we depict the local phase portrait of this equilibrium in Fig. 2.5, where we take ε near zero to enforce (2.18).

Case B. This case is the trivial equilibrium where both intensities are zero, and both gains are equal to the small signal gain, or pump parameter, γ. From (2.10) we see that these steady state values decouple the equations. The local phase space then must be a cross product between the local two-dimensional phase portraits of the individual modes. Recall from the single mode analysis (see Fig. 2.1) that the trivial equilibrium is a saddle point, stable along the G-axis and strongly unstable in the I-direction. This implies that the two-mode trivial equilibrium will have a two-dimensional stable manifold in the (G_1,G_2) plane, and should be strongly unstable in the positive directions of I_1 and I_2.

In fact the Jacobian (2.13), evaluated at this equilibrium, becomes

$$
\begin{bmatrix}
\dfrac{\gamma-\alpha}{\tau} & 0 & 0 & 0 \\[2mm]
-\gamma & -1 & -\beta\gamma & 0 \\[2mm]
0 & 0 & \dfrac{\gamma-\alpha}{\tau} & 0 \\[2mm]
-\beta\gamma & 0 & -\gamma & -1
\end{bmatrix}
\qquad 2.19
$$

When we perform the same transformation as (2.14), the transformed linearized system becomes

$$
\frac{d}{dt}\begin{bmatrix} A \\ B \end{bmatrix} =
\begin{bmatrix}
\dfrac{\gamma-\alpha}{\tau} & 0 \\[2mm]
-(1+\beta)\gamma & -1
\end{bmatrix}
\begin{bmatrix} A \\ B \end{bmatrix}
\qquad 2.20.a
$$

$$\frac{d}{dt}\begin{bmatrix} a \\ b \end{bmatrix} = \begin{bmatrix} \frac{\gamma - \alpha}{\tau} & 0 \\ -(1-\beta)\gamma & -1 \end{bmatrix}\begin{bmatrix} a \\ b \end{bmatrix} . \qquad 2.20.b$$

We see immediately in these equations there are two eigenvalues equal to -1; from the untransformed matrix in (2.19) the associated eigenvectors clearly point along the respective G-axes. The other two eigenvalues are very large, $O(1/\tau)$, and have their largest components in the respective I-axes. This simple analysis confirms that the local phase space is a cross product of the two single-mode neighborhoods. The two-mode trivial steady state point is sketched in Fig. 2.5 as a point on the G_1-axis with arrows indicating the unstable directions primarily along the I-axes.

Cases C and D. In these two cases, only one of the intensities is non-zero; since the parameter values are symmetric, the two cases are equivalent. We take $I_1 > 0$ and $I_2 = 0$ in this discussion. The steady state value for I_1 is approximately $I_s \cong (\gamma - \alpha)/\alpha$, and $G_1 = G_s \cong \alpha$. The steady state coordinates for the other mode are $I_2 = 0$ and $G_2 = \gamma/(1+\beta I_s)$. The Jacobian evaluated at this equilibrium is:

$$\begin{bmatrix} -\varepsilon I_s/\tau & I_s/\tau & -2\varepsilon I_s/\tau & 0 \\ -G_s & -(1+I_s) & -\beta G_s & 0 \\ 0 & 0 & (\gamma - \alpha - 2\varepsilon I_s)/\tau & 0 \\ -\beta\gamma/(1+\beta I_s) & 0 & -\gamma/(1+\beta I_s) & -(1+\beta I_s) \end{bmatrix} ; \qquad 2.21$$

we see that the asymmetry in the steady state values prevents us from making the same transformation of the linearized system as before (equations 2.14). However, we can gain some understanding of the structure of the structure of the local phase space. We notice

that if $I_2 = 0$ in (2.10.a and b), the two equations revert to their single-mode form. This implies that the stable manifold for the two-mode equilibrium includes the entire first quadrant of the (I_1,G_1) plane. These two equations are also always independent of the behavior of G_2; the isolated non-zero value in the last column of the matrix in (2.21) gives the negative eigenvalue, indicating that the G_2-axis also belongs to the stable manifold of this equilibrium. The I_2-direction is strongly unstable, as evidenced by the third column of (2.21), where the third term $(\gamma - \alpha - 2\varepsilon I_s)/\tau$ dominates. If we take a vector with a large I_2-component of the form $[\varepsilon, \varepsilon, 1, \varepsilon]^T$, and premultiply it by the Jacobian (2.21), we produce a vector of the form $[O(\varepsilon), O(\varepsilon), (\gamma - \alpha - 2\varepsilon I_s)/\tau, O(\varepsilon)]$. The approximate eigenvalue and eigenvector confirm the strong instability in the I_2-direction. Physically, this means that a cavity which is configured to allow two oscillating modes will amplify any small-amplitude signal of either mode to switch it on.

For this case, the local phase space looks like the cross product of two different single-mode neighborhoods: the mode-1 neighborhood is a stable spiral; the mode-2 contribution is the saddle associated with the trivial single-mode equilibrium. In a three-dimensional projection (without G_2), this structure is the familiar Shil'nikov saddle-focus (Shil'nikov, 1965) sketched in Fig. 2.6; the fourth dimension is the stable G_2-direction. The two local phase portraits for Cases C and D are included in the two-mode phase diagram in Fig. 2.5. The saddle-focus analysis performed by Shil'nikov (Shil'nikov, 1965-1970) does not apply to our system since there are apparently no homoclinic orbits or cycles which return to the two saddle-focus points. However, we can use numerical integrations to infer how the stable and unstable manifolds of the four equilibria interact and allow periodic motions to occur. (We also note that a modified Shil'nikov approach, using homoclinic cycles instead of homoclinic orbits, may apply to our problem.)
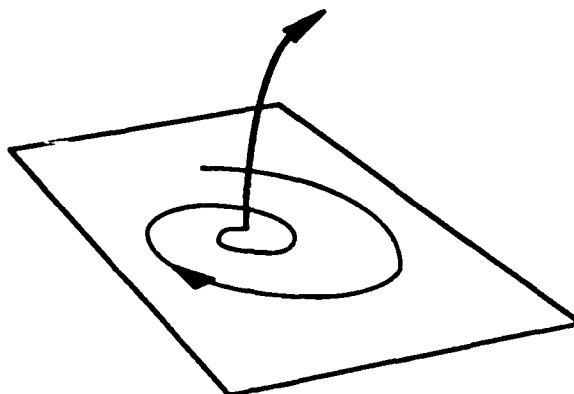
Fig. 2.6 Generic Structure of the Shil'nikov Saddle-Focus.

Numerical Results

Numerical integration of (2.10) with $\varepsilon > \varepsilon_c$ and with many different initial conditions, reveals pulsing behavior like that observed by Baer (Baer, 1986). Figure 2.7 shows a portion of the numeric integration of such a periodic trajectory. Baer uses a close-up sketch like that in Fig. 2.7(b) to examine time segments of the numerical solution and point out several important features of (2.10). The time sequence can be described by four distinct parts:

(1) I_1 is essentially zero, while I_2 is approximately equal to its single-mode equilibrium value. G_1 increases due to external pumping (small signal gain) until it overcomes the losses for mode 1.
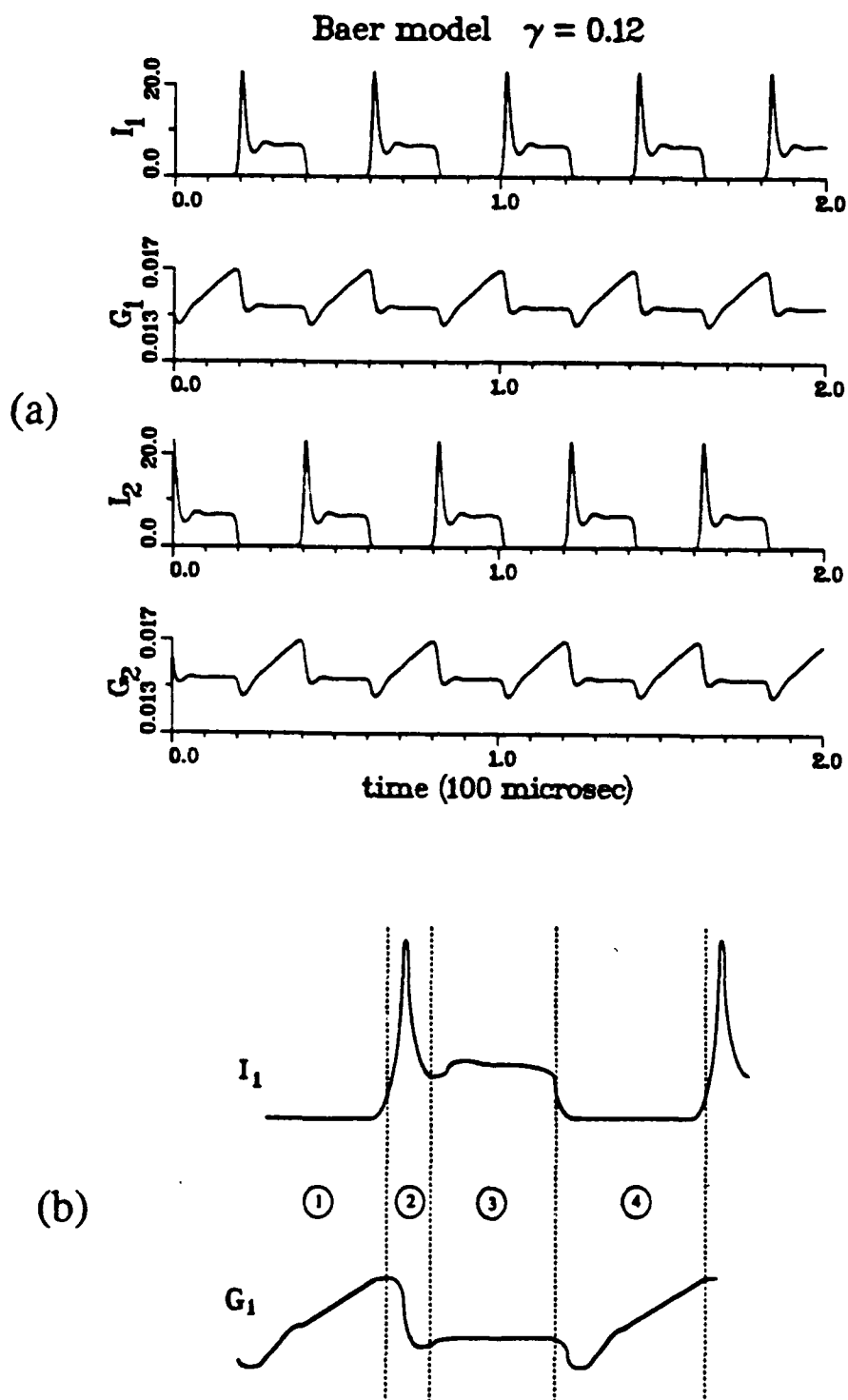
Fig. 2.7 Periodic Numerical Results for the Two-Mode Equations.

(2) With a positive net gain, I_1 now switches on. The intensity spike arises due to the fast time scale of the intensity equations. The sharp increase in intensity saturates the available gain, so G_1 decreases; the sum-frequency losses in mode 2 cause I_2 to switch off.

(3) I_1 and G_1 relax to "quasi-steady-state" values, as if only one mode were active in the cavity. I_2 is essentially zero; G_2 is increasing (like G_1 did in time segment (1)).

(4) G_2 surpasses the mode 2 losses, I_2 switches on and the subsequent sum-frequency losses cause I_1 to shut down. The spiking intensity in I_2 also causes a substantial decrease in the available gain. The sequence begins again.

We notice that when one intensity is very small, the system behaves like the single-mode set of equations (2.1). Another essential feature of the dynamics is the role of the gain variables in determining when the intensities turn on and off. When G_1, for example, rises above a threshold value (determined by the amount of losses experienced by I_1) then I_1 switches on, causing I_2 in turn to switch off. So, except for their transient spiking, the intensity values, either on or off, are determined by the hysteretic cycling of the respective gain variables. This role of the gains will be important in the three mode case later on.

Now we examine the long-term periodic motion in Fig. 2.7(a). All initial conditions we tested led to periodic pulsing where the intensities switch on and off. The time scales of these pulses will later help us to refine parameter values to match experimental output more closely. In the numerical integration, we expect long term unstable behavior of some kind, because the equilibria we examined in the linearized analysis were all unstable when $\epsilon > \epsilon_c$. Within each pulse, we see the intensity behave as if it were the only mode lasing. These observations allow us to give a reasonable sketch of

the phase portrait for the two mode laser. The phase space in Fig. 2.8 actually lies in four dimensions, but we know that when one intensity is very small, the local phase portrait is just like the single-mode case. For this reason the phase portrait can be sketched as two thin-walled slabs, each reproducing the single-mode phase diagram. The non-zero thickness of the I_1-G_1 slab, for instance, represents the portion of phase space where I_2 is small, but non-zero. When one quasi-steady state intensity switches off, there is a quick transition from one spiral to the other, and the other intensity will oscillate toward a quasi-steady state.

The locally single-mode behavior of the two-mode solutions may also be seen from the viewpoint of perturbation theory as follows. Suppose that the (I_1, G_1) slab has its thickness defined for $0 \leq I_2 < \varepsilon$, and $G_2 < \alpha$. We can look at the dynamics of I_1 and G_1 on this slab in terms of a small perturbation away from the single-mode equations. First, we note that the differential equations (2.10.a and b) for I_1 and G_1 are independent of G_2. Next we observe that, for the assumed restrictions on I_2 and G_2, the intensity I_2 monotonically decreases for increasing time. Thus, we do not have the difficulty of a perturbation with oscillations. Since I_2 monotonically decreases between its extreme values in the slab, we only need to examine the perturbation of the first mode's equations at the two extremes of $I_2=0$ and $I_2=\varepsilon$.

When $I_2=0$, equations (2.10.a and b) return to the precise form of the single-mode equations we analyzed in the previous section. We know that, as long as $\gamma > \alpha$, the equilibrium in the interior of the (locally two dimensional) phase space is globally attractive.
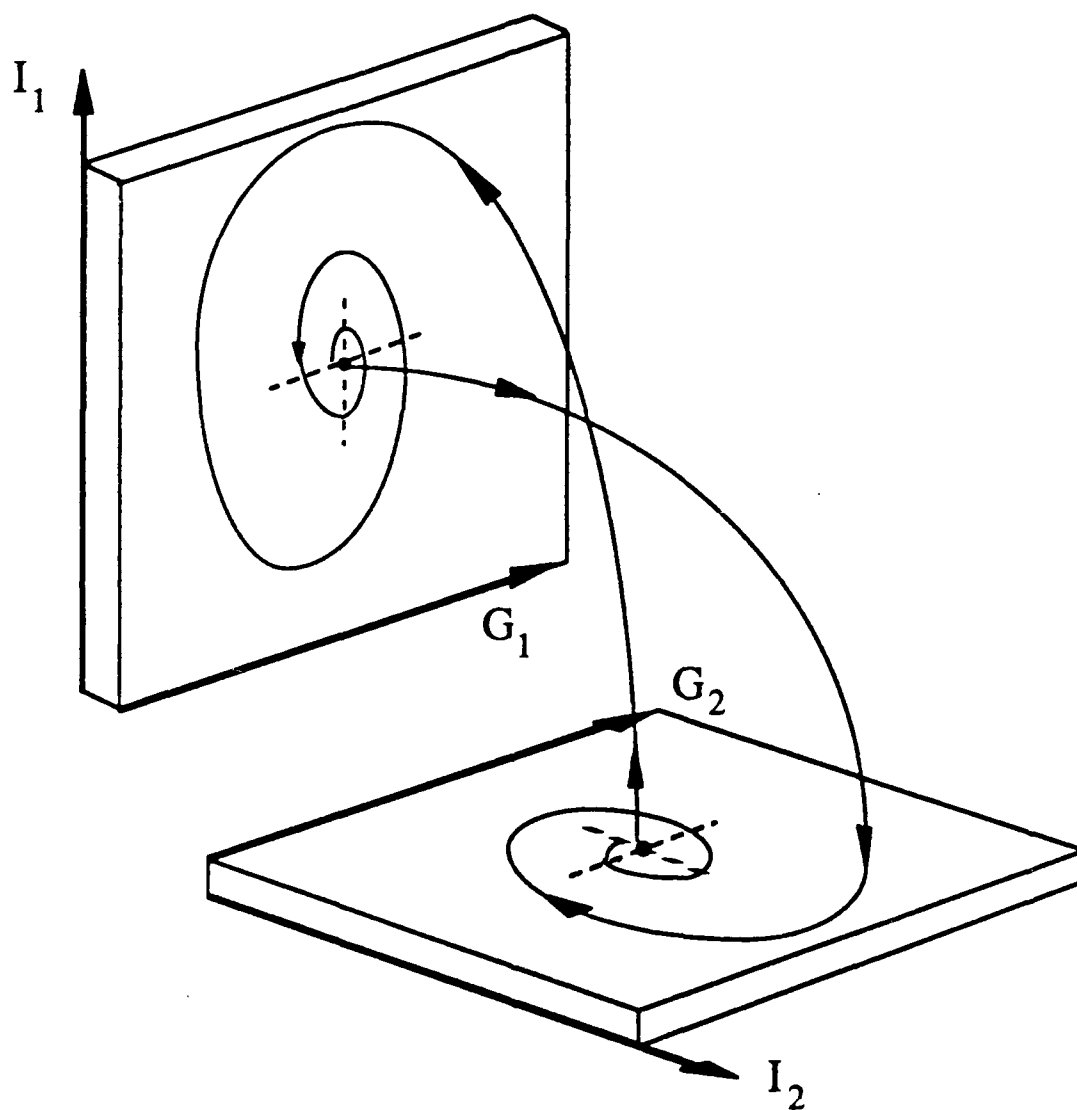
Fig. 2.8 Phase Portrait of the Periodic Flow in the Two-Mode Equations. The spiral on each individual slab corresponds to one mode approaching its quasi-steady-state while the other intensity is negligible. Periodic variations in G_1 and G_2 cause the trajectory to jump from one slab to the other.

At the other extreme we have $I_2 = \varepsilon$. Direct substitution of this value into (2.10) produces:

$$\tau \frac{dI_1}{dt} = I_1 \left(G_1 - [\alpha + 2\varepsilon^2] - \varepsilon I_1 \right) \qquad \qquad 2.22.a$$

$$\frac{dG_1}{dt} = \gamma - G_1 \left([1 + \beta\varepsilon] + I_1 \right). \qquad \qquad 2.22.b$$

These equations may be rescaled to conform to the structure we have used so far for the single-mode equations. Define $q = 1 + \beta\varepsilon$ and let

$$\tilde{t} = qt \qquad\qquad \tilde{\tau} = q\tau \qquad\qquad \tilde{I}_1 = \frac{1}{q} I_1$$

$$\tilde{\varepsilon} = \frac{\varepsilon}{q} \qquad\qquad \tilde{\alpha} = \alpha + \varepsilon^2 \qquad\qquad \tilde{\gamma} = \frac{\gamma}{q} \ .$$

Then the rescaled equations for I_1 and G_1 are:

$$\tilde{\tau} \frac{d\tilde{I}_1}{d\tilde{t}} = \tilde{I}_1 \left(G_1 - \tilde{\alpha} - \tilde{\varepsilon}\tilde{I}_1 \right)$$

$$\qquad\qquad\qquad\qquad\qquad\qquad\qquad 2.23$$

$$\tilde{\tau} \frac{dG_1}{d\tilde{t}} = \tilde{\gamma} - G_1 \left(1 + \tilde{I}_1 \right)_.$$

These equations are basically the same as when we have $I_2 = 0$, except that almost all the variables have a small change of order ε. Clearly, nothing in the single-mode analysis is changed for these equations, so the global attractiveness of the interior equilibrium is maintained; the only difference is that the equilibrium itself is shifted by $O(\varepsilon)$.

Under the restriction that I_2 remain small, the structure of the local flow in the (I_1, G_1) slab does not change for any $I_2 < \varepsilon$. This analysis confirms the thin-walled structure of the phase space in the case where the two-mode flow is periodic (Fig. 2.8).

The sequence of numerical results in Fig. 2.9 depicts the bifurcation which leads from stable steady state intensity output to the periodic pulses observed by Baer, as ε increases through the stability threshold ε_c in (2.18). For a pump strength of 8 times threshold, Fig. 2.9(a) shows the damping of intensity oscillations as the trajectory converges to an equilibrium, for small ε. The stability condition is no longer satisfied in Fig. 2.9(b), and a periodic solution results. We note that the periodic oscillations do not deviate far from the equilibrium values of Fig. 2.9(a); this periodic solution lies near the now unstable steady state point. As ε increases in Figs. 2.9(c)-(e), the periodic flow departs further and further from the unstable steady state, such that, for larger ε, the trajectory has either I_1 or I_2 essentially zero for most of the time. In these cases, the periodic trajectory spends most of its time flattened against one of the phase space slabs sketched in Fig. 2.8.

Finally, Figs. 2.9 through 2.11 illustrate how the character of the pulses change with respect to different parameters. As in the one-mode equations, an increase in ε serves to dampen oscillations within each pulse (Fig. 2.9). Increases in the pumping, γ/α, sharpen the initial spike as each intensity turns on, and raises the quasi-steady-state intensity plateau (Fig. 2.10). In Fig. 2.11, we see how an increase in the cross-saturation β decreases the rate of intensity switching and increases the duration of each pulse.
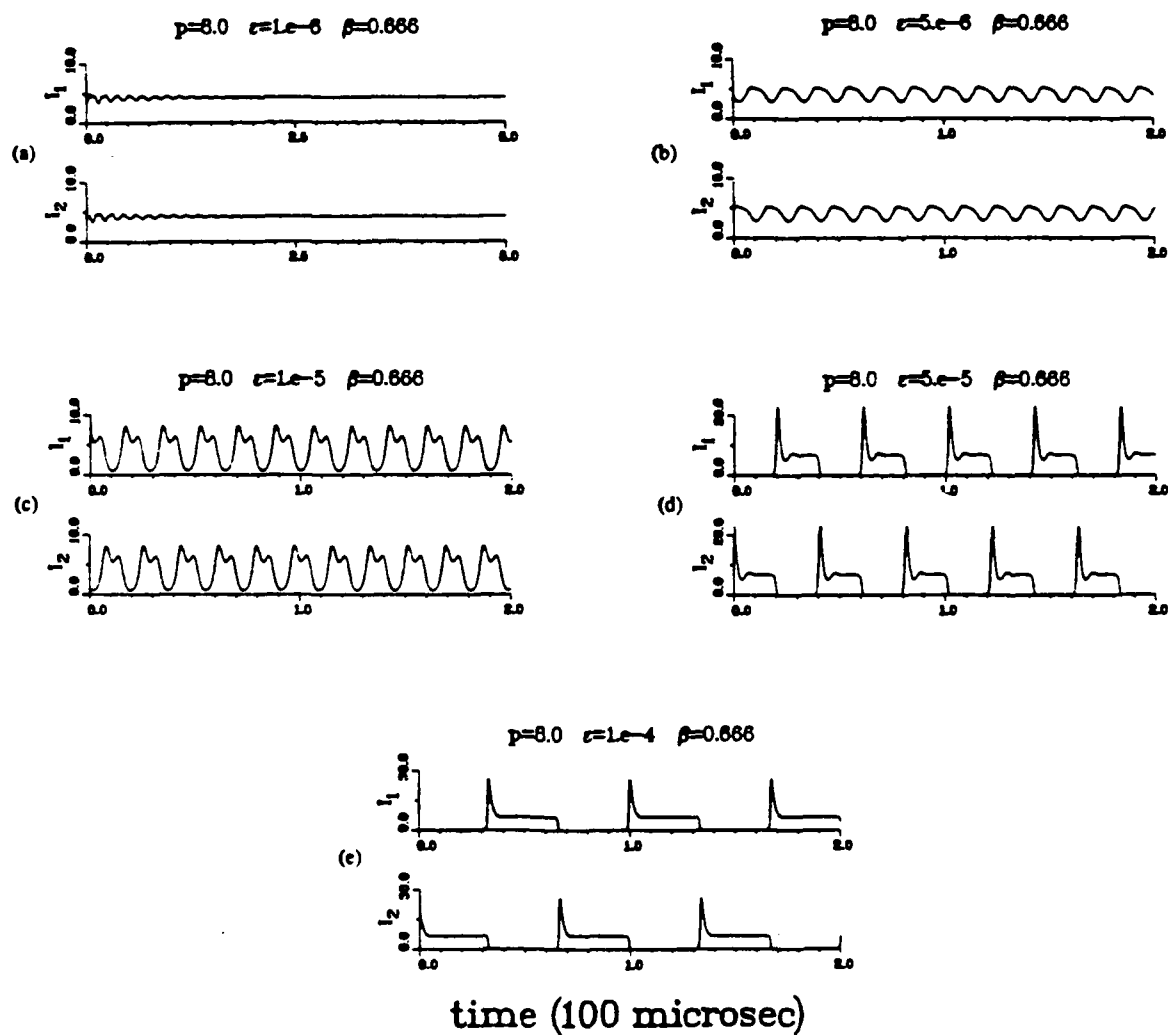
Fig. 2.9   Bifurcation from Stable Steady State to Periodic Orbit. The
control parameter is ε.
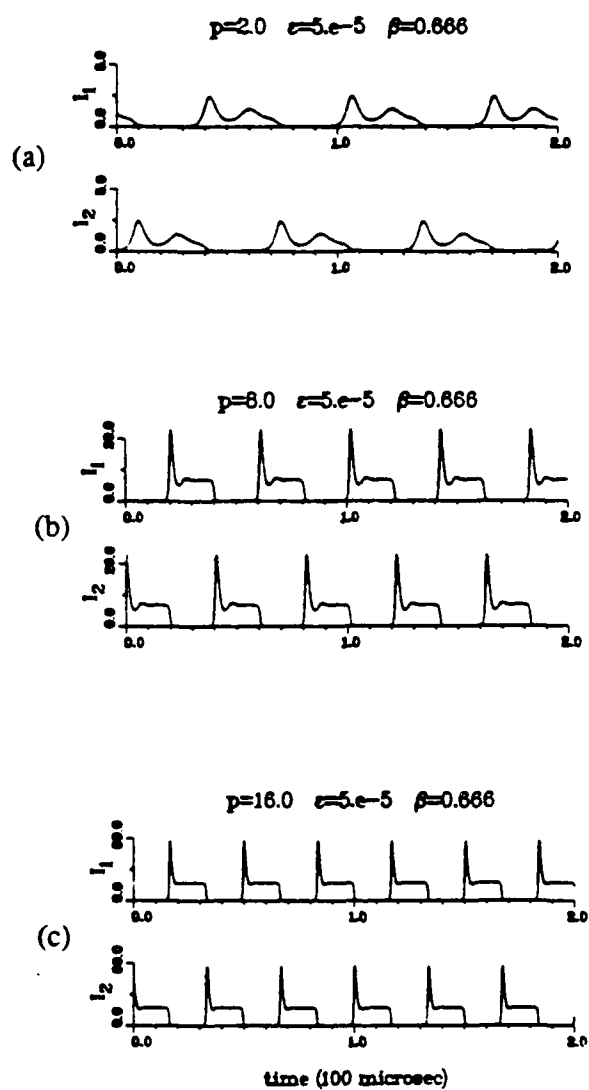
Fig. 2.10   Changes in Pulse Shape as a Function of Pump Strength.
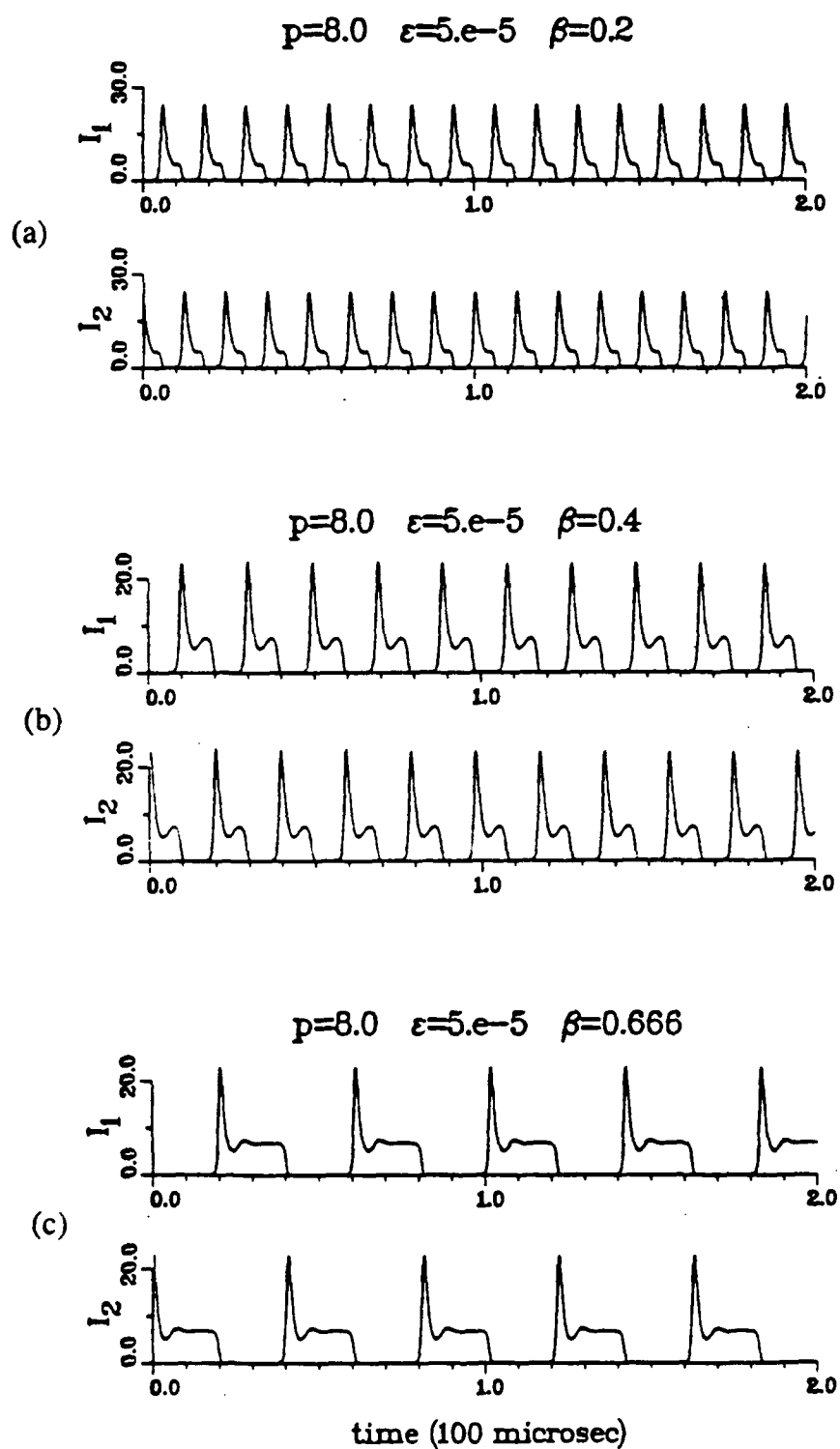
Fig. 2.11 Changes in Pulse Shape as a Function of Cross-Saturation β.

Three-Mode Dynamics

In the experiments performed by Baer, three or more modes were necessary to generate irregular intensity output. In the numerical integration of his multimode model, he also found that one or two modes could only produce steady or periodic motion, while the intensity output for three or more modes displayed large fluctuations in amplitude.

Since the complexity of the equations increases greatly with each additional mode, the analysis which follows is primarily a discussion of the general behavior we observe in numerical experiments with three modes; the numerical results indicate an intermittency route to chaos which we observed by varying the cross saturation parameters.

Analysis

To extend the two-mode equations to an arbitrary number of modes, Baer assumes that each pairwise coupling between modes j and k takes the same form, $2\varepsilon I_j I_k$. The nonlinear differential equations which model the dynamics of N longitudinal modes in the intracavity doubled laser then become:

$$\tau_c \frac{dI_j}{dt} = (G_j - \alpha_j - \varepsilon I_j - 2\varepsilon \sum_{\substack{k=1 \\ k \neq j}}^{N} I_k) I_j$$

2.24

$$\tau_f \frac{dG_j}{dt} = G_j^o - G_j (1 + \beta_j I_j + \sum_{\substack{k=1 \\ k \neq j}}^{N} \beta_{jk} I_k) ,$$

$$j = 1,2,...,N.$$

In our analysis, we assume symmetric parameters, that is, all mode-dependent parameters are set equal: $\alpha_j = \alpha = 0.015$; $G_j^0 = \gamma = 0.12$; $\beta_j = 1.0$; $\beta_{jk} = \beta \in [0,1]$. (Again the intensities are scaled to be dimensionless, so all the variables except for time variables are dimensionless.) This symmetry assumption yields no loss in generality, since the numerical results show no different qualitative behavior for asymmetric parameter values. All the parameter values are listed in Table 3.

Table 3. Parameter Values for the Three-Mode Baer Equations.

Three or More Modes
(symmetric case)

$\tau_c = 0.5 \times 10^{-9}$ sec

$\tau_f = 0.24 \times 10^{-3}$ sec

$\alpha = 0.015$

$\varepsilon = 5.0 \times 10^{-5}$

$\gamma = 0.12$

$\beta \in [0,1]$

Again, the total intensity I_f at the fundamental wavelength is expressed as the sum $I_1 + I_2 + I_3...$, and the total intracavity intensity I_d at the second harmonic wavelength is the combined effect of frequency doubling and sum frequency generation:

$$I_d = \varepsilon \sum_{j=1}^{N} I_j^2 - 2\varepsilon \sum_{\substack{j,k=1 \\ j \neq k}}^{N} I_j I_k \ . \qquad\qquad 2.25$$

In our study of the three-mode equations, we first look for an equilibrium which has all intensities positive and equal (I_s), and all gains equal (G_s). Such an equilibrium requires:

$$G_s - \alpha - 3\varepsilon I_s = 0 \qquad\qquad 2.26.a$$

and

$$\gamma - G_s (1 + [1 + 2\beta] I_s) = 0. \qquad\qquad 2.26.b$$

The uniqueness of this equilibrium (where all intensities are positive, and ε is small) is discussed in Appendix E. There is a simple condition for the stability of this equilibrium, as in the two-mode case.

Proposition 2.2. Let N=3 in (2.24) and let all parameters take on common values, i.e. let $\alpha_j = \alpha$, $G_j^0 = \gamma$, $\beta_{jk} = \beta$, and $b_j = 1$. If $\gamma > \alpha$ and

$$\varepsilon < \frac{\tau \gamma}{I_s G_s}$$

then the equilibrium determined by (2.26) is asymptotically stable.

Proof. The proof proceeds as that of Proposition 2.1. We linearize the equations about the equilibrium given by (2.26), and apply a decoupling transformation to the linearized variables. This time, the transformation is

$$A = I_1 + I_2 + I_3 \qquad\qquad B = G_1 + G_2 + G_3$$

$$a_1 = 3\,I_1 - A \qquad\qquad b_1 = 3\,G_1 - B \qquad\qquad 2.27$$

$$a_2 = 3\,I_2 - A \qquad\qquad b_2 = 3\,G_2 - B$$

This produces three uncoupled pairs of linear equations:

$$\frac{d}{dt}\begin{bmatrix} A \\ B \end{bmatrix} = \begin{bmatrix} -3\,\epsilon\,\frac{I_s}{\tau} & \frac{I_s}{\tau} \\ -G_s\,(1+2\,\beta) & -(1+I_s\,[1+2\,\beta\,]) \end{bmatrix}\begin{bmatrix} A \\ B \end{bmatrix}$$

$$\frac{d}{dt}\begin{bmatrix} a_j \\ b_j \end{bmatrix} = \begin{bmatrix} \epsilon\,\frac{I_s}{\tau} & \frac{I_s}{\tau} \\ -G_s\,(1-\beta) & -(1+I_s\,[1+2\,\beta\,]) \end{bmatrix}\begin{bmatrix} a_j \\ b_j \end{bmatrix}, \quad j = 1,2.$$

$$2.28$$

For both matrices above, we have one negative off-diagonal entry, the positive off-diagonal term is of order 10^6, and the other terms are of order 1. All the eigenvalues, then, are complex. For the first matrix, the real part of the eigenvalues is:

$$Re(\lambda) = \frac{1}{2}\left[-3\,\epsilon\,\frac{I_s}{\tau} - (1 + I_s\,[1 + 2\,\beta]) \right] \qquad 2.29$$

which is always negative. For the second matrix, the real part of the eigenvalues is:

$$Re(\lambda) = \frac{1}{2}\left[\epsilon\,\frac{I_s}{\tau} - (1 + I_s\,[1 + 2\,\beta]) \right]. \qquad 2.30$$

In (2.30), we have $Re(\lambda) < 0$ if and only if

$$\varepsilon < \frac{\tau\,\gamma}{I_s\,G_s}\ ,$$

2.31

where we have used the relationship between I_s and G_s given by (2.26). This completes the proof. □

We can rewrite (2.31) to see the implications of the stability criterion for the experiment. We define p as the percentage above threshold at which the laser is pumped, so that

$$(1 + p)\ =\ \frac{(\gamma - \alpha)}{\alpha}$$

2.32

and we have the following approximations for I_s and G_s:

$$I_s\ =\ \frac{p}{(1 + 2\beta)}\ +\ O(\varepsilon) \qquad G_s\ =\ \alpha + \varepsilon\ .$$

2.33

We substitute (2.33) in (2.31) to get the stability condition

$$\varepsilon\ <\ \tau\,(1 + 2\beta)\,\frac{(1 + p)}{p}\ .$$

2.34

In this form, it is evident that stronger pumping tends to lower the stability threshold for ε. Increases in cross-saturation (β) have the same effect. Raising the stability threshold in

(2.34) by increasing τ (which equals τ_c/τ_f) would require a longer cavity (increasing τ_c) or a different active medium with a shorter upper state lifetime (lowering τ_f).

There are also three steady state points where two intensities are on and the third is off. The local flow near such points resembles that of the two mode case: for instance, if $I_3=0$, then (2.24) decouples into four equations which describe the two-mode dynamics, and two differential equations for I_3 and G_3. The unstable manifolds of steady state points in these regions of the phase space are found (by transformations similar to (2.27)) to have at least one dimension, in the direction of the third intensity; all numerical trajectories generated long-time solutions where either all three modes lased or all three modes turned off.

As in the two-mode equations, there are interesting steady state points where only one intensity is positive and the other two are zero. There are three such points, and the numerical trajectories spend most of their time near these three points. Again, for 'large' ε (ε not satisfying the stability criterion of Proposition 2.2) the local flow around these points resembles the single-mode case, with transient oscillations about a quasi-steady state value of intensity and gain. The periodic pulsing observed for three modes that sequentially switch on and off suggests the phase portrait of Fig. 2.12. When one intensity pulses on, it behaves locally as if the other two intensities did not exist, until another intensity kicks on (as its gain overcomes its losses) and then moves quickly to one of the other thin walls of the phase space. The perturbation analysis we carried out for the thin walls of the two-mode equations, to confirm the locally planar structure of the flow, applies here as well.

Both laboratory and numerical experiments indicate that three modes are the minimum necessary to generate chaotic behavior. However, the three-mode model includes six differential equations. Since we know from the Poincaré-Bendixson theorem
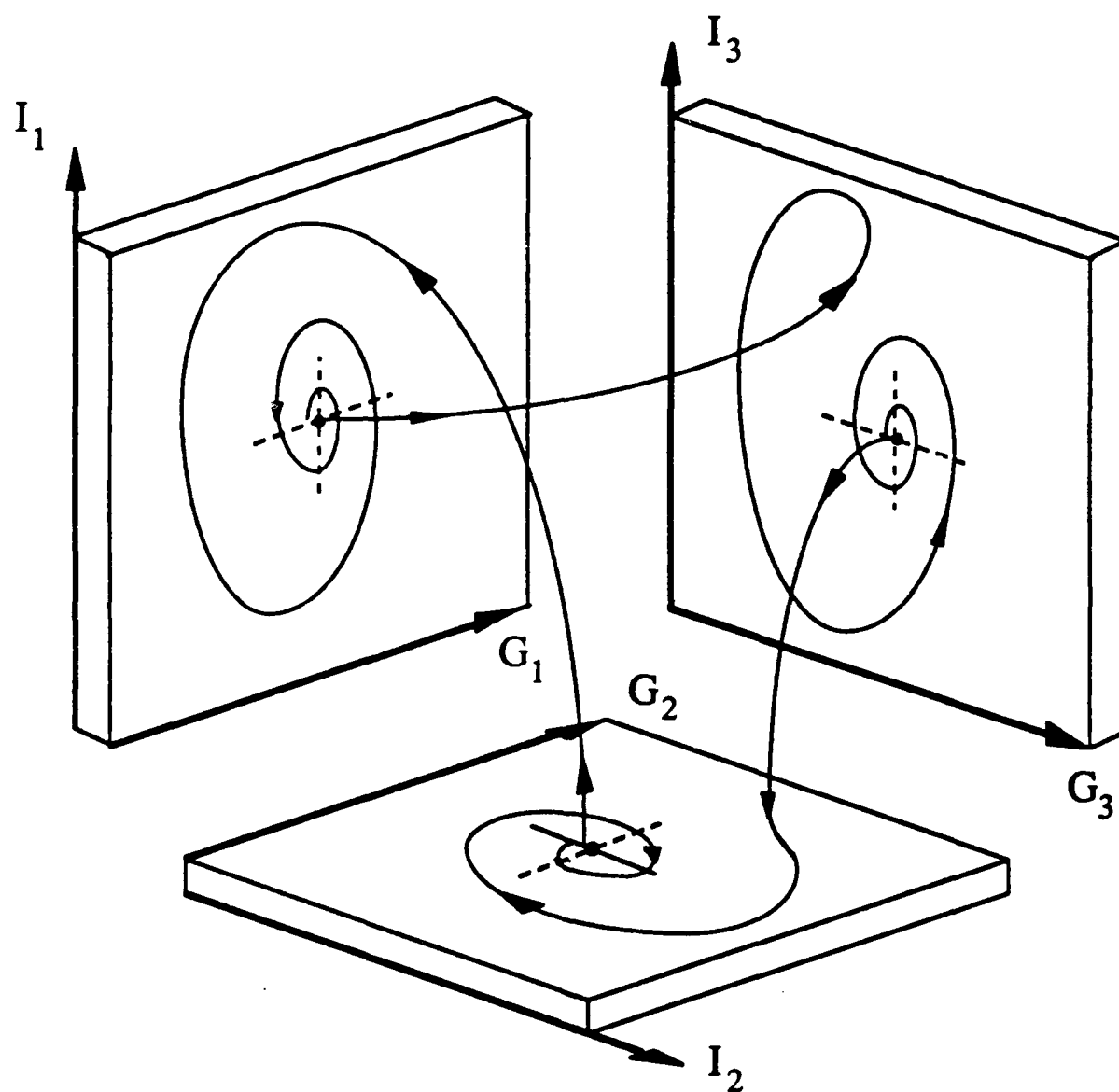
Fig. 2.12 Phase Portrait for Periodic Flow in the Three-Mode Equations.

that three (autonomous) ordinary differential equations is the minimum necessary to generate chaos, we first look for some source of lower dimensional behavior. It appears that the numerical intensity output and its fast Fourier transform are most helpful for visually identifying irregular output as periodic or aperiodic. On the other hand, the time history of the gain variables provides the most information on the transient tendencies of the flow, and on how the transition to chaos takes place. Recall from Fig. 2.7 how G_j deter ines the dynamics of its associated intensity by crossing a threshold which is set by the mode-j losses. This is a consequence of the large difference in time scales in the intensity and gain equations, and permits the gain variables to contain all the pertinent information about non-steady state behavior in the model. For this reason, the numerical analysis in the next section relies primarily on output of the gains.

Numerical Results

Baer found both periodic and chaotic intensity output in numerical integration of his three-mode equations (Baer, 1986). His preliminary findings suggest that the character of the total intensity output depends on the symmetry of the mode-dependent gain and loss parameters.

We look for a single parameter to use as a control variable to observe bifurcations from periodicity to chaos. The unstable behavior in (2.24) is deterministic in origin (there are no random noise terms), and is due to the mode interactions. This is apparent because, without the $I_j I_k$ terms in the equations, the intensities asymptotically approach their respective stable steady states. There are two candidate parameters which influence mode coupling: ε and β. We assume that the nonlinear coupling ε is fixed by the properties of the KTP doubling crystal, so we choose β as the control parameter. Recall that β is the cross

saturation parameter which represents spatial overlap, or how the modes compete for the available gain along the length of the YAG crystal. While β is not straightforward to measure experimentally, it can be varied by changing the placement of the YAG crystal in the cavity (see Fig. 1.6).

The cross saturation β can theoretically assume values between 0 and 2 (Siegman, 1986). If β is very small, the modes are essentially independent of each other and there is no appreciable competition for the gain. Multiple modes may then coexist in steady state operation. If the spatial overlap of the modes is significant, β may be sizeable. In fact, if $\beta > 1$, the competition for gain is so great that only one of the modes can oscillate (see Appendix E). Baer used $\beta = 0.666$ in his calculations and obtained irregular amplitude fluctuations.

In our computations (James, et al., 1990a) we limit the model to three active modes, which is sufficient for chaotic dynamics to occur. (For pump power levels below 3 or 4 times the threshold power, we often see the laser oscillate in only three longitudinal modes, so this is a reasonable restriction.) The behavior of the total fundamental intensity I_f and the total doubled intensity I_d can both display the experimentally observed irregular fluctuations. Again we use the symmetric parameter values in Table 3. With these parameters, and $0 < \beta < 0.2910$, the total intensity is periodic. The individual mode intensities cycle on and off as shown in Fig. 2.13(a); we call this sequence of alternating peak intensities, I_1-I_2-I_3-I_1-..., a "right waltz". The corresponding time history of total intensities is plotted in Fig. 2.13(b) to confirm that the peaks do not average out as they combine in the total intensities. This stable periodic solution coexists in phase space with an analogous "left waltz" whose intensity peaks alternate in the reverse order, I_3-I_2-I_1-I_3-... For these values of β, the two waltzes appear to be the only stable solutions, and initial conditions dictate which waltz is selected.
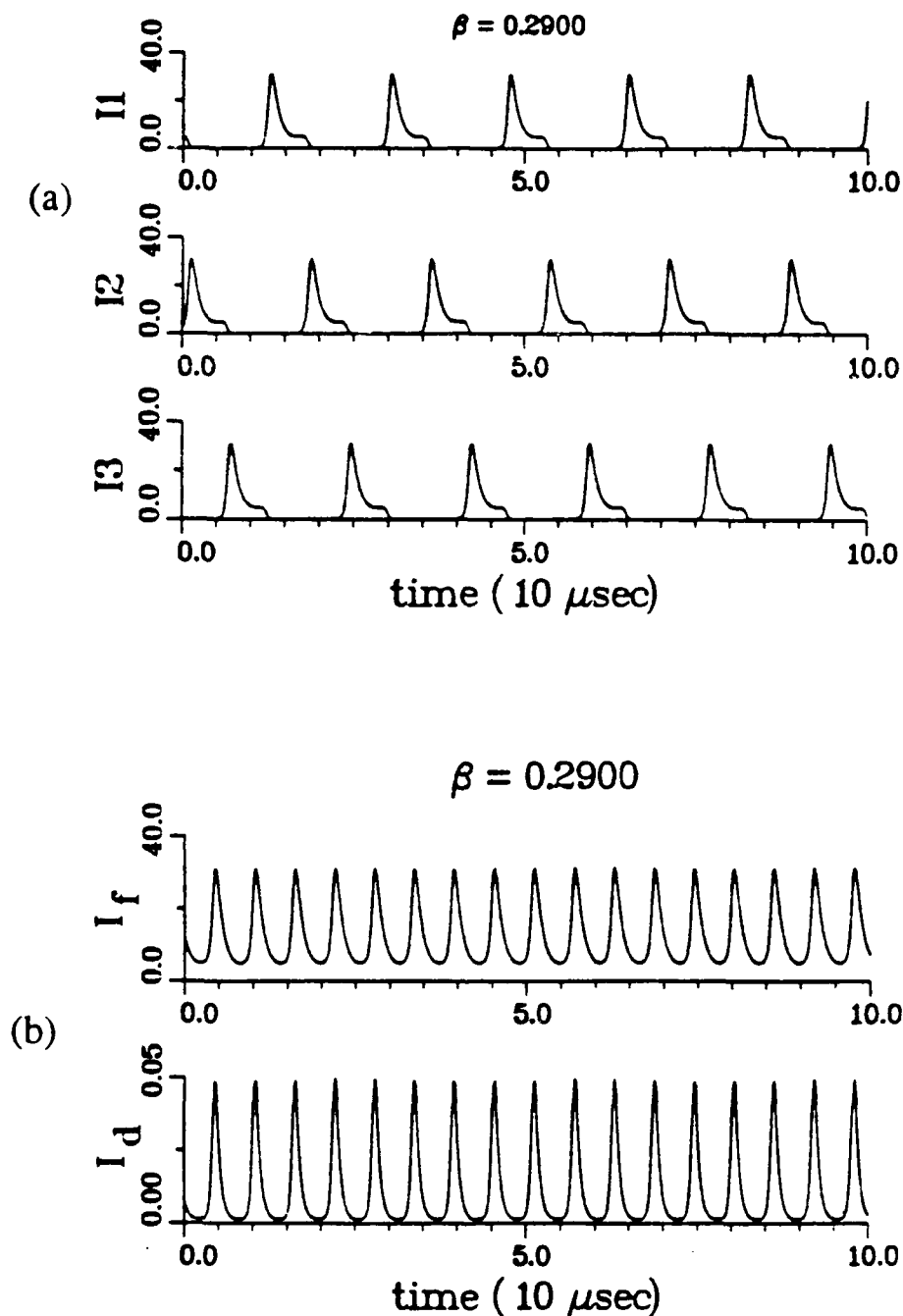
Fig. 2.13 Periodic Numerical Results for the Three-Mode Equations. The regular pattern of intensity peaks in (a) is a "right waltz", the corresponding output in (b) is for the total fundamental intensity I_f and the doubled intensity I_d.

We take $0 < \beta < 0.2910$ and look in the portion of the phase space defined by G_1, G_2 and G_3 to find evidence of a route to chaos. We define the Poincaré map M on the transversal surface $G_1=0.017$ where the points in the flow have the coordinate $G_1=0.017$ and a negative time derivative. (The value of G_1 which defines the plane must be hand-selected after observing the minimum and maximum excursions for G_1 from a sample of the numerical results.) For a (six-dimensional) point x on this surface, M(x) is found by continuing the numerical integration of the flow until the next time that $G_1 = 0.017$ and G_1 is decreasing. M maps a five component vector (I_1,I_2,G_2,I_3,G_3) to another five-vector. However, the relevant dynamics can all be seen in the (G_2,G_3) plane. This two-dimensional projection of the Poincaré map is pictured in Fig. 2.14. (The discrete sequence of β values was hand-selected to illustrate changes in the flow structure near the bifurcation; the approximate bifurcation point was found with a binary search.)

The plot in Fig. 2.14(a) is for 1200 iterations of M when $\beta = 0.2910$. First, we notice the structure of the two S-shaped curves, symmetric across the line $G_2 = G_3$. Each periodic waltz appears in the Poincaré map as a fixed point, so each curve highlights the stable and unstable manifolds of these fixed points. The form of (2.24) requires symmetry in the flow on either side of the hyperplane $G_2 = G_3$, so all the structure above the line must be mirrored below the line. The result of reflecting all the points in Fig. 2.14(a) to the region below $G_2 = G_3$ appears in Fig. 2.14(b). In this way, the 1200 points yield twice the resolution of the map.

We examine the 'flow' of these Poincaré maps more closely in Fig. 2.15(a). The fixed point that represents the left waltz has been reflected onto the point that represents the right waltz. This point C corresponds to a stable periodic orbit in phase space. For $0 < \beta < 0.2910$, all numerical trajectories were attracted to one of the waltzes for all initial conditions we attempted.
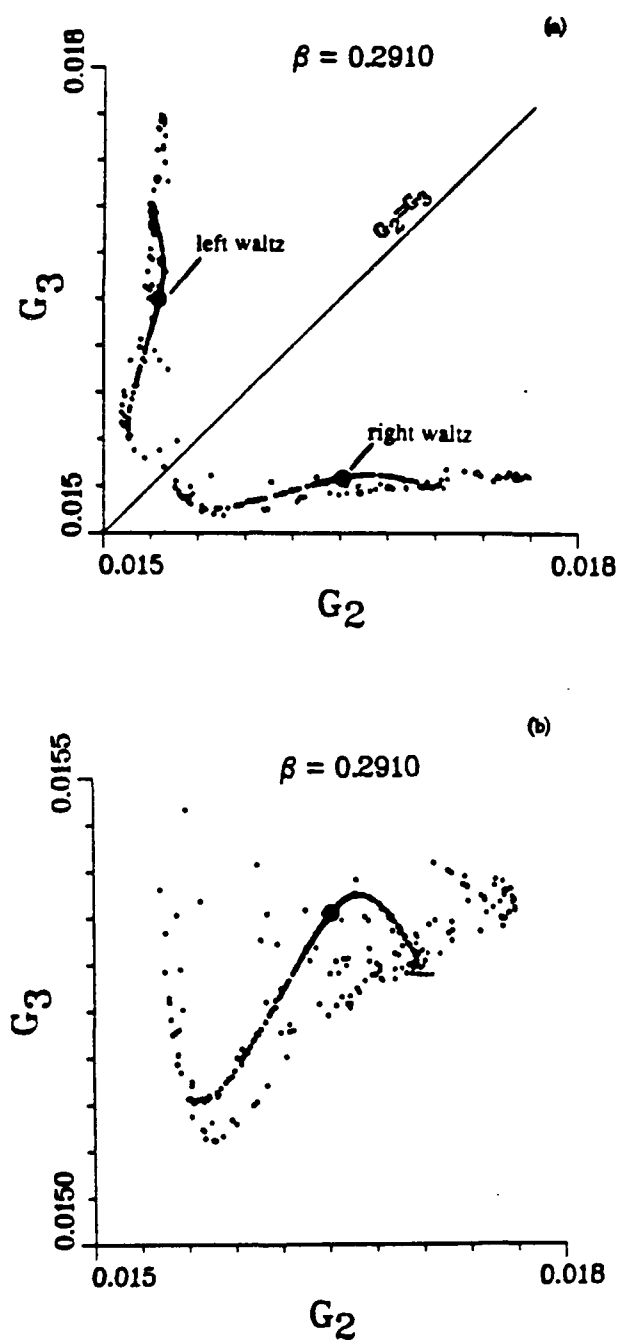
Fig. 2.14 Numerical Poincaré Maps for the Three-Mode Equations. The map
in (a) highlights the flow symmetry in phase space. The points which
correspond to each waltz represent periodic orbits in the full phase
space.The second map (b) contains the same points as (a), but reflected
below the line of symmetry, $G_2 = G_3$.
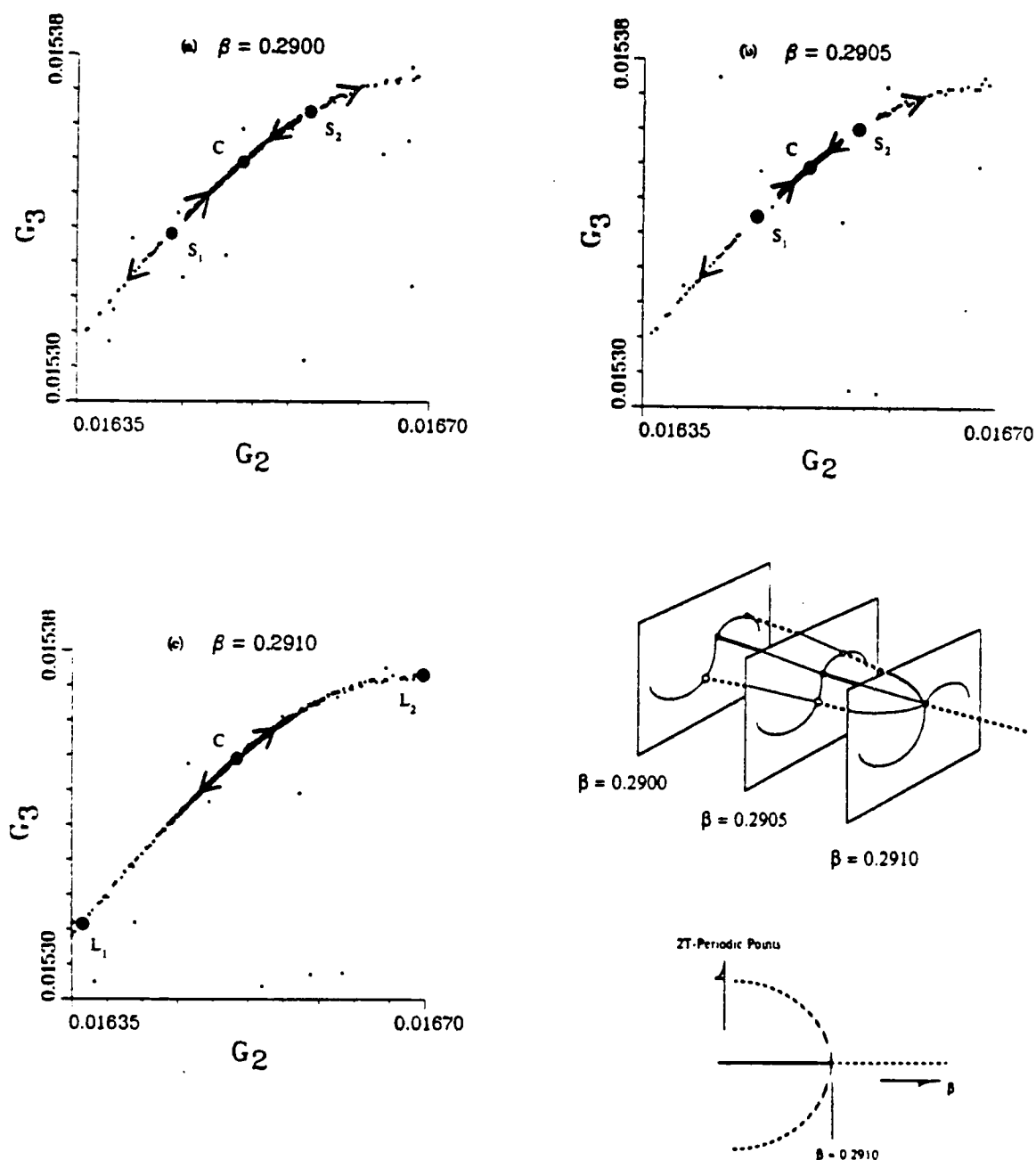
Fig. 2.15 Transition from Periodicity to Intermittency. The first three maps
show the reflected Poincaré Map in a neighborhood of the fixed point C.
The inverse pitchfork bifurcation that results from an increase in β is
shown in (d). Solid lines indicate stable points; dashes indicate
instability. We note that the T-periodic point C is also 2T-periodic.

We can deduce important qualitative features of the flow dynamics from simple observations of how M maps the points on the curve which passes through C. First, points on the curve to one side of C are mapped to the opposite side of C. The point S_1, for instance, is mapped to S_2. This indicates the existence of a Floquet multiplier (of the Jacobian of the map, evaluated at C) with a negative real part. Such a multiplier will eventually signal the type of intermittency in the system. Next, all the points on the curve between S_1 and S_2 are mapped toward C, as indicated by the arrows. (This is a map, not a continuous flow, so the arrows indicate only tendencies of the map.) The negative multiplier still causes points to flip-flop across C, but along this arc they get closer to C at each iteration. Finally, the points outside the S_1-S_2 arc are repelled from S_1 and S_2 until they leave the curve. After falling off the curve, a point will either be mapped towards the opposite waltz or will return to a neighborhood of the S_1-S_2 arc.

The character of the global dynamics in Fig. 2.15(a) with $\beta = 0.2900$ is now more clear. The curve through C is strongly attractive in the transverse direction. The point C is a stable hyperbolic fixed point of M, and corresponds to a periodic solution of the flow, of some period T which depends only weakly on β. The points S_1 and S_2 map onto each other under M, and correspond to an unstable periodic solution of period 2T. There are regions of the phase space that allow passage from the vicinity of one waltz to the other, but once a trajectory approaches the S_1-S_2 arc of one of the waltzes, the trajectory will converge to that particular periodic orbit. In the unreflected G_2-G_3 plane, we then have two stable T-periodic solutions and two unstable 2T-periodic solutions.

In Fig. 2.15(b), with $\beta = 0.2905$, the stable and unstable manifolds of C retain the same structure. The point C is completely stable, while S_1 and S_2 are saddle points in the plane. However, for this increased value of β, the unstable 2T-periodic solution indicated by S_1 and S_2 lies closer to C. In Fig. 2.15(c), $\beta = 0.2910$, and the points S_1 and S_2 have

collapsed onto C, making it a saddle point. As β increases through 0.2910 we get the inverse pitchfork bifurcation sketched in Fig. 2.15(d). The transfer of instability at the critical value (β about = 0.2910) renders the T-periodic solution unstable and provides the mechanism for intermittency (see Appendix C for an overview of intermittency).

The laminar or regular portion of the intermittent flow appears for solutions which pass through the neighborhood of C (Fig. 2.15(c)). This point is still strongly attractive in the transverse direction. Moreover, the periodic orbit is just barely unstable for $\beta \approx 0.3$, so points near C are mapped away very slowly. This implies that initial conditions close to C may appear T-periodic (or even 2T-periodic) for a long time. Such flow constitutes the laminar portion of the intermittent behavior.

Turbulent, or intermittently chaotic, flow appears eventually because the instability of C forces points away from it, and all trajectories must proceed off the end of the L_1-L_2 curve in Fig. 2.15(c). Once off the curve, a trajectory wanders about in a fairly thin attractor in the phase space until it approaches a neighborhood of either waltz. The trajectory then reenters the laminar region of phase space. The typical time history in Fig. 2.16 clearly displays the laminar and turbulent behaviors in the total fundamental intensity.

On the way to characterizing the intermittency, we have already observed the inverse pitchfork bifurcation which suggests that the primary Floquet multiplier passes through -1. We confirmed this analytically by calculating the eigenvalues of an approximation to the Jacobian of M, in the neighborhood of C. We denote the equilibrium C as the vector $c = (c_1,c_2,c_3,c_4,c_5)$ and the unit basis vectors as $\hat{e}_i$, $i = 1,2,3,4,5$. Next we

$$\beta = 0.29201$$
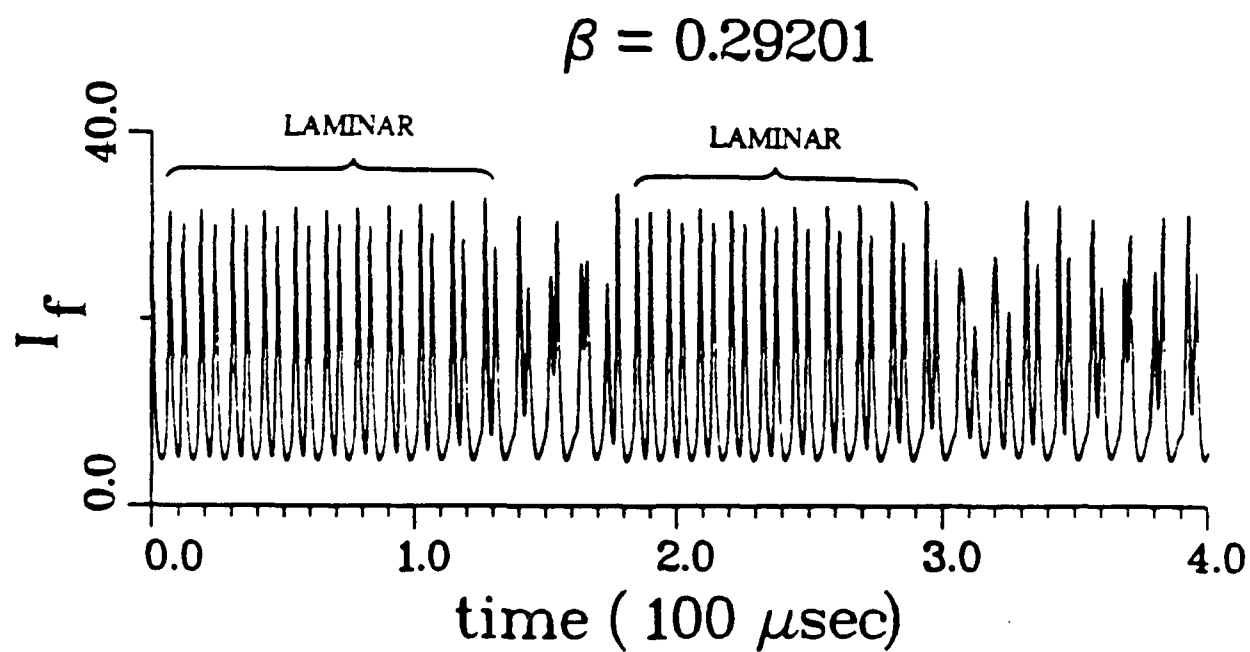
Fig. 2.16 Intermittency in the Total Fundamental Intensity for Three Modes. The numerical time trace displays periods of laminar and turbulent behavior.

define small displacement vectors $h_i = h_i \hat{e}_i$, where the scalar quantity $h_i = 0.001c_i$. We

then formulate a standard approximation to the Jacobian by:

$$J(c) = \left[\frac{M(c) - M(c - h_1)}{h_1}, \cdots, \frac{M(c) - M(c - h_5)}{h_5} \right]. \qquad 2.35$$

This approximation requires J to be nonsingular at c, which is true except for β equal to its

critical bifurcation value, slightly less than 0.2910.

It is straightforward to find approximate coordinates of c when $\beta < 0.2910$, where

c is stable. In such a case, one integrates numerically until the trajectory converges to a

small neighborhood of the periodic orbit. However, for values of β greater than 0.2910, c

is unstable and one must find this point another way; we apply the technique of homotopic

continuation (Hale and Sternberg, 1988; Keller, 1977). In the former reference, Hale and

Sternberg use this method to generate initial conditions near unstable limit cycles in order to

calculate numerical trajectories along unstable manifolds. In our case, we need to identify

the unstable point in the Poincaré section in order to approximate the Jacobian at that point.

We use the Poincaré map M and define a function $F(x) = x - M(x)$. Even though c

is unstable, it is still a zero of F, and we use a discrete Newton's method to find this zero.

We are able solve for these unstable points for values of β up to 0.50.

We plot the eigenvalues of several approximations to J for $\beta \approx 0.3$ in Fig. 2.17.

The periodic point loses its stability when $\beta \approx 0.2910$ and the principal eigenvalue of J

decreases through -1. Since the other eigenvalues remain fairly constant through this range

of β, this clearly characterizes the loss of stability as type III intermittency (Berge, et al.,

1984). Type III intermittency is characterized by: (i) a loss of stability when the principal

eigenvalue of J decreases through -1; (ii) a distribution of the durations of laminar
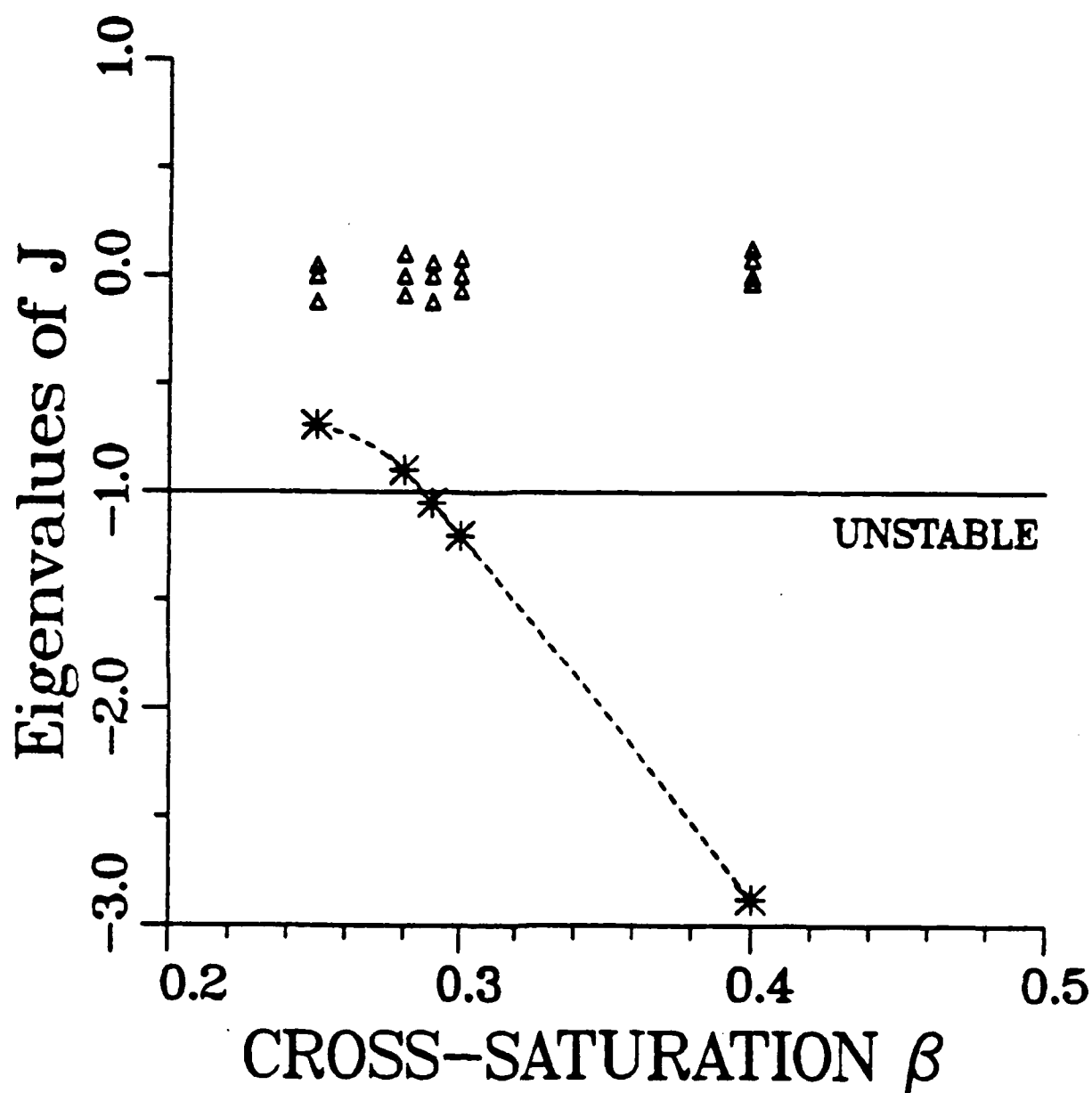
Fig. 2.17 Changes in the Eigenvalues of J as a Function of Cross-Saturation β. The decrease in the principal eigenvalue (denoted by *) through -1 indicates the transfer of stability leading to type III intermittency. All other eigenvalues remain essentially constant. Eigenvalues are calculated for β = 0.25, 0.28, 0.29, 0.30, and 0.40, and are real for β in this range.
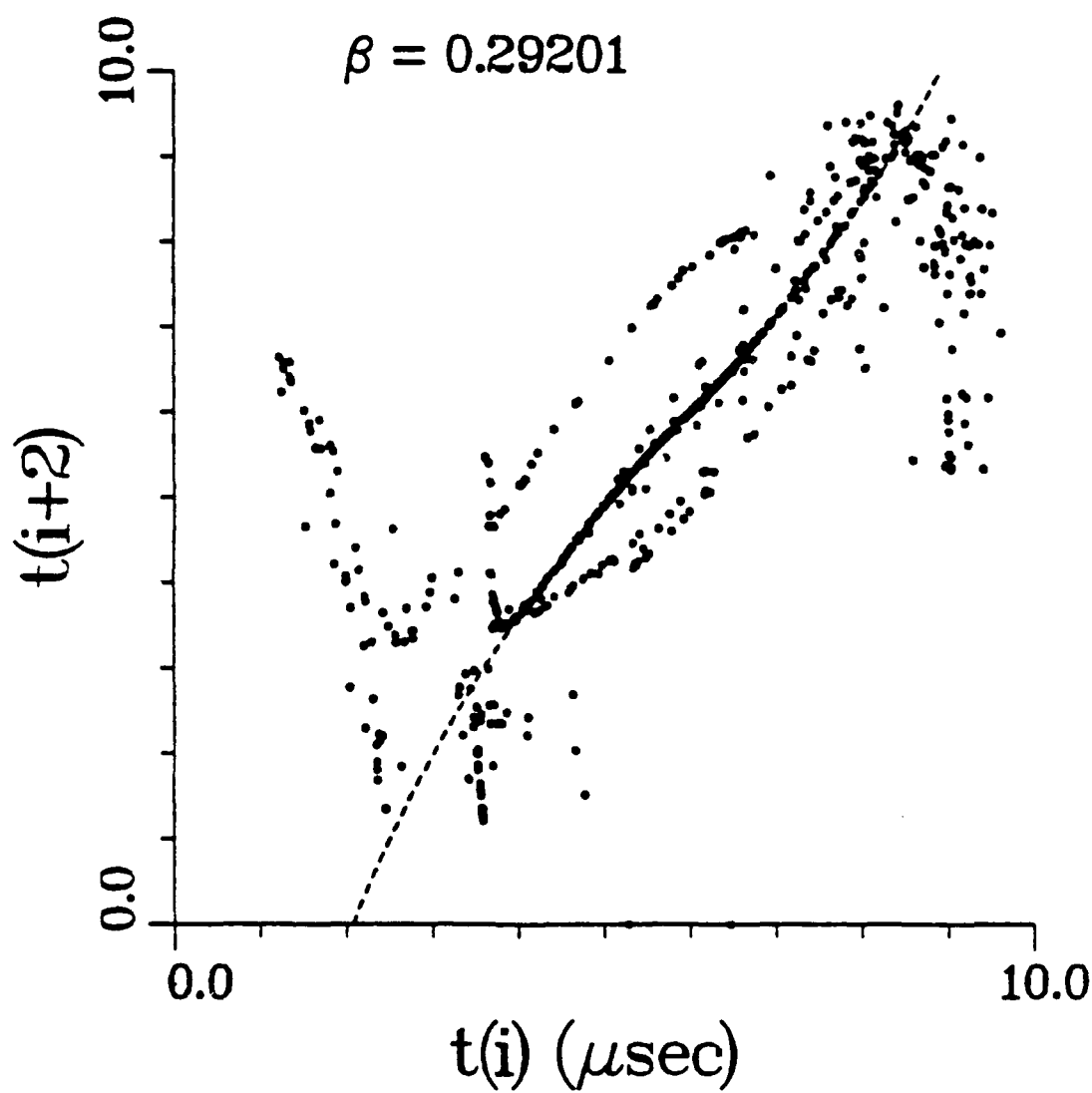
Fig. 2.18 Local Cubic Structure of Peak-to-Peak Return Times. For
β = 0.29201, these are 1000 consecutive peak-to-peak times t(i)
of the total fundamental intensity. The plotted cubic is
0.03(t - 5.9)3 + 1.1(t - 5.9) + 5.9.

flow regions which has an infinitely long tail; (iii) a locally cubic form for the second return map of peak-to-peak times (for our case, we observe peaks in the numerical intensity output). We now examine evidence of the latter two characteristics of type III intermittency (see Appendix C for more details).

Evidence of type III behavior appears in the statistics of the time spacing between peaks in the total intensity. We begin with a long numerical trajectory for the example $\beta = 0.29201$ (part of which is shown in Fig. 2.16) and create a sequence $\{t_1, t_2, t_3,...\}$ of 1000 peak-to-peak times. In Fig. 2.18 we plot the second return times for this sequence, i.e. $t(i+2)$ versus $t(i)$. The resulting figure displays the locally cubic form which is typical of the generic return map that generates type III intermittency (Pomeau and Manneville, 1980; Appendix C).

The type of intermittency is also evident in the distribution of the durations of laminar flow in a single trajectory. Pomeau and Manneville indicate the approximate distribution which is characteristic of this type of intermittency (Pomeau and Manneville, 1980). We define laminar behavior in our numerical trajectory as flow whose intersection with the plane $G_1 = 0.17$ lies on the L_1-L_2 curve in Fig. 2.15(c). Since the time of return to the plane remains nearly constant for points near C, we approximate the duration of laminar flow by counting the number of consecutive points which stay on the curve. The distribution of this count in Fig. 2.19 conforms to the model distribution described by Pomeau and Manneville. The long tail in this histogram is weighted (in the limit of infinite time) such that the distribution is not normalizable. A meaningful characteristic time scale, then, is an average of the inverse of the laminar flow duration. We find the period of the Poincaré map in the laminar region to be approximately 18 μsec. We then define the time
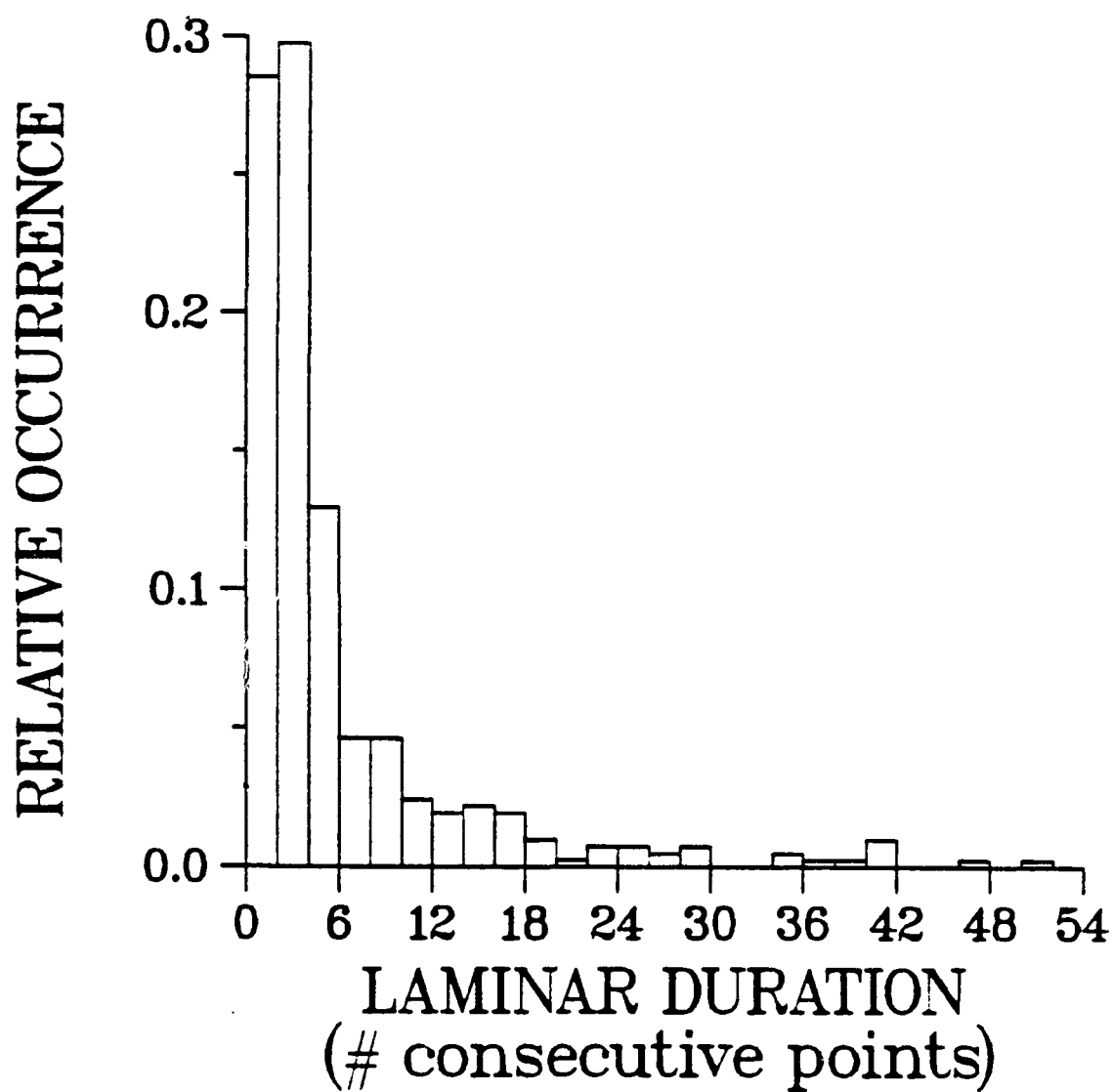
Fig. 2.19 Distribution of the Durations of Laminar Behavior. The relative occurrence is calculated with respect to 410 laminar regions in a single trajectory.

duration of laminar flow $t_l = (18\ \mu sec) \times$ (n: the number of consecutive points on L_1-L_2) and calculate the average $<1/t_l> \approx 1/70\ \mu sec^{-1}$.

The transition from intermittency to 'complete' chaos, for larger values of β, is difficult to detect numerically. The L_1-L_2 curve in Fig. 2.15(c) is an unstable manifold of C, and flow on that curve eventually returns to a neighborhood of C's stable manifold. However, the thinness of the attractor around L_1-L_2 obscures the trajectories returning to C. We conjecture that, at some value of β between 0.4 and 0.6, the unstable manifold becomes tangent to the stable manifold. The complications in the flow contingent with the creation of such a tangency are sufficient to produce chaos (Chow and Hale, 1982; Peitgen, 1982).

When $0.4 < \beta < 0.96$, the flow is chaotic on a strange attractor like the one depicted in Fig. 2.20(a). The chaotic intensity output for $\beta = 0.60$, the approximate experimental value used by Baer, is shown in Fig. 2.20(b). Another transition occurs for β between 0.96 and 0.98. We observe an inverse cascade which stabilizes the flow, and for $\beta > 0.98$ the only allowed solutions are those for which a single intensity is stable and nonzero, while the other two intensities are forced to zero. This behavior persists for values of β up to 2.0. Thus, the range of β in which modes may coexist is from 0 to 1; one way to obtain single-mode laser operation is to increase β which increases the competition between modes.

For all the cases we considered, different initial conditions made no difference in the character of the flow. That is, we found no instances of stable periodic orbits coexisting with locally stable steady state points, or with small regions of phase space with strange attractors. However, the coexistence of two periodic solutions (the left and right waltz) in phase space do make the choice of initial conditions more important. The shape of the basins of attraction for each waltz, for example, remains an open question.
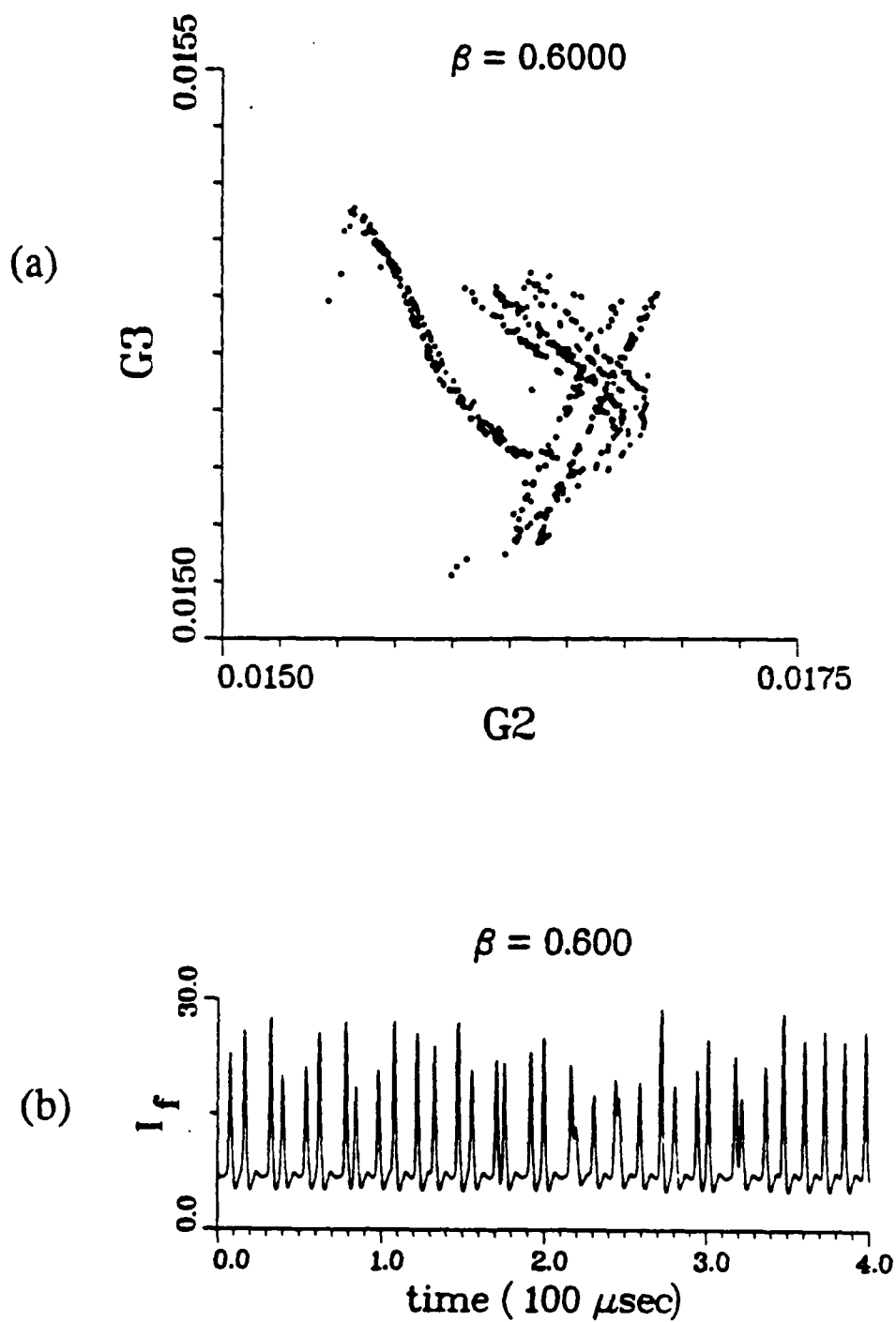
Fig. 2.20 Chaotic Numerical Trajectory for Three Modes. The chaotic flow
on the Poincaré map in (a) corresponds to the total fundamental
intensity output in (b).

Conclusions

The analysis of Baer's rate equation model for intracavity frequency doubling has allowed us to develop a better understanding of the phase space dynamics. A laser oscillating with a single-mode can only proceed to an asymptotically stable steady state. A two-mode laser can operate in steady state, with a doubling crystal in the cavity, as long as the doubling efficiency (quantified by ε) is small. For more efficient doubling, the two modes pulse on and off periodically, with each pulse resembling the single-mode behavior over short times. No chaos is observed in a two-mode intracavity doubled Nd:YAG laser, but the nonlinear coupling in the doubling process is clearly responsible for the instablility of steady state solutions to the rate equations. Using Baer's extension of the rate equations to multiple longitudinal modes, we showed that the three-mode case displays the complete range of behavior from steady state intensity output, to periodic pulses, to intermittency and chaos. We proved explicit stability conditions on the nonlinear coupling parameter ε for the two-mode and three-mode cases. Finally, we found an intermittent route to chaos, by varying the cross-saturation parameters which affect how the modes compete for the available gain medium.

The discovery of intermittency in the model for the intracavity doubled Nd:YAG laser holds a special significance. There are countless examples of chaotic dynamics exhibited in laser systems (see the References on "Experiments Displaying Intermittency" and "Chaos in Lasers"), but there are very few instances of chaotic phenomena reported for linear laser cavities (as opposed to ring lasers) with only passive optical elements. Another similar laser which has demonstrated chaotic dynamics is the laser cavity with a saturable absorber (see the References on "Three-Level Lasers" and "Lasers with Saturable Absorbers"). Virtually all other chaotic lasers either include an artificial modulation of the

pump source or intracavity elements, or require additional feedback loops outside the cavity to generate a destabilizing nonlinear effect (see References of "Modulated Parameters"). In the next chapter we portray the intracavity doubled Nd:YAG laser as a paradigm for the study of nonlinear dynamics in lasers.

CHAPTER III

A NEW MODEL FOR THE DOUBLING PROCESS

Introduction

Ideally, the more we understand the source of chaos through a theoretical model, the better we can control the stability of the experimental system. M. Oka and S. Kubota hypothesize that the instabilities in an intracavity doubled YAG laser are due to interactions among longitudinal modes with different spatial polarizations (Oka and Kubota, 1988). They eliminate the chaotic fluctuations, in a laser very similar to the one studied by Baer, by inserting a quarter wave plate (QWP) in the cavity, rotated at a 45 degree angle with respect to the KTP crystal fast axis.

Furthermore, they present theoretical and experimental evidence of the crucial role of polarization in the dynamics of intracavity frequency doubling. In particular, the KTP crystal is cut to maximize the doubling process by tal ing advantage of the KTP's birefringence (Fan, et al., 1987; Ito, et al., 1975; Yao and Fahlen, 1984); Oka and Kubota report that the intensity output from an intracavity doubled Nd:YAG laser is polarized in two orthogonal directions. Their observations of the quarter wave plate's influence on the intensity output make it clear that any reasonable model of intracavity doubling must account for the birefringence of the cavity elements.

Oka and Kubota also outline the initial steps of an analysis technique which we find essential for modelling the doubling process correctly. They use the Jones matrix

representations (see Appendix D) of the KTP crystal and QWP to calculate the green production by two modes lasing in orthogonal polarization directions.

In the first section of this chapter, we complete the work begun by Oka and Kubota and develop a general model of intracavity doubling for a Class B laser with any number of birefringent elements and without reference to a specific cavity configuration. We account for the frequency doubling of modes which lase in the same polarization direction, as well as in orthogonal polarization directions. Our analysis is the first to include the possibility of birefringence in the YAG crystal. We also establish the crucial connection between the theoretical second-harmonic loss terms and the multimode rate equations. In our new rate equations, the important elements of the doubling process are reduced to two parameters. The analysis section includes the proof of stability criteria, for steady state solutions to those equations, which successfully predict simple ways to eliminate the chaotic fluctuations from the total intensity output. Then we apply our general results to three specific laser cavities with and without quarter wave plates. Finally, our numerical results generate approximate bifurcation diagrams for two particular alignments of the polarized longitudinal modes, and we present several interesting comparisons of numerical and experimental data.

Derivation

Our first goal in this section is to derive analytic expressions which describe how electric fields, with frequencies near the YAG fundamental frequency, combine to produce light at the doubled frequency. We will then show how these expressions alter the rate equations proposed in (Baer, 1986). We begin with the following assumptions:

(i)   Each longitudinal mode is a time-dependent electric field (E-field) whose frequency is one of the frequencies allowed by the standing wave approximation. (The intensity of each mode is the squared magnitude of its E-field.)

(ii)   Light propagates in the cavity as a plane wave, along the direction of the cavity's optical axis (see Fig. 1.4).

(iii)   The laser beam cross-section is constant along the length of the cavity; transverse mode structure does not affect the dynamics of the doubling process.

(iv)   The only optical elements present in the cavity are birefringent materials, and each element has orthogonal fast and slow axes of propagation for the electric field.

(v)   Reflection at the cavity mirrors has no effect on the polarization state of an E-field.

Under the above assumptions, we can define a coordinate system in the plane of the propagating light, and define a complex E-field with two time-dependent coordinates. Each coordinate includes a magnitude and phase. We can describe the propagation of this field through the cavity by multiplication with 2-by-2 matrices (Hecht and Zajac, 1979; Oka and Kubota, 1988; Appendix D). Assumptions (i)-(v) also guarantee that the round trip matrix, which results from combining only passive birefringent optical components, has a special structure which allows us to generalize the analysis.

Specifically, the round trip matrix is produced by multiplying only two types of matrices. The first matrix $C(\delta)$ describes passage through a birefringent material which induces a relative phase delay δ, and is diagonal:

$$C(\delta) = \begin{bmatrix} e^{i\delta/2} & 0 \\ 0 & e^{-i\delta/2} \end{bmatrix}.$$

3.1

The other type of matrix R(φ) accounts for the relative angular positions of the fast axes of two adjacent optical elements (see fig. 3.1):

$$R(\varphi) = \begin{bmatrix} \cos\varphi & -\sin\varphi \\ \sin\varphi & \cos\varphi \end{bmatrix}.$$ 3.2

Both matrices belong to SU(2), the group of complex unitary matrices whose determinant equals 1. (Recall that groups are closed under multiplication.) The matrix C has the additional property of having complex conjugates along its diagonal. In fact, we now prove that any round trip matrix made up of such components is also unitary, symmetric, and has conjugate diagonal elements. The round trip matrix also has off-diagonal entries which are purely imaginary.
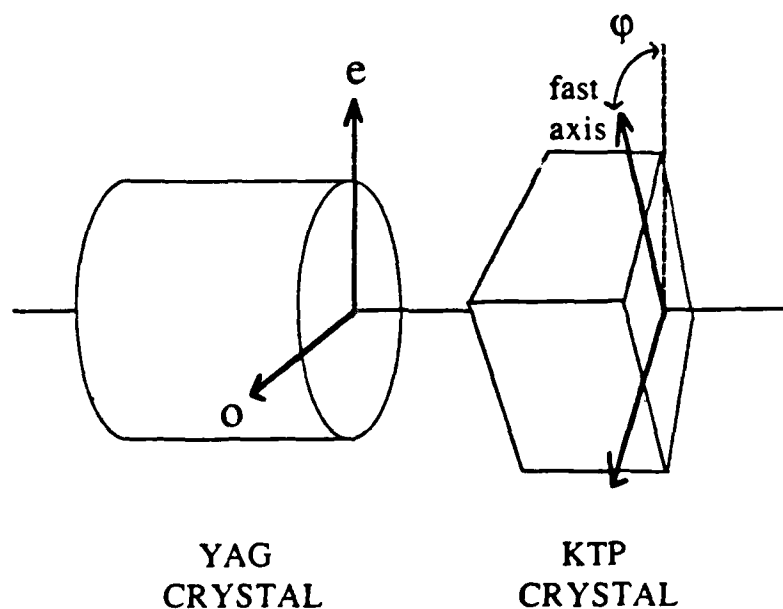
Fig. 3.1   Relative Angular Position of Two Adjacent Birefringent Elements. The angle φ lies between the respective fast axes.
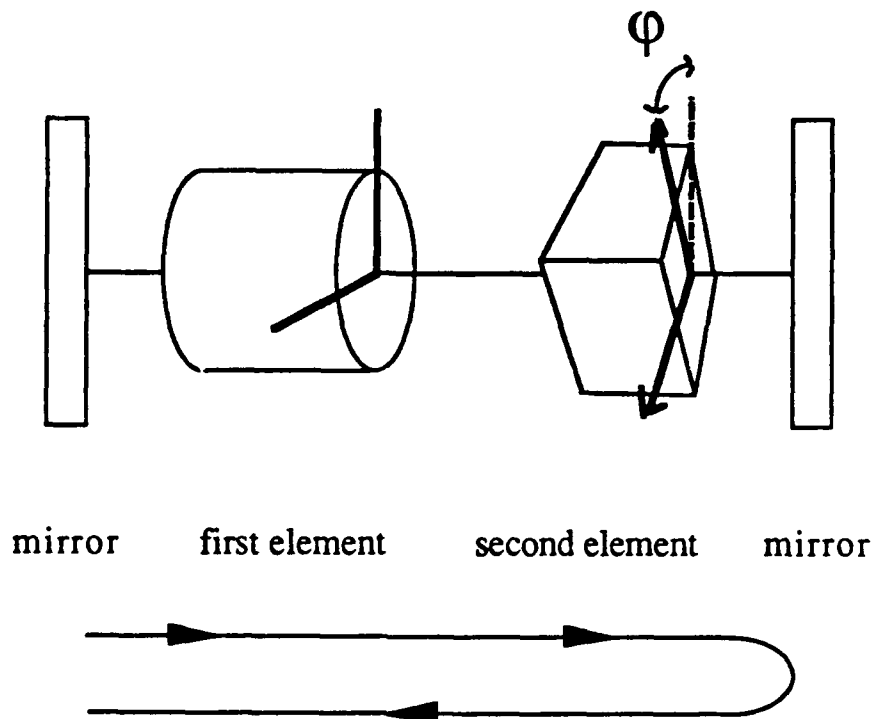
Fig. 3.2 Schematic Construction of a Round Trip Matrix M. The arbitrary
reference point for the start of this round trip is chosen to be the
left cavity mirror.

The special structure of the round trip matrix M relies on the fact that any rotation

experienced in a single pass through the cavity must be matched with a counter-rotation on

the return passage. For example, the round trip matrix for a cavity with two birefringent

elements has the following structure (fig. 3.2):

return through	counter	second	mirror	second	rotation	first
first element	rotation	element	(identity)	element		element

$$M \quad = \quad C(\delta_1) \quad R(\varphi_1) \quad C(\delta_2) \quad I \quad C(\delta_2) \quad R(-\varphi_1) \quad C(\delta_1)$$

3.3

$$= \begin{bmatrix} a & 0 \\ 0 & \bar{a} \end{bmatrix} \begin{bmatrix} \cos\varphi_1 & -\sin\varphi_1 \\ \sin\varphi_1 & \cos\varphi_1 \end{bmatrix} \begin{bmatrix} b & 0 \\ 0 & \bar{b} \end{bmatrix}^2 \begin{bmatrix} \cos\varphi_1 & \sin\varphi_1 \\ -\sin\varphi_1 & \cos\varphi_1 \end{bmatrix} \begin{bmatrix} a & 0 \\ 0 & \bar{a} \end{bmatrix}.$$

(The bar $(^-)$ represents complex conjugation.) The most general round trip matrix, with N different elements, is given by:

$$M = C(\delta_1) R(\phi_1) \cdots R(\phi_{N-1}) C(\delta_N) C(\delta_N) R(-\phi_{N-1}) \cdots R(-\phi_1) C(\delta_1) . \qquad 3.4$$

To prove the proposition below, we observe some elementary properties of the unitary matrix

$$\Sigma = \begin{bmatrix} 0 & 1 \\ -1 & 0 \end{bmatrix} . \qquad 3.5$$

We note that this matrix rotates vectors by $\pi/2$, and has the following properties:

(a) $-\Sigma^2 = I$, the identity.

(b) $-\Sigma \begin{bmatrix} a & b \\ c & d \end{bmatrix} \Sigma = \begin{bmatrix} d & -c \\ -b & a \end{bmatrix}$, for arbitrary complex a,b,c and d.

(c) $\Sigma C \Sigma = -C^*$, for matrices C defined above.

(d) $\Sigma R \Sigma = -R$, for matrices R defined above. This also follows from property (a) since all rotations of the plane commute.

We can now show:

Proposition 3.1. Let the round trip matrix M be defined by (3.4). Then
M ∈ SU(2) and has the form:

$$M = \begin{bmatrix} a & iy \\ iy & \bar{a} \end{bmatrix} \qquad 3.6$$

where $a \in C$, $y \in \Re$; and the eigenvectors of M are real and orthogonal.

Remarks. The fact that the eigenvectors of M are real indicates an important
property of the laser output. A real E-field vector, in the Jones theory, represents linearly
polarized light. Since we calculate our round trip matrix beginning at one of the cavity
mirrors, this implies that the intensity output from such a laser is linearly polarized,
regardless of the amount of birefringence, or relative angular position, of the intracavity
elements.

As we calculate the eigenvalues and eigenvectors of M, we note that the derivation
of the general model for intracavity doubling only requires the existence of orthogonal
eigendirections. However, later applications to specific laser cavities need the functional
form of the eigenvectors, so we present the necessary equations here.

Proof. The unitary character of M follows from the closure of SU(2) under
multiplication. The symmetry of M is directly shown, since each matrix C is diagonal, and
for $j = 1, 2,..., N-1$ we have $R(\phi_{N-1})^T = R(\phi_{N-1})^* = R(-\phi_{N-1})$ (we distinguish here
between the Hermitian adjoint A^* and the transpose A^T which involves no complex
conjugation):

$$M^T = [\ C(\delta_1)\ R(\phi_1)\ \cdots\ R(\phi_{N-1})\ C(\delta_N)\ C(\delta_N)\ R(-\phi_{N-1})\ \cdots\ R(-\phi_1)\ C(\delta_1)\ ]^T$$

$$= C(\delta_1)^T\ R(-\phi_1)^T\ \cdots\ R(-\phi_{N-1})^T\ C(\delta_N)^T\ C(\delta_N)^T\ R(\phi_{N-1})^T\ \cdots\ R(\phi_1)^T\ C(\delta_1)^T$$

$$= M.$$

Suppose A is a symmetric matrix, with elements

$$A\ =\ \begin{bmatrix} a & c \\ c & d \end{bmatrix}.$$

Then (b), above, implies that $\Sigma\ A\ \Sigma\ =\ -\ A^*$ if and only if A has the desired form of (3.6). That is, property (b) requires that $d = \bar{a}$, and $c = -\ \bar{c}$ which means c must be purely imaginary. This part of the proof is completed by observing that

$$\Sigma\ M\ \Sigma\ =\ \Sigma\ C(\delta_1)\ R(\phi_1)\ \cdots\ R(\phi_{N-1})\ C(\delta_N)\ C(\delta_N)\ R(-\phi_{N-1})\ \cdots\ R(-\phi_1)\ C(\delta_1)\ \Sigma$$

$$=\ -\ \Sigma\ C(\delta_1)\ \Sigma^2\ R(\phi_1)\ \Sigma^2\ \cdots\ \Sigma^2\ R(-\phi_1)\ \Sigma^2\ C(\delta_1)\ \Sigma$$

$$=\ -\ C^*(\delta_1)\ R(\phi_1)\ \cdots\ R(\phi_{N-1})\ C^*(\delta_N)\ C^*(\delta_N)\ R(-\phi_{N-1})\ \cdots\ R(-\phi_1)\ C^*(\delta_1)$$

$$=\ -\ (M^*)^T\ =\ -\ M^*.$$

(The minus sign appears in the second equality because there are even numbers of C and R factors, but an odd number of Σ^2 terms inserted in the multiplication. The last equality

comes from the symmetry of M.) Therefore, M has complex conjugate diagonal entries and purely imaginary off-diagonals, as in (3.6). Since M is unitary, its eigenvalues have magnitude 1, its eigenvectors are orthogonal, and $|a|^2 + y^2 = 1$, which simplifies several calculations.

In the case where $y = 0$, the eigenvalues and orthonormal eigenvectors of M are simply:

$$\lambda_1 = a \qquad w_1 = \begin{bmatrix} 1 \\ 0 \end{bmatrix}$$

$$\lambda_2 = \bar{a} \qquad w_2 = \begin{bmatrix} 0 \\ 1 \end{bmatrix} . \qquad \qquad 3.7$$

For $y \neq 0$, the eigenvalues and orthogonal, but unnormalized, eigenvectors are:

$$\lambda_{1,2} = \frac{1}{2}\left[(a + \bar{a}) \pm \sqrt{(a + \bar{a})^2 - 4}\,\right]$$

$$\qquad \qquad \qquad 3.8.a$$

$$= Re(a) \pm \sqrt{[Re(a)]^2 - 1}$$

$$w_1 = \begin{bmatrix} 2\,Im(a) - \sqrt{4 - (a + \bar{a})^2} \\ 2\,y \end{bmatrix}$$

$$\qquad \qquad \qquad 3.8.b$$

$$w_2 = \begin{bmatrix} 2\,Im(a) + \sqrt{4 - (a + \bar{a})^2} \\ 2\,y \end{bmatrix} . \qquad 3.8.c$$

The components of w_1 and w_2 are always real for M in the form of (3.6).

For the remaining discussion, we take M to have the form in (3.6). The next step in the analysis is to recognize that only those E-fields which are eigenvectors of M will survive multiple round trips through the cavity. The physical reason for this is clear: the lasing process is sustained by the cascade of stimulated emission which occurs because the cavity mirrors are carefully aligned to reflect an E-field directly onto itself. Similarly, the polarization state of an E-field that replicates after each round trip maximizes its amplification. The only fields which replicate after a round trip are eigenvectors of M. Thus, we can understand the propagation of longitudinal modes in the cavity by studying the round trip matrix M.

Moreover, the eigenvectors of a unitary matrix are orthogonal. This fact has great physical significance: given a fixed cavity configuration, there are exactly two candidate polarization directions in which any mode can oscillate. Our goal now is to examine the pairwise coupling of modes which oscillate either in the same polarization direction, or in orthogonal polarization directions.

It is interesting to recall that $|\lambda|$ is identically 1 for a unitary matrix. This implies that an E-field (which points in an eigendirection) could oscillate forever in a perfect laser cavity (with no sources of gain or loss) with no increase or attenuation. However, in a real laser cavity, energy is input from the pump and energy leaks out via transmission through mirrors and scattering in the cavity; the time evolution of the E-field amplitudes depends on the continual interactions of these gains and losses. Therefore, the important elements in this part of the analysis are not the eigenvalues, but the eigenvectors.

We want to examine the coupling of two modes which may be polarized in parallel or orthogonal directions. No other analysis to date has accounted for these two distinct ways the modes can interact. Suppose we have a laser cavity whose round trip matrix has the structure described by Proposition 3.1. We can explicitly calculate how the intensities

of two modes combine to produce an intensity at the doubled frequency. To do this, we follow the approach outlined in (Oka and Kubota, 1988) but in a much more general setting.

We define normalized vectors **u** and **v** in one of two ways, with respect to the eigenvectors of M in (3.8): either $\mathbf{u} = \mathbf{v} = \mathbf{w}_i/|\mathbf{w}_i|$ ($i = 1$ or 2) so the vectors are parallel; or $\mathbf{u} = \mathbf{w}_1/|\mathbf{w}_1|$ and $\mathbf{v} = \mathbf{w}_2/|\mathbf{w}_2|$ so **u** is orthogonal to **v**. These two vectors identify the polarization directions for two fields oscillating in the cavity. Given **u** and **v**, we define two time-dependent E-fields:

$$\mathbf{E}_1(\omega_1, t) = |E_1(t)|\, e^{i(\omega_1 t + \varphi_1)} \begin{bmatrix} u_1 \\ u_2 \end{bmatrix}$$

$$\mathbf{E}_2(\omega_2, t) = |E_2(t)|\, e^{i(\omega_2 t + \varphi_2)} \begin{bmatrix} v_1 \\ v_2 \end{bmatrix},$$

<div align="right">3.9</div>

where ω_1 and ω_2 are allowed frequencies for longitudinal modes, $|E_1(t)|$ and $|E_2(t)|$ are the magnitudes of the respective fields, and φ_1 and φ_2 are arbitrary initial phases. (For this discussion, we suppress the sinusoidal spatial variation of the fields, see Fig. 1.6.) The field amplitudes and phases are time dependent, but the polarization directions determined by the eigenvectors are constant.

It is important to note two different time scales present in the E-field expressions (3.9). The first time scale is that of the frequency ω_i which is determined primarily by the length of the cavity. This extremely high frequency is on the order of 10^{14} Hz (see Appendix B). The other time scale at work in (3.9) is the cavity decay rate of the E-field, determined mainly by the transmission losses at the output mirror and the cavity round trip time. For a cavity length of 3.0 cm and a transmission of 0.1%, the cavity decay rate (Appendix B) is on the order of 10^7 Hz, many orders of magnitude slower than the phase

oscillations. We will, very shortly, average the fields over several periods of the faster oscillations, to simplify the study of the field amplitude dynamics.

The E-field vectors are defined relative to some fixed coordinate reference in the cavity. We take the coordinate axes to be the fast and slow (or extraordinary and ordinary) axes of the doubling crystal; call these the e- and o-axes respectively. Let E_e denote the total E-field in the e-direction, that is, the sum of the first components of E_1 and E_2. Similarly define E_o as the sum of the second components of E_1 and E_2. The electric fields E_e and E_o in the doubling crystal combine to produce a new field $P_d(\omega_1,\omega_2,t)$, approximately at the doubled frequency, according to the following relation (Ito, et al., 1970):

$$P_d(\omega_1,\omega_2,t) = d_{eff}\, E_e(\omega_1,\omega_2,t)\, E_o(\omega_1,\omega_2,t) \qquad\qquad 3.10$$

$$= d_{eff}\left[\,|E_1(t)|\, u_1\, e^{i(\omega_1 t + \varphi_1)} + |E_2(t)|\, v_1\, e^{i(\omega_2 t + \varphi_2)}\right]$$

$$\times\ \left[\,|E_1(t)|\, u_2\, e^{i(\omega_1 t + \varphi_1)} + |E_2(t)|\, v_2 e^{i(\omega_2 t + \varphi_2)}\right]\ .$$

The effective nonlinear coefficient d_{eff} (m/V), for the KTP crystal, indicates how efficiently the doubling crystal converts the E-fields from the fundamental frequency to the doubled frequency (Ito, et al., 1975; Shen, 1984). We assume, for the moment, that the KTP crystal is the first cavity element encountered in the round trip, so the eigenvector components u_j and v_j in (3.10) are real. This is not true in general; we deal with the more general case later.

We could calculate the new doubled intensity I_d explicitly as the square magnitude of P_d, i.e. $I_d = P_d\, P_d^*$. However, the oscillations at frequencies ω_1 and ω_2 are sufficiently

fast to treat the field amplitudes $|E_j(t)|$ as constants over several time periods of order $(1/\omega_1)$, and derive a good approximation to I_d by averaging:

$$I_d(t) \approx\; <P_d(\omega_1,\omega_2,t)\,P_d^*(\omega_1,\omega_2,t)> \qquad\qquad 3.11$$

$$= d_{eff}^2\Big(I_1^2(t)\,u_1^2\,u_2^2 + I_2^2(t)\,v_1^2\,v_2^2 + I_1(t)\,I_2(t)\,[u_1\,v_2 + u_2\,v_1]^2\Big),$$

where $<\;>$ indicates a time average over an interval on the order of $t \in [\,0,\,100/\omega_1\,]$, and $I_j = E_jE_j^*$. The I_1^2 and I_2^2 terms represent frequency doubling by the second harmonic generation of each mode. The I_1I_2 cross term corresponds to sum-frequency generation by the combination of the two modes.

We scale the coefficient d_{eff}, usually expressed in (m/V), to correspond to our dimensionless coupling coefficient ε:

$$\varepsilon = \frac{d_{eff}^2}{4\,\varepsilon_0\,c\,D^3}\,, \qquad\qquad 3.12.a$$

where c is the speed of light, ε_0 is the permittivity constant ($8.8 \times 10^{-12}\,C^2/N\text{-}m^2$), and D is an appropriate atomic length parameter for the doubling crystal. (The factor of 4 in the denominator arises from the definition of another coefficient derived below, in (3.13).) This scaling actually renders ε in units of inverse watts, but a later scaling of our differential equations makes ε dimensionless.

The relative weights of the coefficients in (3.11) are determined by the eigenvectors of the round trip matrix; they inherit very simple relationships from the special structure of the matrix. First, we label the coefficients as:

$$g_1 = 4\,u_1{}^2\,u_2{}^2$$

$$g_2 = 4\,v_1{}^2\,v_2{}^2 \qquad\qquad 3.12.b$$

$$\sigma = 4\,(\,u_1\,v_2 + u_2\,v_1)^2\,.$$

We next observe that the normalized vector **u** can be expressed as a function of some angle φ, i.e. $u_1 = \cos\varphi$ and $u_2 = \sin\varphi$. If we have the case of two modes with parallel polarizations, then $g_1 = g_2$ trivially. If we have $\mathbf{u} \perp \mathbf{v}$ then we can write **v** as $v_1 = \sin\varphi$ and $v_2 = -\cos\varphi$, and we see again that $g_1 = g_2$. So in all cases, we have g_1 identically equal to g_2. We let g denote the common value of this doubling parameter which can take on values from 0 to 1.

The second coefficient σ has one form if $\mathbf{u} = \mathbf{v}$, and another if **u** is orthogonal to **v**. This distinction is extremely important in modeling the doubling process since σ is the coefficient of the term which describes the sum-frequency generation of the two modes. The values of g and σ determine the relative contributions of second harmonic generation and sum-frequency generation to the overall production of the green light.

If $\mathbf{u} = \mathbf{v}$, i.e. the modes are in the same polarization state, then

$$\sigma = 4(2\cos\varphi\sin\varphi)^2 = 4g, \qquad\qquad 3.13$$

and the doubled intensity is:

$$I_d(t) = \varepsilon\,(\,g\,I_1{}^2 + g\,I_2{}^2 + 4\,g\,I_1\,I_2\,). \qquad\qquad 3.14$$

On the other hand, if $\mathbf{u} \perp \mathbf{v}$ and the modes lase in orthogonal polarization directions, then

$$\sigma = 4(-\cos^2\varphi + \sin^2\varphi)^2 = 4(\cos 2\varphi)^2 = 4(1 - [\sin 2\varphi]^2) = 4(1-g), \qquad 3.15$$

and the intensity at the doubled frequency is:

$$I_d(t) = \epsilon (g I_1^2 + g I_2^2 + 4[1-g] I_1 I_2). \qquad 3.16$$

Relations similar to (3.14) and (3.16) were derived by Oka and Kubota, but only for a cavity with a QWP, and only for three particular angles of the QWP. Their results also require the two contributing modes to be orthogonal. Our equation is derived in a much more general setting which allows for **u** and **v** to be either parallel or orthogonal, and applies to a cavity with any number of birefringent elements.

Recall that we derive (3.14) and (3.16) for **u** and **v** with real components. We now show

Proposition 3.2. The relationships (3.13) and (3.15) between coefficients g and σ hold for E-fields (3.9) at any position in the cavity, where the eigenvectors may be complex.

Remark. The specific value of g depends on the location of the doubling crystal in the cavity, and must be calculated from the eigenvectors of the round trip matrix which starts at one face of the doubling crystal.

Proof. If the KTP crystal is the cavity element nearest a mirror (Fig. 3.3(a)), then **u** and **v** indicate how much of the E-fields lie along the e- and o-axes of the KTP. These vectors may then be used in (3.10) to determine the E-field at the doubled frequency.
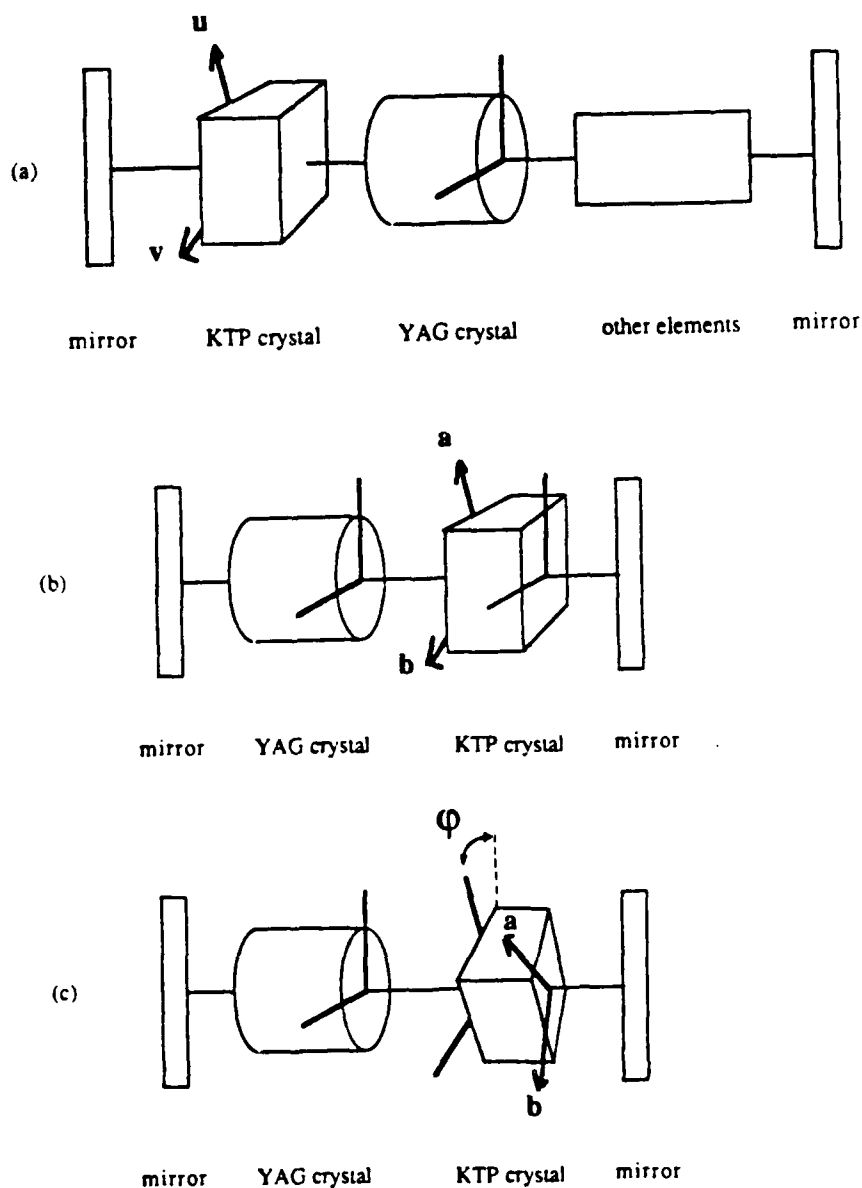
Fig. 3.3 Generic Cavity Configurations Referenced in the Proof of
Proposition 3.2. (a) The eigenvectors **u** and **v** are identified at
the input face of the KTP crystal. (b) Complex eigenvectors **a**
and **b** are shown for the two-element cavity; the fast axes of the
YAG and KTP crystals are parallel. (c) The KTP crystal has been
rotated at angle φ with respect to the YAG fast axis.

Suppose, however, the KTP crystal is the second cavity element (Fig. 3.3(b)), and the two birefringent elements have their fast axes parallel. Then the complex round trip eigenvectors **a** and **b**, at the KTP crystal, can be computed by propagating **u** and **v** through the first birefringent element (with induced phase delay ξ):

$$\mathbf{a} = C(\xi)\,\mathbf{u} = \begin{bmatrix} e^{i\xi/2} & 0 \\ 0 & e^{-i\xi/2} \end{bmatrix} \begin{bmatrix} u_1 \\ u_2 \end{bmatrix} = \begin{bmatrix} e^{i\xi/2}\,u_1 \\ e^{-i\xi/2}\,u_2 \end{bmatrix} \qquad \mathbf{b} = \begin{bmatrix} e^{i\xi/2}\,v_1 \\ e^{-i\xi/2}\,v_2 \end{bmatrix}. \qquad 3.17$$

We use these vectors to calculate the doubled E-field P_d as we did in (3.10):

$$P_d(\omega_1,\omega_2,t) = d_{\text{eff}}\,E_e(\omega_1,\omega_2,t)\,E_o(\omega_1,\omega_2,t) \qquad\qquad 3.18$$

$$= d_{\text{eff}}\Big[\,|E_1(t)|\,a_1\,e^{i(\omega_1 t + \varphi_1)} + |E_2(t)|\,b_1\,e^{i(\omega_2 t + \varphi_2)}\Big]$$

$$\times \Big[\,|E_1(t)|\,a_2\,e^{i(\omega_1 t + \varphi_1)} + |E_2(t)|\,b_2 e^{i(\omega_2 t + \varphi_2)}\Big]\,.$$

When we compute the time-average of the doubled intensity I_d,

$$I_d(t) \approx\, < P_d(\omega_1,\omega_2,t)\,P_d^*(\omega_1,\omega_2,t) > \qquad\qquad 3.19$$

$$= \Big\langle d_{\text{eff}}^2\Big[\,|E_1(t)|\,a_1\,e^{i(\omega_1 t + \varphi_1)} + |E_2(t)|\,b_1 e^{i(\omega_2 t + \varphi_2)}\Big]$$

$$\times \Big[\,|E_1(t)|\,a_2\,e^{i(\omega_1 t + \varphi_1)} + |E_2(t)|\,b_2 e^{i(\omega_2 t + \varphi_2)}\Big]$$

$$\times \Big[\,|E_1(t)|\,\bar{a}_1\,e^{-i(\omega_1 t + \varphi_1)} + |E_2(t)|\,\bar{b}_1 e^{-i(\omega_2 t + \varphi_2)}\Big]$$

$$\times \Big[\,|E_1(t)|\,\bar{a}_2\,e^{-i(\omega_1 t + \varphi_1)} + |E_2(t)|\,\bar{b}_2 e^{-i(\omega_2 t + \varphi_2)}\Big]\,\Big\rangle$$

$$= d_{\text{eff}}^2 \Big\langle \Big[\,E_1^2|a_1|^2 + E_1 E_2\big(a_1\bar{b}_1\,e^{-i([\omega_1-\omega_2]t + \varphi_1-\varphi_2)} + c.c.\big) + E_2^2|b_1|^2\,\Big]$$

$$\times \Big[\,E_1^2|a_2|^2 + E_1 E_2\big(a_2\bar{b}_2\,e^{-i([\omega_1-\omega_2]t + \varphi_1-\varphi_2)} + c.c.\big) + E_2^2|b_2|^2\,\Big]\Big\rangle$$

$$= d_{eff}^2 \langle [E_1^2 u_1^2 + E_1 E_2 \, u_1 v_1 \, 2\cos([\omega_1-\omega_2]t+\varphi_1-\varphi_2) + E_2^2 v_1^2]$$

$$\times [E_1^2 u_2^2 + E_1 E_2 \, u_2 v_2 \, 2\cos([\omega_1-\omega_2]t+\varphi_1-\varphi_2) + E_2^2 v_2^2] \rangle$$

$$= d_{eff}^2 \Big(I_1^2(t) \, u_1^2 \, u_2^2 + I_2^2(t) \, v_1^2 \, v_2^2 + I_1(t) \, I_2(t) \, [u_1 \, v_2 + u_2 \, v_1]^2 \Big) \,, \qquad \text{3.19, cont.}$$

we get the exact expression for I_d we found in (3.11) with the same u_1, u_2, v_1 and v_2. Thus, for complex eigenvectors of the form (3.17), the coefficient relationships (3.13) and (3.15) still hold.

We next consider the case in Fig. 3.3(c), where the doubling crystal is the second cavity element and its fast axis is positioned at a non-zero angle φ with respect to the first element's fast axis. The eigenvectors $\mathbf{a}$ and $\mathbf{b}$ at the face of the KTP are now given by

$$\mathbf{a} = R(-\varphi) \, C(\xi) \, \mathbf{u} = \begin{bmatrix} \cos\varphi & \sin\varphi \\ -\sin\varphi & \cos\varphi \end{bmatrix} \begin{bmatrix} e^{i\xi/2} & 0 \\ 0 & e^{-i\xi/2} \end{bmatrix} \begin{bmatrix} u_1 \\ u_2 \end{bmatrix}$$

$$= \begin{bmatrix} cu_1 e^{i\xi/2} + su_2 e^{-i\xi/2} \\ -su_1 e^{i\xi/2} + cu_2 e^{-i\xi/2} \end{bmatrix}, \quad c = \cos\varphi \quad s = \sin\varphi$$

$$\mathbf{b} = R(-\varphi) \, C(\xi) \, \mathbf{v} = \begin{bmatrix} cv_1 e^{i\xi/2} + sv_2 e^{-i\xi/2} \\ -sv_1 e^{i\xi/2} + cv_2 e^{-i\xi/2} \end{bmatrix}. \qquad \text{3.20}$$

We need not calculate P_d directly for this case, we only need show that $\mathbf{a}$ and $\mathbf{b}$ have the same form as (3.17), in which case the relations (3.13) and (3.15) are valid, but the specific value of g may be different. To show this, recall that unitary matrices preserve

length and angles. Therefore, **a** and **b** as defined in (3.20) are orthonormal and have the form (3.17).

The complex vectors (3.20) at the face of the KTP crystal are found for the case where the KTP is separated from the cavity mirror by another birefringent element. For the most general cavity, where the KTP may be preceded by more intracavity elements, the eigenvectors at the KTP are found by multiplying **a** and **b** (3.20) by more diagonal matrices $C(\xi_j)$ and rotation matrices $R(\varphi_j)$; the complex eigenvectors always have the form of (3.17). However, the specific value of g computed from these eigenvectors depends on the particular cavity configuration. For example, in the two-element case above (3.20), we find

$$g = 4 \, |a_1|^2 \, |a_2|^2 = c^2 s^2 + u_1^2 u_2^2 - c^2 s^2 u_1^2 u_2^2 \, 4\cos^2\xi \qquad 3.22$$
$$+ \, cs u_1 u_2 \, 2 \cos\xi \, \cos 2\varphi \, (u_2^2 - u_1^2),$$

which is not identically equal to $4u_1^2 u_2^2$. ▢

With the expressions in (3.14) and (3.16), and the rate equations used by Baer (without doubling terms), we produce new rate equations which account for the polarization states of multiple longitudinal modes. We still treat the second harmonic production as losses in the intensities oscillating at the fundamental frequency. We then insert these losses into the intensity rate equations (2.24) as follows. The squared intensity terms in (3.14) and (3.16) represent frequency doubling losses in the respective intensities. Although these terms appear in both equations, they represent the same doubling process, so we only count each term once and place it as a loss term in the respective intensity

equation. We assume the I_1I_2 cross terms are shared equally between the contributing modes.

Suppose there are N longitudinal modes I_j in one polarization direction, and P modes $\tilde{I}_j$ in the other orthogonal direction. We then have a new set of rate equations, for the intensities and gains, which depend on the doubling coefficient g:

$$\tau_c \frac{dI_j}{dt} = (G_j - \alpha_j - g \epsilon I_j - 2 g \epsilon \sum_{\substack{k=1 \\ k \neq j}}^{N} I_k - 2 (1 - g) \epsilon \sum_{m=1}^{P} \tilde{I}_m) I_j \qquad \text{3.23.a}$$

$$\tau_c \frac{d\tilde{I}_j}{dt} = (\tilde{G}_j - \tilde{\alpha}_j - g \epsilon \tilde{I}_j - 2 g \epsilon \sum_{\substack{k=1 \\ k \neq j}}^{P} \tilde{I}_k - 2 (1 - g) \epsilon \sum_{m=1}^{N} I_m) \tilde{I}_j \qquad \text{3.23.b}$$

$$\tau_f \frac{dG_j}{dt} = G_j^o - G_j (1 + \beta_j I_j + \sum_{\substack{k=1 \\ k \neq j}}^{N} \beta_{jk} I_k + \sum_{m=1}^{P} \tilde{\beta}_{jm} \tilde{I}_m) \qquad \text{3.23.c}$$

$$\tau_f \frac{d\tilde{G}_j}{dt} = \tilde{G}_j^o \quad \tilde{G}_j (1 + \tilde{\beta}_j \tilde{I}_j + \sum_{\substack{k=1 \\ k \neq j}}^{P} \tilde{b}_{jk} \tilde{I}_k + \sum_{m=1}^{N} b_{jm} I_m) \qquad \text{3.23.d}$$

In (3.23.a and c), j = 1, 2, ..., N; in (3.23.b and d), j = 1, 2, ..., P. The new coefficients b_{jk} and $\tilde{b}_{jk}$ are simply additional cross saturation terms. The intensities I_j and $\tilde{I}_j$ are intensities at the fundamental frequency; the general equation for total green intensity is found be combining all the doubling loss terms:

$$I_d = g\epsilon \sum_{j=1}^{N} I_j^2 + g\epsilon \sum_{j=1}^{P} \tilde{I}_j^2$$

$$+ 4(1-g)\epsilon \sum_{j,k=1}^{N,P} I_j \tilde{I}_k \qquad\qquad 3.24$$

$$+ 2g\epsilon \sum_{\substack{j,k=1 \\ j \neq k}}^{N} I_j I_k + 2g\epsilon \sum_{\substack{j,k=1 \\ j \neq k}}^{P} \tilde{I}_j \tilde{I}_k$$

It is important to note the general nature of (3.23): the most restrictive assumption made was that the cavity only includes birefringent optical components. The coefficient g depends on the cavity configuration, but g always lies between 0 and 1, and the form of the differential equations is always the same.

We see that Baer's multimode equations (2.24) are a specific case of the above system. If we take all modes to oscillate in the same polarization direction, (3.23) immediately returns Baer's model, where a factor of $g\epsilon$ replaces ϵ.

The analysis carried out by Oka and Kubota is also a special case of the above equations. They calculated the doubled intensity I_d and derived the expression in (3.16) for the special cases of $g = 0$ (when the QWP angle is 0 or $\pi/2$) and $g = 1$ (when the QWP angle is $\pi/4$). Therefore (3.23) with $N = P = 1$ is the general two-mode system of equations for the laser studied by Oka and Kubota.

To summarize, Oka and Kubota initiated a powerful and straightforward approach to create a theoretical model for the doubling process, but they left several significant loose ends. First, they only studied the pairwise coupling of modes which oscillate in orthogonal polarization states. Secondly, they only carried out the analysis of a system with a QWP set at three specific angles. Finally, they stopped short of making a connection between their analysis and the rate equations in order to study the resulting dynamical system. Our

analysis ties up these loose ends, and produces a general model which applies to laser cavities with and without QWP's, or any other birefringent element. Moreover, all the pertinent information regarding the doubling losses has been reduced to the two parameters ϵ and g.

Analysis

Our new equations (3.23) and Baer's original equations (2.24) differ by terms of order ε, so it will not be surprising to see that the structures of most of the steady state points in our new model are very similar to those discussed in Chapter II. However, the steady state intensities we wish to analyze may now have intensities which are polarized in one of two orthogonal directions, so we must consider all combinations of polarization directions. The following subsections address the analysis of steady state solutions where only one intensity is non-zero, where two intensities are non-zero, and lastly when three modes are lasing. Two general cases are treated first: the case where an arbitrary number of modes all lase in the same polarization direction; the case with an equal number of modes in each of the two orthogonal directions.

To simplify the analysis we assume the mode-dependent parameters are symmetric, scale time as in the two-mode Baer equations (2.10), and take $\beta_j = \tilde{\beta} = 1$, so that (3.23) becomes:

$$\tau \frac{dI_j}{dt} = (G_j - \alpha - g\varepsilon I_j - 2g\varepsilon \sum_{\substack{k=1 \\ k \neq j}}^{N} I_k - 2(1-g)\varepsilon \sum_{m=1}^{P} \tilde{I}_m) I_j \qquad 3.25.a$$

$$\frac{dG_j}{dt} = \gamma - G_j (1 + I_j + \sum_{\substack{k=1 \\ k \neq j}}^{N} \beta I_k + \sum_{m=1}^{P} \beta \tilde{I}_m) \qquad 3.25.b$$

$$j = 1, 2, ..., N$$

$$\tau \frac{d\tilde{I}_j}{dt} = (\tilde{G}_j - \alpha - g\epsilon\tilde{I}_j - 2g\epsilon\sum_{\substack{k=1 \\ k \neq j}}^{P} \tilde{I}_k - 2(1-g)\epsilon\sum_{m=1}^{N} I_m)\tilde{I}_j \qquad \text{3.25.c}$$

$$\frac{d\tilde{G}_j}{dt} = \gamma - \tilde{G}_j(1 + \tilde{I}_j + \sum_{\substack{k=1 \\ k \neq j}}^{P} \beta\tilde{I}_k + \sum_{m=1}^{N} \beta I_m) \qquad \text{3.25.d}$$

$$j = 1, 2, ..., P$$

and we use the parameter values for our own experiment configuration (developed in Appendix B and listed in Table 4).

Arbitrary Number of Mc.les in the Same Polarization Direction. To address the case of N modes all in the same polarization direction, we set $P = 0$ in (3.25). As in our

Table 4. Parameter Values Used for Equations (3.25)

$$\tau = \tau_c / \tau_f = 2.0 \times 10^{-6}$$

$$\alpha = 0.01$$

p = pump strength, percent above threshold

$$\gamma = (1 + p) \times \alpha$$

$$\epsilon = 5.0 \times 10^{-5}$$

$$\beta = 0.6$$

previous three-mode analysis, we seek a steady state that has all intensities equal (I_S) and all gains equal (G_S). These steady state values must satisfy:

$$G_S - \alpha - g\,\varepsilon\,(2N-1)\,I_S = 0$$

$$\gamma - G_S\,(1 + I_S\,[\,1 + \beta\,(N-1\,)\,]\,) = 0.$$

3.26.a

The approximate solutions to (3.26.a) are

$$G_S = \alpha + O(\varepsilon)$$

3.26.b

$$I_S = \frac{(\gamma - \alpha)}{\alpha\,[1 + \beta(N-1)]} + O(\varepsilon) = \frac{p}{[1 + \beta(N-1)]} + O(\varepsilon).$$

Our analysis proves the following stability condition:

Proposition 3.3. If $P = 0$, $\gamma > \alpha$, and

$$g < \frac{\tau\,[1+(N-1)\beta]}{\varepsilon}\left[\frac{1+p}{p}\right],$$

then the steady state point described by (3.26) is an asymptotically stable steady state solution of equations (3.25).

Proof. We linearize (3.25) about the symmetric steady state, and carry out the same transformation technique used in the three-mode stability analysis in Chapter II. For this case, we let

$$A = \sum_{j=1}^{N} I_j \qquad\qquad B = \sum_{j=1}^{N} G_j$$

$$a_k = N\, I_k - A \qquad\qquad b_k = N\, G_k - B\,, \qquad k = 2,3,...,N\,,$$

3.27

where I_j and G_j are the variables which represent perturbations away from the steady state point. The transformed linearization decouples into pairs of equations whose eigenvalues can be calculated directly:

$$\frac{d}{dt}\begin{bmatrix} A \\ B \end{bmatrix} = \begin{bmatrix} g\,\epsilon\,\dfrac{I_s}{\tau}(1-2\,N) & \dfrac{I_s}{\tau} \\ -G_s\,(1-\beta+\beta\,N) & -(1+I_s\,[1+\beta\,(N-1)]) \end{bmatrix}\begin{bmatrix} A \\ B \end{bmatrix}$$

3.28.a

$$\frac{d}{dt}\begin{bmatrix} a_k \\ b_k \end{bmatrix} = \begin{bmatrix} g\,\epsilon\,\dfrac{I_s}{\tau} & \dfrac{I_s}{\tau} \\ -G_s\,(1-\beta) & -(1+I_s\,[1+\beta\,(N-1)]) \end{bmatrix}\begin{bmatrix} a_k \\ b_k \end{bmatrix}$$

3.28.b

The steady state values I_s and G_s are of order 1, so the matrices above are dominated by the positive off-diagonal I_s/τ term which is of order 10^6. The other off-diagonal terms are

always negative, so the eigenvalues of both matrices are complex. The real part of the eigenvalues for the matrix in (3.28.a) is:

$$Re(\lambda) = \frac{1}{2}\left[\frac{I_s}{\tau} g \, \varepsilon \, (1 - 2\,N) - (1 + I_s \, [1 + (N - 1)\beta])\right] . \qquad 3.29$$

Both terms in this expression are negative for all N, so $Re(\lambda)$ is always negative and the local (A,B) plane is part of the stable manifold for the steady state point.

The real part of the eigenvalues for the second matrix, in (3.28.b) is:

$$Re(\lambda) = \frac{1}{2}\left[\frac{I_s}{\tau} g \, \varepsilon - (1 + I_s \, [1 + (N - 1)\beta])\right] . \qquad 3.30$$

In this case, the stability of the equilibrium depends on the particular parameter values. The stability criterion reduces to

$$g < \frac{\tau \, [1+(N-1)\beta]}{\varepsilon} \left[\frac{1+p}{p}\right] + O(\varepsilon). \qquad 3.31$$

where the $O(\varepsilon)$ correction comes from applying the I_s approximation (3.26.b) to (3.30).

$\square$

As a check on the analysis to this point we see that, for $N = 3$ and $g = 1$, (3.31) returns the same stability criterion for ε as for the Baer model in Proposition 2.2.

The stability condition on g in (3.31) has the following implications for the experiment. First consider the effect of ε on stability. On one hand, one might hope to maximize ε in an experiment to get the most efficient production of green light; on the other

hand, (3.31) indicates that larger values of ε decrease the range of g where the steady state intensity is stable. This means that the quality of the KTP crystal, which determines the effective frequency doubling, strongly affects the stability of the intensity output. The other terms in (3.31) also suggest ways to increase the stable range of g. Lowering the pump strength, i.e. decreasing p, raises the stability threshold. An increase in the number of modes (for a fixed pump power) or an increase in the cross saturation β also have the effect of increasing g's stability range. The stability threshold can also be increased via changes in the time constant τ (which equals τ_c/τ_f). We can increase the cavity round trip time τ_c by lengthening the cavity, or decrease τ_f by using a gain medium that has a faster upper state decay rate than Nd:YAG. We note that all these means for increasing the stable range for g also tend to lower the total green output: lower pump strength, less efficient doubling, etc. Preliminary experiments to date confirm all the implications made by this analysis.

The upper bound on g in (3.31) implies that the intensity output is stable only when there is little green production, since for N modes in the same direction, the doubled intensity I_d is proportional to g (see (3.14), or (3.32) below). This important difference between the multimode operation in this case and Baer's model is illustrated by the terms which combine to give us the total doubled intensity I_d. The doubled intensity for Baer's model appears in (2.25); for our model, the relation is

$$I_d = g\varepsilon \sum_{j=1}^{N} I_j^2 + 2 g\varepsilon \sum_{\substack{j,k=1 \\ j \neq k}}^{N} I_j I_k \; . \qquad\qquad 3.32$$

In Baer's model, I_d is proportional to ε, so theoretically, as long as there is a doubling crystal, the laser will output some amount of green light. In our model however,
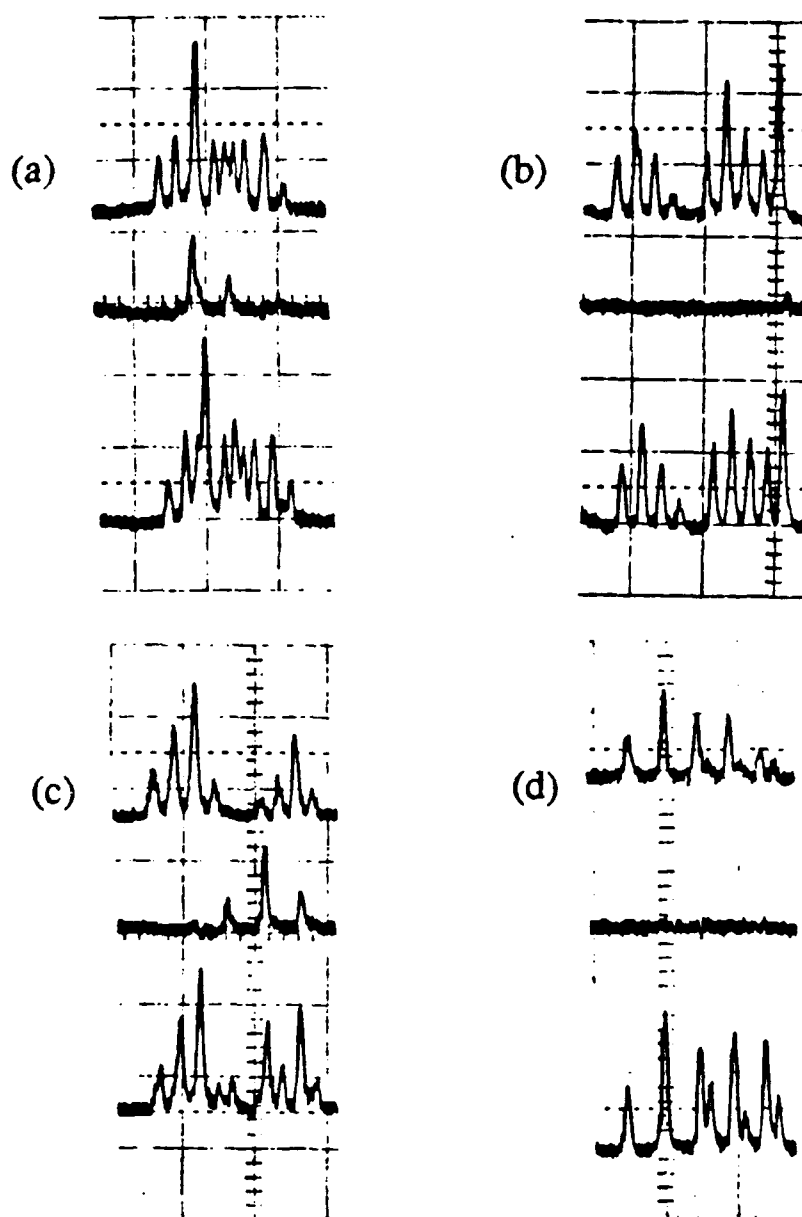
Fig. 3.4 Experimental Observations of Mode Structure for
Several KTP Crystal Rotation Angles. The angles are measured with
respect to an arbitrary zero. Longitudinal modes are identified by
spikes in the output from a confocal Fabry-Perot interferometer. In each
plot, the first line shows the modes in the polarization direction with the
strongest output; the second line shows the modes in the orthogonal
direction; the third line displays the total mode output. (a)-(c) Cases where
we observed stable fundamental and doubled output. (d) Case where the
fundamental output was stable and no green light was observed.

the doubled intensity is proportional to $g\varepsilon$. This means it should be possible to rotate the cavity elements, or control their birefringence, to make $g = 0$ and completely eliminate the doubled intensity, but still have intensity output at the fundamental frequency. This hypothesis has been confirmed in the laboratory (Fig. 3.4(d)), where we observed a case with five modes lasing at the fundamental frequency, all in the same polarization direction and the KTP crystal was rotated such that no green light was produced even with a pump strength of five times the fundamental intensity threshold. With the KTP crystal in this position, the intensity output was stable. For other angular settings of the KTP crystal, at a comparable pump level, green light was seen during stable steady state operation. We note that the number of modes in each polarization direction changes with rotation of the KTP crystal; the explicit stability condition (3.31) only holds for cases where all active modes oscillate in the same polarization direction.

Equal Number of Modes in Each Polarization Direction. The next case of interest considers (3.25) with the same number of modes N in each polarization direction (P = N). The steady state point where all intensities are equal and all gains are equal is nearly identical to the previous case:

$$G_s = \alpha + O(\varepsilon) \qquad\qquad 3.33$$

$$I_s = \frac{(\gamma - \alpha)}{\alpha\,[1 + \beta(2N - 1)]} + O(\varepsilon) = \frac{p}{[1 + \beta(2N - 1)]} + O(\varepsilon).$$

The linearized analysis of this steady state point is carried out much like before, but this time, the appropriate decoupling transformation is:

$$A = \sum_{j=1}^{N} I_j + \sum_{j=1}^{N} \tilde{I}_j \qquad\qquad B = \sum_{j=1}^{N} G_j + \sum_{j=1}^{N} \tilde{G}_j$$

$$a_k = N(I_k + \tilde{I}_k) - A \qquad\qquad b_k = N(G_k + \tilde{G}_k) - B, \qquad\qquad 3.34$$

$$C = \sum_{j=1}^{N} I_j - \sum_{j=1}^{N} \tilde{I}_j \qquad\qquad D = \sum_{j=1}^{N} G_j - \sum_{j=1}^{N} \tilde{G}_j$$

$$c_k = N(I_k - \tilde{I}_k) - C \qquad\qquad d_k = N(G_k - \tilde{G}_k) - D$$

$$k = 2,3,...,N.$$

Using this transformation we show:

Proposition 3.4. If $P = N$, $\gamma > \alpha$, $g \neq 0$, and

$$g > \left[\frac{2N}{4N-1}\right] - \frac{1}{4N-1} \frac{\tau[1+(2N-1)\beta]}{\varepsilon}\left[\frac{1+p}{p}\right] \qquad \text{(for all N>0)} \qquad 3.35.a$$

and

$$g < \frac{\tau[1+(2N-1)\beta]}{\varepsilon}\left[\frac{1+p}{p}\right] , \qquad \text{(for N>1)} \qquad 3.35.b$$

then the steady state point defined by (3.33) is an asymptotically stable solution of (3.25).
In the case of $g = 0$, the stability condition is

$$\varepsilon < \frac{\tau}{2N} \frac{(1+p)}{p} [1 + \beta(2N - 1)] . \qquad\qquad 3.35.c$$

Proof. The time derivatives of the transformed variables in (3.34) form a system of equations which decomposes into coupled pairs of differential equations. The eigenvalues of the resulting 2-by-2 matrices yield the stability conditions (3.35) as follows. (Much of the derivation is identical to that of the previous proposition, except a factor of 2N replaces the factor of N.)

The eigenvalues associated with the differential equations for A and B are complex with negative real parts, indicating asymptotic stability in the (A,B) plane; the calculation is the same as in Proposition 3.2. Similarly, the matrices for the a_j and b_j equations all yield eigenvalues whose real parts dictate the stability condition (3.35.b) which closely resembles the condition of Proposition 3.2. This stability condition accounts for the pairwise interaction of modes which oscillate in the same polarization direction. We note that, when N=1, there are no a_j or b_j transformations and no pairs of modes in parallel polarization states which can couple, so (3.35.b) need not be satisfied for the steady state to be stable.

The eigenvalues associated with c_j and d_j generate the same stability condition (3.35.b) as the eigenvalues for a_j and b_j. The new stability constraint (3.35.a) appears in the equations for C and D. The coefficient matrix of the differential equations for C and D is:

$$\left[\begin{array}{cc} I_s\epsilon(2N+[1-4N]g)/\tau & I_s/\tau \\ - G_s(1+\beta) & - f \end{array} \right] , \qquad 3.36$$

where

$$f = 1 + I_s [1+(2N-1)\beta].$$

The matrix (3.36) has complex eigenvalues with real part equal to the trace of (3.36). To guarantee stability of the steady state point, the real part must be negative, which requires (3.35.a) to be satisfied for all N>0. If we let g=0 in (3.36), we get the constraint in (3.35.c) which is more stringent than (3.35.b). As before, the inequalities in (3.35) are accurate to $O(\varepsilon)$ due to our approximations for I_s. □

Armed with these two general results, we now examine several specific stability conditions when the laser operates in one, two, or three modes, for different combinations of polarization directions.

Single-Mode Operation. When the laser has only one longitudinal mode, there is no mechanism for sum-frequency generation. It also means that N = 1 and P = 0 in (3.25) and the single-mode equations in our new model are identical to the single-mode Baer model. The analysis for these equations shows the non-trivial steady state to be globally attractive when $\gamma > \alpha$; this case is treated in depth in Chapter II.

Two-Mode Operation. There are two orthogonal candidate directions for each of the two active modes, so there are two different cases to consider. The first is the case where both modes are oriented in the same polarization direction. The second case has one mode in each of the two polarization directions. Both cases are particular examples of the general analyses performed above.

For two modes in the same polarization direction, we simply set N = 2 in the result of Proposition 3.3 to get:

$$g < \frac{\tau [1+\beta]}{\varepsilon} \left[\frac{1+p}{p}\right] . \qquad 3.37$$

The stability constraint for two modes polarized in orthogonal directions comes from setting N = 1 in (3.35.a):

$$g > \frac{2}{3} - \frac{1}{3} \frac{\tau[1+\beta]}{\varepsilon}\left[\frac{1+p}{p}\right] . \qquad 3.38$$

The important difference in (3.37) and (3.38) lies in the relative amount of doubled intensity I_d produced in each case during stable steady state operation of the laser. Recall that, for the case of two modes in the same polarization direction, I_d is proportional to g. Thus, the requirem⌐ ⌐.37) means that stable laser operation is achieved only with relatively weak ⌐⌐een output. On the other hand, (3.38) requires g to exceed a particular threshold. In this case (3.16) indicates that significant stable green output may be obtained, primarily through second harmonic generation. Therefore, to produce stronger doubled intensity output, we would prefer the laser to operate in single mode, or in two orthogonally polarized modes, rather than with two (or more) modes lasing in the same polarization direction. Experiments which take advantage of such a mode structure are discussed in the applications section of this chapter.

The case with two modes in the same polarization direction is essentially identical to Baer's two-mode model (Baer, 1986); our new equations simply have a factor of $g\varepsilon$ where Baer had only ε. The structure of the phase space is therefore identical to the two-mode phase space studied in Chapter II.

For the case of two orthogonally polarized modes, however, there are other steady state points which have a different local structure than we have discussed to this point. There are two steady states which have one intensity (say I_{1s}) non-zero and the other intensity (I_{2s}) zero. The approximate steady state values in this case are:

$$I_{1s} = \frac{\gamma - \alpha}{\alpha} + O(\epsilon) \qquad G_{1s} = \alpha + O(\epsilon)$$

$$I_{2s} = 0 \qquad\qquad G_{2s} = \frac{\gamma}{1 + \beta I_s} + O(\epsilon) \ .$$

3.39

In all the systems of equations we have studied until now, the stable manifold of (3.39) includes the (I_1, G_1) plane and a 1-dimensional unstable manifold points strongly in the direction of I_2. However, when we linearize (3.25) about this point (with N=P=1), we find a condition for the asymptotic stability of this point:

$$G_{2s} < \alpha + 2(1\text{-}g) \epsilon \, I_{1s}$$

3.40.a

which (within $O(\epsilon)$) requires:

$$\alpha(2\text{-}\beta) < 2\epsilon(1\text{-}g) \ .$$

3.40.b

This condition may be difficult to realize experimentally, since α is typically $O(10^{-3})$ and ϵ is $O(10^{-5})$. It is a theoretically feasible constraint, however, particularly for β near 2; under this condition, two equilibria described by (3.39) can coexist in phase space with the stable steady state in (3.33) (or the periodic orbit which bifurcates out of that point). This more complicated structure of the phase space persists for the cases of larger number of modes which do not all align in the same polarization direction.

Three-Mode Operation. While this case has an additional mode and two more equations than the previous section, there are only two basic combinations of modes to

consider. The first case has all three modes lasing in the same polarization direction; the second has two modes in one direction and the third mode in the orthogonal polarization direction. The linearized analysis we carry out for the three-mode equations is not very different from what we have done so far; the numerical studies of the three-mode dynamics in a later section illustrate more substantial differences.

We begin with the simpler case of all three modes in the same polarization state. When we set $N = 3$ and $P = 0$ in (3.25), we find that the equations essentially become Baer's model (2.24) with the important difference that the $g\epsilon$-term now appears where there used to be only an ϵ. The stability criterion for the interior steady state point (with all modes non-zero and equal) is found by setting $N = 3$ in (3.31):

$$ g < \frac{\tau\,[1+2\beta]}{\epsilon} \left[\frac{1+p}{p}\right] . \qquad 3.41 $$

This is the same condition we would get by applying the stability analysis of Chapter II, and taking the stability criterion (2.34) to be a constraint on $g\epsilon$ instead of ϵ. The applications section of this chapter will examine specific functional forms of g to look for parameter ranges where g is small.

Now we turn to the more involved case of the three-mode laser where two modes oscillate in one polarization direction (call this the y direction) while the third mode oscillates in the orthogonal (x) direction. This case does not fit the template of any of the general cases we have considered thus far, so we must restart the analysis.

As in the discussion of three-mode steady state points in Chapter II, (3.25) has three steady states where one intensity is non-zero and the other two intensities are zero.

When the positive intensity (I_s) is the third mode in the x direction, and the steady state values for I_1 and I_2 (in the y direction) are zero, the steady state gain values are:

$$G_{1s} = G_{2s} = \frac{\gamma}{1+\beta I_s} + O(\epsilon) \qquad G_{3s} = \alpha + O(\epsilon) \qquad\qquad 3.42$$

and (3.25) has the following linearized equation for I_1 and I_2:

$$\tau \frac{dI_j}{dt} = I_j \left(G_{js} - \alpha - 2(1\text{-}g)\,\epsilon\, I_s \right), \quad j = 1, 2. \qquad\qquad 3.43$$

The steady state point in question has a stable manifold which includes the (I_3,G_3) plane, corresponding to its single-mode behavior, as long as $\gamma > \alpha$. There are also two stable directions along the G_1 and G_2 axes. In the three-mode Baer model we saw that the unstable manifold for such a point is two-dimensional, locally pointing in the directions of the opposing two intensities. For our new model, the right side of (3.43) can be negative, in which case this steady state would stable; the condition under which this occurs is precisely the inequality (3.40.b) shown above.

A stability condition similar to (3.43) results when we consider the steady state point that has I_1 or I_2 non-zero while the other two intensities are zero. The important observation here is that when the new model (3.25) has modes lasing in both polarization directions, there are parameter ranges for which there are basins of attraction for these steady state points. The three-mode Baer model has two periodic waltzes which are simple reflections of each other, but the only stable solutions have all modes on. The new model, however, has coexisting stable attractors with different structures (for some parameter

values), and the selection of initial conditions dictates onto which attractor a numerical trajectory falls.

There are, of course, three more steady state points with two intensities on while the third is off. We first illustrate this case with the example with $I_{1s} = I_{2s} = I_s > 0$ and $I_{3s} = 0$. The linearization of (3.25) about this point produces a differential equation for I_3 nearly identical to (3.43):

$$\tau \frac{dI_3}{dt} = I_3 (G_{3s} - \alpha - 4(1\text{-}g) \, \epsilon \, I_s) . \qquad 3.44$$

The associated condition for stability reduces to:

$$\alpha < 2\epsilon(1\text{-}g) . \qquad 3.45$$

Thus, there are parameter ranges where two modes can lase with the third mode off, and small perturbations at the frequency of the third intensity (physically due to spontaneous emission noise) will not be amplified to allow the third mode to lase.

A similar analysis holds true if we examine the steady state point where I_{1s} and I_{3s} are positive while $I_{2s} = 0$. In this case the I_2 equation governs the stability of the point, and the stability constraint requires $\epsilon > \alpha$. This condition is not likely to be realized physically, so the linearized analysis indicates that a small perturbation in I_2 will be amplified such that the mode will turn on.

We conclude the study of this mode arrangement (two modes orthogonally polarized with respect to a third mode) with the stability analysis of the steady state where all intensities are positive, and all gains are positive. Due to the alignment of the modes in different polarization directions, the steady state equations for (3.25) do not allow all three

intensities to be equal, in general. Instead, we have a common steady state value (I_s) for modes 1 and 2, with a slightly different value (I_{3s}) for mode 3. The steady state quantities must satisfy:

$$G_{1s} = G_{2s} = G_s = \alpha + 3g\epsilon I_s + 2(1\text{-}g)I_{3s}$$

$$\gamma - G_s(1 + [1\text{+}\beta]I_s + \beta I_{3s}) = 0$$

<div align="right">3.46</div>

$$G_{3s} = \alpha + g\epsilon I_{3s} + 4(1\text{-}g)\epsilon I_s$$

$$\gamma - G_{3s}(1 + I_{3s} + 2\beta I_s) = 0 .$$

We find numerically (with parameter values in Table 4) that these four equations have positive solutions I_s and I_{3s} only for $0.99 < g < 1$; these solutions have extremely small intensities compared to the steady state intensities for the single mode case with comparable pump powers. Thus, we expect to not see steady state behavior for modes in these polarization states.

To determine the stability of the steady state point with non-negative intensities, we employ the following transformation:

$$A = I_1 + I_2 \qquad B = G_1 + G_2 \qquad C = I_3$$

<div align="right">3.47</div>

$$a = I_1 - I_2 \qquad b = G_1 - G_2 \qquad D = G_3 .$$
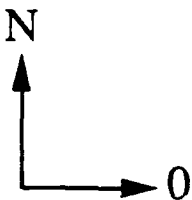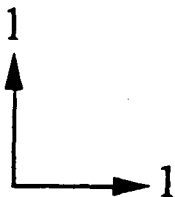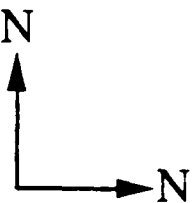
The eigenvalues for the 4-by-4 matrix associated with the A, B, C and D differential equations were found numerically to have negative real parts (using the EISPACK eigenvalue routine RG). The eigenvalues associated with a and b analytically yield the condition

$$g \frac{\epsilon}{\tau} I_s \; < \; 1 \; + \; [1+\beta] \, I_s \; + \; \beta \, I_{3s} \qquad\qquad 3.48$$

for which the steady state point is stable.

The main stability results of this section are summarized below in Table 5. When all modes oscillate in the same polarization direction (a), g must be small to assure stable intensity output; the green output for stable operation must also be relatively weak. When two active modes oscillate in orthogonal polarization directions (b), the stability criterion requires g to be relatively large, and the model predicts substantial stable green production. For N modes in each polarization direction (c), the stability of the intensity output depends on the overlap of two inequalities. The next section applies the general derivation of this chapter to specific laser cavities and addresses the calculation of g for different cavity configurations.

Table 5.   Summary of Stability Results for Steady States of (3.25).

number of modes in each polarization direction	stability condition

(a)

N

↑

└──→ 0

$$g < \frac{\tau\,[1 + (N - 1)\,\beta]}{\varepsilon}\left[\frac{1 + p}{p}\right]$$

(b)

1

↑

└──→ 1

$$g > \frac{2}{3} - \frac{1}{3}\,\frac{\tau\,[1 + \beta]}{\varepsilon}\left[\frac{1 + p}{p}\right]$$

(c)

N

↑

└──→ N

$$g > \left[\frac{2N}{4N - 1}\right] - \frac{1}{4N - 1}\,\frac{\tau\,[1 + (2N - 1)\,\beta]}{\varepsilon}\left[\frac{1 + p}{p}\right]$$

and

$$g < \frac{\tau\,[1 + (2N - 1)\,\beta]}{\varepsilon}\left[\frac{1 + p}{p}\right]$$

Applications

The round trip matrix calculated by Oka and Kubota (Oka and Kubota, 1988) includes two birefringent elements, the KTP crystal and the quarter wave plate, and the relative angle of their respective fast axes. We decided to investigate the effect of adding the birefringence of the YAG crystal to our analysis, after G. Kintz of Spectra-Physics suggested that we might increase our total green output by stressing the YAG crystal to induce birefringence. The possibility of any birefringence in the YAG has not been considered in previous analyses of intracavity doubled YAG lasers (Baer, 1986; Oka and Kubota, 1988; Wu and Mandel, 1985 and 1987; James, et al., 1990a and 1990b). Thus, the first application of our generalized round trip matrix will be a cavity which contains only a birefringent YAG rod and KTP doubling crystal, with no QWP. The second application will be our version of the round trip matrix for the cavity with a QWP, which includes the YAG birefringence in the analysis. Finally we apply our round trip matrix analysis to the "twisted mode" cavity which includes two QWP's in the intracavity doubled laser (Evtuhov and Siegman, 1965; Otsuka and Iwasaki, 1976; Fry and Henderson, 1986; Wallmeroth and Peuser, 1988).

Cavity Without Quarter Wave Plates

The round trip matrix M_1 for the cavity which includes only the YAG and KTP crystals depends on three parameters: the YAG phase delay ξ, the KTP phase delay δ, and the relative angle φ between the fast axes of the two crystals (Fig. 3.1). Recall from Chapter I that the difference in indices of refraction n_1 and n_2 is the birefringence of a material; we express this birefringence in terms of the relative phase delay induced between

the two coordinates of a propagating field. We assume that the ambient, unstressed, birefringence of the YAG crystal is small, such that n_1 - n_2 is of the order 10^{-6}. This produces a phase delay ξ of about 0.01π for a 5mm long crystal. The value of ξ can be increased significantly by applying stress to the YAG crystal. The KTP crystal, on the other hand, is inherently birefringent and is cut so its birefringence enhances the frequency doubling process (Fan, et al., 1987; Ito, et al., 1975; Shen, 1984; Yao and Fahlen, 1984). The phase delay δ induced by the KTP crystal may assume values from 0 to 2π, and may be adjusted by controlling the temperature of the KTP, a procedure recommended to us by T. Baer. The relative angle φ can be changed by the simple rotation of either the YAG or the KTP crystal.

We now evaluate the round trip matrix M_1 by the multiplication detailed in (3.1) through (3.4). The result is:

$$M_1 = \begin{bmatrix} a & iy \\ iy & \bar{a} \end{bmatrix}, \qquad\qquad 3.49$$

$$a = e^{i\xi} (\cos^2\varphi \; e^{i\delta} + \sin^2\varphi \; e^{-i\delta})$$

$$y = \sin 2\varphi \sin \delta \; .$$

The eigenvectors w_1 and w_2 for M_1 have already been presented in their general form in (3.8); we recall them here, for reference:

$$w_{1,2} = \begin{bmatrix} 2 \, \text{Im}(a) \pm \sqrt{4 - (a + \bar{a})^2} \\ 2 \, y \end{bmatrix}_. \qquad\qquad 3.50$$

The functional dependence of the doubling parameter g on the three parameters ξ, δ, and φ can now be calculated from the normalized eigenvector components: $g = 4(w_1(1)w_1(2))^2/|w_1|^2$, as derived in (3.12). Our aim is to evaluate g for different parameter values, and search for parameters which yield a value of g that satisfies the stability criteria (3.31), (3.35), or (3.38) found in the previous section.

The doubling parameter g is plotted in Figs. 3.5 and 3.6 as a function of the three angular parameters ξ, δ, and φ. All three variables upon which M_1 depends theoretically take on any value from 0 to 2π. There are symmetries, however, which reduce the range of values we need to consider for each variable. For instance, the fast axis of either crystal is not an axis which radiates out from the center of the crystal, but represents a direction that traverses the entire cross section of the crystal. Thus the angular position $\varphi = 0$ is identical to the position $\varphi = \pi$, and we only need to consider values of φ between 0 and π. Moreover, g is π-periodic in δ, and symmetric about $\pi/2$ in φ and ξ. The shaded regions in Fig. 3.5 indicate the parameter values where g satisfies (3.31) for N=3, p=5.0 and other parameters as listed in Table 4. In Fig. 3.6, the shaded regions indicate parameters for which g satisfies (3.38) (one mode in each polarization direction) for any pump strength, i.e. the plane is shaded for $g > 2/3$.

The first plot in Fig. 3.5 is for a YAG crystal with extremely small phase delay $\xi = 0.01\pi$. This phase delay corresponds to a birefringence of about 1 part in 10^6, which is approximately what we measured for the (unstressed) YAG crystal in our experiment. The figure shows that g is very small for nearly all angles φ and KTP phase delays δ. The theory indicates that this laser configuration generally produces stable output when all the modes oscillate in the same polarization direction. Otherwise, we expect to observe periodic or chaotic intensity output. For increasing values of YAG phase delay
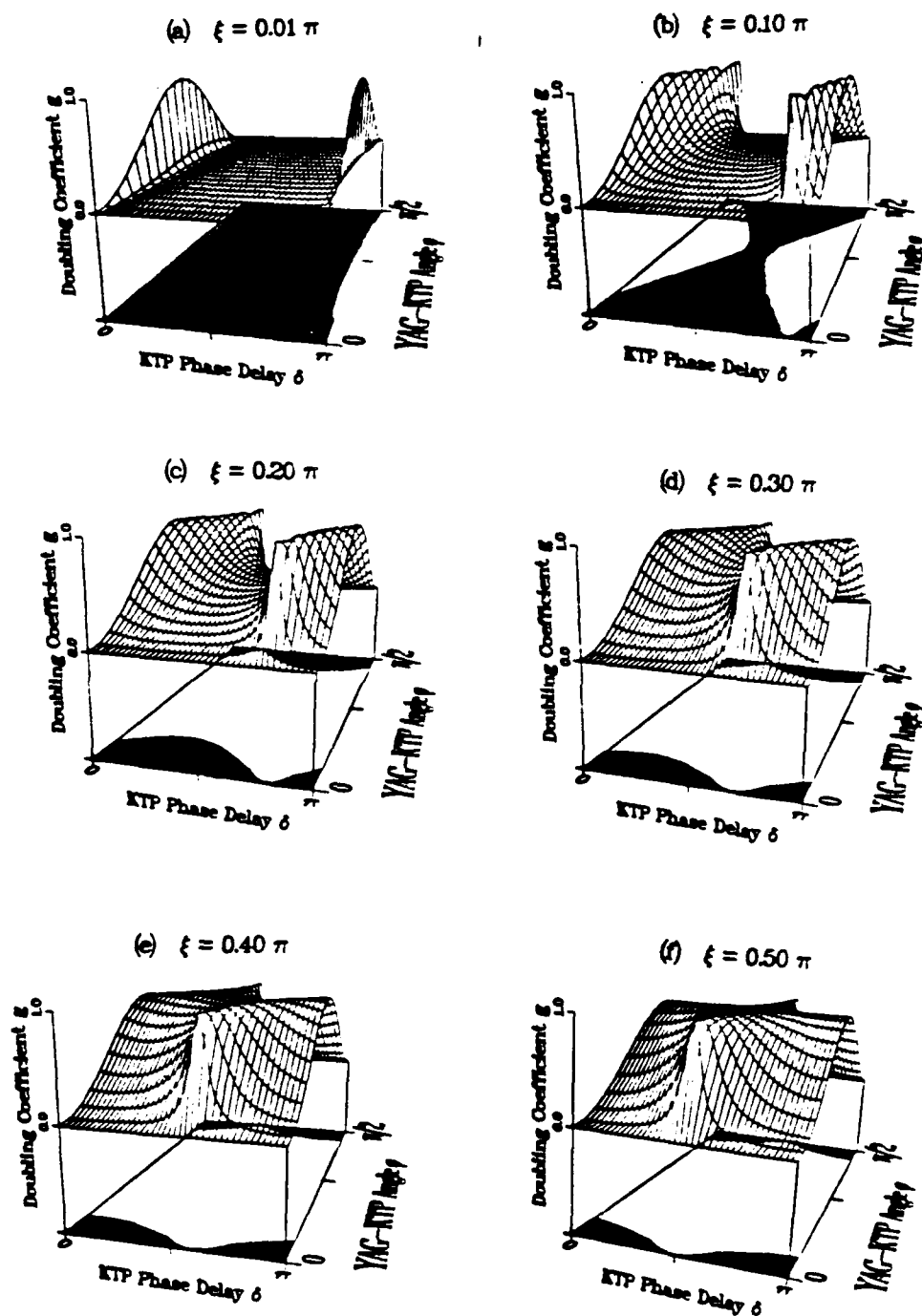
Fig. 3.5 Stability Regimes for g with Three Modes in the Same Polarization State.
The shaded regions correspond to parameters where g satisfies (3.31)
for N=3 and p=5.0.

(a) $\xi = 0.01\,\pi$

(b) $\xi = 0.10\,\pi$

(c) $\xi = 0.20\,\pi$

(d) $\xi = 0.30\,\pi$

(e) $\xi = 0.40\,\pi$

(f) $\xi = 0.50\,\pi$
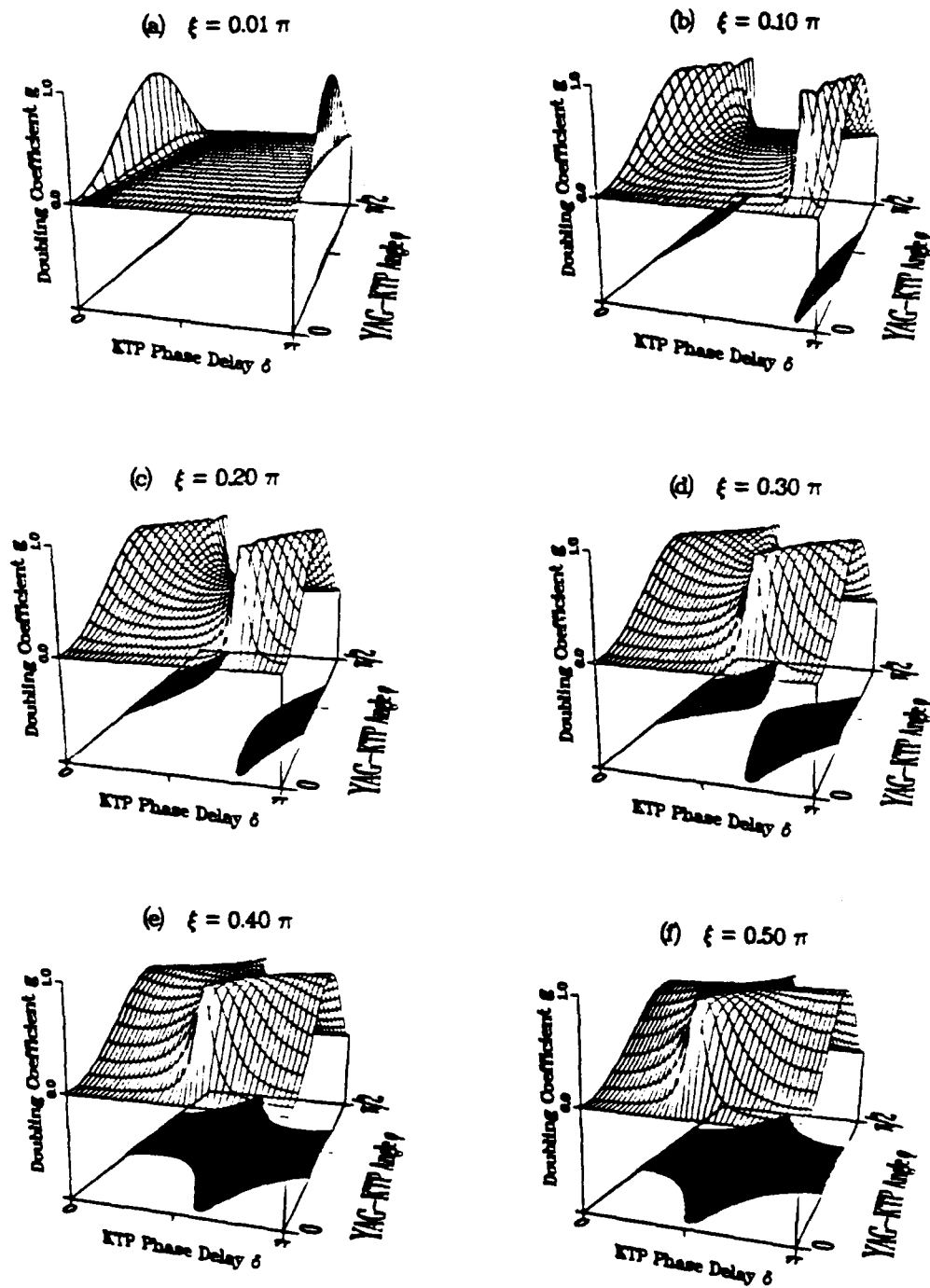
Fig. 3.6 Stability Regimes for g with Two Modes in Orthogonal Polarization States.
The shaded regions correspond to parameters where g > 2/3, satisfying (3.38).

(Figs. 3.5(b) through (f)) the size of the stable region shrinks, but there are always some finite areas of parameter space where stable operation of the laser can be obtained.

In Fig. 3.6, the stable regions are larger for higher values of YAG birefringence. That means that, if the laser operates with one mode in each orthogonal polarization direction, it is to our advantage to induce birefringence in the YAG to generate more green light. The "twisted mode" technique causes the laser to behave exactly this way; we discuss this method below in the third application section.

In the laboratory, it is not feasible to constantly measure all three of these parameters in real time, so we can not necessarily trace a specific line on a particular g-surface which corresponds to turning a single knob in the experiment. However, we do expect these surface plots to give a reasonable estimate of the relative sizes of stable and unstable portions of the parameter space, and to indicate conditions under which we might be confident to find always-stable or always-unstable steady state output. In fact, the plots in Fig. 3.5 were the first evidence we saw that the birefringence of the YAG, and the position of its fast and slow axis, had any influence on the dynamics of intracavity doubling. They led directly to our first success with stabilizing the intensity output in the laboratory by rotating the KTP crystal in the cavity. Figure 3.7 shows a sequence of experimental total intensity traces as a function of the angle between the YAG and KTP crystal fast axes. The reported angles are given relative to an arbitrarily selected zero. The sequence shows the character of the intensity output progressing from stable steady state, to periodicity, to chaotic behavior, and returning again to stable periodic output. The theoretical model predicts exactly this kind of transition.
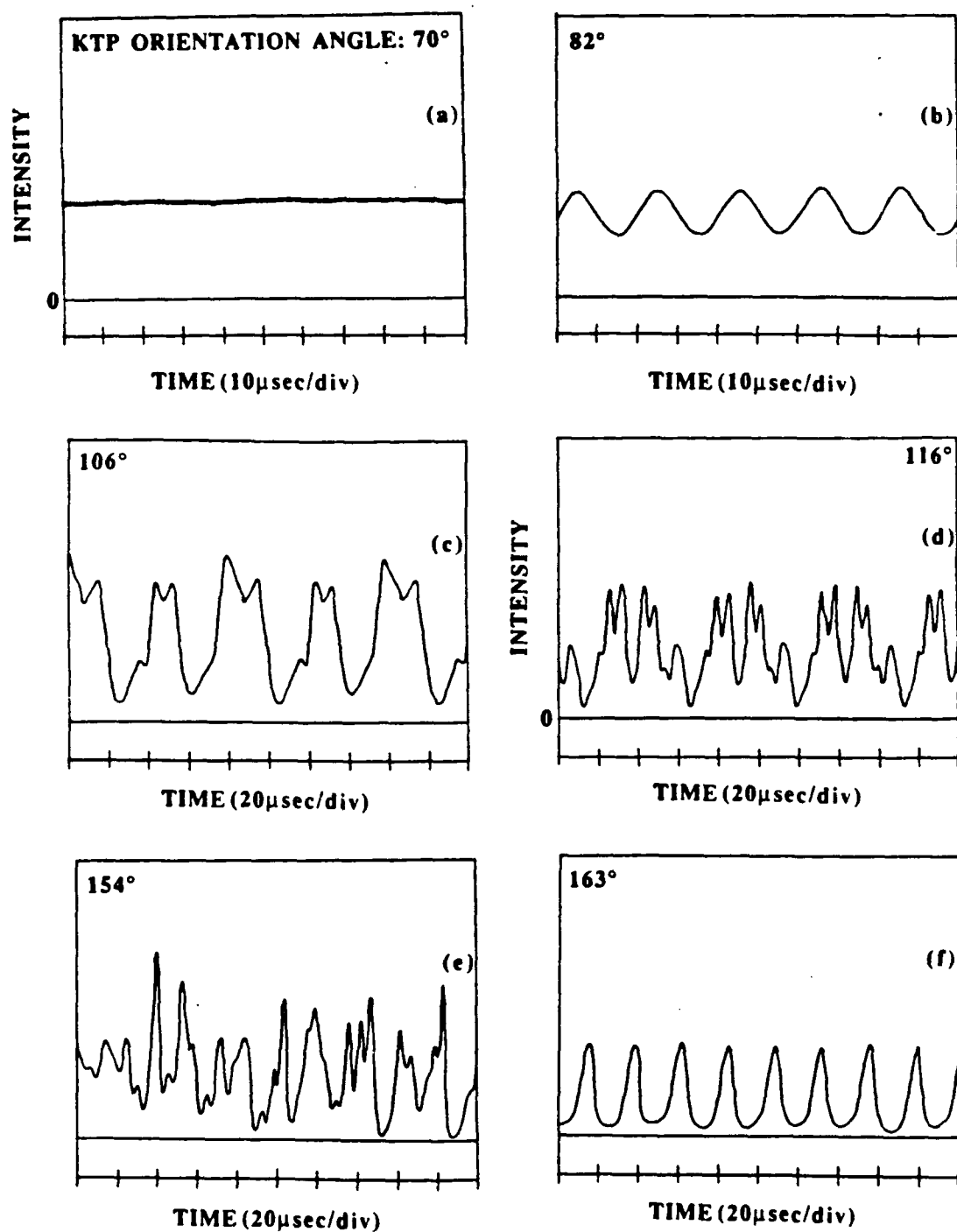
Fig. 3.7 Experimental Intensity Output as a Function of KTP Orientation Angle. The reported angle is the KTP crystal position relative to an arbitrary zero. All other parameters are constant for the six plots.

Cavity With Quarter Wave Plate

We now return to the cavity configuration studied in (Oka and Kubota, 1988) but we include the birefringent YAG crystal in the analysis. This case, then, includes three birefringent optical elements and two relative rotatory positions (Fig. 3.8). The phase delay induced by the quarter wave plate is fixed at $\pi/2$, so there are four free parameters: the YAG induced phase delay ξ, the KTP phase delay δ, the relative angle φ of the YAG and KTP fast axes, and the angle ψ between the fast axes of the KTP crystal and the QWP.

The round trip matrix M_2 for this configuration again produces a matrix of the form of (3.49), but this time,
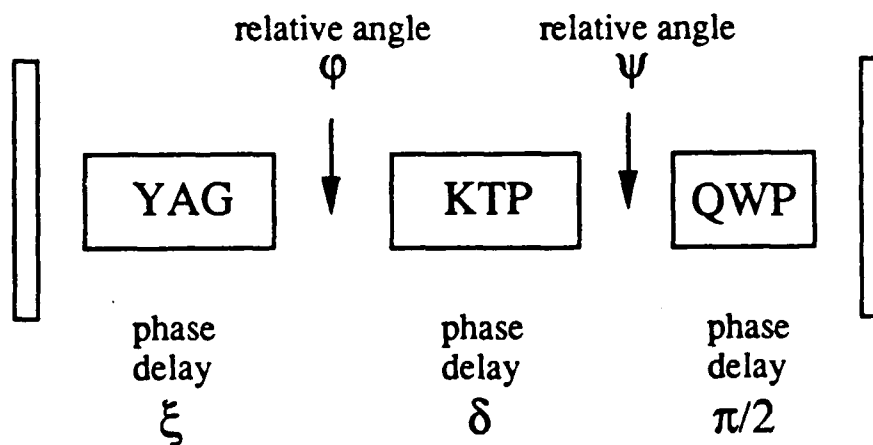
Fig. 3.8   Schematic of the Cavity with Quarter Wave Plate. This configuration has four free parameters: ξ, δ, φ, and ψ.

$$a = e^{i(\xi+\pi/2)} [\cos 2\varphi \, (e^{i\delta} - 2\sin^2\varphi \cos \delta) - \sin 2\varphi \sin 2\psi]$$

3.51

$$y = \sin 2\varphi \cos 2\psi \cos \delta + \cos 2\varphi \sin 2\psi .$$

We are especially interested in the values of g for $\psi = 0$ (or, equivalently $\pi/2$) and $\psi = \pi/4$ because these are the angles studied by Oka and Kubota. They found in their experiment that, for $\psi = \pi/4$, the laser operates in a stable steady state, with no artificial restrictions on the number of modes. When the QWP is rotated such that $\psi = 0$ or π, they observe chaotic intensity output at both the fundamental and doubled frequencies. They report no information about the ranges of angles over which they observe either stable or chaotic output.

Several sample plots of the g-surfaces calculated from the eigenvectors of M_2 appear in Fig. 3.9, where we take $\psi = 0$. The plots are shaded for parameters where g satisfies (3.31), i.e. for three modes with parallel polarizations. We see portions of parameter space in Fig. 3.9 where the steady state intensity is unstable, consistent with Oka's findings. However there are also values of the YAG phase delay ξ for which the model predicts the laser will operate in a stable steady state, almost the entire parameter plane in Fig. 3.9(a), for example. It is interesting to notice how Fig. 3.9 illustrates that $\psi=0$ is equivalent to having no QWP but a KTP crystal with phase delay $(\delta+\pi/2)$, see Fig. 3.5.

When we set $\psi = \pi/4$, where Oka reports stable output, we find that $g \equiv 1$. From Table 5 we see that $g \equiv 1$ implies stability only for the single mode laser, or the laser operating with two orthogonally polarized modes. We can thus infer from Oka's results that the cavity configuration with $\psi = \pi/4$ forces the laser to operate in one of these two

states. We can also return to Fig. 3.9(a), for instance, to see that the stability condition in Table 5(b) is not satisfied for almost the entire parameter plane; this is consistent with Oka's findings if their laser operated with two orthogonally polarized modes.

We emphasize that the functional form of g depends strongly on the YAG birefringence, even when the induced phase delay ξ is extremely small. In our own experiments, we have observed cavity configurations where the intensity output is unstable (periodic or chaotic) for all QWP angles except for a tiny range of 1 or 2 degrees; we have equally seen cases where the intensity output is stable for all QWP angles excepting a small range of 5 to 10 degrees. The four angular variables ξ, δ, φ and ψ appear to be sufficient to account for this wide variety of behavior in the experiment.
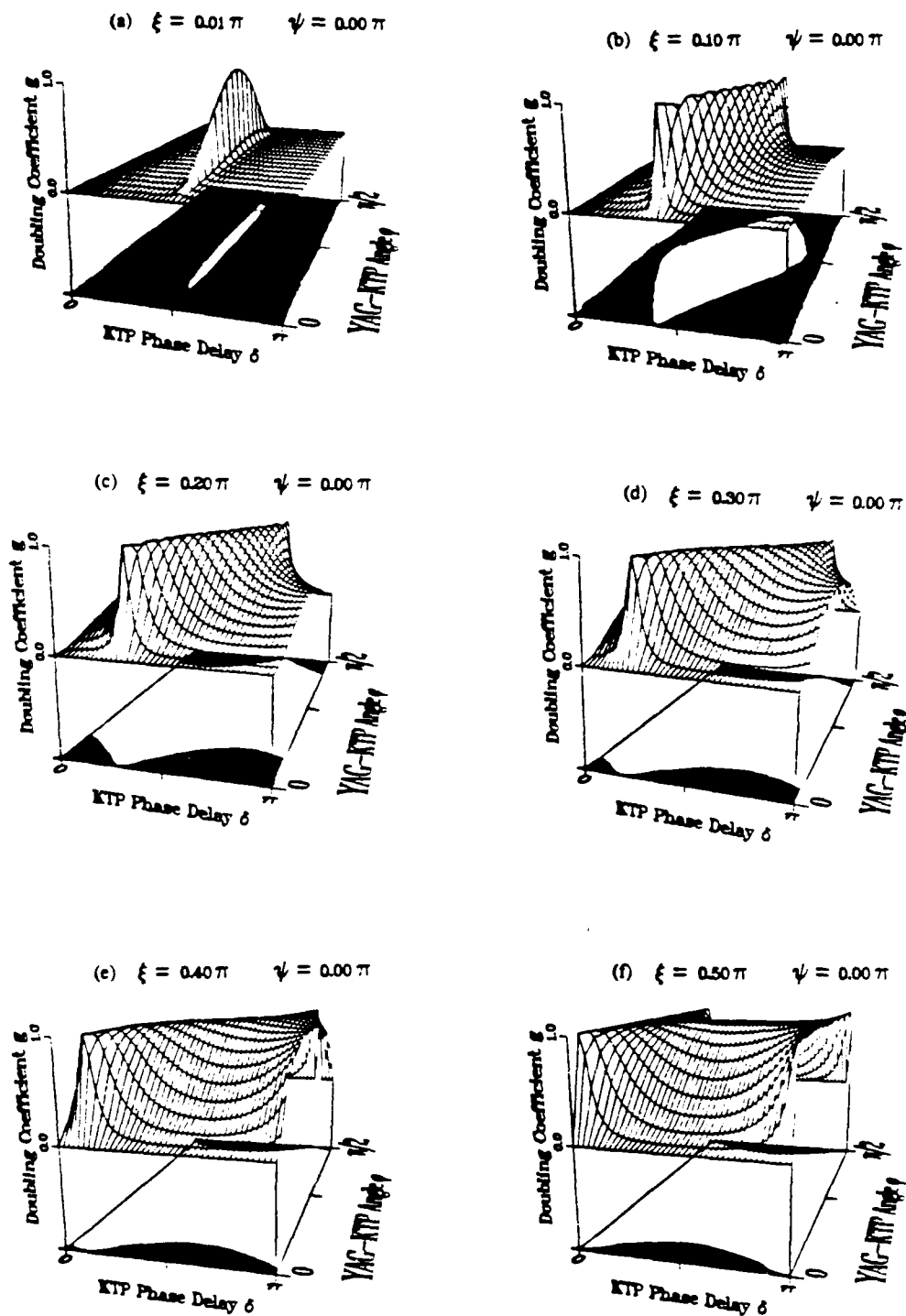
Fig. 3.9 Stability Regimes for g with Quarter Wave Plate Angle $\psi = 0$.
The shaded regions correspond to parameters where g satisfies (3.31)
for $N=3$ and $p=5.0$.

Twisted Mode Cavity With Two Quarter Wave Plates

The "twisted mode" cavity for an intracavity doubled laser includes two QWP's, one adjacent to each cavity mirror (Fig. 3.10). This configuration generates circularly polarized light which combines in the YAG crystal to form a beam that has constant amplitude along the length of the YAG (Evtuhov and Siegman, 1965; Otsuka and Iwasaki, 1976; Fry and Henderson, 1986; Wallmeroth and Peuser, 1988). A uniform depletion of available gain results, and forces the laser to operate with, at most, one longitudinal mode in each polarization direction. In our model, that means the stability criterion in (3.38) applies directly to this cavity.

The general round trip matrix M_3 for this cavity has five free parameters (Fig. 3.10): the YAG phase delay ξ, KTP phase delay δ, the angle ψ_1 between the first QWP and the YAG fast axes, the angle ψ_2 between the KTP crystal and the second QWP axes, and the angle φ between the YAG and the KTP crystal fast axes. We take only a special case of M_3 here to illustrate the application of our theory to this laser.
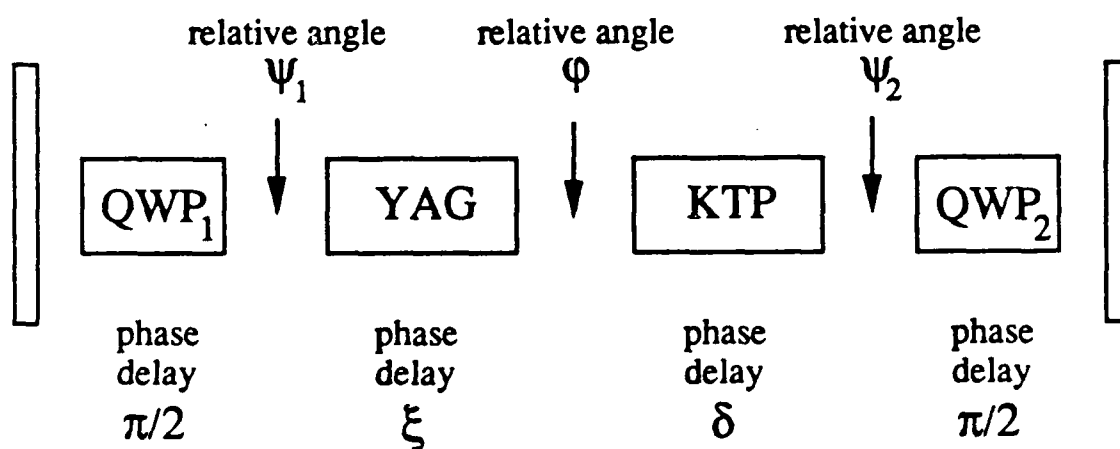
Fig. 3.10 Schematic for the Twisted Mode Laser Configuration.

Suppose the fast axes of the YAG and KTP crystal are parallel, the first QWP is rotated $\pi/4$ with respect to this common axis, and the second QWP is rotated - $\pi/4$. In this case we find that M_3 is the identity matrix, regardless of the values of δ and φ. All vectors are eigenvectors of the identity, which seems to imply that any field vector will replicate after a round trip through the cavity. However, there are other experimental factors which affect the longitudinal modes. First, the twisted mode configuration allows no more than two modes to lase, and they must oscillate in orthogonal polarization directions. Furthermore, the polarization alignment that produces green light most efficiently is when the E-fields are polarized at $\pi/4$ with respect to the KTP axes. The eigenvectors associated with these fields have components of equal magnitude, which implies that the doubling coefficient g for this configuration equals 1, by (3.22). This maximal value for g always satisfies the stability criterion (3.38), so the laser in this configuration always operates in a stable steady state. This interesting analytical result is consistent with the experimental results reported in the above references on twisted mode cavities.

Numerical Results

A new ingredient in our system of equations (3.23) is the identification of a polarization state with each longitudinal mode. The associated intensity variable I_j belongs to one of two groups of similarly polarized modes, and pairwise mode interactions depend on whether the participating modes oscillate in parallel or orthogonal directions. The new doubling terms have no effect on the single-mode dynamics of (3.23) since the changes involve couplings between pairs of modes. Numerical integrations of the two-mode case also produce no new qualitative behavior: the only limiting behaviors are stable steady states and periodic orbits.

Many interesting results are seen in numerical integrations of (3.23) with three modes. We now report the results of extensive integrations for the case where all three modes have the same polarization state, and for the case of two modes in one polarization direction with a third orthogonally polarized mode. In each case, we integrate (3.23) for enough values of the pump strength p and the doubling coefficient g to generate approximate bifurcation diagrams in the (p,g) plane. We find different trends, in the two cases, for the average green intensity in stable versus chaotic output. In the latter case, we also find parameters that produce numerical results which closely match particular experimental data.

Three Modes in the Same Polarization Direction

The numerical data discussed in this section appear at the end of the chapter in Fig. 3.17. The computer program POLYAG3 integrates (3.23) with three modes in the same polarization state; a program listing appears in Appendix F. A wide range of solutions are summarized in the approximate bifurcation diagram in Fig. 3.11. The curves in the bifurcation diagram roughly separate the regions in the (g,p) plane where we observe qualitatively similar solutions. We note that for all pump levels, stable intensity behavior was observed for small g, as predicted by (3.31). Moreover, for any fixed g, stronger pumping produces more unstable behavior, as we see in experiments.

To associate particular numerical data in Fig. 3.17 with the bifurcation diagram (Fig. 3.11) we find that periodic output is most easily identified in the intensity time traces, and confirmed by simple structure in the associated FFT (see, e.g. Fig. 3.17(a)). Quasi-periodic output can have erratic time histories, but appears quite structured in the numerical
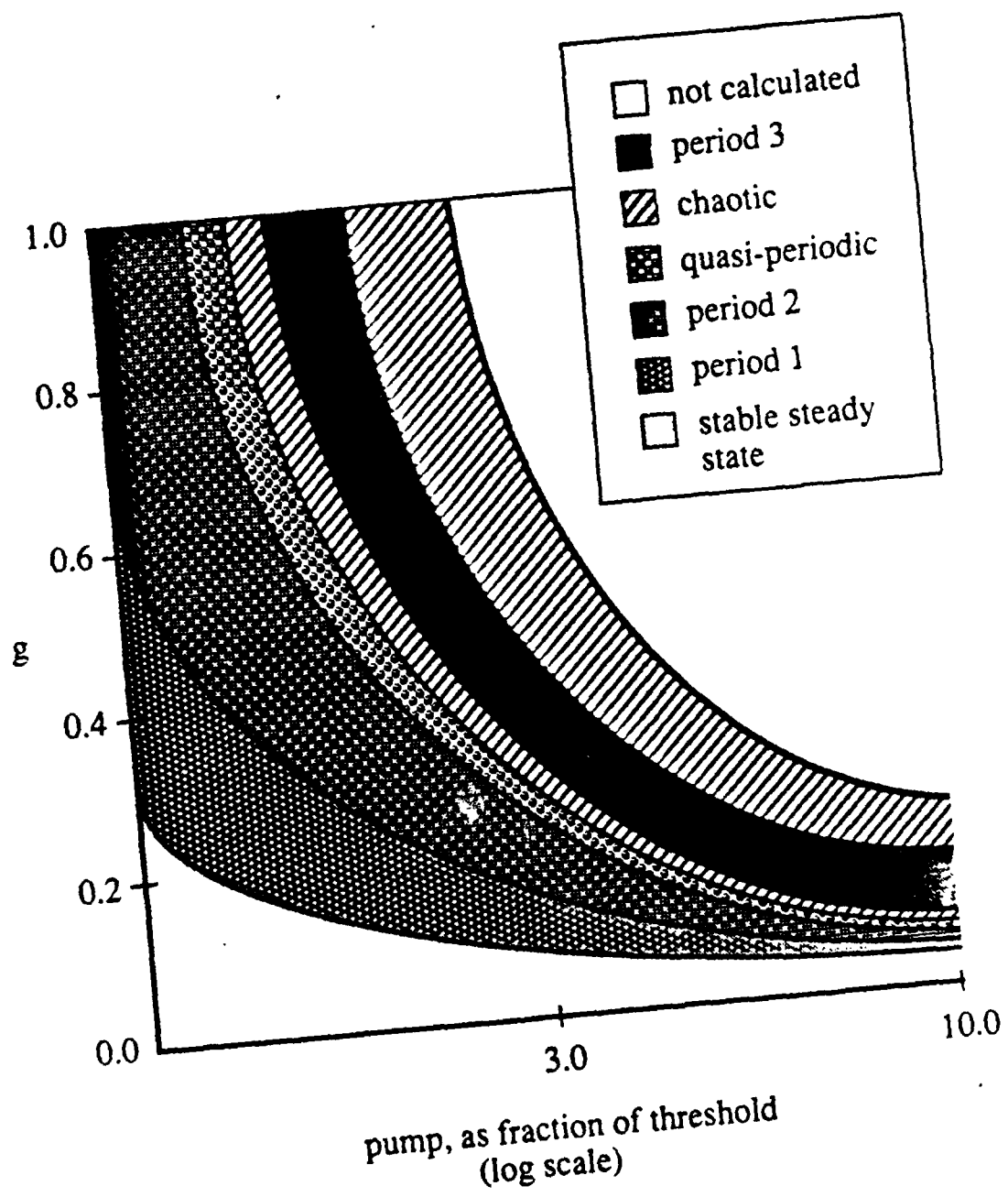
Fig. 3.11 Bifurcation Diagram for (3.25) with N=3 and P=0.
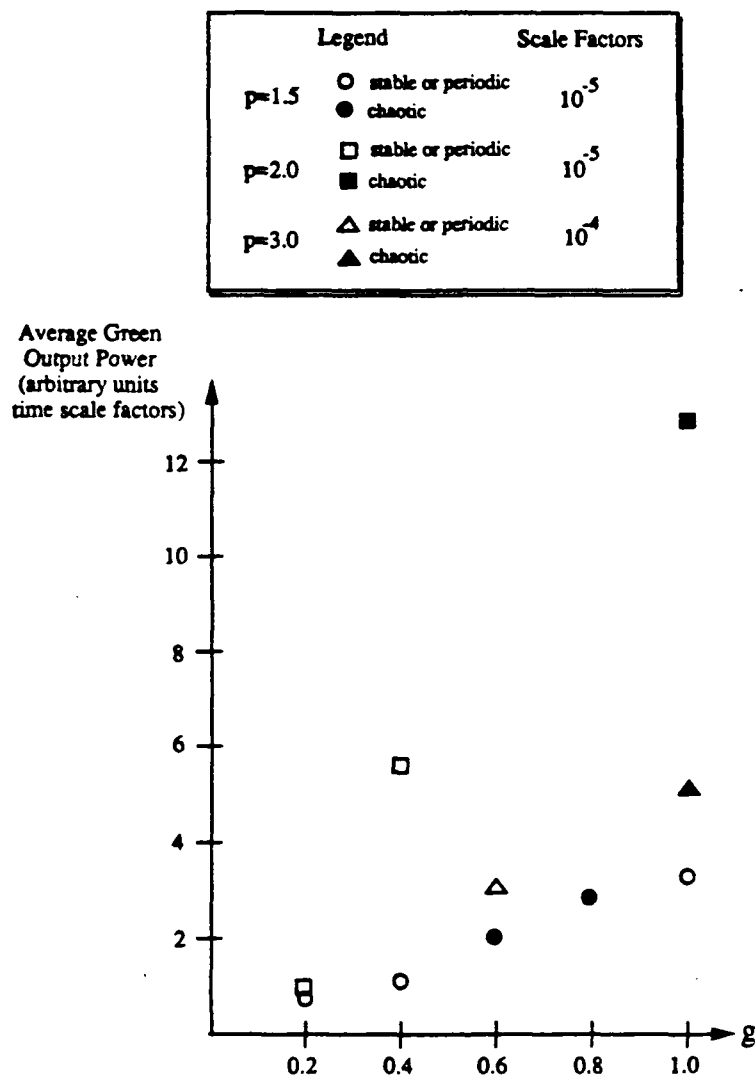
Fig. 3.12 Comparison of Average Green Output Power during Stable and
Chaotic Behavior in (3.25) with N=3 and P=0. The total average
green output does not depend on the character of the intensity
output, but strictly on the value of g.
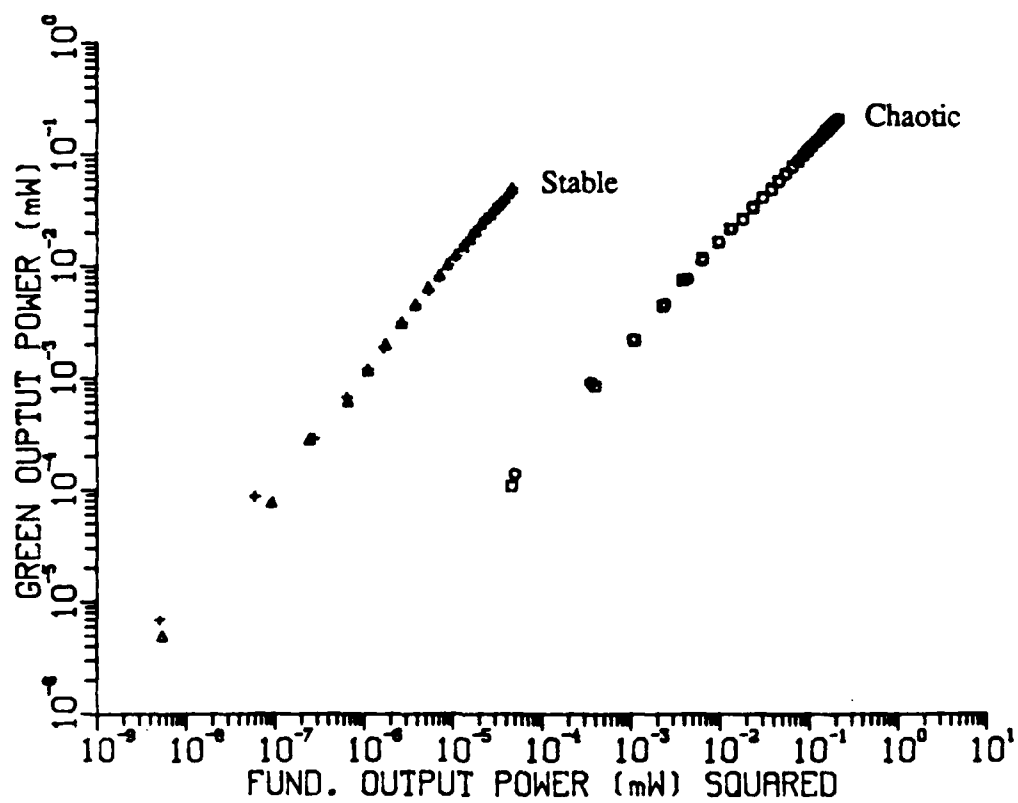
Fig. 3.13 Experimental Measurements of Average Green Output Power.
For a given fundamental intensity (horizontal axis), this laser
configuration produces more green in stable operation. We have
observed output from other configurations where the opposite is true.

Poincaré maps (Fig. 3.17(j)) and shows regular structure in its FFT (Fig. 3.17(i)). Chaotic output tends to fill out the Poincaré section and broaden the associated FFT (Fig. 3.17(t)).

We also calculated the average green output power for the total intensities plotted in Fig. 3.17. At a given pump power, the average green output tended to be stronger for chaotic operation than it did for stable or periodic output (Fig. 3.12). This tendency is expected for extracavity doubling (Teich and Diament, 1968; Diament and Teich, 1969; Teich, et al., 1970) but it is not always true in the experimental measurements we have made (Fig. 3.13). This suggests that the laser was not operating with all modes in the same polarization state when the measurements were taken. If we recall the equation for the doubled intensity for N modes with the same polarization (3.32) we see one sum of squared intensities, due to second harmonic generation, and a second sum of cross terms due to sum-frequency generation. The numeric time histories (Fig. 3.17) display sharper spikes for chaotic output than for periodic behavior, so that each individual intensity spends most of its time near zero. This means that most of the cross terms in the second sum of (3.32) are small relative to the frequency doubling terms. Since the total green output is larger in chaotic output, it implies that the sum-frequency generation is dominated by second harmonic generation in chaotic intensity behavior.

Two Modes in one Polarization Direction: Third Mode Orthogonally Polarized

The numerical data for this case were output from computer program POLYAG2 and are illustrated in Fig. 3.18 at the end of this chapter. These solutions are summarized in the bifurcation diagram in Fig. 3.14 which has several important differences from the previous diagram (Fig. 3.11). First of all, no stable steady state solutions were observed
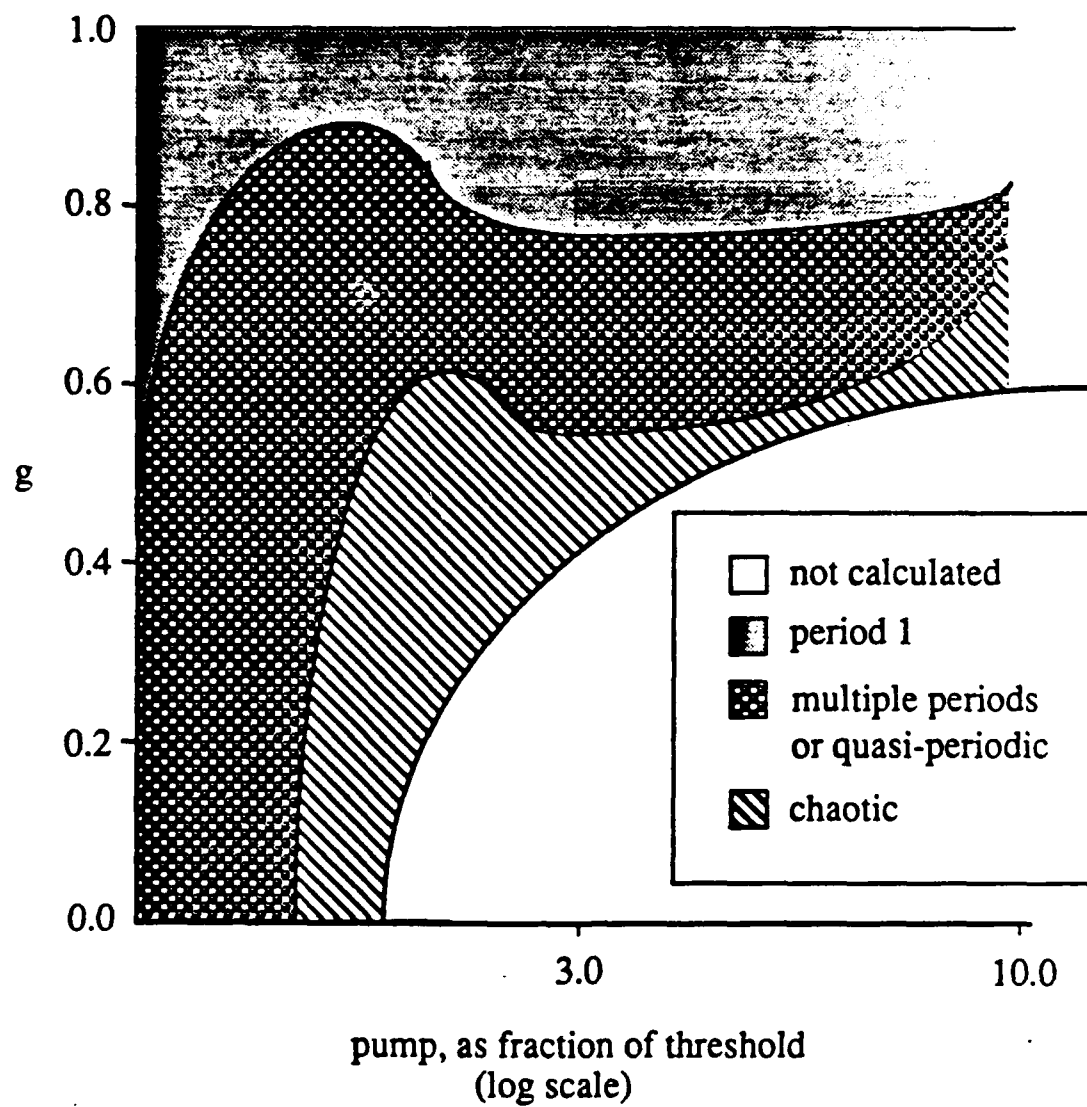
Fig. 3.14 Bifurcation Diagram for (3.25) with N=2 and P=1.

$\alpha=0.01$ $p=2.0$ $\beta=0.55$ $g=0.44$

(a)

(b)

(c)

(d)

Laboratory Experiment

Numerical Experiment
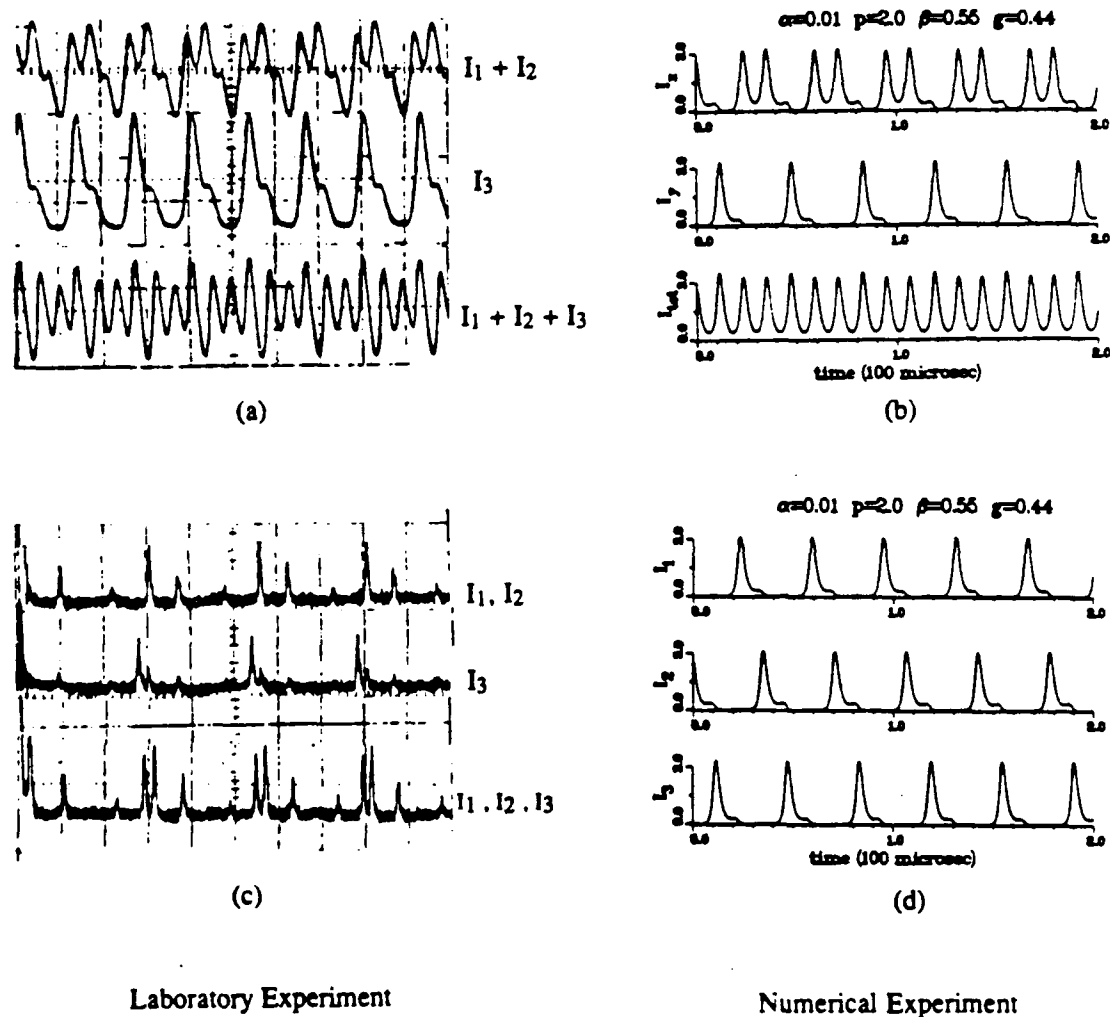
Fig. 3.15 Comparison of Experimental and Numerical Time Histories. Both samples
have two modes in one polarization direction with a third orthogonal mode.
(a) Experimental time traces. Line 1 shows the intensity in the x direction,
(b) Numerical integration of (3.25) with N=2 and P=1. The total time of this
plot matches the time scale of the experimental data. (c) Fabry-Perot output
showing the distribution of modes in the x and y directions. (d) The
same numerical data as (b) with the time histories for modes 1 and 2 separated.

Average Green
Output Power
(arbitrary units
time scale factors)
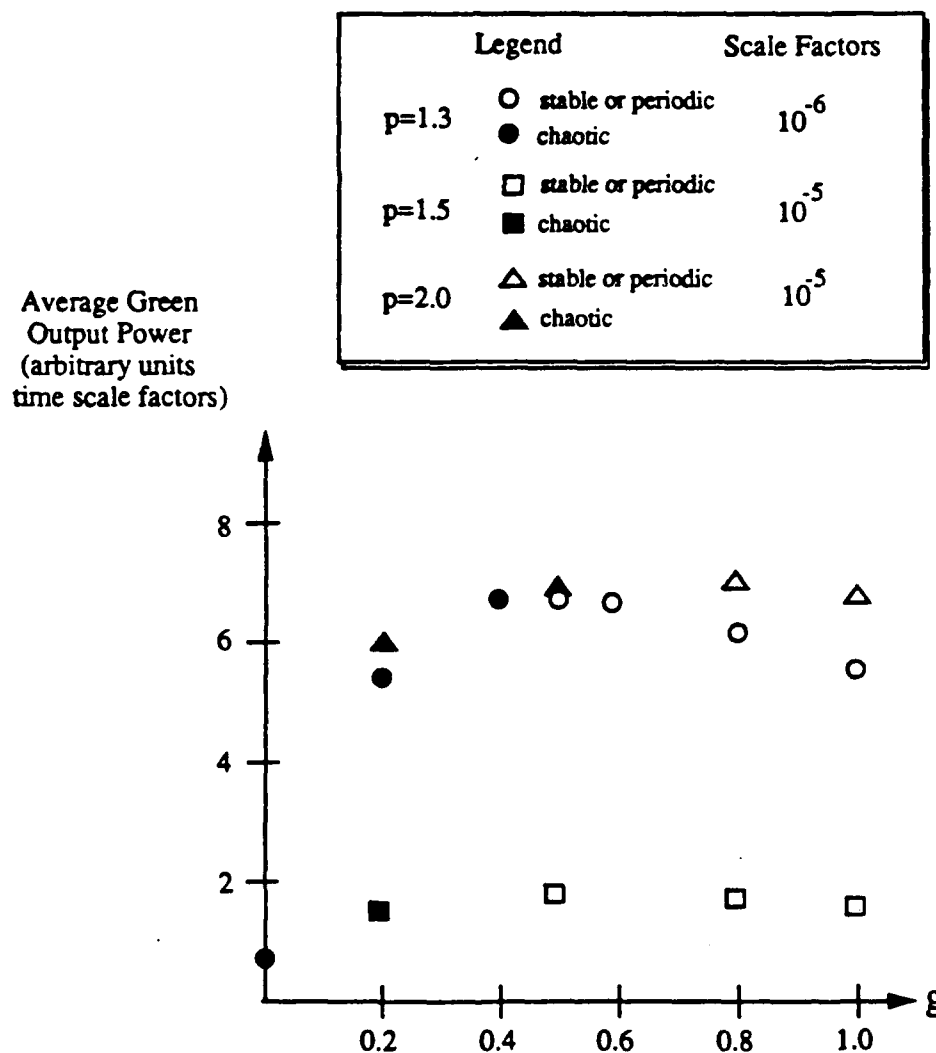
Fig. 3.16 Comparison of Average Green Output Power during Stable and
Chaotic Behavior in (3.25) with N=2 and P=1. For a given pump
power (which corresponds to a fixed average fundamental intensity
power in the numerical model) chaotic time histories tend to
produce less green output.

for this case. This is due to the absence of an interior (all modes "on") steady state solution to (3.46) for most values of g. Secondly, the stable periodic behavior in this case occurs for g near 1. Lastly, this set of equations requires a much smaller time step and is more difficult to integrate for g near 0, because the intensity coupling in the sum frequency terms dominates the intensity derivatives in (3.23) and makes the time derivatives very steep.

In Fig. 3.15 we make a direct comparison of experimental and numerical data. The time traces in Fig. 3.15(a) are the fundamental intensity output in two orthogonal polarization directions, with the total intensity output plotted in the third line. The cavity included a QWP, and was pumped at about 2 times threshold. The best parameter set we found to match the data was $\alpha=0.01$, $p=2.0$, $\beta=0.55$, and $g=0.44$; the numerical solution appears in Fig. 3.15(b). To our knowledge this is the first successful match of numerical integration to three-mode output (with different polarization directions). We note that the numerical output closely reproduces the time scales of the pulses in addition to the relative peaks and pulse shapes.

As in the previous case, we calculated the average green output for some of the integrations plotted in Fig. 3.18, to compare the output for periodic and chaotic intensity behavior. We found that for a fixed pump power, the average green output was less for chaotic time histories than it was for periodic output (Fig. 3.16). This is partially explained by the equation for total green output intensity (3.24). There are many cross terms which represent the contributions of sum frequency generation; we discussed above that one of the terms in every $I_j I_k$ pair is usually negligible in chaotic time traces, so the cross term sums can become small for chaotic intensity behavior. We hypothesize that this causes the total green output to decrease as illustrated in Fig. 3.16.

Conclusions

This chapter reports the development and analysis of a new model for intracavity doubling. The model is derived in a very general framework that applies to intracavity doubling in any class-B laser with passive birefringent intracavity elements. The analysis of this model has led to successful predictions of ways to eliminate intensity fluctuations in the output from a frequency doubled laser. The key ingredients in the model include the birefringence of the active medium, and the different sum frequency generation by modes which oscillate in parallel or in orthogonal polarization directions. The model produces close matches to experimental data in both the qualitative features and time scales of intensity output from an intracavity frequency doubled Nd:YAG laser. Furthermore, our analysis and numerical results completely characterize the intensity behaviors for one, two, and three modes.
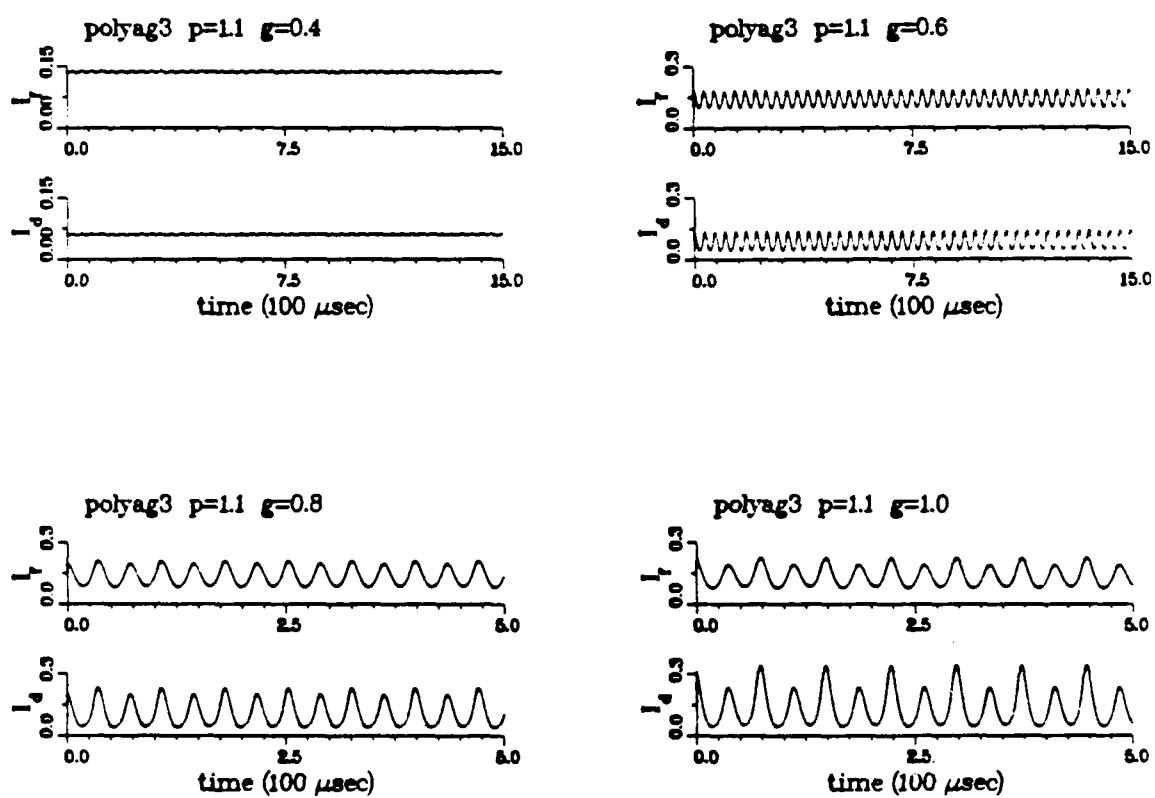
Fig. 3.17 Numerical Integrations of (3.25) with N=3 and P=0.
(a) Total intensity output for p=1.1.
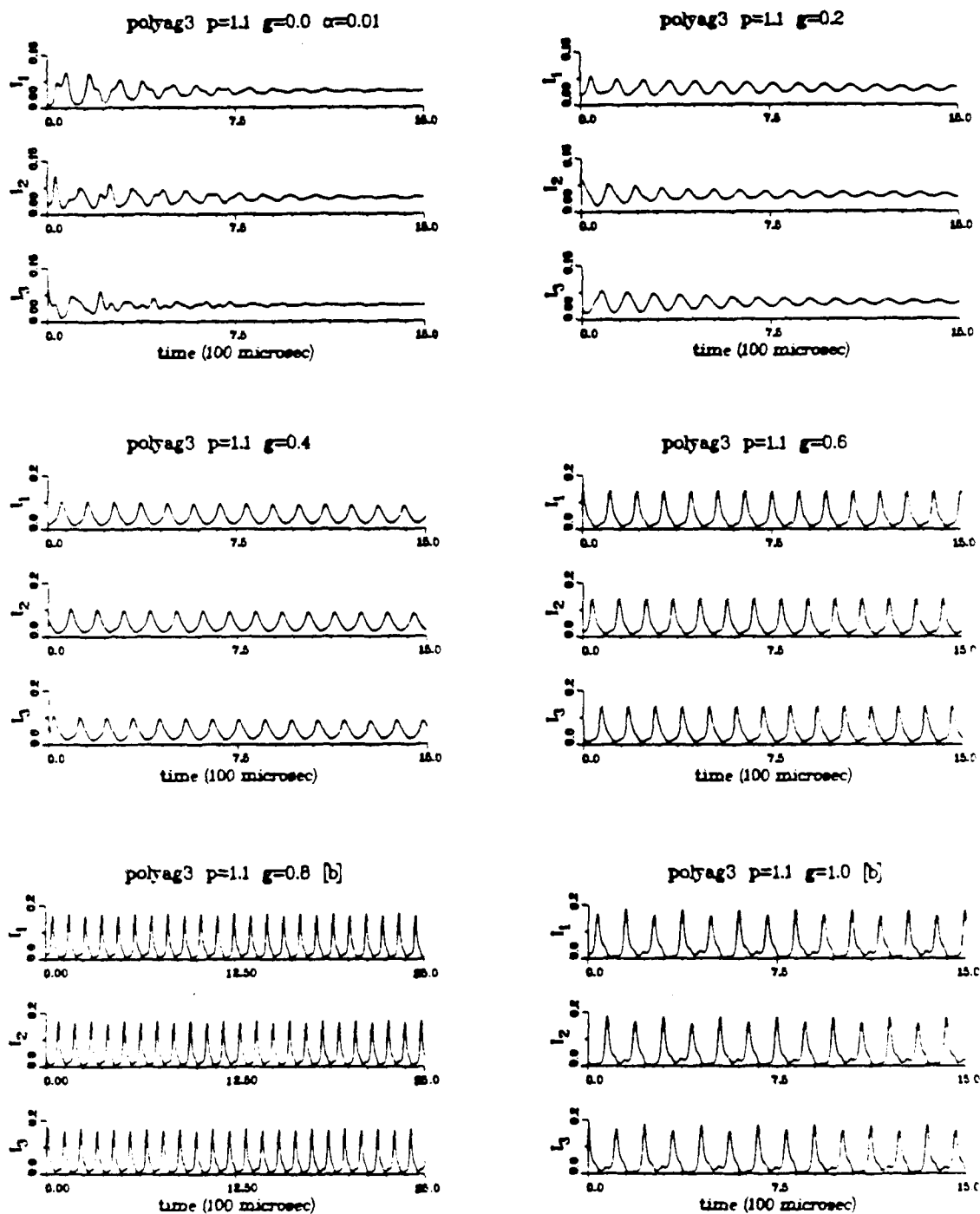
Fig. 3.17 (b) Individual mode time traces for p=1.1, corresponding to
the output in (a).
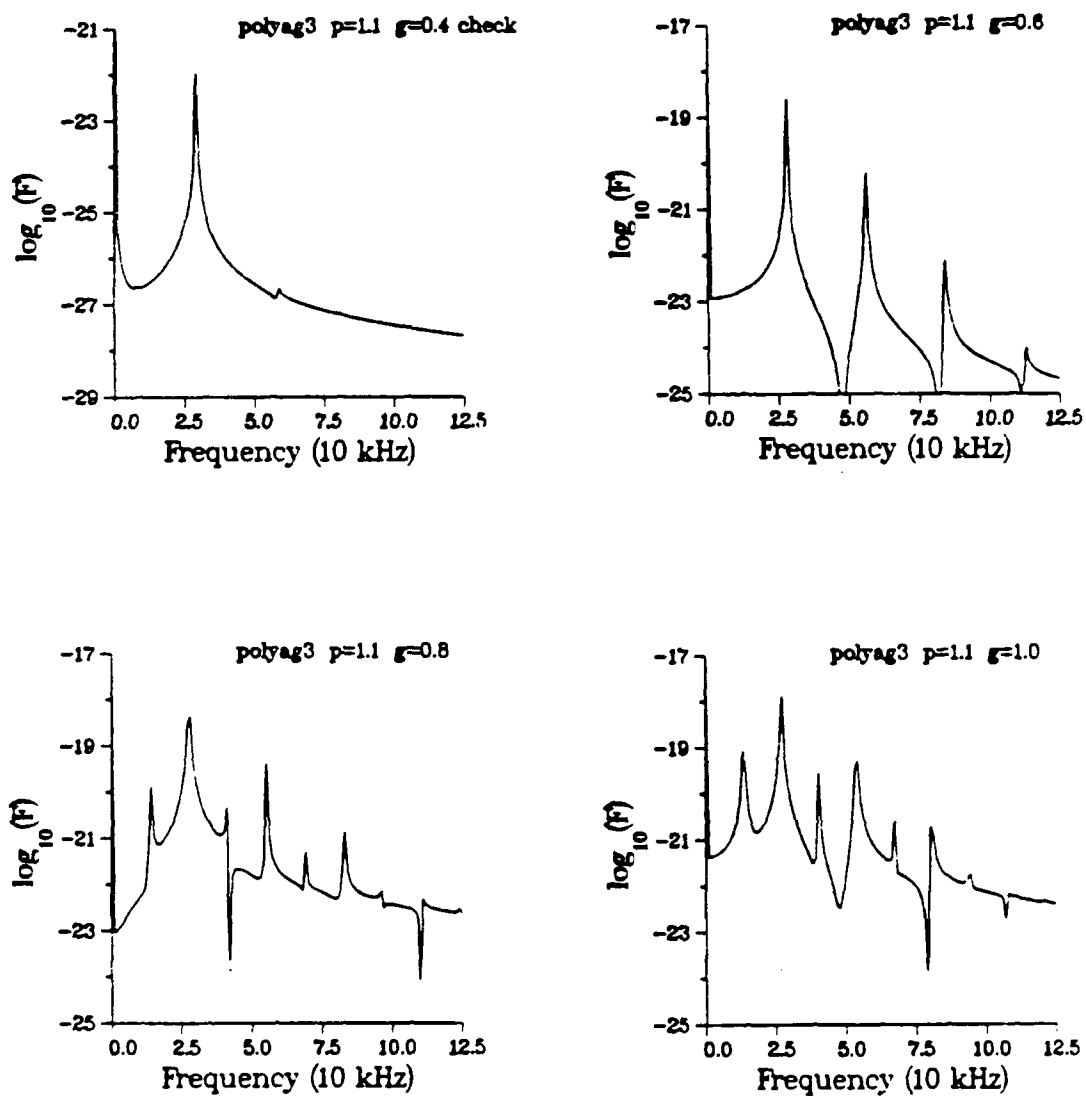
Fig. 3.17 (c) FFT's for the output in (a)

153
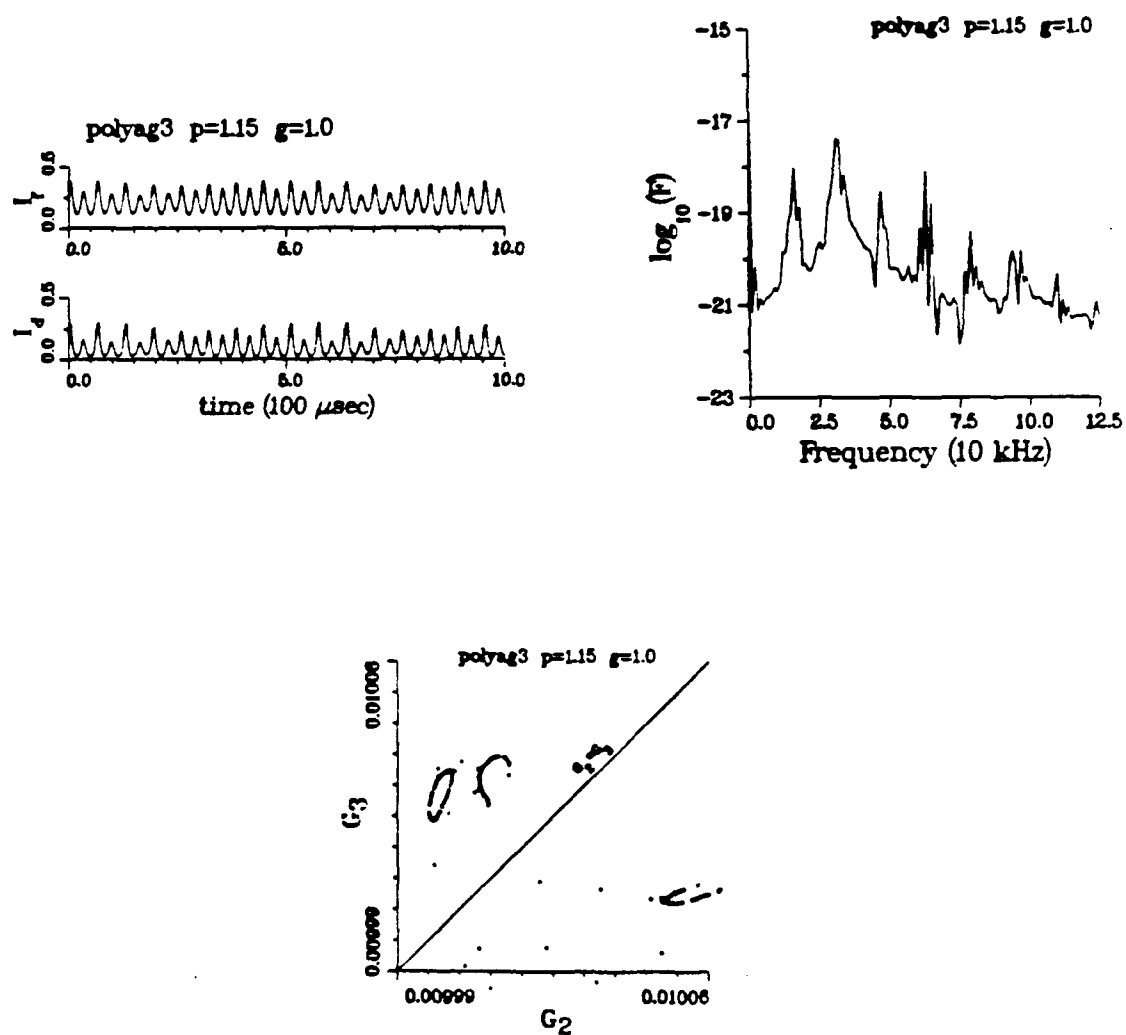
Fig. 3.17 (d) Output for p=1.15, including numerical Poincaré map.
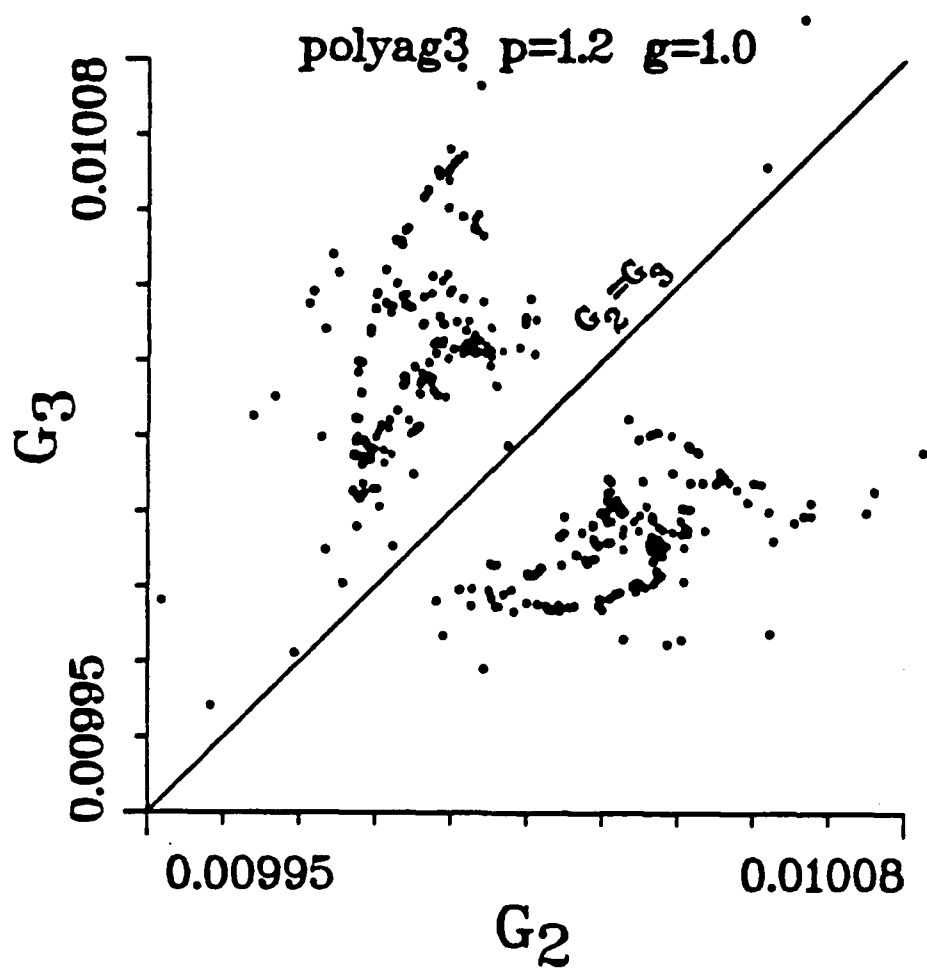
Fig. 3.17 (e) Poincaré map for p=1.2 showing chaotic flow.
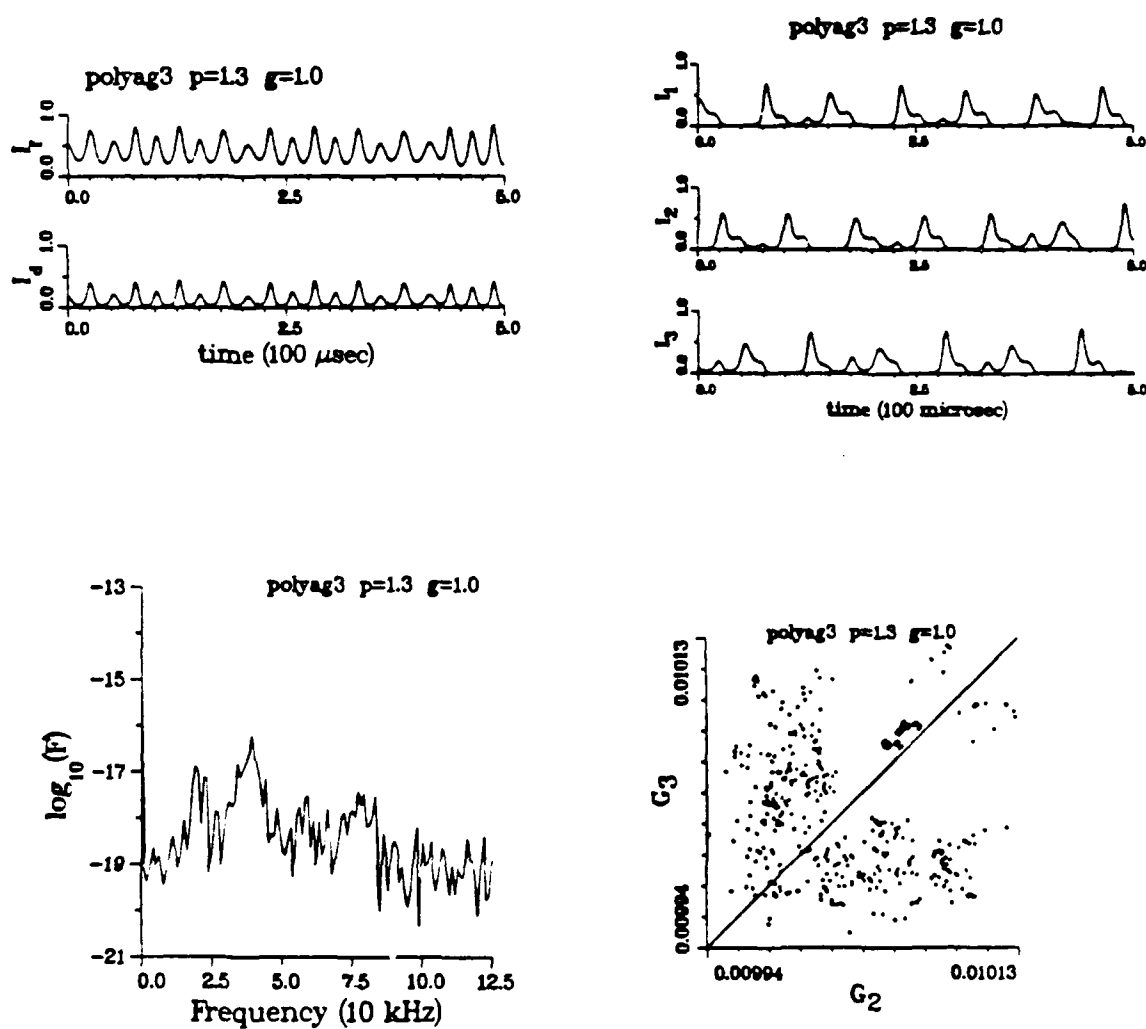
Fig. 3.17 (f) Output for p=1.3, g=1.0.

polyag3 p=1.5 g=0.2

polyag3 p=1.5 g=0.4

polyag3 p=1.5 g=0.6

polyag3 p=1.5 g=0.8

polyag3 p=1.5 g=0.8 [b]

polyag3 p=1.5 g=1.0
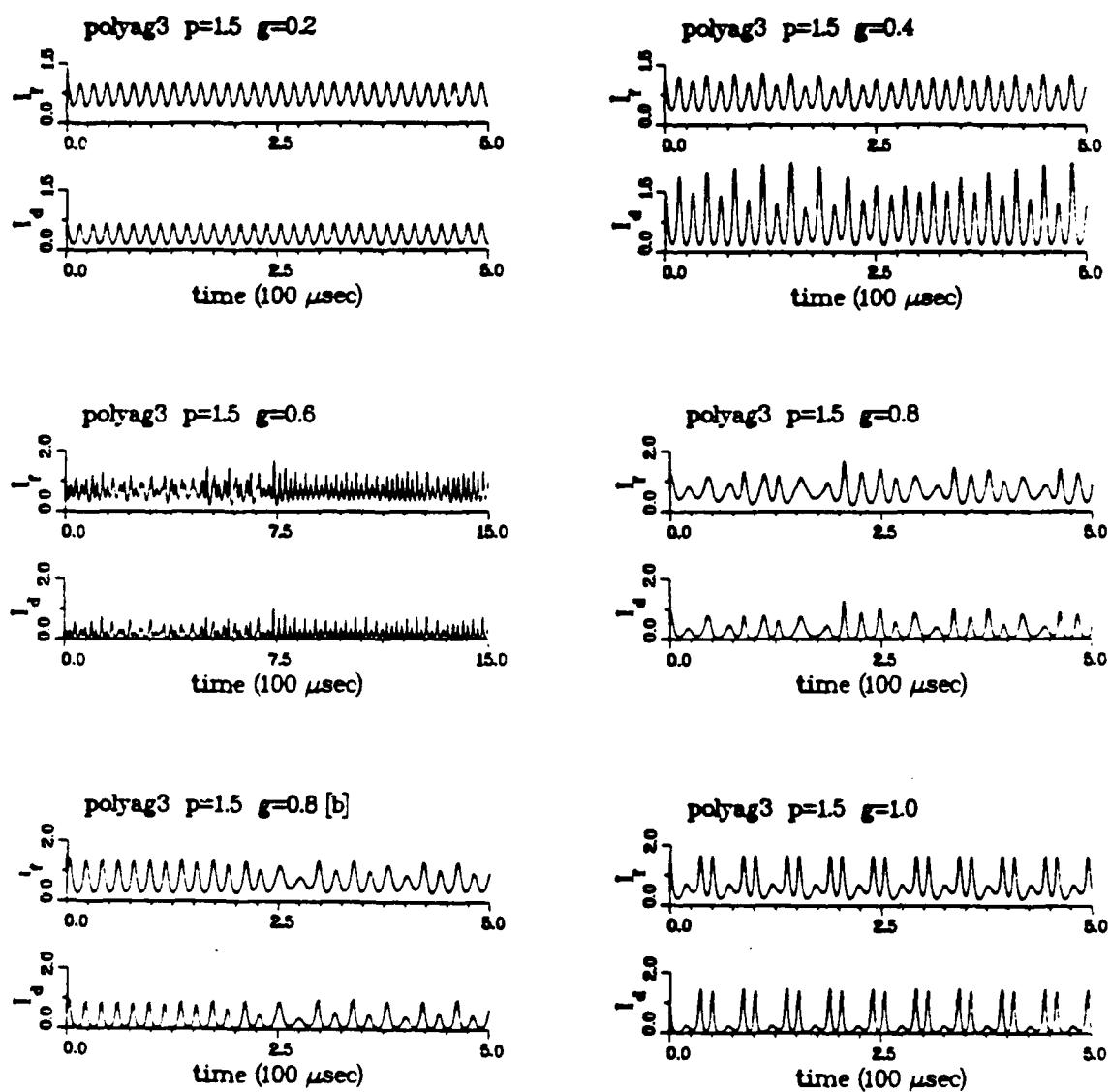
Fig. 3.17 (g) Total intensity time histories for p=1.5.
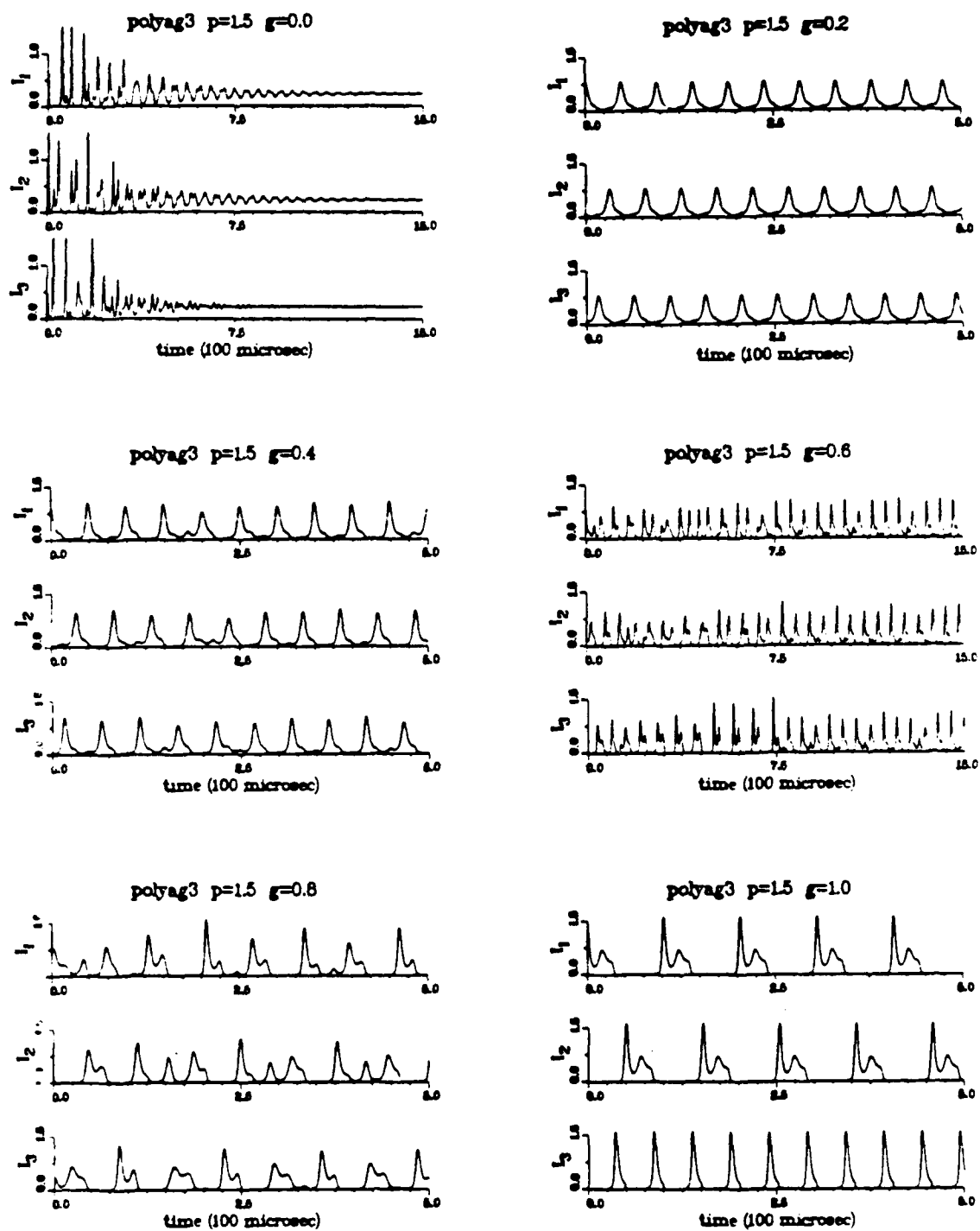
Fig. 3.17 (h) Individual mode time traces corresponding to (g).
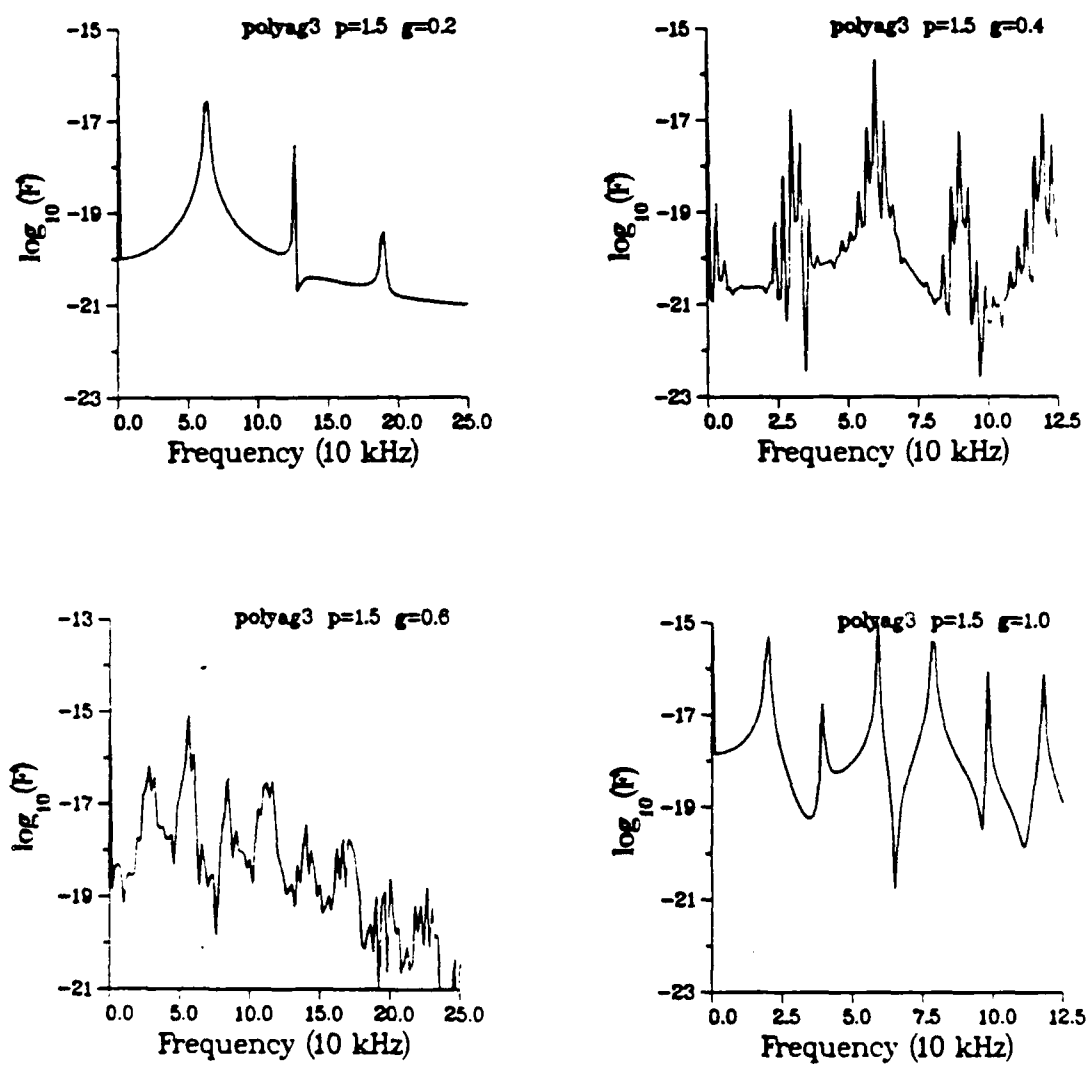
Fig. 3.17 (i) FFT's corresponding to the output in (g).
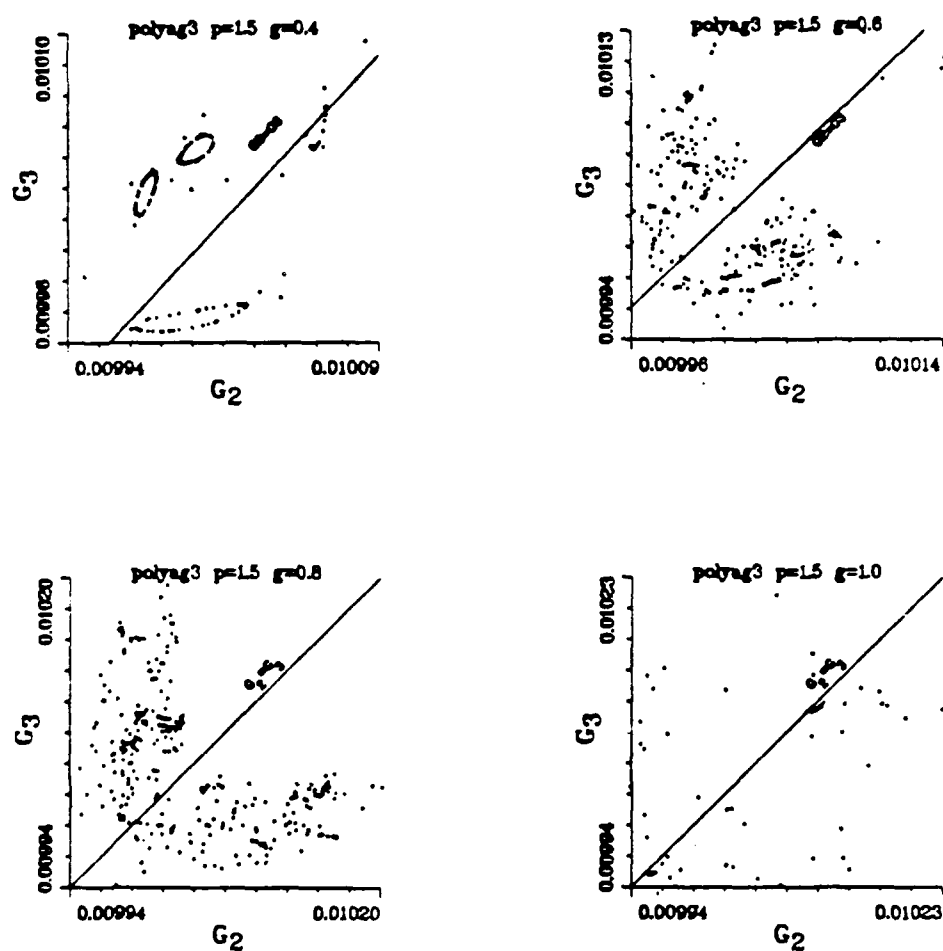
Fig. 3.17 (j) Numerical Poincaré maps corresponding to the output in (g).

polyag3 p=2.0 g=0.2

polyag3 p=2.0 g=0.4

polyag3 p=2.0 g=0.8

polyag3 p=2.0 g=1.0

time (100 μsec)

time (100 μsec)
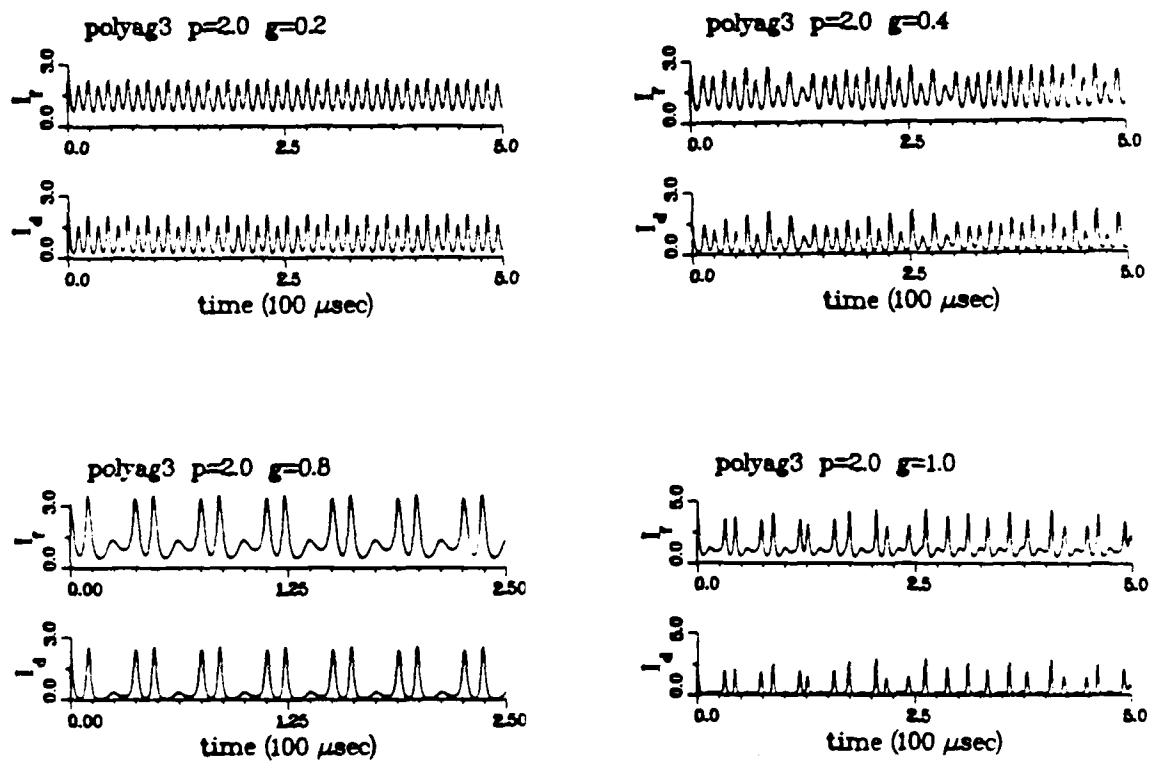
Fig. 3.17 (k) Total intensity output for p=2.0.
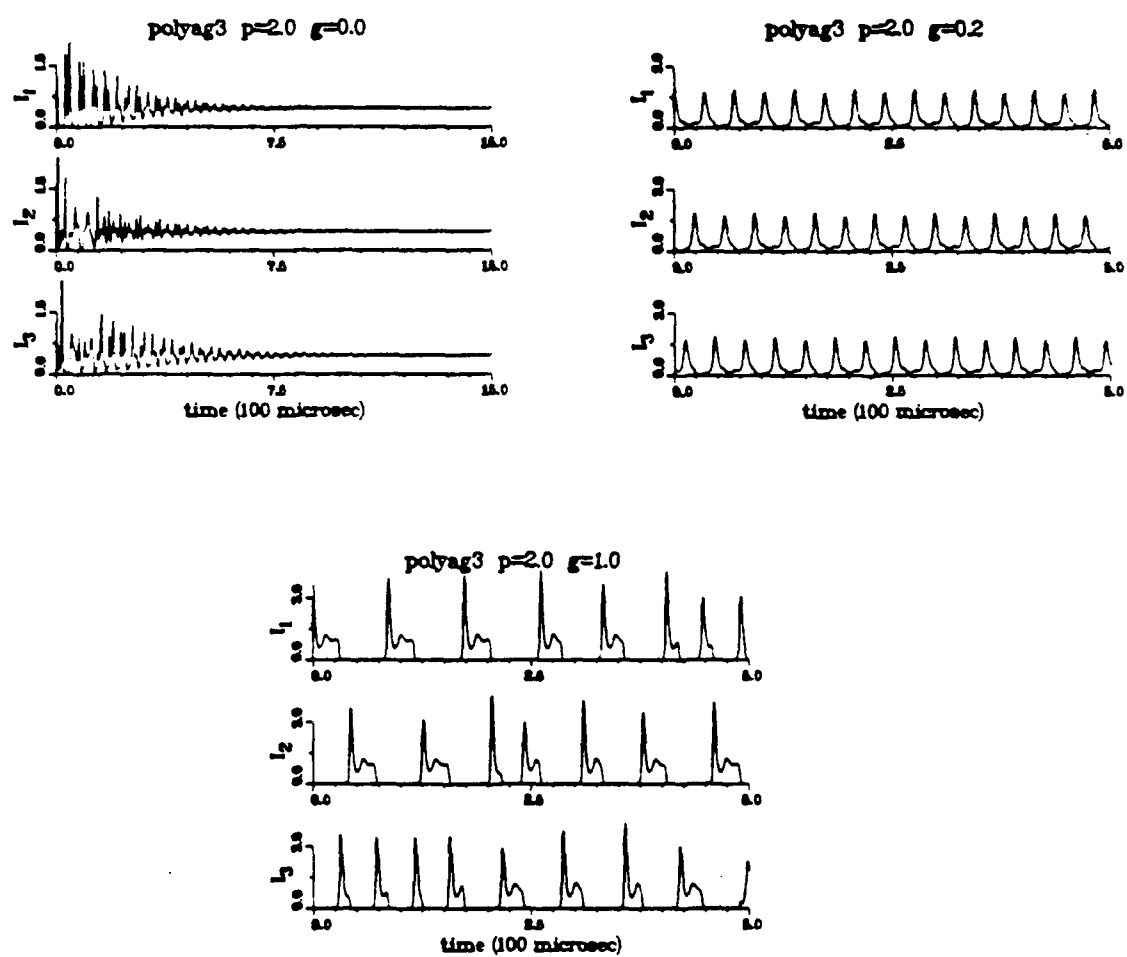
Fig. 3.17 (l) Individual mode time traces corresponding to (k).
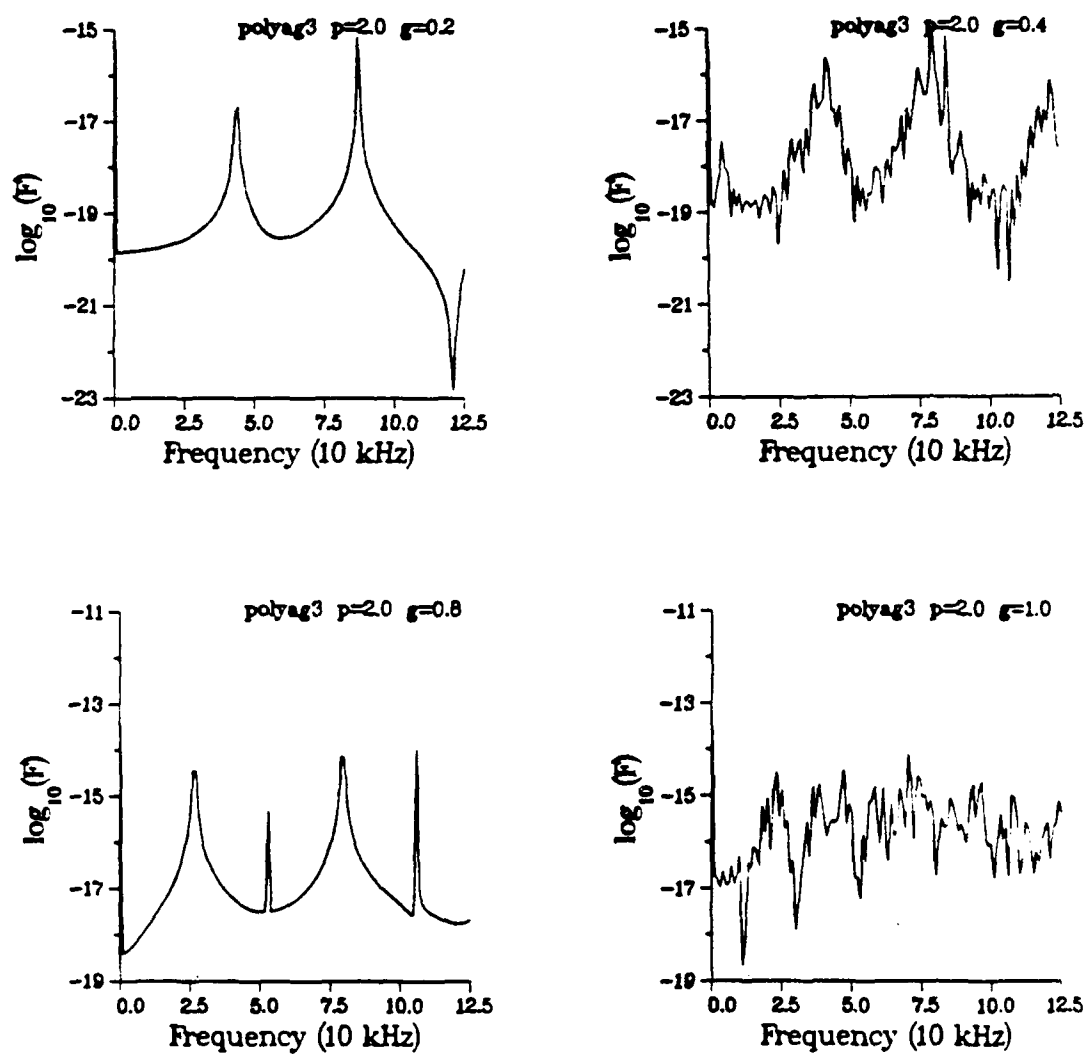
Fig. 3.17 (m) FFT's corresponding to the output in (k).
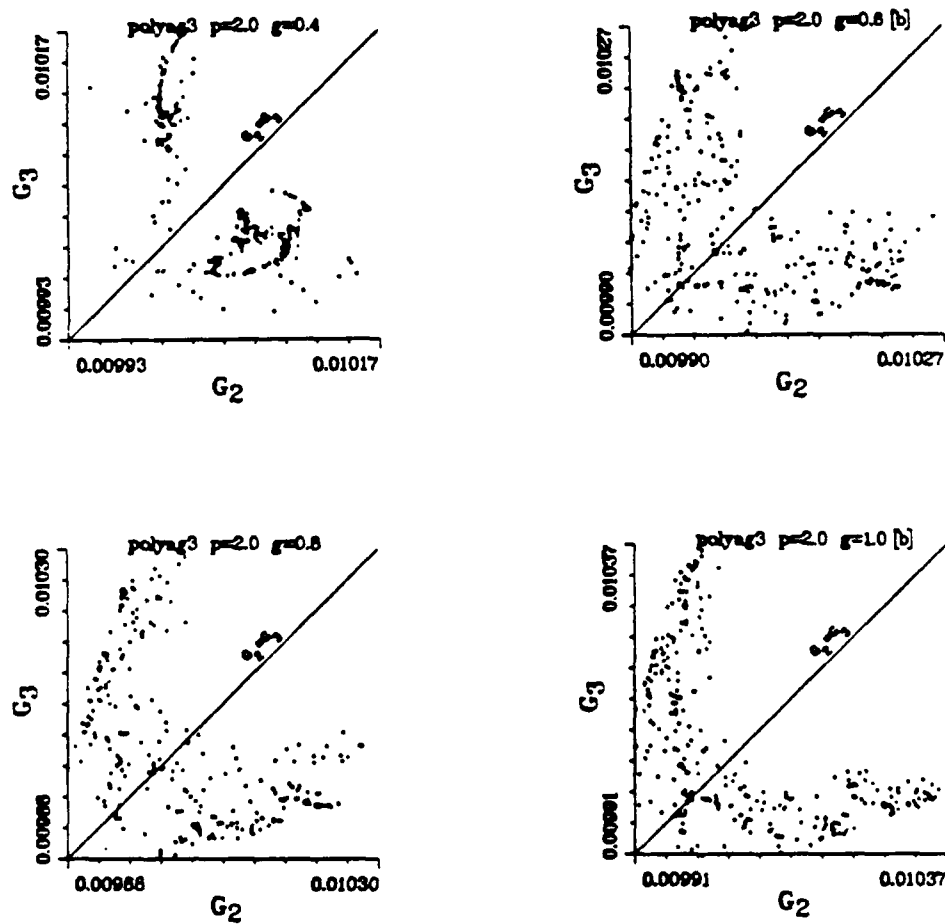
Fig. 3.17 (n) Poincaré maps for the output in (k).
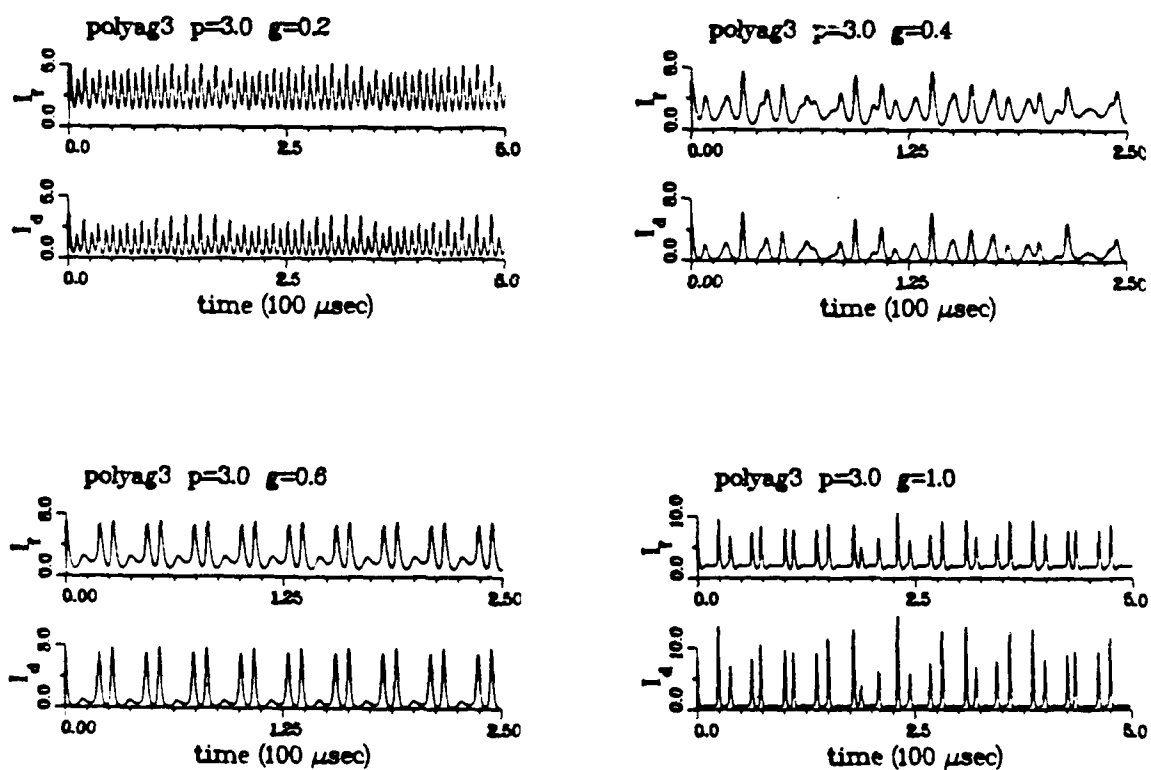
Fig. 3.17 (o) Total intensity time traces for p=3.0.

polyag3 p=3.0 g=0.0

polyag3 p=3.0 g=0.2

time (100 microsec)

time (100 microsec)

polyag3 p=3.0 g=1.0

time (100 microsec)
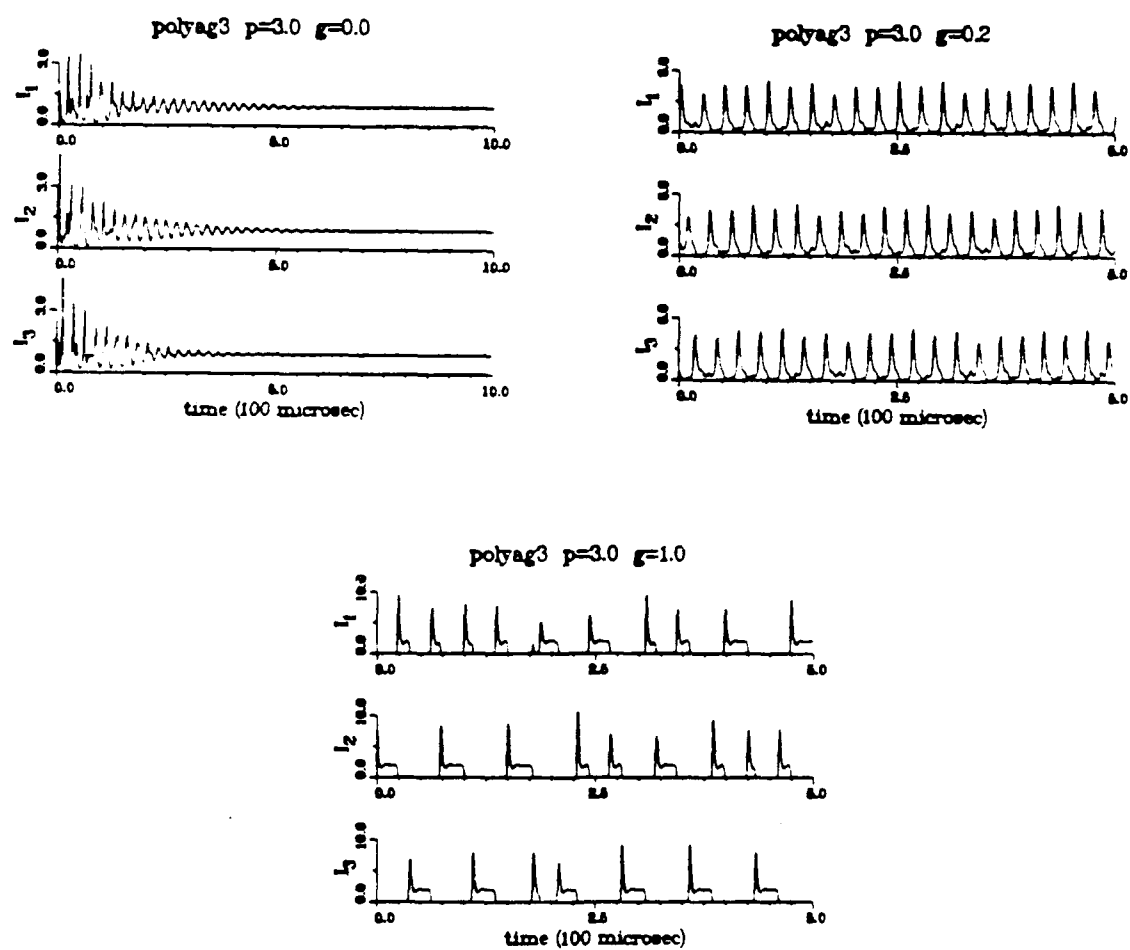
Fig. 3.17 (p) Individual mode output for (o).
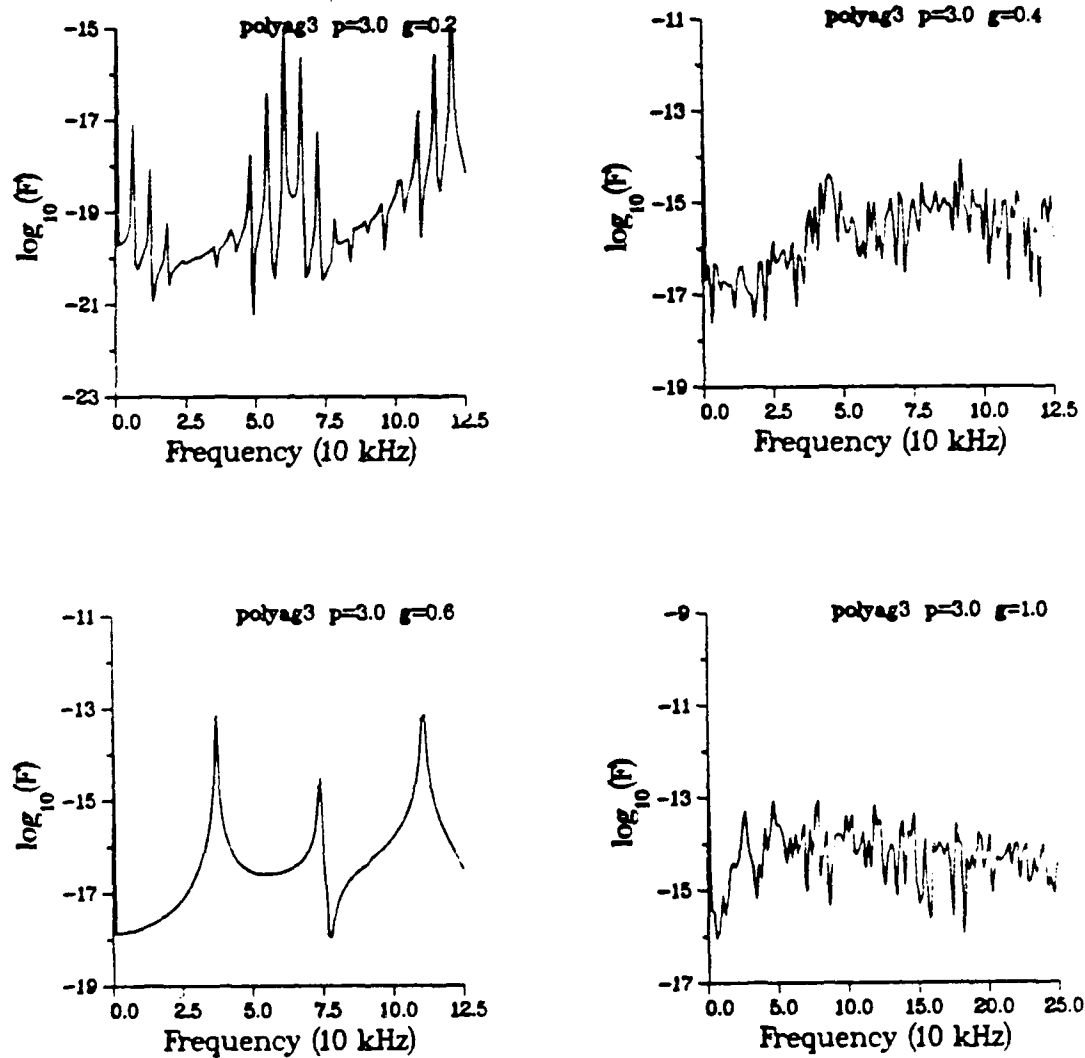
Fig. 3.17 (q) FFT's corresponding to (o).
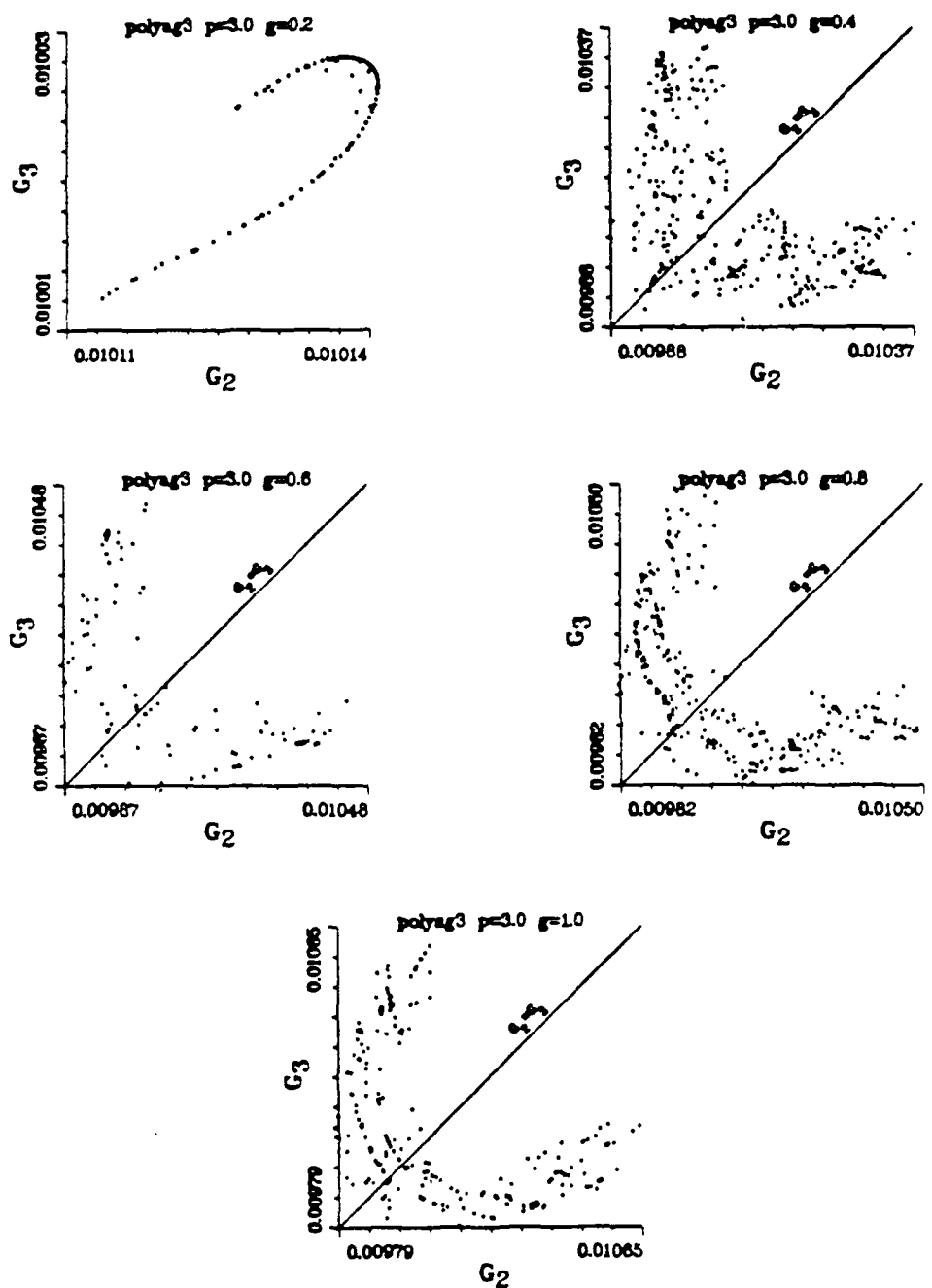
Fig. 3.17 (r) Poincaré maps corresponding to (o).

polyag3 p=5.0 g=0.0

polyag3 p=5.0 g=0.2

time (100 microsec)

time (100 microsec)

polyag3 p=5.0 g=0.2

time (100 μsec)

polyag3 p=5.0 g=0.2
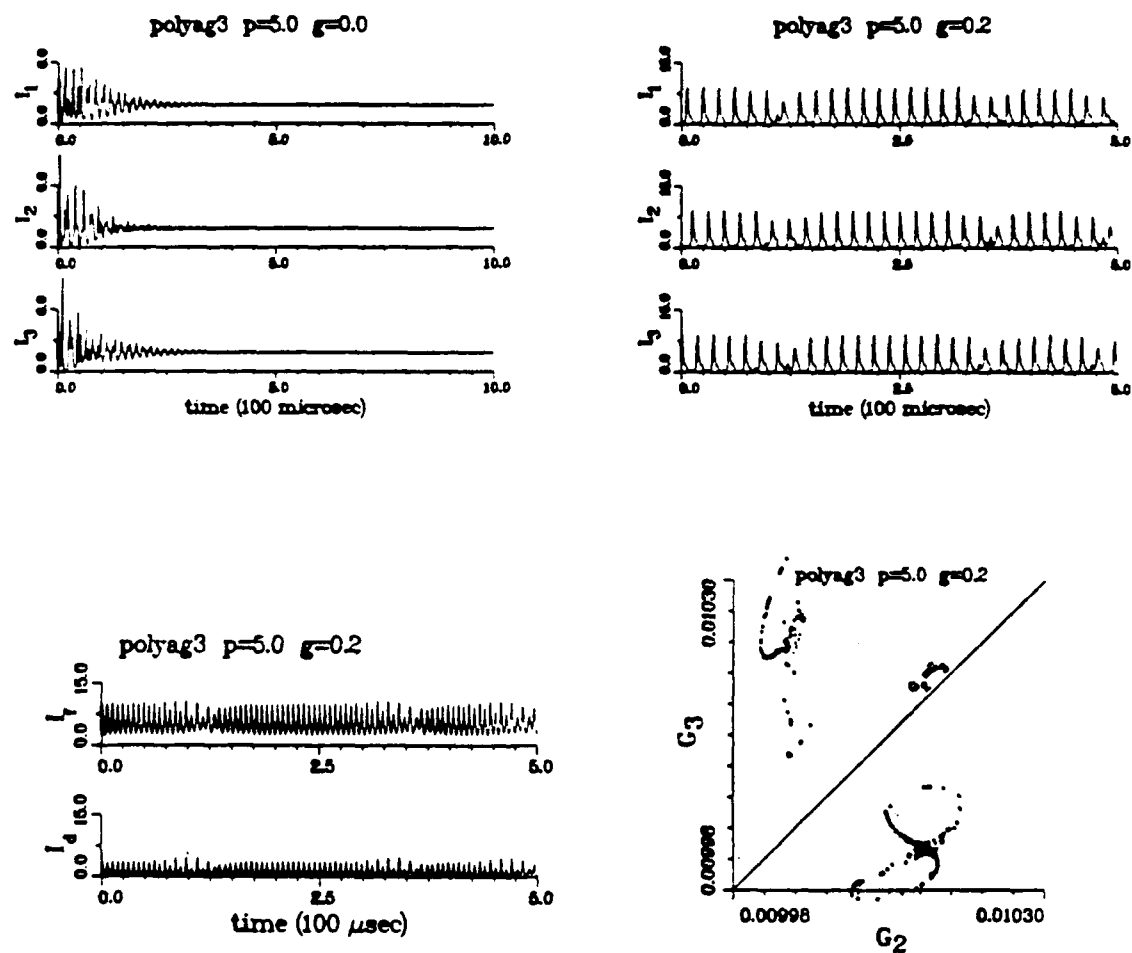
Fig. 3.17 (s) Output for p=5.0.
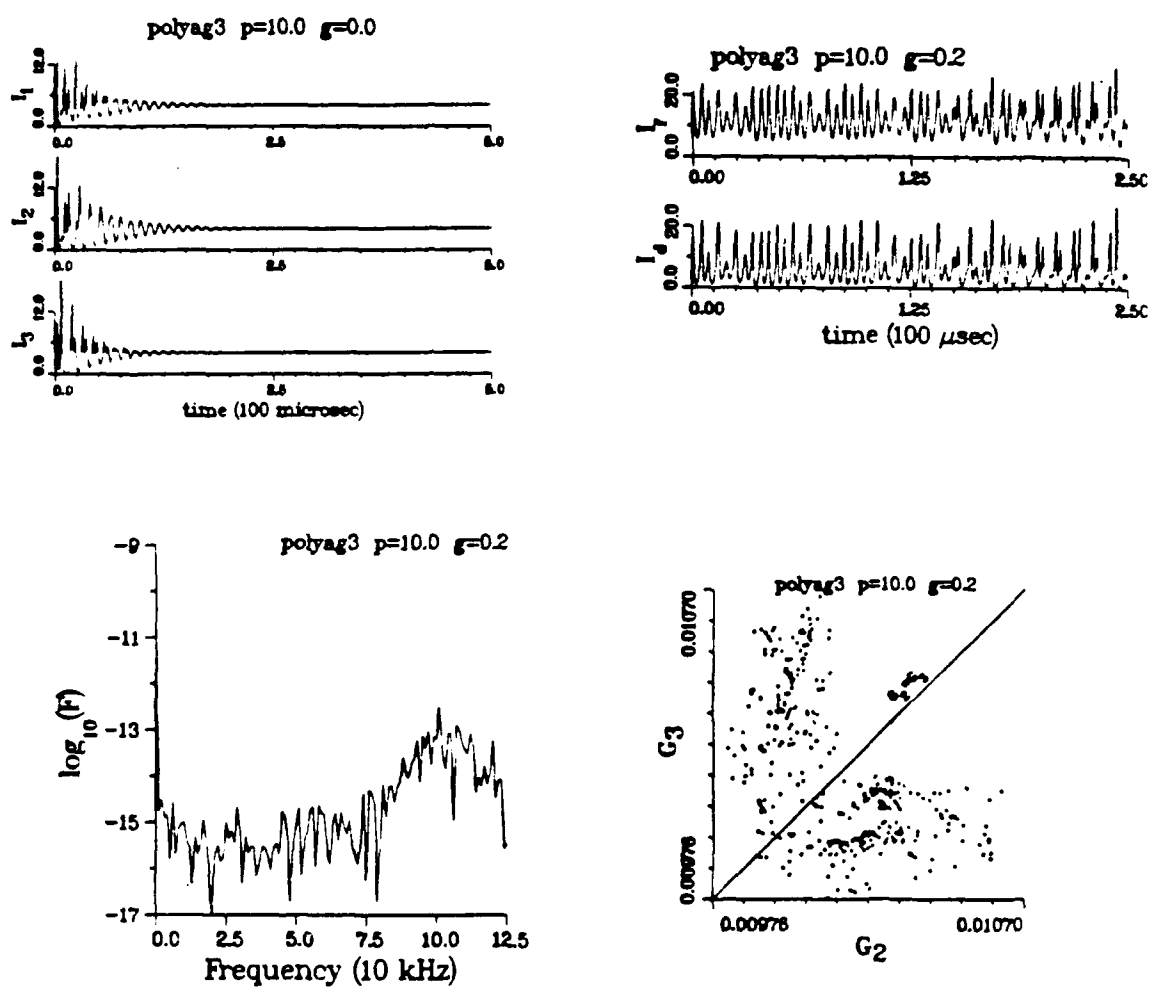
Fig. 3.17 (t) Output for p=10.0.
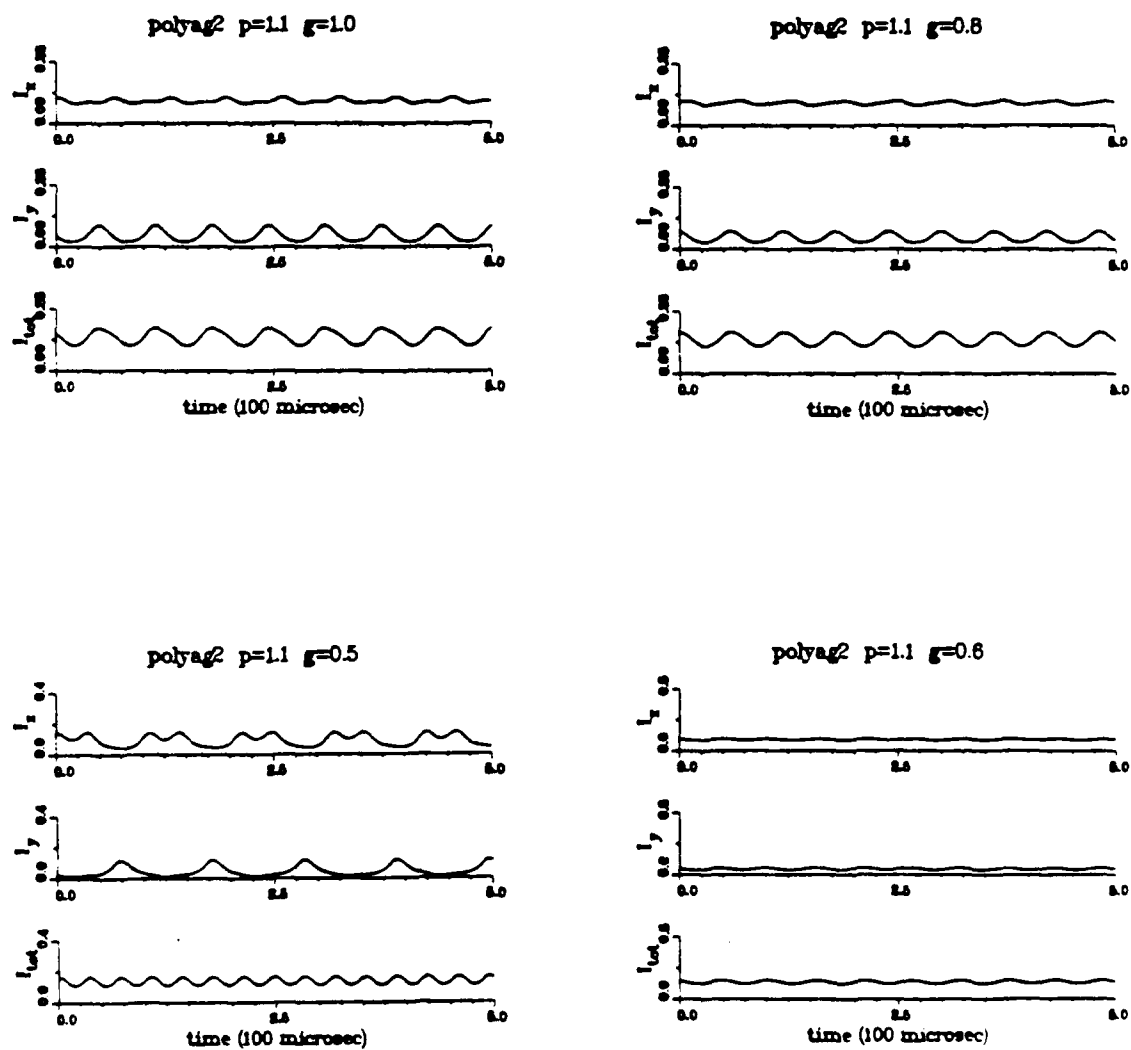
Fig. 3.18 Numerical Integrations of (3.25) with N=2 and P=1.
(a) Intensity output for p=1.1. $I_x = I_1 + I_2$. I_y is I_3.
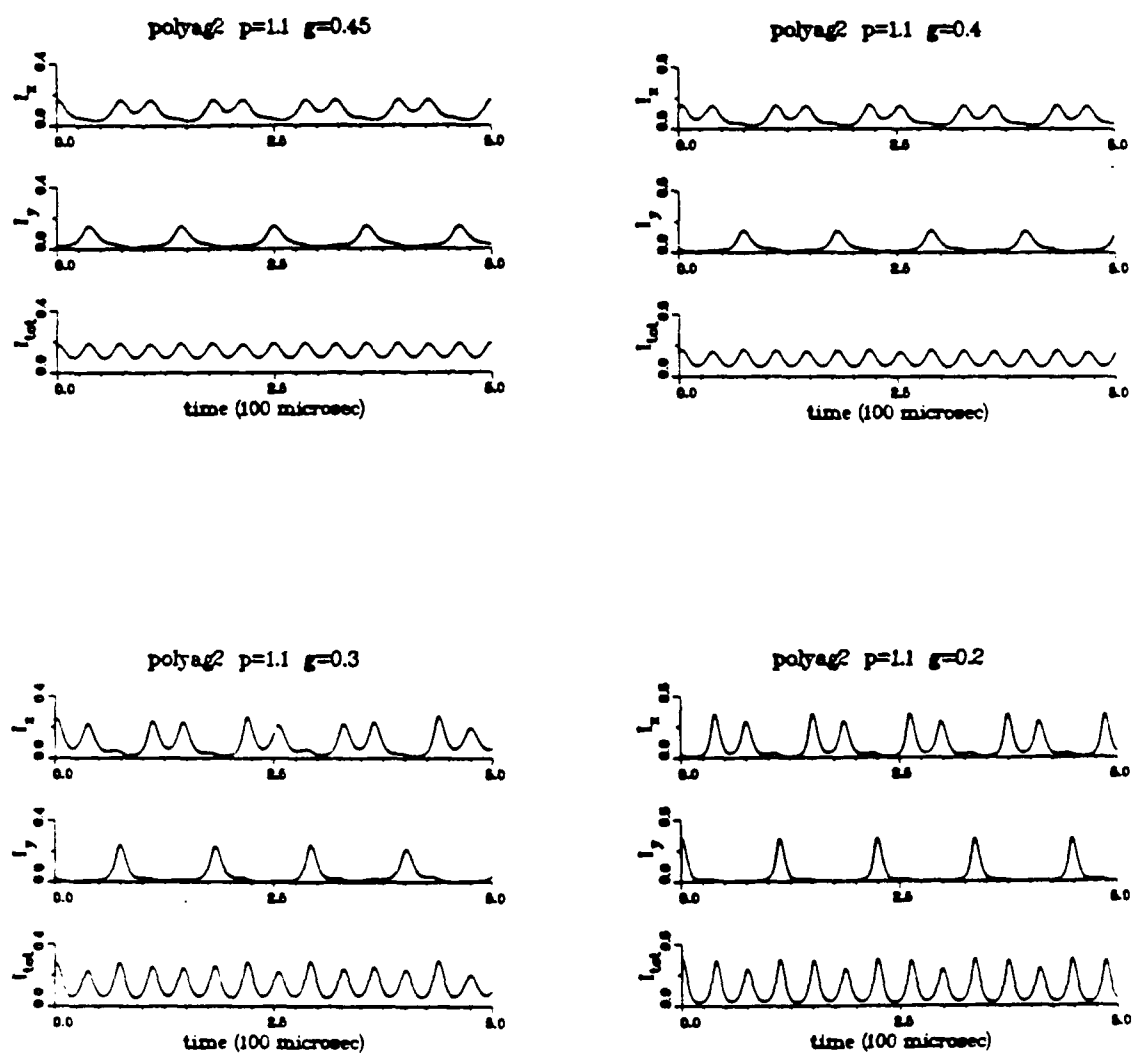
Fig. 3.18 (b) Intensity output for p=1.1, continued.
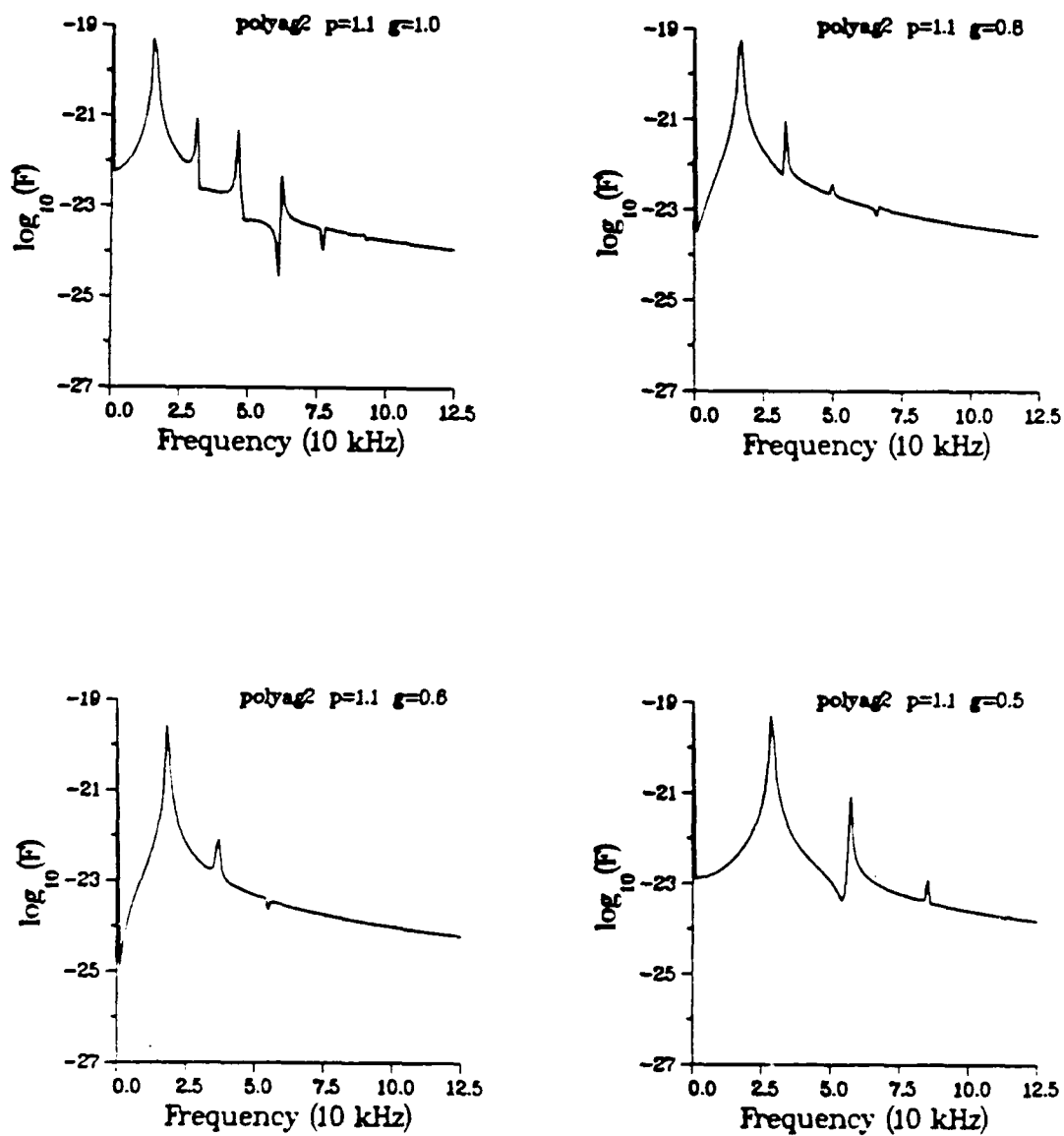
Fig. 3.18 (c) FFT's corresponding to (a).
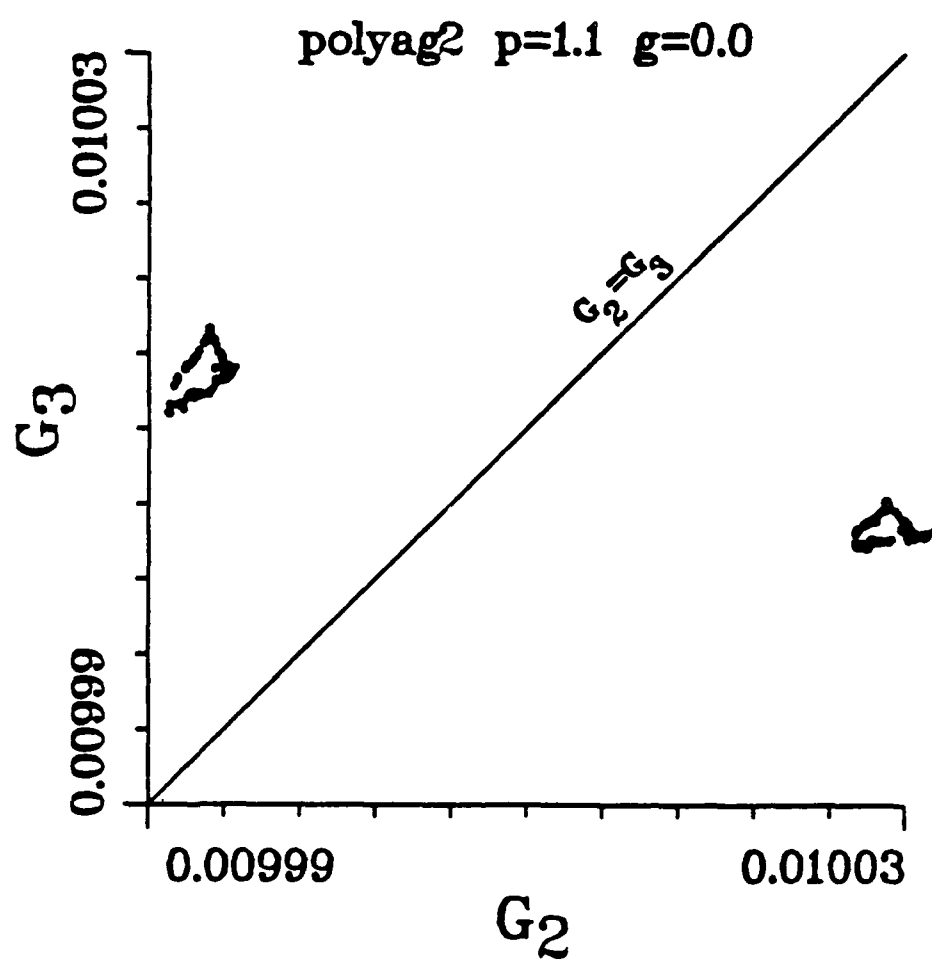
Fig. 3.18 (d) Numerical Poincaré map for p=1.1, g=0.0 with qu~ si-periodic output.
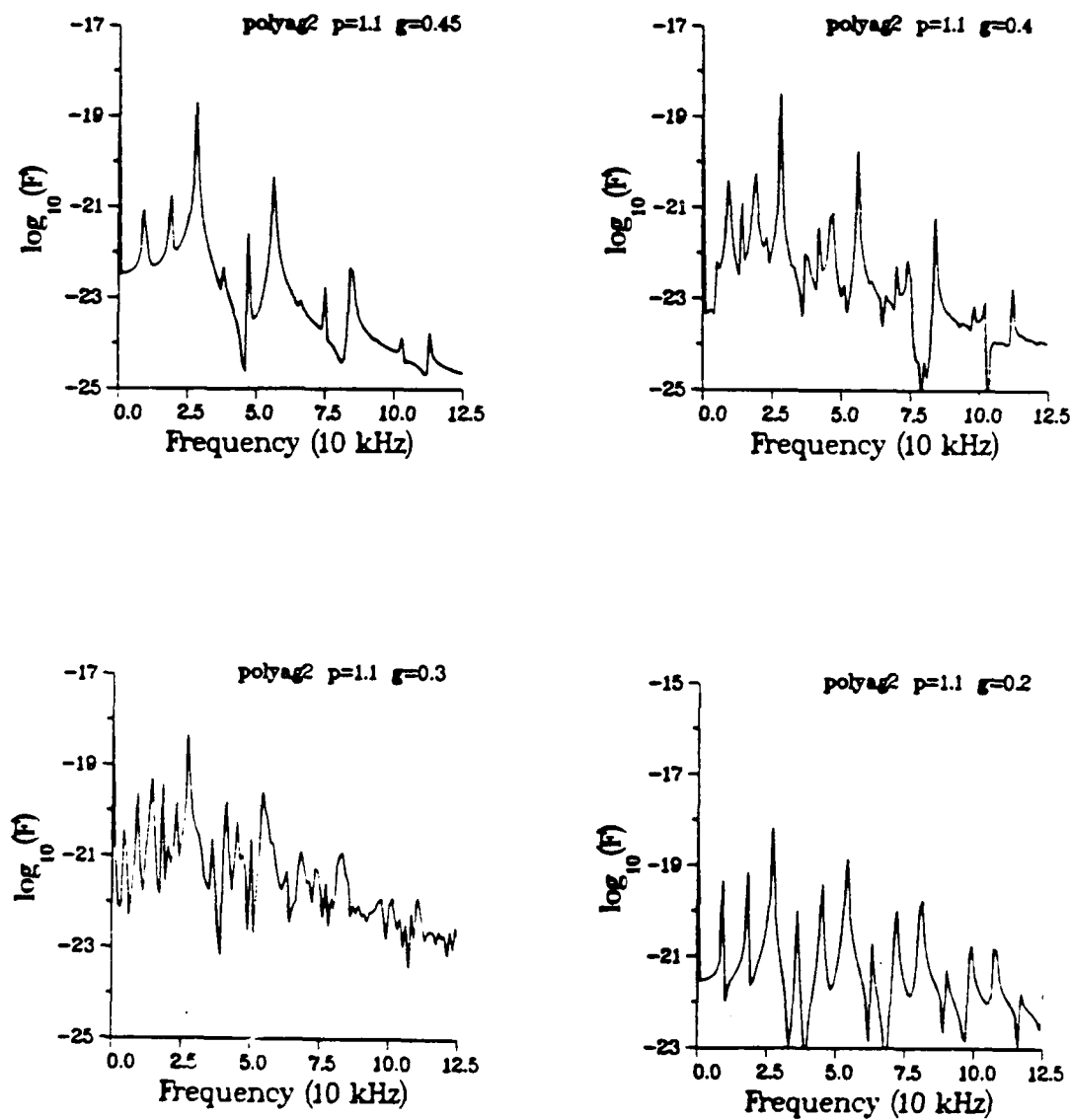
Fig. 3.18 (e) FFT's corresponding to (b).

polyag2 p=1.3 g=1.0

polyag2 p=1.3 g=0.8

polyag2 p=1.3 g=0.6

polyag2 p=1.3 g=0.5
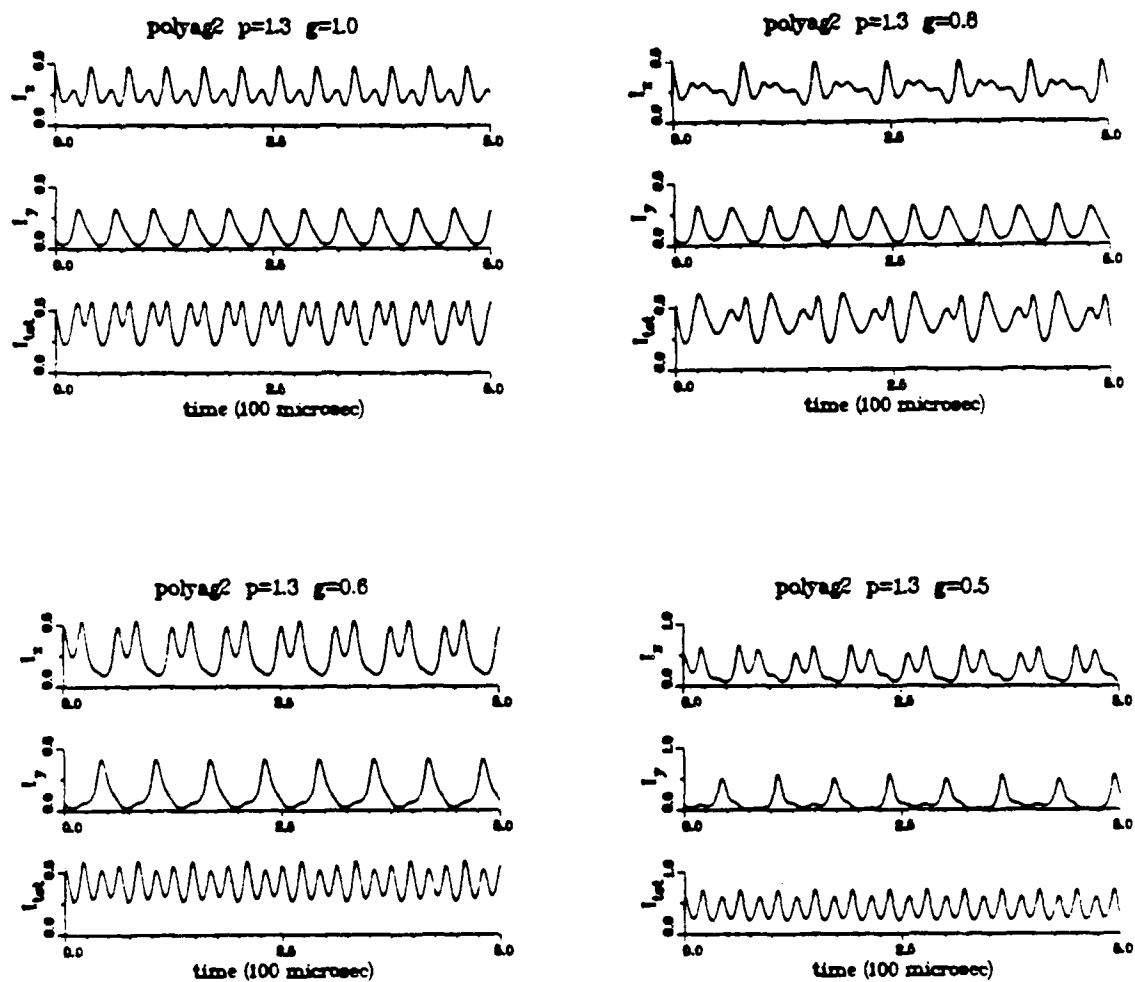
Fig. 3.18 (f) Intensity output for p=1.3.
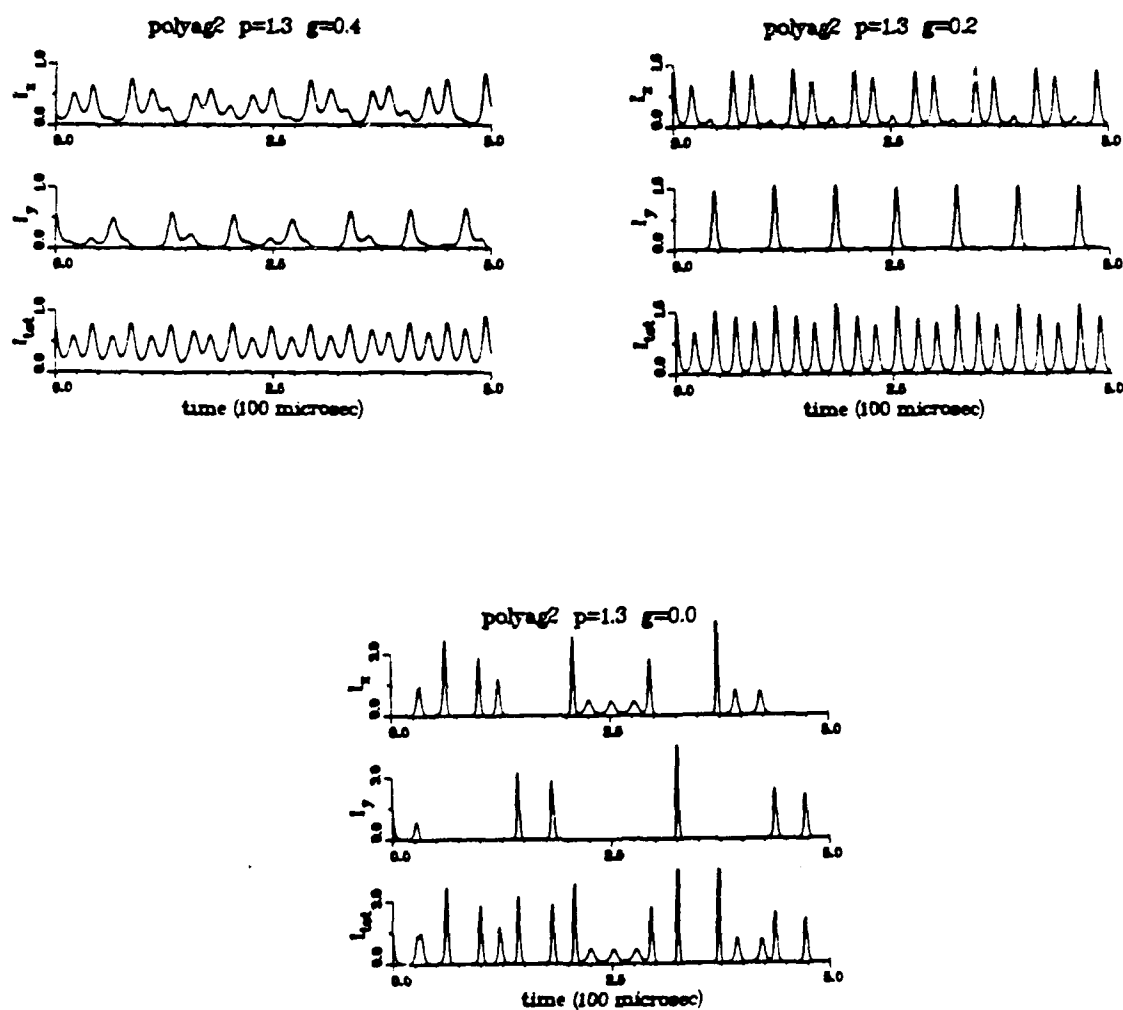
Fig. 3.18 (g) Intensity output for p=1.3, continued.
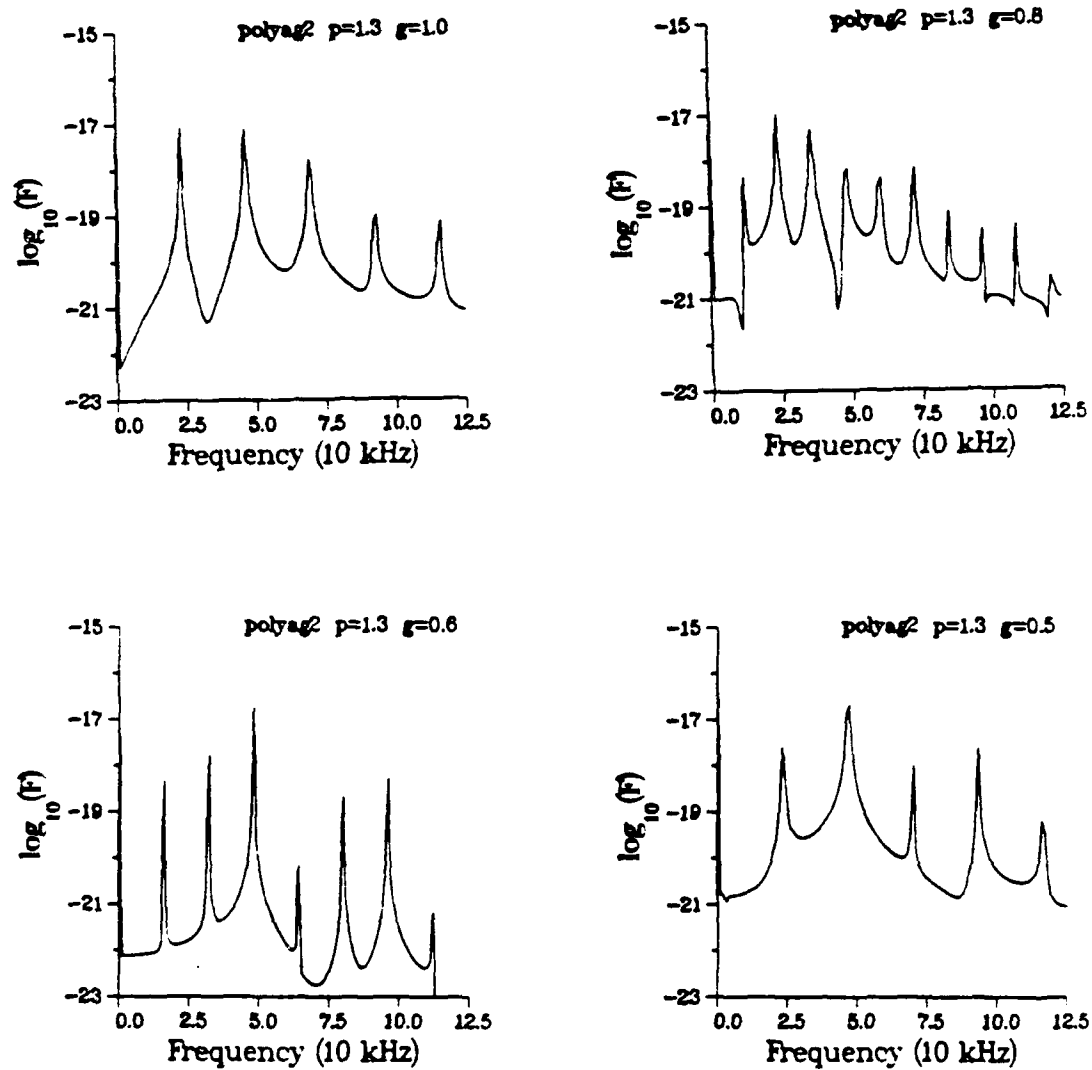
Fig. 3.18 (h) FFT's corresponding to (f).
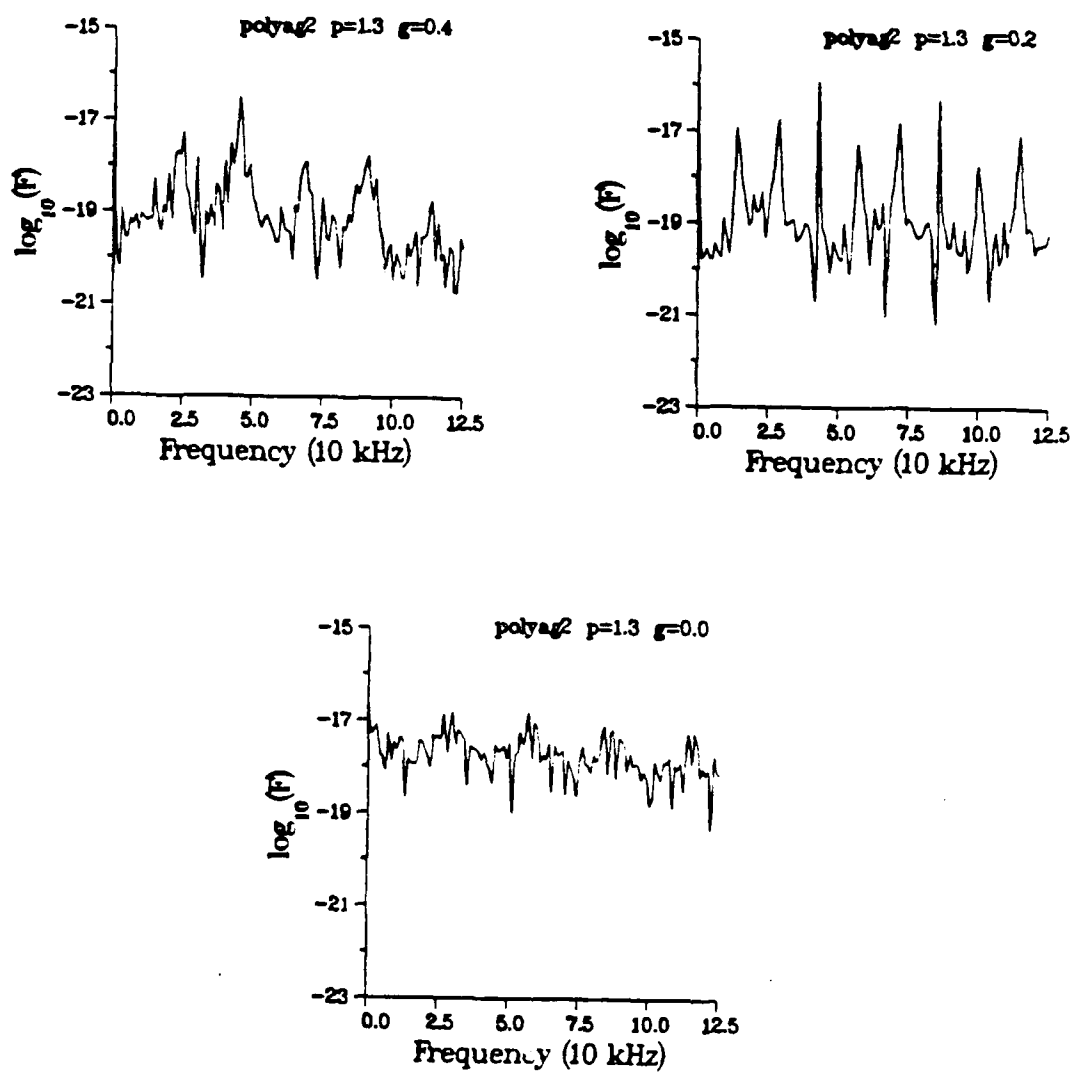
Fig. 3.18 (i) FFT's for the output in (g).
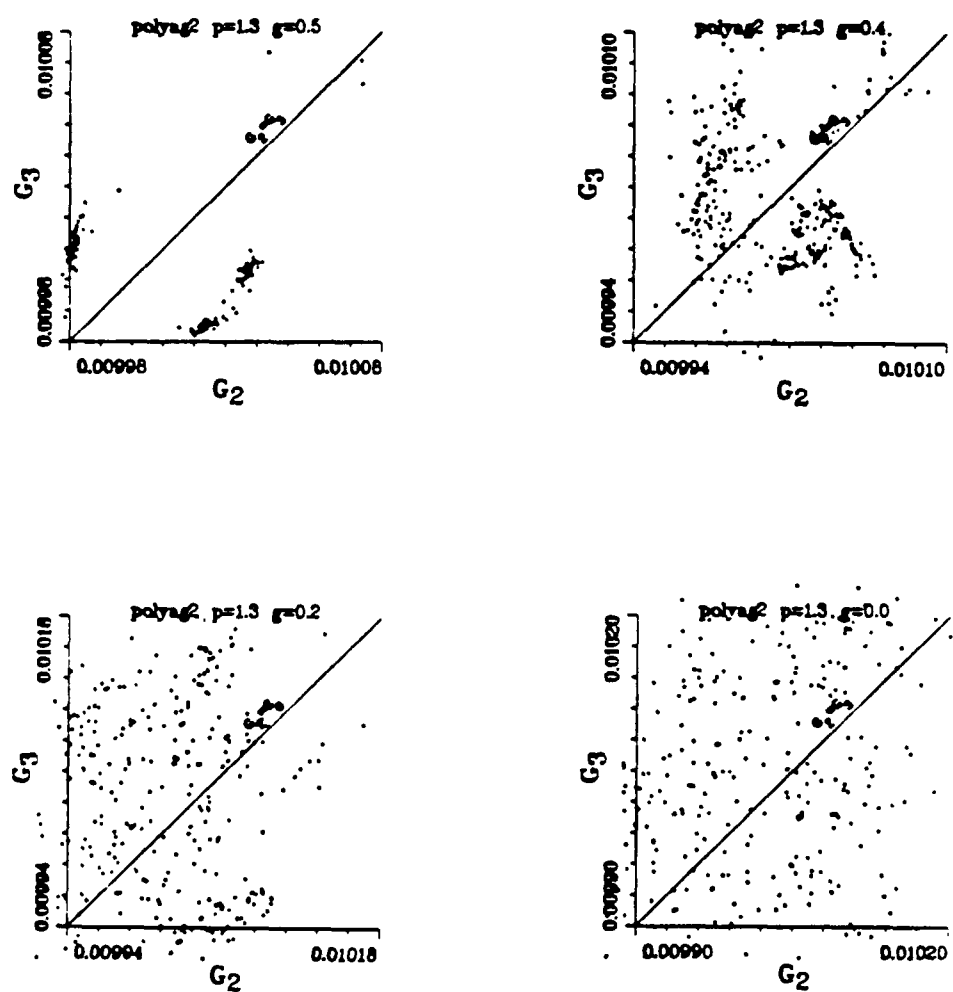
Fig. 3.18 (j) Poincaré maps corresponding to (f) and (g).
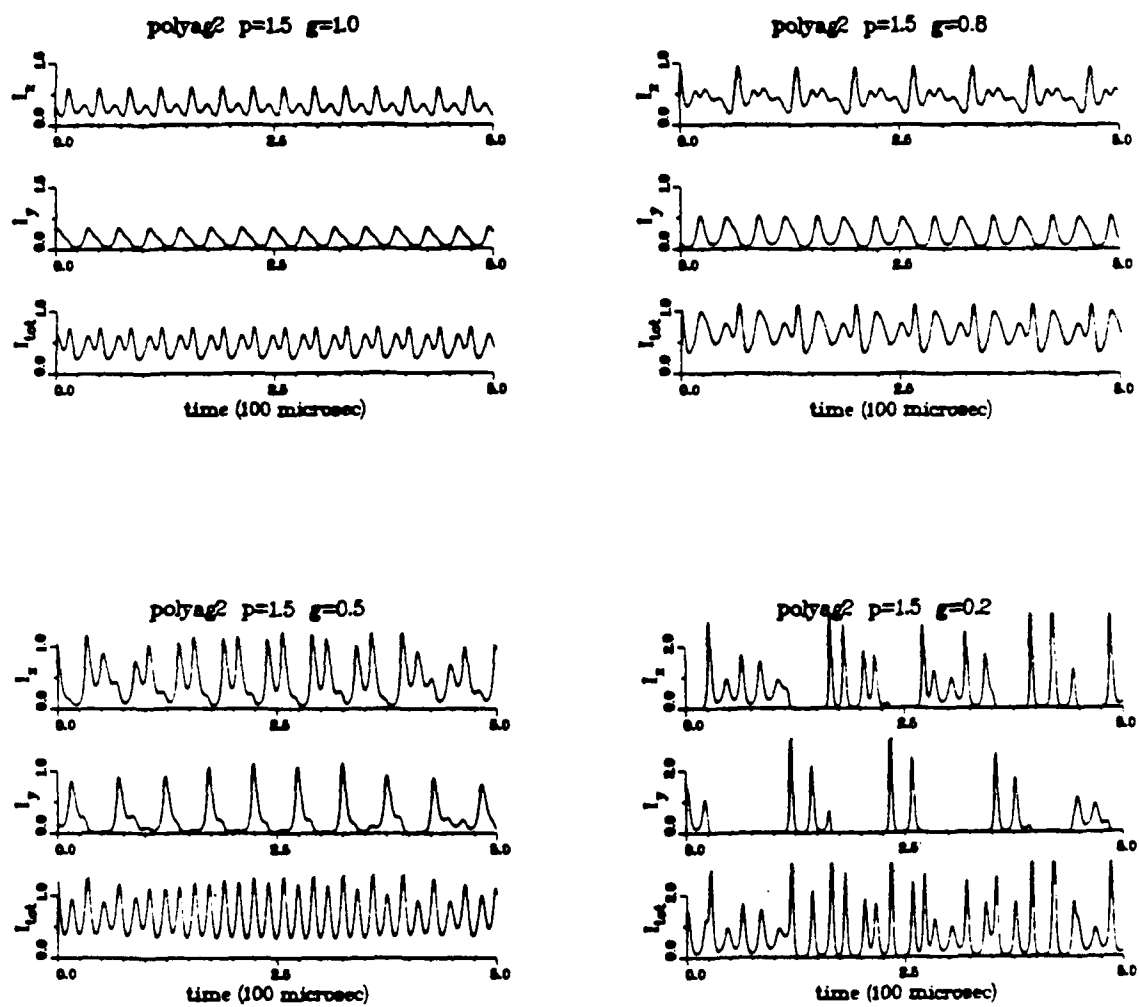
Fig. 3.18 (k) Intensity output for p=1.5.
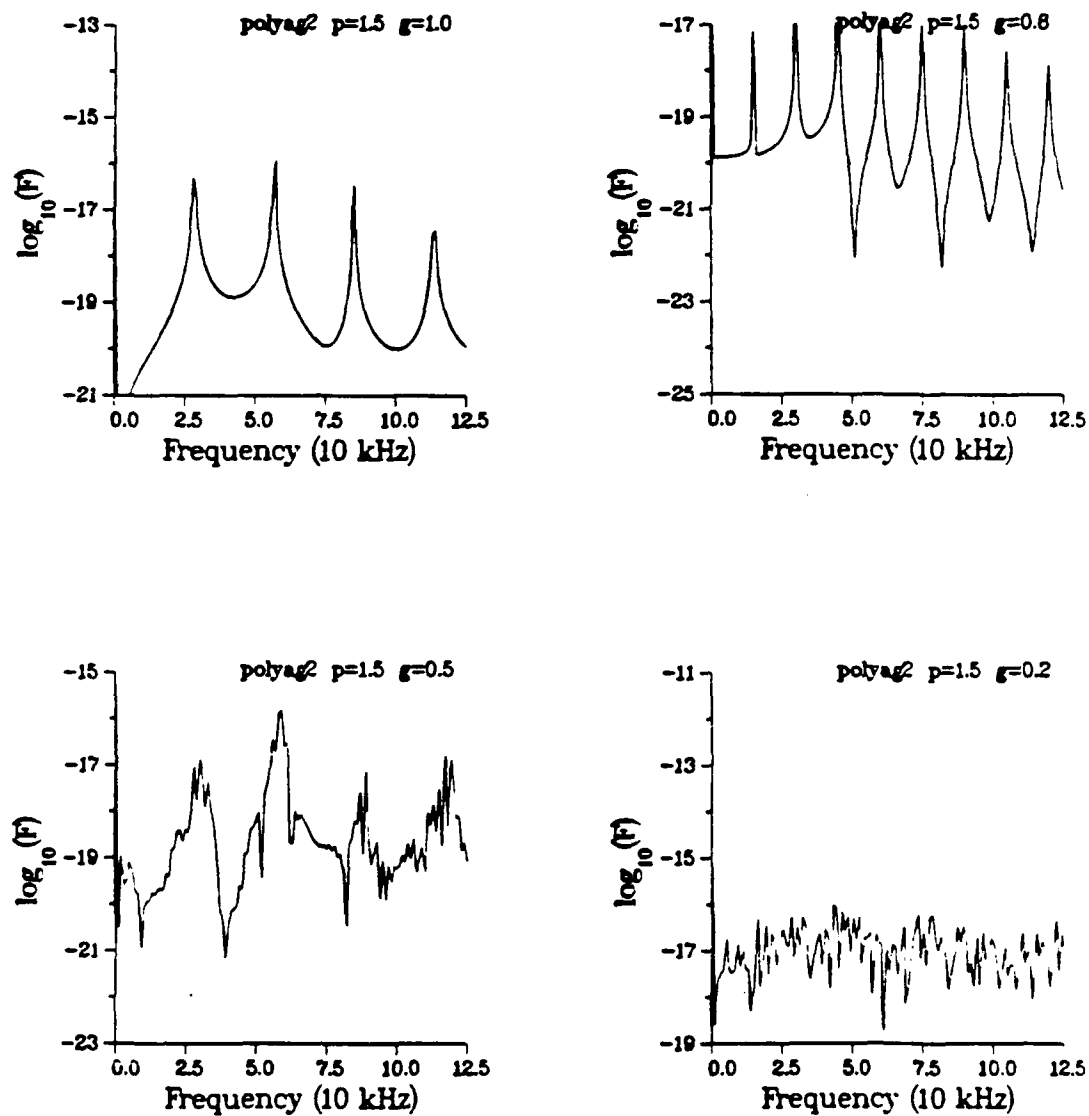
Fig. 3.18 (l) FFT's corresponding to (k).
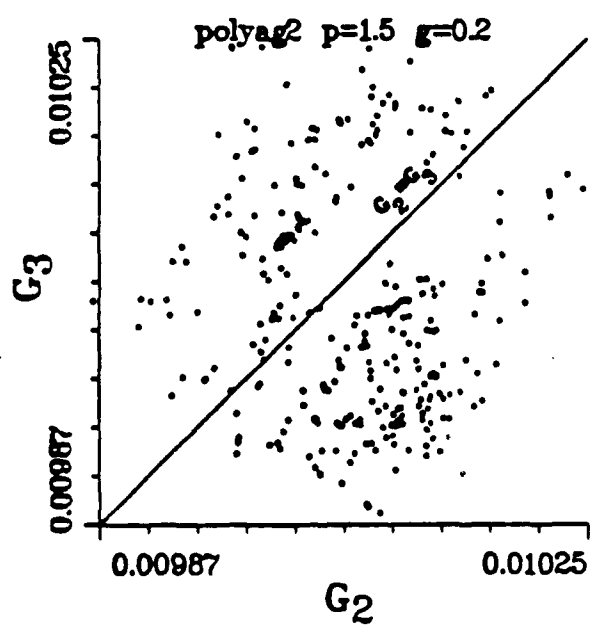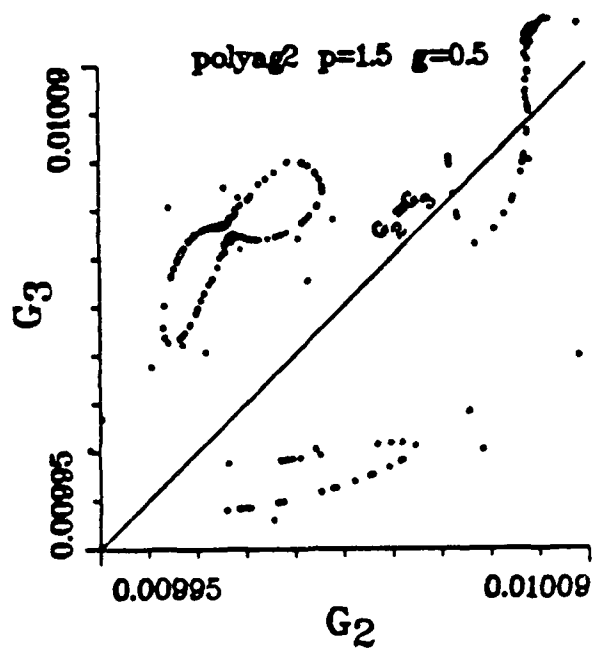
Fig. 3.18 (m) Poincaré maps for the output in (k).

polyag2 p=2.0 g=1.0

polyag2 p=2.0 g=0.8

polyag2 p=2.0 g=0.5

polyag2 p=2.0 g=0.2
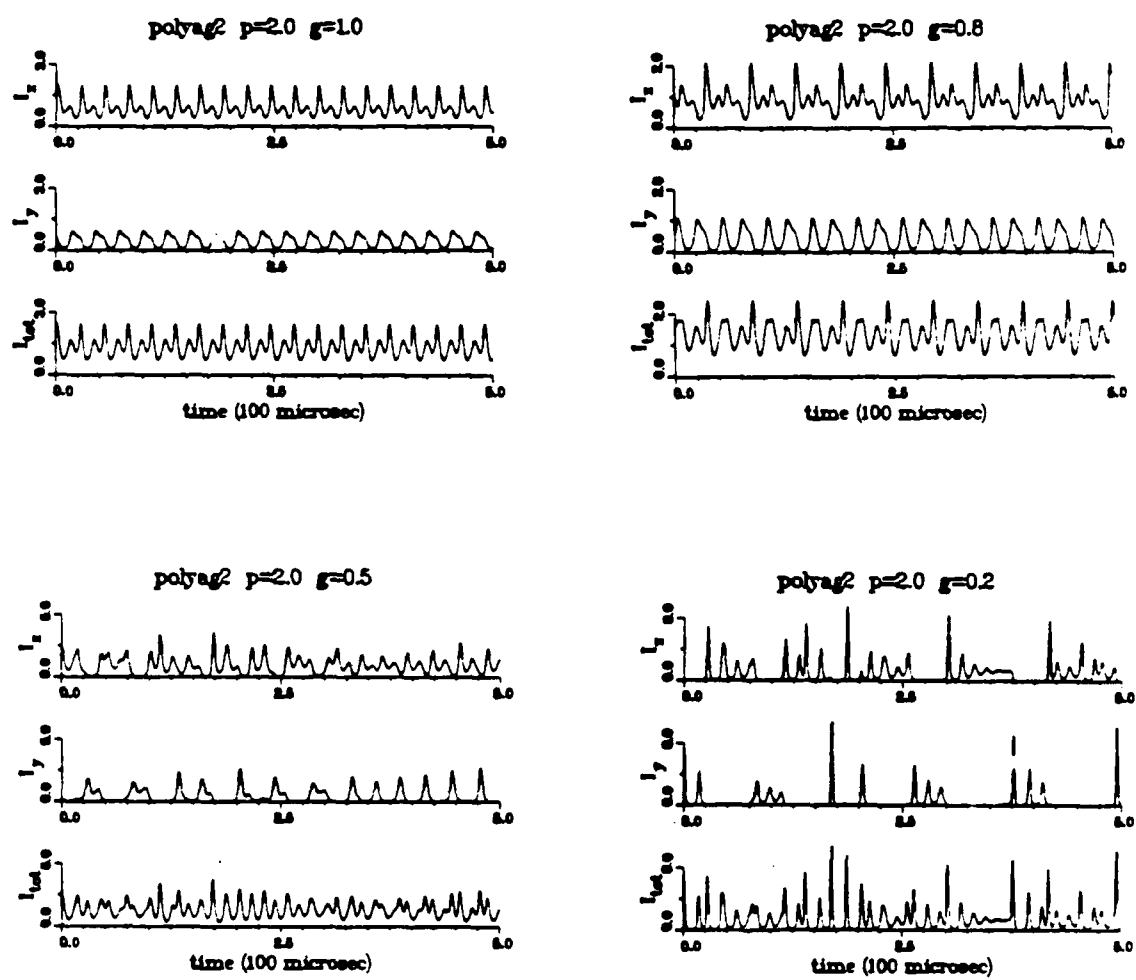
Fig. 3.18 (n) Intensity output for p=2.0.
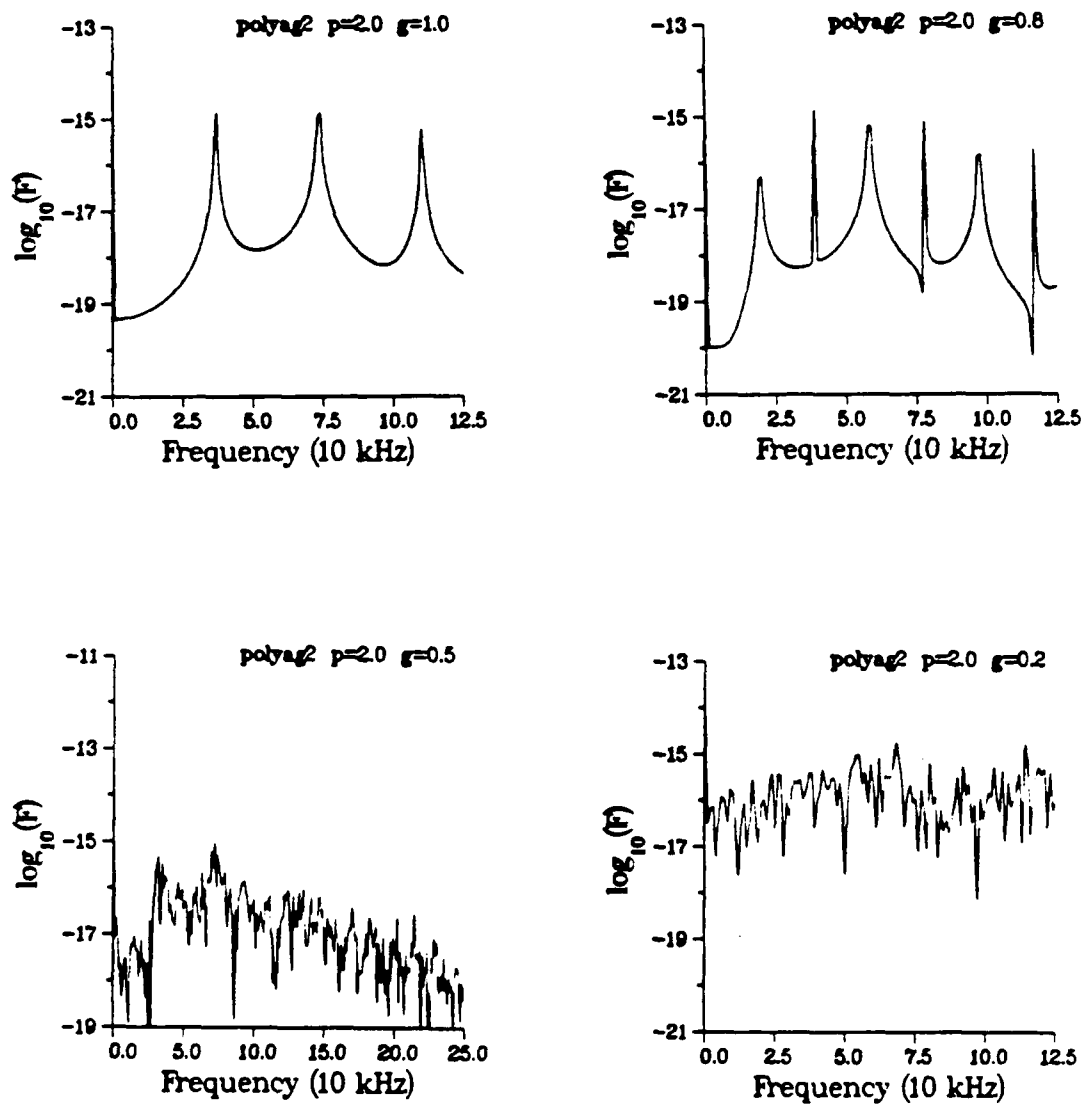
Fig. 3.18 (o) FFT's for the output in (n).
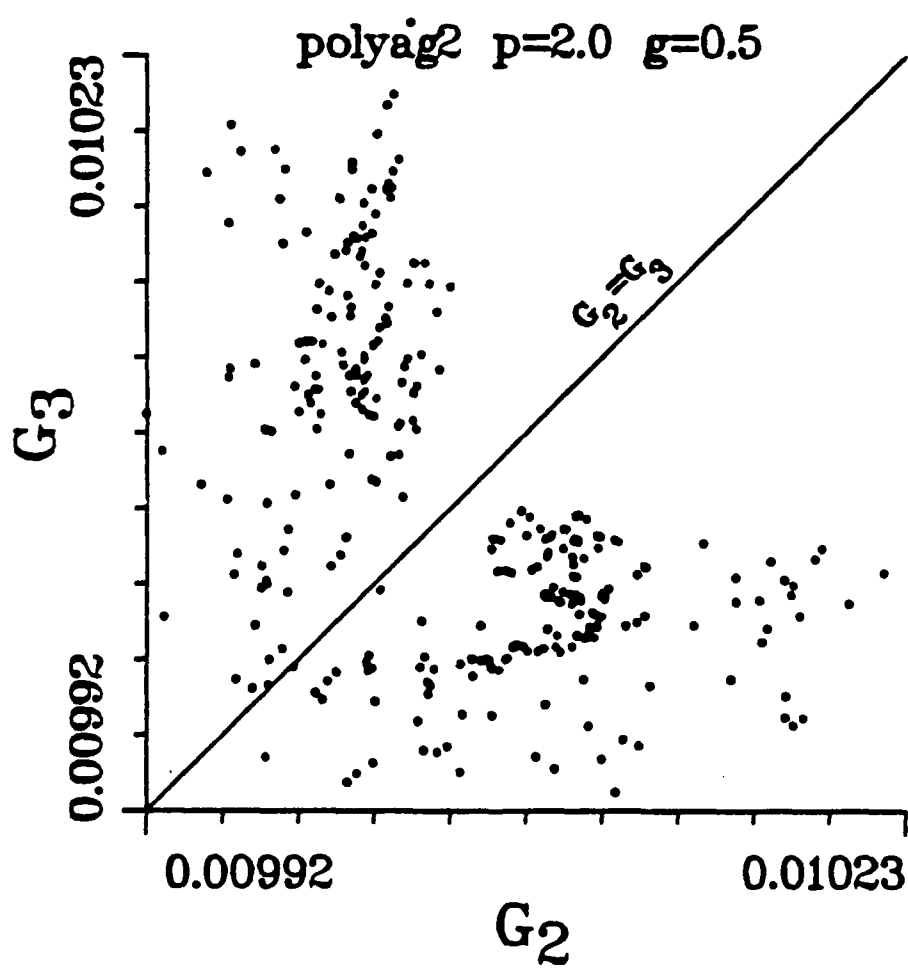
Fig. 3.18 (p) Poincaré map for p=2.0, g=0.5 showing chaotic output.

polyag2 p=3.0 g=1.0

polyag2 p=3.0 g=0.8

time (100 microsec)

time (100 microsec)

polyag2 p=3.0 g=0.5

time (100 microsec)
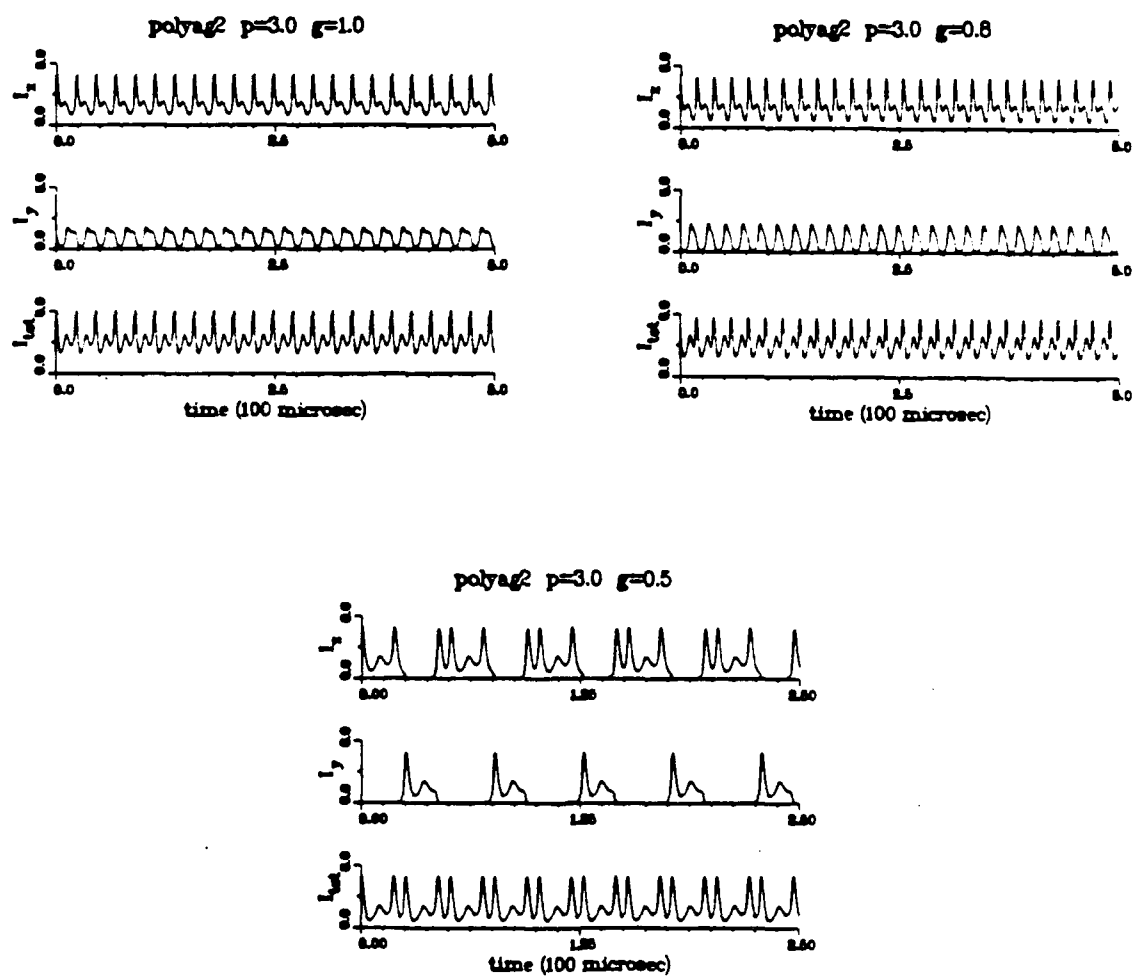
Fig. 3.18 (q) Intensity output for p=3.0.
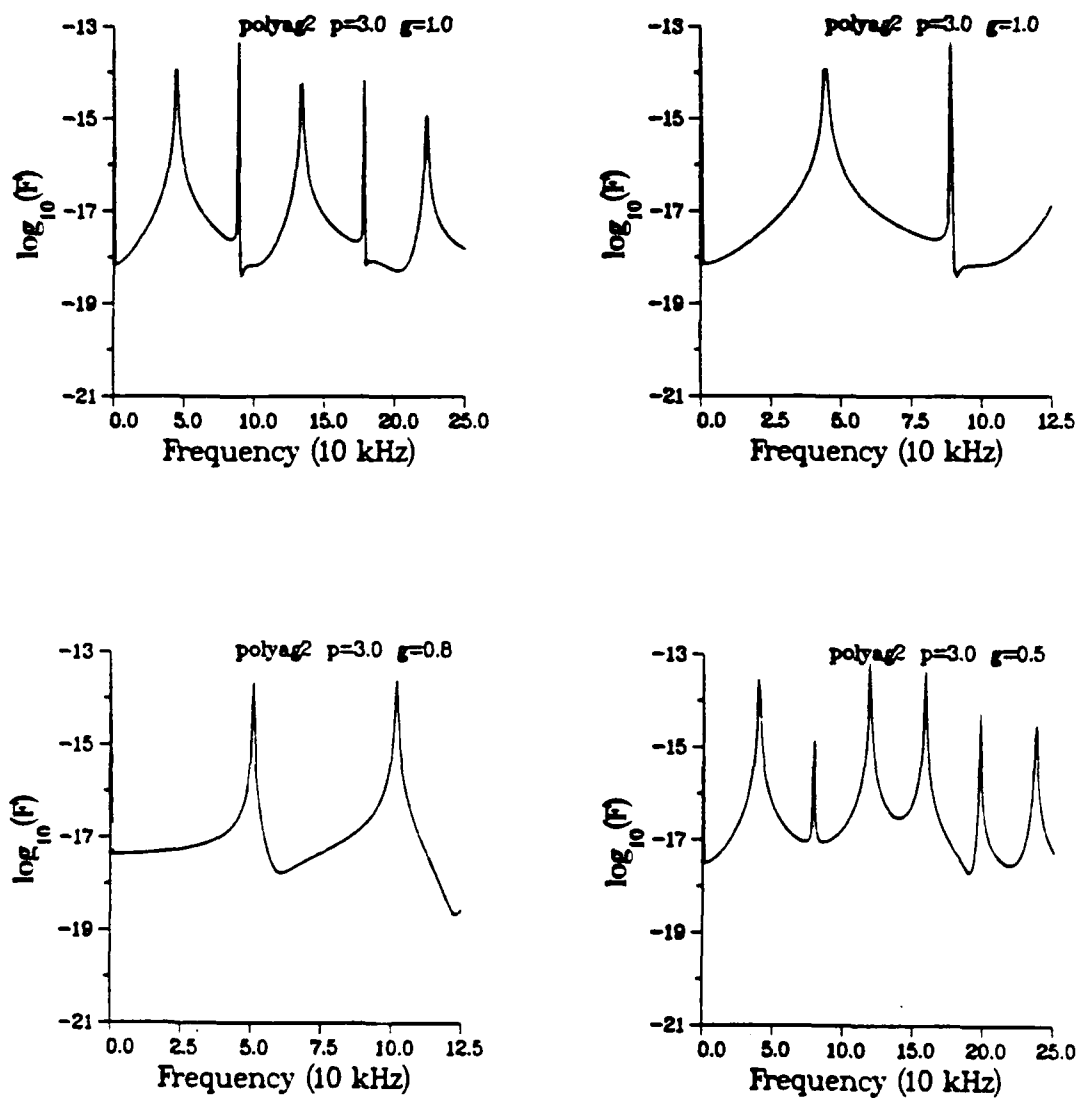
Fig. 3.18 (r) FFT's for the output in (q).
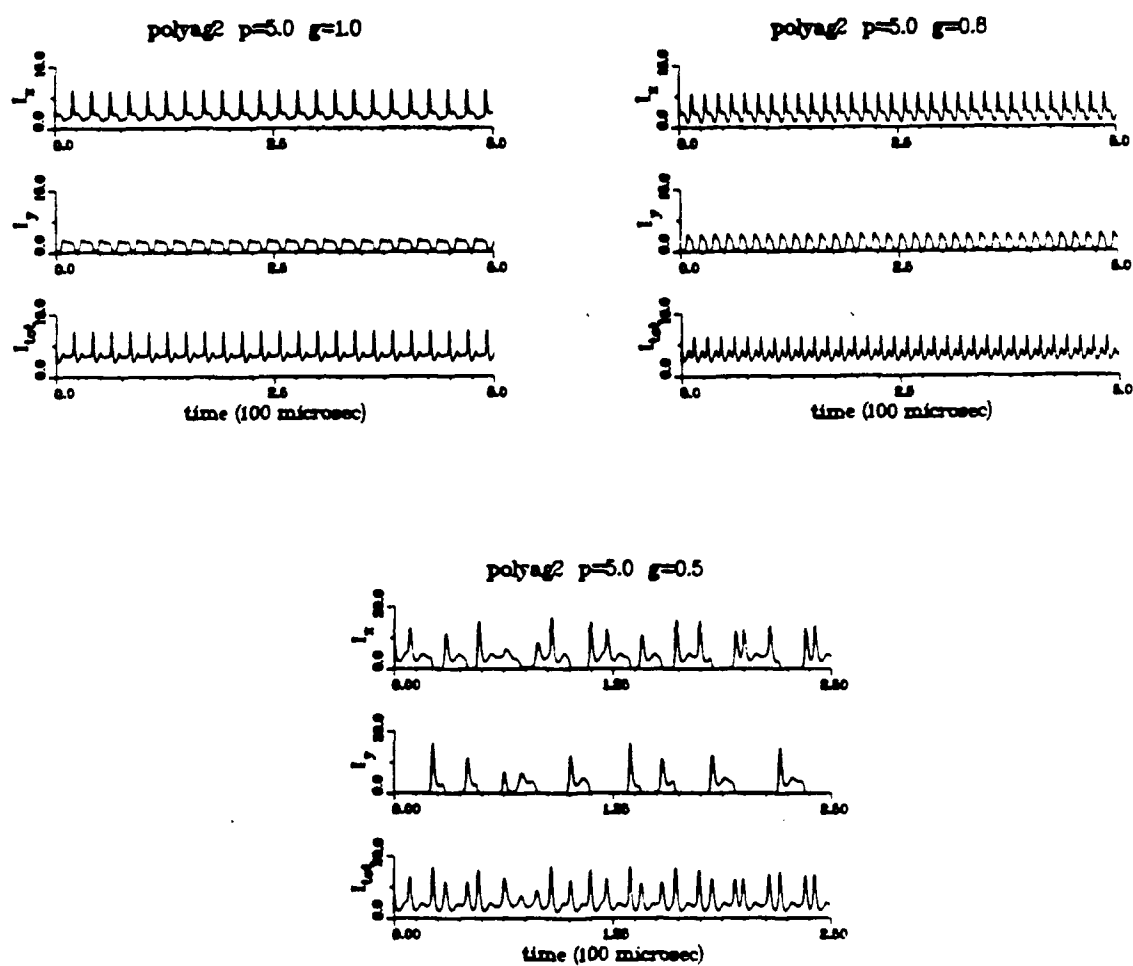
Fig. 3.18 (s) Intensity output for p=5.0.
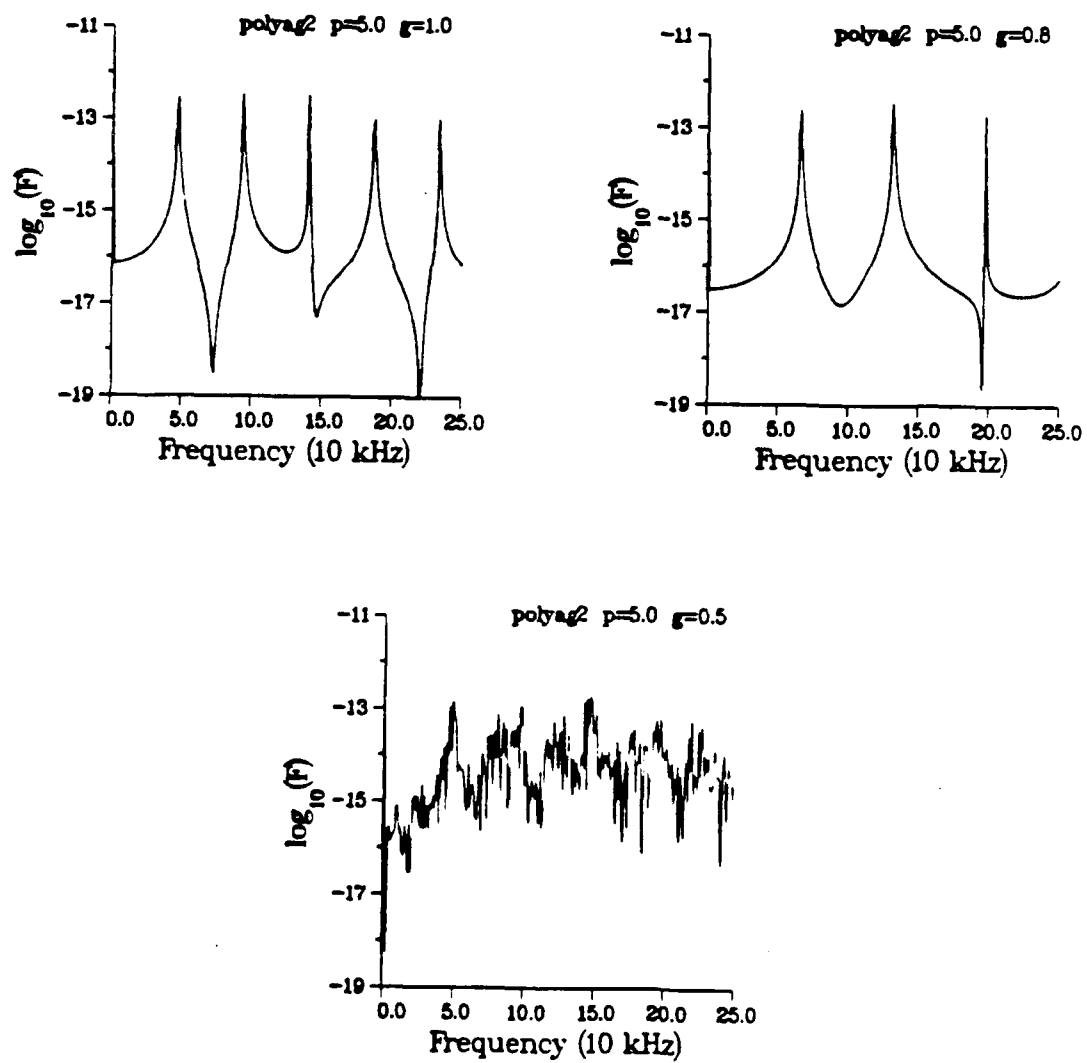
Fig. 3.18 (t) FFT's for the output in (s).
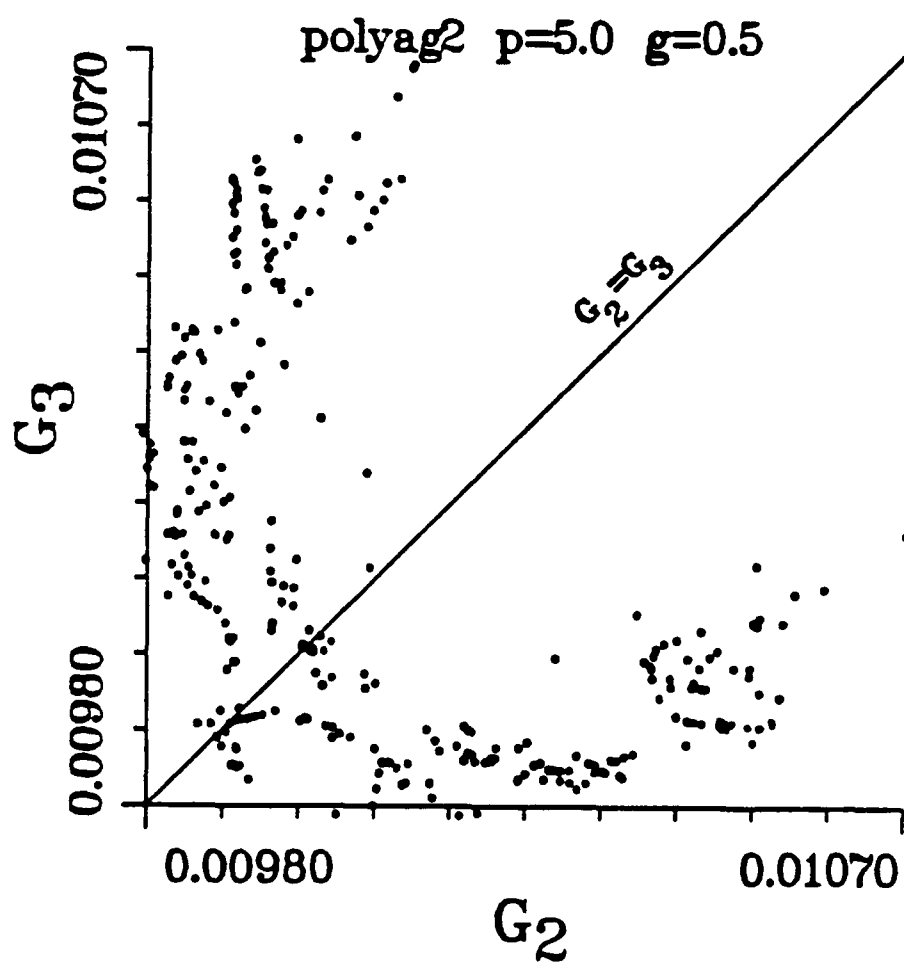
Fig. 3.18 (u) Poincaré map for p=5.0, g=0.5 showing chaotic output.

191
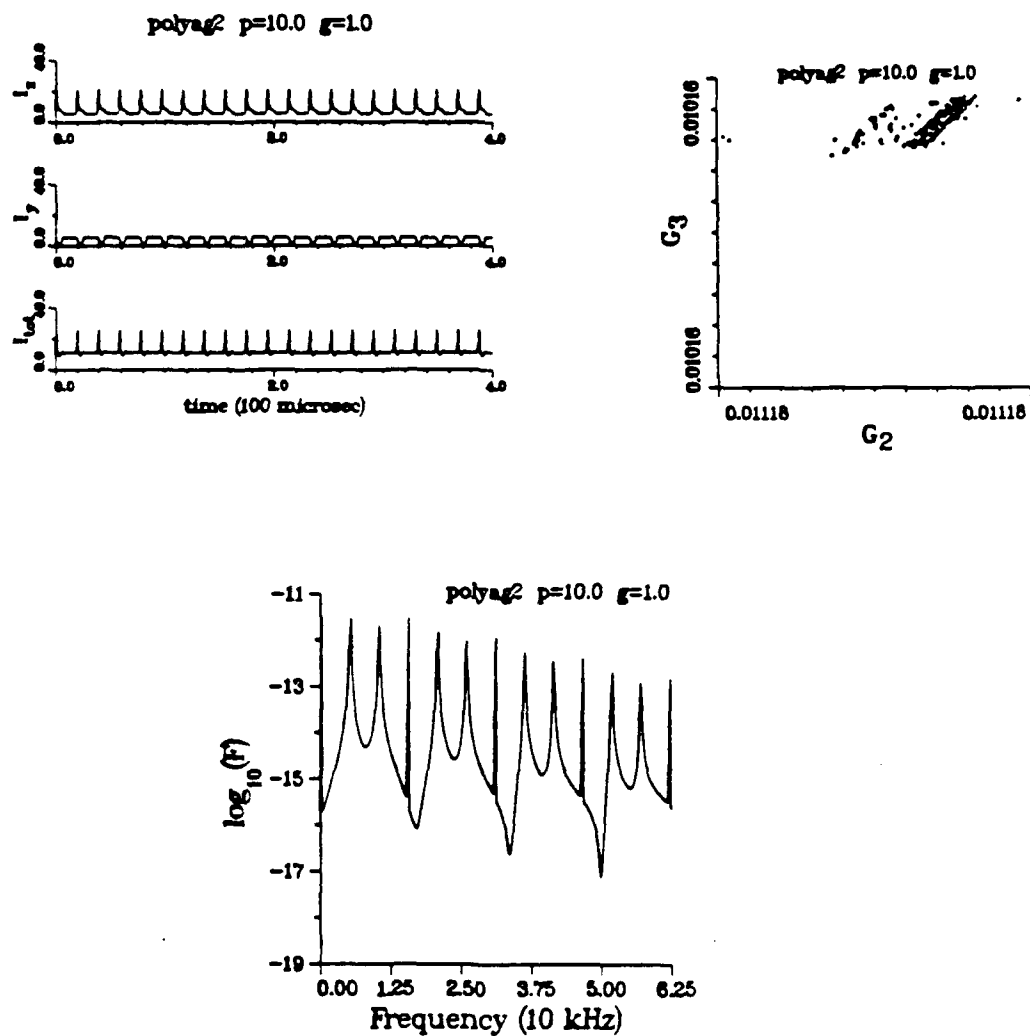
Fig. 3.18 (v) Output for p=10.0.

CHAPTER IV

VARIATIONS OF THE RATE EQUATIONS

Introduction

The round trip matrix approach initiated by Oka and Kubota (Oka and Kubota, 1988) is essential to the derivation of our new model for intracavity doubling presented in Chapter III. However, before we had completed that derivation, we investigated several possible changes in the rate equations, to see how the laser output progresses from the stable behavior for a quarter wave plate angle of $\pi/4$, to the chaotic output seen when the QWP angle is 0. This chapter explains two different sets of rate equations we developed in the course of our research.

The first set of equations is derived from the Maxwell-Bloch equations, a more fundamental set of physical relations than the rate equations used by Baer. The new equations we derive contain more information about the properties of the longitudinal modes and include new terms which describe couplings between gain variables. Numerical integration of this model exhibits certain qualities of experimentally observed intensities which have not been predicted by previous models. This new model will be the subject of further research.

A second set of rate equations is derived for a YAG laser with three energy levels instead of the two levels we have assumed thus far in the thesis. This idea was suggested to us by E. Arimondo who has had great success modeling the single-mode dynamics of

CO_2 lasers using a three-level model (De Tomasi, et al., 1989; Arimondo, et al., 1983, 1987, 1988; Arimondo, 1988; Hennequin, et al., 1988). Initial numerical tests of our equations indicate that, for the intracavity doubled Nd:YAG laser, the three-level model does not produce any new qualitative features of the intensity dynamics. This validates the two-level approximation for the intracavity doubled YAG.

The chapter concludes with a brief discussion of how the rate equations can be simply modified to study systems with modulated parameters. For example, there is substantial interest in studying the effects of a periodically modulated pump on intensity output. One can also investigate the influence of noise terms on the system of equations. The changes necessary in the differential equations to study these effects are outlined in the final section.

The issue in this chapter is not how to model the intracavity doubling, but how to derive appropriate multimode rate equations. To simplify the rate equations in this chapter, we collect all the doubling losses into a single variable D_j for each mode j. The complete forms for these doubling terms are the subject of Chapter III. While the new models discussed in this chapter are derived in full detail, the complete analysis of each model remains open as a topic for future research.

Derivation from Maxwell-Bloch Equations

General Derivation

The derivation in this section is largely taken from an appendix in a recent report on chaos in dye lasers (McMackin, et al., 1988). The article concerns multimode instabilities where some of the cavity-dependent parameters have significantly different values than

those of our Nd:YAG laser. However, many of the assumptions made in the McMackin article also apply to our problem. We retrace the exact steps followed by McMackin to get from the Maxwell-Bloch equations (see Appendix A for more details) to a coupled set of ordinary differential equations for longitudinal mode amplitudes and population inversions. From that point we depart from McMackin's development to introduce a new approach to removing the troublesome spatial dependence of these equations. The equations we get are similar to Baer's rate equations (Baer, 1986), but they present a different treatment of the population inversions and carry more information about the individual modes.

As in the McMackin article, we assume the Nd:YAG laser is a system with two energy levels, with an energy difference between the two levels of $\hbar \bar{\omega}$ (For the values of these and other constants and parameters in this chapter, see Appendix B.) We define $S(z,t)$ as the atomic polarization, or dipole coherence, of the active medium, and define $W(z,t)$ as the population inversion, expressed as a difference in the probability of an ion (Nd^{3+}) being in the upper state, minus the probability of being in the lower state. The spatial dependence of these variables is along the length of the optical axis in the cavity, indicated by the z-axis (see Fig. D.1). The variables S and W describe properties of the active medium, so S and W are non-zero only over the length δz of the YAG crystal which we define for $z \in (z_1, z_1 + \delta z)$. In our experiment, where the input mirror is deposited on one end of the YAG crystal, we have $z_1 = 0$.

The time dependence of S and W are governed by the Maxwell-Bloch equations of motion:

$$\frac{d}{dt} S(z,t) = -\rho S(z,t) - \frac{id}{\hbar} E(z,t) W(z,t) \qquad 4.1.a$$

$$\frac{d}{dt} W(z,t) = -\Gamma (W(z,t) - W_0) + \frac{id}{2\hbar} S^*(z,t) E(z,t) - \frac{id}{2\hbar} S(z,t) E^*(z,t) . \qquad 4.1.b$$

The parameter ρ is the dipole dephasing rate, the decay rate of the polarization; and d is the transition dipole moment, a scaled value of the (square root of) the upper state lifetime Γ. The parameter W_0 represents an equilibrium value for $W(z,t)$ when there is no lasing; a way to determine W_0 will be presented shortly.

The complex electric field $E(z,t)$ must also obey the wave equation

$$\left[\frac{\partial^2}{\partial z^2} - \frac{1}{c^2} \frac{\partial^2}{\partial t^2} \right] E(z,t)\, e^{-i\bar{\omega}t} = \frac{\partial^2}{\partial t^2} \frac{N_0}{c^2 \varepsilon_0}\, d\, S(z,t)\, e^{-i\bar{\omega}t} \qquad 4.2$$

In (4.2), c is the speed of light, and N_0 is the number density of active molecules in the gain medium. We take Dirichlet (E = 0) boundary conditions at both ends of the cavity, and separate variables by expanding $E(z,t)$ in terms of Fourier components $u_l(z)$ whose coefficients are the field amplitudes of the longitudinal cavity modes:

$$E(z,t) = \sum_l A_l(t)\, u_l(z)\, e^{-i\Delta_l t} \qquad , l = 0, \pm 1, \pm 2, \ldots \qquad 4.3$$

where $A_l(t)$ is the amplitude of the lth longitudinal mode; $\Delta_l = \omega_l - \bar{\omega} = l\Delta$; $\Delta = \pi c/L$, and $u_l(z) = \sin(k_l z)$ are the mode functions for a standing wave cavity, where $k_l = \omega_l/c$.

The first step is to substitute the expansion in (4.3) into the wave equation and calculate the time derivative of the individual mode amplitudes. When we carry out the substitution, apply the time derivatives, and integrate with spatial mode $u_l(z)$, we get:

$$\frac{L}{2}\left[-A_l'' + 2i\,\omega_l A_l'(t) \right] = \frac{N_0\, d\, e^{i\Delta_l t}}{\varepsilon_0} \int_{\pi_l}^{\pi_l + \Delta_l} u_l(z)\left[S'' - 2i\,\bar{\omega}\, S' - \bar{\omega}^2 S \right] dz$$

$$\ldots\ 4.4$$

where the primes (') indicate time derivatives. The reduction to (4.4) used only the orthogonality of the spatial modes $u_l(z)$. The equation can be simplified further by making several assumptions about the relative time scales in the equation :

$$A_l'' \ll \overline{\omega} A_l' \qquad \Delta_l \ll \overline{\omega} \qquad S' \ll \overline{\omega} .$$

When we neglect the small terms, the differential equation for the field amplitude becomes

$$\frac{d}{dt} A_l(t) = i \overline{\omega} N_o d e^{i\Delta_l t} \frac{1}{\varepsilon_o L} \int_{z_l}^{z_l + \delta z} u_l(z) S(z,t) dz \qquad 4.5$$

In a Class B laser like the Nd:YAG, the dipole dephasing rate ρ is much faster than any of the other time scales, so the value of $S(z,t)$ is essentially instantaneously determined by the other variables. We adiabatically eliminate the polarization $S(z,t)$ by setting the derivative in (4.1.a) to zero:

$$S(z,t) \approx \frac{- i d E(z,t) W(z,t)}{\hbar \rho} . \qquad 4.6$$

We now combine (4.1), (4.5), and (4.6) to produce the coupled nonlinear ordinary differential equations for the mode amplitudes and inversion:

$$\frac{d}{dt} A_l(t) = -\Gamma_l A_l(t) + \tilde{b} \sum_n A_n(t) e^{i\Delta_{nl}t} \int_{z_l}^{z_l+\delta_l} W(z,t) \, u_n(z) \, u_l(z) \, dz \qquad 4.7.a$$

$$\frac{d}{dt} W(z,t) = -\Gamma (W(z,t) - W_o) - \tilde{a} \, W(z,t) \sum_{m,n} A_m(t) A_n^*(t) \, u_m(z) \, u_n(z) e^{i\Delta_{mn}t} \qquad 4.7.b$$

where Γ_l is the cavity loss experienced by the lth mode, $\Delta_{nl} = (n - l)/\Delta$, and

$$\tilde{a} = \frac{d^2}{\rho \hbar^2} \qquad\qquad \tilde{b} = \frac{N_o \, \bar{\omega} \, d^2}{\epsilon_o \, \hbar \, L \, \rho} \, . \qquad 4.8$$

The equilibrium inversion W_o is defined below in the section on the single-mode model.

The spatial dependence in (4.7) makes the equations difficult to solve even numerically. To simplify the problem, we would like to avoid the discretization of space necessary to account for the spatial dependence of the inversion. Still another difficulty is the presence of the time-dependent exponential terms which renders (4.7) non-autonomous. We address these problems in the following developments of specific models for the cases of one, two, and three longitudinal modes.

Single-Mode Model

The application of (4.7) to the single-mode case accomplishes two goals. The first is to determine how the parameter W_o relates to the threshold for lasing. In particular, W_o will be scaled to correspond to the pumping parameter of our previous rate equations (2.24 and 3.25). The second goal is to outline our approach for dealing with the spatial

dependence of the inversion. The same approach will be used in the two- and three-mode cases.

For only one mode, (4.7) becomes

$$\frac{d}{dt} A_1(t) = -\Gamma_1 A_1(t) + \tilde{b} A_1(t) \int_{z_1}^{z_1 + \Delta z} W(z,t) u_1^2(z) \, dz \qquad 4.9.a$$

$$\frac{d}{dt} W(z,t) = -\Gamma (W(z,t) - W_o) - \tilde{a} W(z,t) |A_1(t)|^2 u_1^2(z) \qquad 4.9.b$$

Recall that $u_1(z) = \sin(k_1 z)$, and that the spatial integral is over the length of the YAG crystal. Our first simplification is to define a new variable:

$$\overline{W}(t) = \frac{1}{L} \int_{z_1}^{z_1 + \Delta z} W(z,t) \, dz \qquad 4.10$$

The new variable $\overline{W}(t)$ simply represents a spatial average of the population inversion over the length of the active medium. If we now integrate (4.9.b) over the entire cavity length L, we get

$$\frac{d}{dt} \overline{W}(t) = \Gamma W_o - \Gamma \overline{W} - \frac{\tilde{a}}{L} |A_1(t)|^2 \int_{z_1}^{z_1 + \Delta z} W(z,t) u_1^2(z) \, dz \quad . \qquad 4.11$$

The right side of (4.11) still has spatial dependencies to be integrated, but we see that the same integral appears in the mode equation (4.9.a). We next calculate a reasonable approximation for this integral in terms of $\overline{W}(t)$ by applying a simple identity to the u_1^2 term,

$$\int_{z_1}^{z_1+dz} W(z,t)\,\sin^2(k_1 z)\,dz \;=\; \int_{z_1}^{z_1+dz} W(z,t)\,[1 - \cos(2k_1 z)]\,dz \qquad 4.12$$

and neglect the fast oscillations of the high-frequency cosine term, to arrive at the approximation:

$$\int_{z_1}^{z_1+dz} W(z,t)\,\sin^2(k_1 z)\,dz \;\cong\; \frac{1}{2}\int_{z_1}^{z_1+dz} W\,dz \;=\; \frac{L}{2}\,\overline{W}\;. \qquad 4.13$$

The single mode equations, in this 0th order approximation, are now

$$\dot{A} = -\Gamma_1\,A + b\,A\,\overline{W} \qquad\qquad 4.14.a$$

$$\dot{\overline{W}} = \Gamma\,W_0 - \overline{W}\,(\Gamma + a\,|A|^2\,) \qquad\qquad 4.14.b$$

where $a = \tilde{a}/2$, and $b = \tilde{b}L/2$. We now let $I = |A|^2$, so (4.14) becomes a scaled version of Baer's single-mode rate equations (2.1):

$$\dot{I} = 2\,I\,(b\overline{W} - \Gamma_1) \qquad\qquad 4.15.a$$

$$\dot{\overline{W}} = \Gamma\,W_0 - \overline{W}\,(\Gamma + a\,I\,)\;. \qquad\qquad 4.15.b$$

We determine the parameter W_0 by examining the equilibrium values for I and $\overline{W}$. The steady state value for $\overline{W}$, $\overline{W}_s = \Gamma_1/b$, is independent of the equilibrium intensity. The steady state intensity I_s, on the other hand, depends on W_0 and $\overline{W}_s$:

$$I_s = \frac{\Gamma}{a\overline{W}_s} (W_0 - \overline{W}_s)$$

4.16

So there is a positive, physically attainable intensity only if W_0 is greater than the threshold quantity Γ_1/b, and we define W_0 to reflect its relationship to the pump strength, as follows. Let p be the percentage above threshold at which the laser is being pumped. Then let $W_0 = (1 + p) \Gamma_1 / b$. The parameter W_0 now represents the pump strength, relative to threshold, in terms of fundamental cavity parameters.

At this point, we could also add the effect of intracavity doubling to (4.15). We simply treat the doubling process as a loss for the intensity, which oscillates at the fundamental frequency, and include the additional loss term in the intensity equation (4.15.a). We know from previous chapters that the correct loss term in the single-mode equation is $- \varepsilon I^2$; but to keep the focus of this chapter on the new rate equations, we insert the doubling losses with a general time-dependent term D_1, so that (4.15.a) becomes:

$$\dot{I} = 2 I (b\overline{W} - \Gamma_1 - D_1)$$

4.17

We note that the fast exponential contributions to the doubling terms are averaged out in (3.14) and (3.16), so the phases of the doubling process do not appear in the field amplitude equations.

The single-mode equations in this form correspond exactly to those used by Baer (2.1). As discussed in Chapter II, the only single-mode dynamics observed in the laser are transients which lead to steady state intensity output. The truncation of (4.9) at the 0th order exhibits such behavior, so this truncation is adequately justified. Higher order truncation will be necessary in the multimode equations.

Two-Mode Model

In this section we simplify (4.7) to model a standing wave laser with two longitudinal modes. We used subscripts 1 and 2 in previous chapters to identify two different modes. In this new model the subscripts carry more meaning: the absolute difference in subscripts |m-n| tells how many cavity mode spacings separate the two modes. This spacing directly affects the degree of spatial overlap and explicitly appears in the new two-mode equations.

To clarify some of the longer equations which follow, we shorten the notation of integration over the YAG crystal to be simply $\int_{\delta z}$. Also recall that our cavity has its input mirror deposited on the surface of the YAG, so the lower limit of integration, z_1, equals zero. This is not the case for all intracavity doubled YAG lasers, but we point out in the development where any changes need to be made for cavities where $z_1 \neq 0$.

Let the integer indices m and n (m≠n) denote two longitudinal modes. The two-mode version of (4.7) gives the following equations for the electric field amplitudes A_m and A_n and the inversion W:

$$\dot{A}_m = -\Gamma_m A_m + \tilde{b}\left[A_m \int_{\delta z} W u_m^2 dz + A_n e^{-i\Delta_{mn}t}\int_{\delta z} W u_m u_n\, dz \right] \qquad 4.18.a$$

$$\dot{A}_n = -\Gamma_n A_n + \tilde{b}\left[A_m e^{i\Delta_{mn}t}\int_{\delta z} W u_m u_n\, dz + A_n \int_{\delta z} W u_n^2 dz \right] \qquad 4.18.b$$

$$\dot{W} = -\Gamma(W - W_o) - \tilde{a}\,W\left[|A_m|^2\,u_m^2 + |A_n|^2\,u_n^2 + A_m\,A_n^*\,u_m\,u_n\,e^{i\Delta_{nm}t} + A_m^*\,A_n\,u_m\,u_n\,e^{-i\Delta_{nm}t}\right]$$

$$\ldots \quad 4.18.c$$

Recall that W depends on both space (z) and time in (4.18).

This is the first time in our analysis where we encounter a non-autonomous system of equations. The nonlinear couplings between the modes include terms with exponential factors that oscillate at a frequency of order Δ, which is extremely fast in our system, on the order of 10 GHz (see Appendix B). For the moment, we assume that these fast oscillations average to zero and we ignore these terms during the reduction of (4.18). After we arrive at a reasonable approximation to (4.18) which is independent of z, we will return to the issue of how to justify this averaging.

Under the assumption that the exponential terms in (4.18) average to zero, the system is autonomous. We again introduce the averaged inversion $\overline{W}$ defined in (4.10). Like in the single mode case (4.11), the differential equation for $\overline{W}$ contains spatial integrals:

$$\dot{\overline{W}} = -\Gamma(\overline{W} - W_o) - \tilde{a}\left[A_m\int_{\mathstrut} Wu_m^2 dz + A_n\int_{\mathstrut} Wu_n^2\,dz\right]; \qquad 4.19$$

We would like to approximate these integrals, in addition to those in (4.18.a and b), in order to eliminate the spatial dependence of the equations. Our first attempt was to approximate the integrals in terms of $\overline{W}$ and constant terms, and truncate the equations at this 0th order approximation. Numerical integration of the resulting equations (including

the frequency doubling terms) only produced solutions which converged to a stable steady state, for all initial conditions and all parameter settings we attempted. These results were not consistent with Baer's observations of a two-mode laser, so we continued the hierarchy of equations by defining new variables:

$$W_{ij} = \frac{1}{L} \int_{\Delta} W\, u_i\, u_j\, dz \ ,$$

4.20

where i and j take on values in the set of indices of the oscillating E-fields. This definition simplifies (4.18):

$$A_m = -\Gamma_m\, A_m + 6\, A_m\, W_{mm}$$

4.21.a

$$A_n = -\Gamma_n\, A_n + 6\, A_n\, W_{nn}$$

4.21.b

$$\dot{W} = -\Gamma\, (W - W_0) - \bar{a}\, [\, I_m\, W_{mm} + I_n\, W_{nn}\,] \ .$$

4.21.c

However, we still need to simplify the differential equations for W_{mm} and W_{nn}, which both have the form:

$$\dot{W}_{mm} = -\Gamma\, (W_{mm} - \tfrac{1}{2} W_0) - \frac{\tilde{a}}{L} \left[\, I_m^2 \int_{\Delta} W\, u_m^4\, dz + I_n^2 \int_{\Delta} W\, u_m^2\, u_n^2\, dz \right] .$$

4.22

The derivative (4.22) is found by multiplying (4.18.c) by u_m^2 and integrating.

For the integrals that have fourth order integrands, we need approximations in terms of the lower order variables W, W_{mm}, and W_{nn}. Expanding the second integral in (4.22), we see the different frequencies of the contributing terms:

$$\int_{\delta z} W\, u_m^2\, u_n^2\, dz \;=\; \int_{\delta z} W \sin^2(k_m z)\, \sin^2(k_n z)\, dz$$

$$= \; \frac{1}{4}\int_{\delta z} W\, dz \;+\; \frac{1}{8}\int_{\delta z} W \cos[2(k_m+k_n)z]\, dz \;-\; \frac{1}{4}\int_{\delta z} W \cos[2k_m z]\, dz$$

$$- \; \frac{1}{4}\int_{\delta z} W \cos[2k_m z]\, dz \;+\; \frac{1}{8}\int_{\delta z} W \cos[2(k_m-k_n)z]\, dz \;. \qquad 4.23$$

We assume the magnitude of the second integral is negligible, since $\cos[2(k_m+k_n)z]$ oscillates much faster than any other term. We also note that the first, third and fourth integrals are simply W, W_{mm}, and W_{nn}. Our final assumption is that the $\cos[2(k_m-k_n)z]$ oscillation in the last integrand is slow enough that we can factor it out of the integral as its average value from 0 to δz, i.e. we take:

$$\int_{\delta z} W \cos[2(k_m-k_n)z]\, dz \;\approx\; q_{mn} \int_{\delta z} W\, dz\;,$$

$$4.24$$

$$q_{mn} \;\equiv\; \frac{1}{2}\Big[1 + \cos[2(k_m-k_n)\delta z]\Big]\;.$$

When $|\,m-n\,| = 1$, $q_{mn} \approx 0.9$, and for $|\,m-n\,| = 2$, $q_{mn} \approx 0.65$, so the cosine term is nearly constant over the length of the YAG crystal and the approximation is good for closely spaced modes. (Note that the first term of q_{mn} is 1/2 because the lower limit of

integration is zero for our cavity, where the input mirror is deposited on the end of the YAG crystal. For a cavity with the YAG rod at an arbitrary coordinate z_1, the general form of q_{mn} is $(1/2)\{\cos[2(k_m-k_n)z_1] + \cos[2(k_m-k_n)(z_1+\delta z)]\}$.)

With the approximation in (4.24), we complete the reduction of (4.23):

$$\frac{1}{L} \int_{\delta} W \, u_m^2 \, u_n^2 \, dz \approx \left[\frac{q_{mn}}{8} - \frac{1}{4}\right]\overline{W} + \frac{1}{2}[W_{mm} + W_{nn}] \, . \qquad 4.25$$

We also need an expansion like (4.25) in the case where m=n, which makes $q_{mm} = 1$. In this case, we need no approximation:

$$\frac{1}{L} \int_{\delta} W \, u_m^4 \, dz = -\frac{1}{8}\overline{W} + W_{mm} \, . \qquad 4.26$$

We now combine (4.21), (4.22), (4.25) and (4.26) to produce a first order truncation to (4.7) which models a general two-mode class-B laser:

$$\dot{A}_m = -\Gamma_m A_m + 6 A_m W_{mm} \qquad 4.27.a$$

$$\dot{A}_n = -\Gamma_n A_n + 6 A_n W_{nn} \qquad 4.27.b$$

$$\dot{W} = -\Gamma(W - W_0) - \tilde{a}[I_m W_{mm} + I_n W_{nn}] \qquad 4.27.c$$

$$\dot{W}_{mm} = \Gamma W_o/2 - W_{mm}[\Gamma + \tilde{a}I_m + \tilde{a}I_n/2] - \tilde{a}I_n W_{nn}/2 + \tilde{a}\bar{W}[I_m + (q_{mn} - 2)I_n]/8$$

$$4.27.d$$

$$\dot{W}_{nn} = \Gamma W_o/2 - W_{nn}[\Gamma + \tilde{a}I_n + \tilde{a}I_m/2] - \tilde{a}I_m W_{mm}/2 + \tilde{a}\bar{W}[I_n + (q_{mn} - 2)I_m]/8 .$$

$$4.27.e$$

These equations are very similar to the rate equations (2.8). When we make a correspondence between W_{mm} and the gain variable G_m, we see that our field equations (4.27.a and b) directly reproduce Baer's intensity equations (2.8.a and c). Also, the first terms in (4.27.d and e) correspond to the gain equations (2.8.b and d) for a cross saturation β of 1/2. The additional terms in (4.27.d and e), and the new equation for the average inversion $\bar{W}$ (4.27.c) directly couple the dynamics of W_{mm} and W_{nn}. These new terms do not appear in other multimode equations for intracavity doubling. We interpret the relations (4.27.c,d, and e) as follows. The differential equation for $\bar{W}$ (4.27.c) describes how the overall population inversion changes in time. The variables W_{mm} and W_{nn} represent first order corrections to the average inversion, at frequencies of the respective modes. All three inversion variables are directly coupled in (4.27.c,d and e) because the two lasing modes are competing for a single pool of excited particles whose average inversion is measured by $\bar{W}$.

The effect of the mode separation in (4.27) is carried in the coefficient q_{mn}. For further separation, q_{mn} becomes smaller and decreases some of the coupling in (4.27.d and e). We will later see in the three mode case how certain ranges of pump strength "select" different mode separations, so that some mode pairs cannot coexist at particular pump levels. This phenomenon is not observed in the previous rate equations (2.24) since they include no information regarding mode spacing.
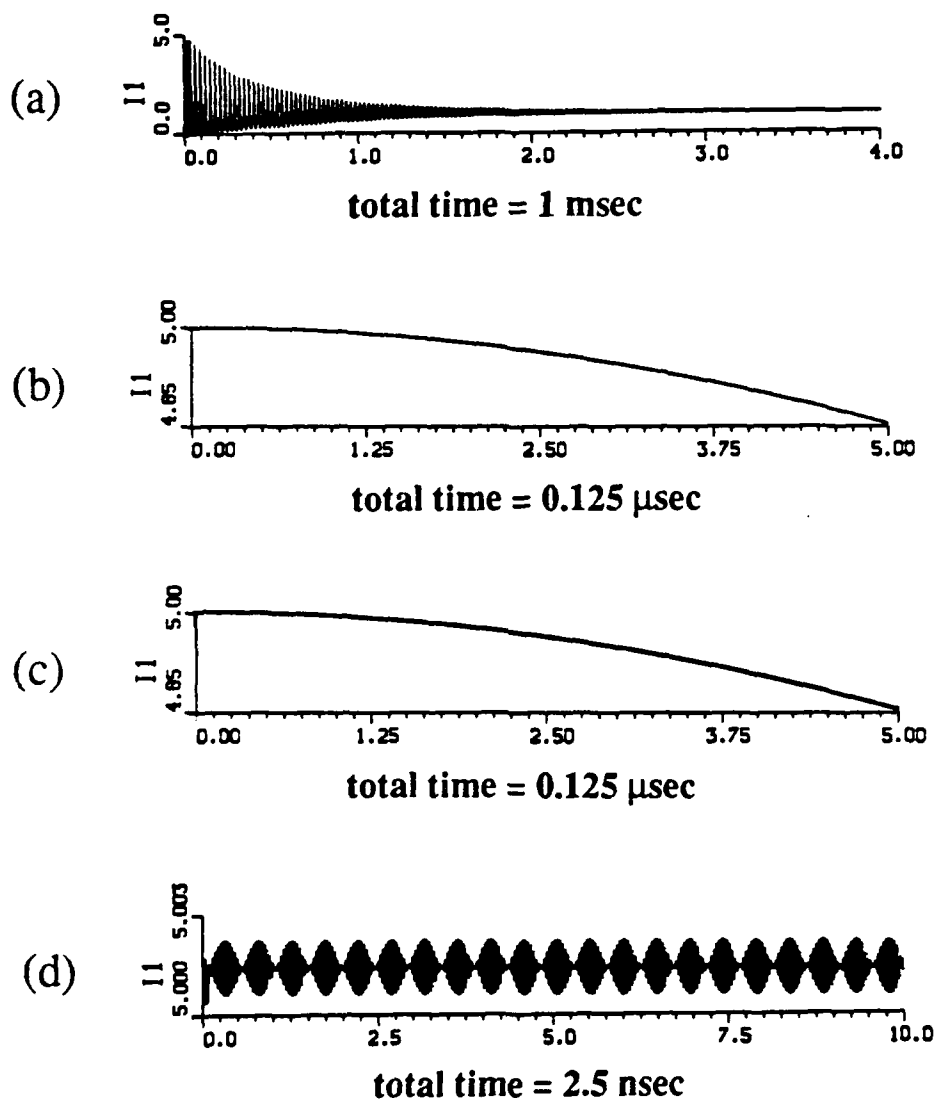
Fig. 4.1   Numeric Integration of (4.7) With and Without Fast Exponential Terms.
Note the large difference in time scales in the four plots. (b) and (c)
represent a small segment of (a); (d) is an even smaller segment of (c).
The plots suggest we can average the fast oscillations out of (4.7) with
no loss of important dynamical information.

We used a sample integration of a single mode, with the coefficient ε set to zero, to numerically examine the influence of the fast oscillations in (4.7) which we have neglected up to this point. The numerical time history shown in Fig. 4.1(a) does not include the fast oscillations; the oscillation frequency is extremely high, so the long computation time forced us to make our comparison on a very short time scale (Fig. 4.1(b) and (c)). The numerical solutions with and without the fast exponentials are indistinguishable; the close up of the solution computed with the fast terms (Fig. 4.1(d)) suggests that the fast oscillations have a negligible effect on the slower motion of (4.27).

With a better intuition of the relative magnitudes of the fast and slow oscillations in (4.18), we now take a perturbative approach to averaging the fast terms to zero. We let m=1, n=2 in (4.18), and the additional variable W_{12} is defined by (4.20). Let A be the vector $(A_1, A_2, \overline{W}, W_{11}, W_{22}, W_{12})$, so we can express (4.27) as

$$\dot{A} = F(A) \qquad\qquad 4.28$$

where F, the right hand side of (4.27), does not include the fast exponentials that appear in (4.18). Since W_{12} is included in A, but does not appear in (4.27), we take $dW_{12}/dt = 0$ in F. This is the averaged equation where we have assumed that the effect of the exponential terms is negligible. We want to compare (4.28) to (4.18), rewritten here in the first order truncation:

$$\dot{A}_1 = -\Gamma_1 A_1 + \overline{b} A_1 W_{11} - D_1 + \overline{b} A_2 W_{12} e^{-i\Delta t} \qquad 4.29.a$$

$$\dot{A}_2 = -\Gamma_2 A_2 + \overline{b} A_2 W_{22} - D_2 + \overline{b} A_1 W_{12} e^{+i\Delta t} \qquad 4.29.b$$

$$\dot{\overline{W}} = -\Gamma(\overline{W} - W_o) - \tilde{a}[I_1 W_{11} + I_{22} W_{22}]$$
$$- \tilde{a}[A_1 A_2^* W_{12} e^{i\Delta t} + c.c] \qquad 4.30.a$$

$$\dot{W}_{11} = \Gamma W_o/2 - W_{11}[\Gamma + \tilde{a}I_1 + \tilde{a}I_2/2] - \tilde{a}I_2 W_{22}/2 + \tilde{a}\overline{W}[I_1 + (q_{12} - 2)I_2]/8$$
$$- \tilde{a}[A_1 A_2^* W_{1112} e^{i\Delta t} + c.c]$$
$$4.30.b$$

$$\dot{W}_{22} = \Gamma W_o/2 - W_{22}[\Gamma + \tilde{a}I_2 + \tilde{a}I_1/2] - \tilde{a}I_1 W_{11}/2 + \tilde{a}\overline{W}[I_2 + (q_{12} - 2)I_1]/8 .$$
$$- \tilde{a}[A_1 A_2^* W_{1222} e^{i\Delta t} + c.c]$$
$$4.30.c$$

$$\dot{W}_{12} = -\Gamma W_{12} - \tilde{a}[I_1 W_{1112} + I_{22} W_{1222}]$$
$$- \tilde{a}[A_1 A_2^* W_{1122} e^{i\Delta t} + c.c] . \qquad 4.30.d$$

We note that $W_{12} = W_{21}$ by definition; the frequency doubling losses have been combined in D_1 and D_2; "c.c." stands for complex conjugate, and the four-subscript variables are defined like the W_{ij} in (4.20):

$$W_{ijkl} = \frac{1}{L} \int_{\&} W u_i u_j u_k u_l \, dz . \qquad 4.31$$

The W_{ijkl} must be approximated in terms of the lower order variables; this is accomplished by the same sort of procedure carried out in (4.23) through (4.25). For the averaging

problem at hand, it suffices to note that such approximations exist. We write (4.29) and (4.30) in the general form:

$$\dot{A} = F(A) + G(A, 1/\Delta, t) \qquad\qquad 4.32$$

where the function G includes all the fast exponential terms, as well as the entire W_{12} equation (4.30.d). The small parameter in G is $1/\Delta$, the inverse of the frequency spacing between modes; Δ is $O(10\ GHz)$. Over short time intervals, where A is essentially constant, G averages to zero, so we would like to show that G represents only a small perturbation to the averaged system of equations (4.28). We show this using a simple transformation suggested to us by Jack Hale, found in Chapter 7 of his text on ordinary differential equations (Hale, 1969):

$$B_1 = A_1 + \frac{1}{\Delta} (b\, A_2\, W_{12}\, e^{-i\Delta t}) \qquad\qquad 4.33.a$$

$$B_2 = A_2 - \frac{1}{\Delta} (b\, A_1\, W_{12}\, e^{+i\Delta t}) \;. \qquad\qquad 4.33.b$$

Under this transformation, (4.32) becomes

$$\dot{B} = F(B) + \frac{1}{\Delta}\, G'(B, 1/\Delta, t) \;; \qquad\qquad 4.34$$

and the function G' is continuous, along with its first derivative, and bounded (see the discussion of the absorbing rectangles U_i in Chapter II). Then the theorem from which we draw (4.33) (Hale, 1969) may be summarized for our problem as follows. Given the

properties of G and G' above, there exists a critical frequency ω_c such that, for all $\Delta > \omega_c$, an asymptotically stable solution of the perturbed system (4.34) remains within a small neighborhood of a corresponding asymptotically stable (steady state or periodic) solution of (4.32). In our particular system of equations (4.29) and (4.30), we do not yet know the critical value ω_c, but the numerical evidence of Fig. 4.1 suggests that our experimentally determined Δ is sufficiently large to justify the averaging.

Initial numerical integrations of (4.27), with frequency doubling included, display dynamics very similar to those of the Baer rate equations for two modes (Fig. 4.2). For most parameter ranges, the two intensities pulse on and off periodically as in the cases studied in Chapter II.
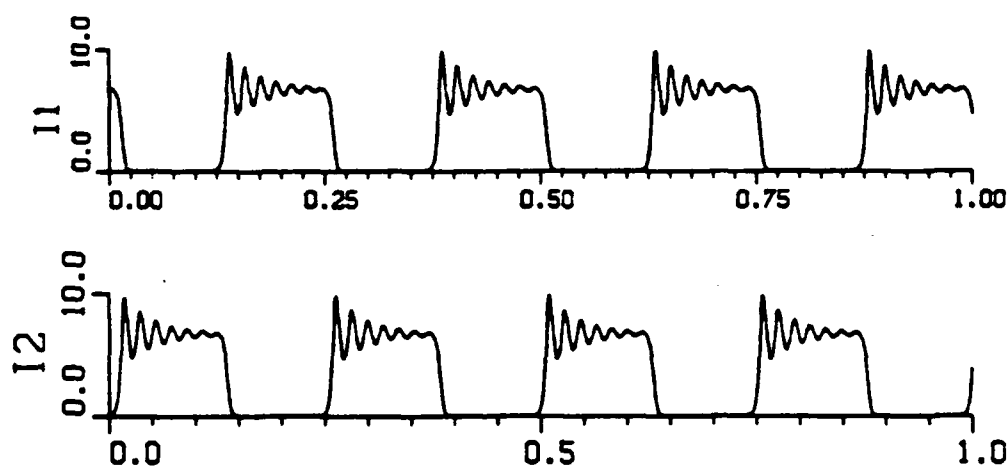
Fig. 4.2   Numerical Integration of the Two-Mode Equations (4.27). Pumping is 5 × threshold. Total plot time is 100 µs.

Model for Three or More Modes

All the tools we require to build the model for three or more modes were developed in the previous section, so we proceed directly to the general form of (4.27) for N modes. In the last section we structured the equations to make it simpler to compare the new equations with the form of Baer's rate equations. Here, we scale the variables and restructure the new equations to simplify the generalization to N modes. Along with (4.24) and (4.25) we require the following scalings:

$$b = \bar{b}\, L \qquad I_j = |A_j|^2 \qquad \tilde{I}_j = \frac{\bar{a}}{\Gamma}\, I_j \qquad \tilde{D}_j = \frac{\Gamma}{\bar{a}}\, D_j \qquad f_j = \frac{b}{\Gamma_j}$$

$$\tilde{W}_j = \frac{b}{\Gamma_{n_1}}\, W \qquad \tilde{W}_{jj} = f_j\, W_{jj} \qquad \theta_j = \frac{\Gamma}{2\Gamma_j}$$

$$\text{4.35.a}$$

$$t_{new} = \Gamma\, t \qquad F_{ij} = \frac{\Gamma_i}{\Gamma_j} \qquad \varepsilon_j = \frac{\Gamma}{\bar{a}\Gamma_j}\, \varepsilon$$

$$p = \text{pump} \ (>1)$$

with intracavity doubling losses represented by D_j which are now formed with ε_j instead of ε. Recall that the phase contributions to the doubling terms D_j were averaged out. We include the general form of D_j, for N modes I_j in one polarization direction and P modes I_j' in the orthogonal direction, we have:

$$D_j = -g \epsilon_j I_j + 2 g \epsilon_j \sum_{k=1}^{N} I_k + 2 (1-g) \epsilon \sum_{k=1}^{P} I_k' \ . \qquad \text{4.35.b}$$

We have arbitrarily scaled W with respect to Γ_{n1}, as a reference point; this allows us to simplify the general form of the equations (with tildes removed from scaled variables to avoid clutter):

$$\theta_j \dot{I}_j = I_j (W_{jj} - 1 - D_j) \qquad\qquad j=n_1, n_2,..., n_N$$

$$\dot{W} = f_1 p - W - \sum_{k=1}^{N} F_{k1} I_k W_{kk} \qquad\qquad \text{4.36}$$

$$\dot{W}_{jj} = \frac{f_j}{2} p - W_{jj} - \sum_{k=1}^{N} I_k \ [(W_{jj} + F_{kj} W_{kk})/2 - \frac{1}{8} (q_{jk} - 2) F_{1j} W]$$

$$j=n_1, n_2,..., n_N \ ,$$

where $\{n_j, j=1,...,N\}$ is the indexing set for the N modes. We have again neglected the fast exponential terms of (4.7) which average to zero. The assignment of polarization directions to I_j in (4.36) has been suppressed here.

An interesting feature of (4.36) is the connection between pump strength and allowable mode separation. We observe this connection in numerical solutions of (4.36) for three modes, where we assume mode-2 is centered between two symmetric side modes, 1 and 3. First we let the frequency spacing to each side mode be only one cavity mode spacing (c/2L), and we numerically integrate (4.36) with no frequency doubling ($\epsilon = 0$) until the system reaches a stable steady state. We also impose 5% higher losses on the side

modes than on the central mode. Under these conditions, we find that different pump strengths produce a wide range of relative steady state intensities for the center and the side modes (Fig. 4.3(a)). When we reset the intermode spacing to twice the cavity mode spacing (c/L), the range of pump values where all three modes are on differs from the previous case (Fig. 4.3(b)). This evidence indicates that the level of pumping, combined with the cavity's gain profile, weeds out certain frequencies and enhances others. This is consistent with the results reported by McMackin in a comparable model for dye lasers.

A numerical integration of (4.36) appears in Fig. 4.4, with N=3 (all modes in the same polarization direction) and modes separated by one cavity mode spacing. The total fundamental intensity trace in Fig. 4.4(b) shows a different kind of intensity output than we have seen in other models. We see similar beating in some experimental output (Fig. 4.4(c)); the information about mode spacing included in this new model seems necessary to reproduce this phenomenon. We note that the time scales of the numerical and laboratory experiments do not coincide, so more integrations are necessary to observe the changes in output intensity as the mode separation is changed.

$p = 7.0$

$p = 6.0$

$p = 5.0$

$p = 4.0$

$p = 3.0$

$p = 2.0$

$p = 1.5$

(a) one cavity mode
     spacing

(b) two cavity mode
     spacings
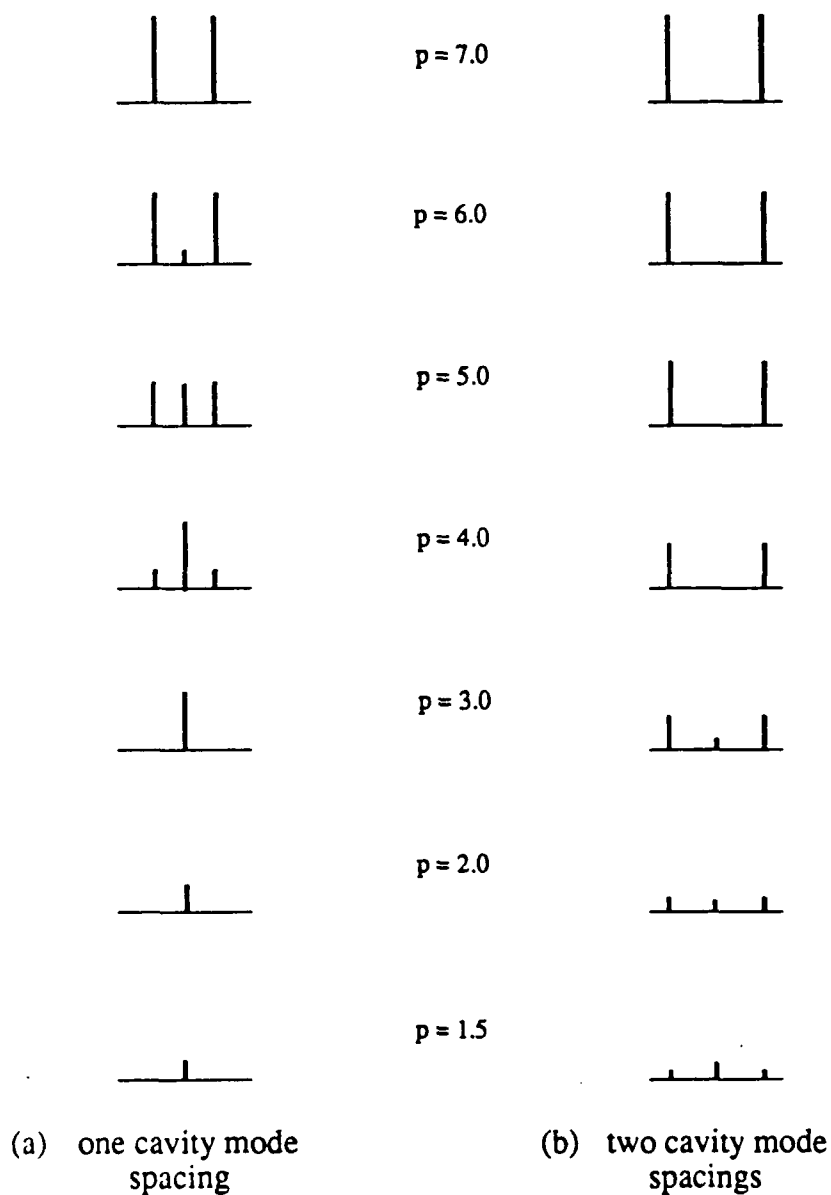
Fig. 4.3 Changes in Steady State Intensities as Functions of Pump Strength.
          (a) steady state limits of (4.36) for modes separated by one cavity mode
          spacing, with 5% greater loss for side modes. (b) modes are separated
          by two cavity mode spacings.
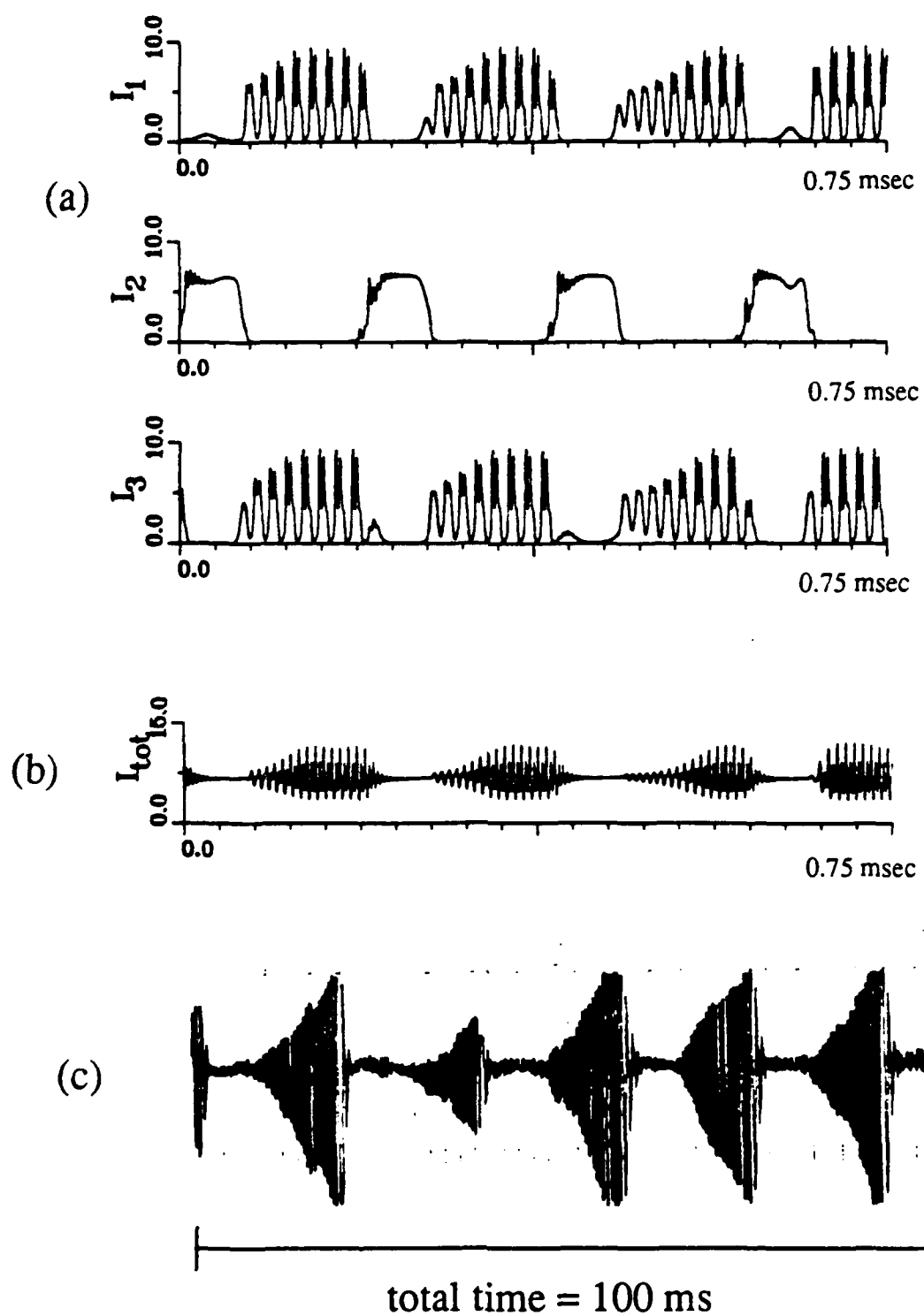
Fig. 4.4 Slow Beating in Three-Mode Systems. (a) individual intensities in numerical
results, (b) total intensity of numerical integrations, (c) experimental
output of total intensity. Note the difference in time scales.

Summary

This section followed the approach of (McMackin, et al., 1988) to develop a general set of rate equations, for a multimode class-B laser, with features not included in other models. In these equations, the population inversion is treated as a spatially averaged quantity with first order corrections whose frequencies are those of the active longitudinal modes. Spatial overlap is accounted for explicitly by the coupling coefficients which depend on the frequency spacings between neighboring modes. Numerical integrations show how the pump strength and mode asymmetries interact to select preferred longitudinal mode frequencies, and exhibit slow beating in the total intensity which has not yet been observed in integrations of other models.

Three-Level Model

In Chapter I we approximate the lasing process in a YAG as a two-level transition (Fig. 1.3). There are actually four energy bands or levels involved in the process, but we assume that two of the decay rates (out of E_3 and E_1) are so fast that we can neglect their role in the laser dynamics. The time scales of these energy transitions are unique to each active medium; the two-level approximation is invalid for other types of lasers. The CO_2 laser is an important example of such a laser, where the decay out of the lower lasing level E_1 is slow enough it mush be included in the rate equation model. Dynamically, the need for the third level in the CO_2 equations is necessary because chaotic behavior is observed for single-mode output. If the model includes only intensity and gain equations, the Poincaré-Bendixson theorem prohibits any chaotic dynamics; the single-mode equations need another dimension to produce chaos.
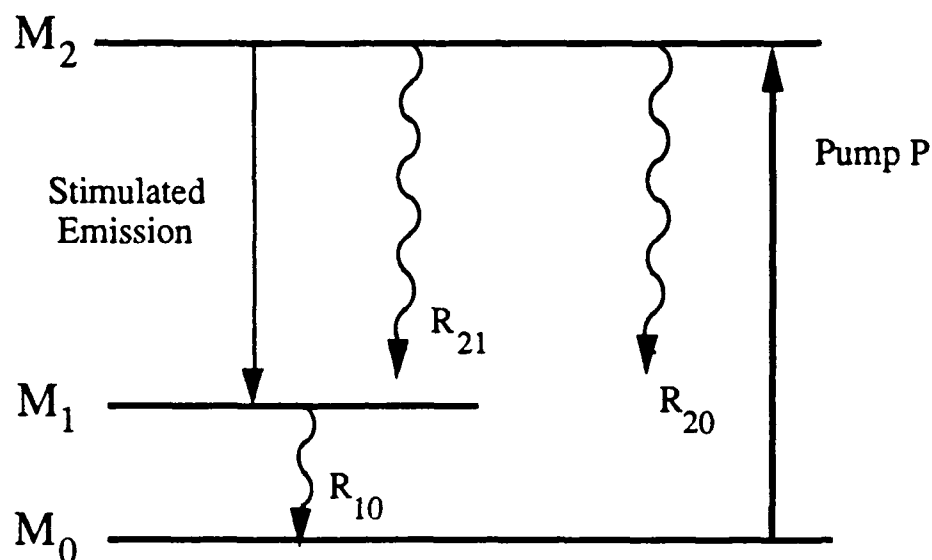
Fig. 4.5 Three-Level Rate Equation Scheme.

We now formulate a three-level rate equation model for the intracavity doubled YAG laser, inferred from the schematic of energy transitions in Fig. 4.5. The approach and the notation used here follow the discussions in (Tachikawa et al., 1987; De Tomasi et al., 1989). We assume the transient population in the highest energy level E_3 is negligible, and let M_2, M_1 and M_0 be the populations of the respective energy levels. The pump rate P excites ions from E_0 to E_2 in the three-level approximation. The lasing transition due to stimulated emission is shown between E_2 and E_1. The other three energy transitions are spontaneous decay rates between the three levels, where R_{20}, for instance, is the spontaneous decay from E_2 to E_0.

We normalize M_1, M_2 and M_3 so their sum is 1, and define $D = M_2 - M_1$ (inversion) and $S = M_1 + M_2$. The rate equations for D, S and the single-mode intensity

I can be written directly by including the appropriate gain or loss terms in Fig. 4.5. First of all, we know the intensity dynamics depend on D and not on S and if we scale time $t_{new} = 2\Gamma_1 t$ in terms of the cavity decay rate Γ_1 then we write the scaled differential equation for intensity:

$$\dot{I} = I (BD - 1 - \text{frequency doubling terms}, \qquad 4.37$$

where B is a scaling for the population inversion D. There are five relevant energy transitions in the differential equation for the inversion:

$$\dot{D} = \frac{1}{2\Gamma_1} (PM_0 - 2ID[2\Gamma_1 b] - R_{20}M_2 + R_{10}M_1 - 2R_{21}M_2) \qquad 4.38$$

where the terms represent the pump transition and stimulated emission and the three effects of spontaneous emission. We note that the $R_{10}M_1$ term is positive since it serves to increase the inversion; there is a factor of 2 in the last term because the transfer of one excited particle from level 2 to level 1 increases the value of D by 2.

Similarly, we write the relevant transitions for S:

$$\dot{S} = \frac{1}{2\Gamma_1} (PM_0 - R_{20} M_2 - R_{10} M_1) . \qquad 4.39$$

The transitions between levels 2 and 1 do not explicitly influence the dynamics of S since S is the sum of these two populations.

We now rewrite these differential equations in terms of the Maxwell-Bloch variables derived in the previous section. This allows us to see how the additions of the third level to the model changes the single-mode equations (4.14). We observe that R_{21} is

the upper state decay rate we call Γ (which is 4.0×10^3 s^{-1} for Nd:YAG); we assume that

particles decay from E_2 to E_0 at the same rate, so $R_{20} = \Gamma$. We also include a new

parameter $\Gamma_0 = R_{10}$ (2.0×10^6 s^{-1}). The single-mode equations for the three-level

intracavity doubled laser are then

$$\theta \; \dot{I} \;=\; I \, (\, W \,-\, 1 \,-\, \text{doubling terms}) \qquad\qquad 4.40.\text{a}$$

$$\dot{W} \;=\; (\, 1 + p \,) \,-\, \tfrac{1}{2} W \, (\, 5 \,+\, g_0 \,+ 2I \,) \,-\, \tfrac{1}{2} S \, (\, 1 - g_0 \,) \qquad\qquad 4.40.\text{b}$$

$$\dot{S} \;=\; (\, 1 + p \,) \,-\, \tfrac{1}{2} W \, (\, 1 \,-\, g_0 \,) \,-\, \tfrac{1}{2} S \, (\, 1 \,+\, g_0 \,) \qquad\qquad 4.40.\text{c}$$

where p is the pump percentage above threshold, $g_0 = \Gamma_0/\Gamma$, W is the average population

inversion, θ is a small (dimensionless) time constant, and cavity losses have been scaled to

1. Numerical integrations of (4.40) show the same qualitative behavior as (4.14): transient

oscillations to a stable steady state. No periodic or aperiodic solutions were observed for

integrations with several values of pumping p and coupling coefficient ε (in the doubling

term). Our next step is to generalize (4.40) for two and three modes.

When we compare (4.40) to a similarly scaled version of (4.14) we see that the new

terms in (4.40.b) due to the presence of the third energy level are

$$-\tfrac{1}{2} W \, (\, 3 \,+\, g_0 \,) \,-\, \tfrac{1}{2} S \, (\, 1 \,-\, g_0 \,) \,. \qquad\qquad 4.41$$

To get two-mode equations comparable to (4.27), we note that the intensity equations

(4.27.a and b) do not change in the three-level model, so we begin by adding (4.41) to the

scaled W equation (4.27.c):

$$\dot{W} = (1+p) - W - I_1 W_{11} - I_2 W_{22}$$

$$-\frac{1}{2} W (3 + g_0) - \frac{1}{2} S (1 - g_0).$$

4.42

The differential equation for S in the two mode case is the same as before (4.40.c). Recall that W_{11} is defined (4.20) as a normalized integral of W with sine functions. We define new variables S_{jj} the same way:

$$S_{ij} = \frac{1}{L} \int_{\underline{k}} S \, u_i \, u_j \, dz$$

4.43

and we get the following equations:

$$\dot{W}_{11} = \frac{1}{2}(1+p) - W_{11} - I_1 W_{1111} - I_2 W_{1122} - \frac{1}{2}(3+g_0) W_{11} - \frac{1}{2}(1-g_0) S_{11}$$

4.44.a

$$\dot{S}_{11} = \frac{1}{2}(1+p) - \frac{1}{2}(1-g_0) W_{11} - \frac{1}{2}(1+g_0) S_{11}$$

4.44.b

where W_{iijj} is defined by (4.25); the equations for W_{22} and S_{22} have the same form as (4.44). This is a straightforward correction to the the previous rate equations (4.27). Most importantly, the S_{jj} equations do not introduce any new four-index integrals which require approximation. Therefore, these equations need no more simplification to model the two-

mode dynamics, as long as the three-level approximation to the lasing process is valid. We can also directly generalize the correction terms for an arbitrary number N of modes:

$$\theta \, \dot{I}_j \;=\; I_j \, (\, W_{jj} - 1 - \text{doubling terms}) \qquad\qquad 4.45.\text{a}$$

$$\dot{W} \;=\; (1+p) - W - \sum_{k=1}^{N} I_k \, W_{kk} \qquad\qquad 4.45.\text{b}$$

$$-\frac{1}{2} W \, (3 + g_0) - \frac{1}{2} S \, (1 - g_0)$$

$$\dot{W}_{jj} \;=\; \frac{1}{2}(1+p) - W_{jj} - \sum_{k=1}^{N} I_k \, W_{jjkk} \qquad\qquad 4.45.\text{c}$$

$$-\frac{1}{2}(3+g_0) \, W_{jj} - \frac{1}{2}(1-g_0) \, S_{jj}$$

$$\dot{S}_{jj} \;=\; \frac{1}{2}(1+p) - \frac{1}{2}(1 - g_0) \, W_{jj} - \frac{1}{2}(1 + g_0) \, S_{jj} \; , \qquad\qquad 4.45.\text{d}$$

$$j = 1, \, 2, \, ..., \, N.$$

Initial numerical integrations of the two-mode equations (Fig. 4.6) and the three-mode equations ((4.45) with N=3) show no new types of solutions; two modes display steady state and periodic behaviors, and the transitions to chaos are not noticeably different for three-modes. These results confirm validity of the two-level assumption made for the rate equations in Chapters I and II.
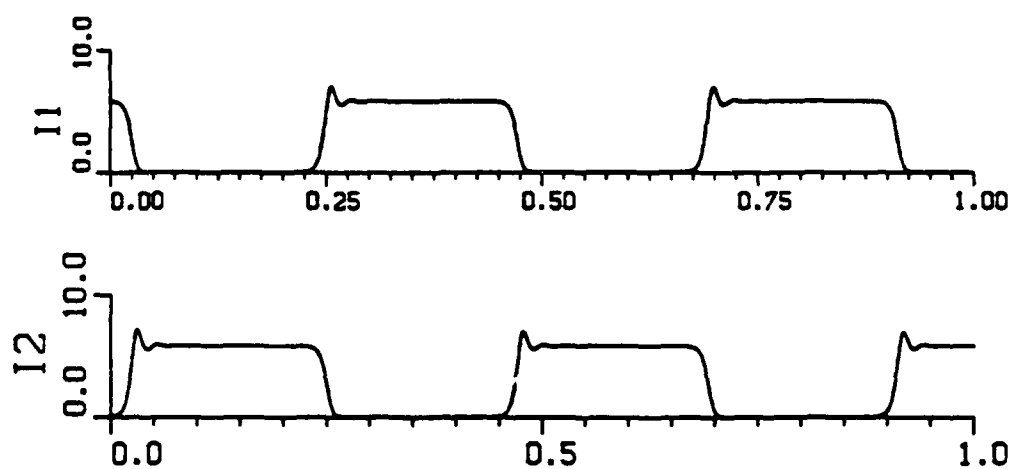
Fig. 4.6 Numerical Results for Two Modes in the Three-Level Model. The total
time is 1 μsec.

Modulated Parameters

The rate equations (3.25) developed in Chapter III are deterministic equations that can generate chaotic intensity time histories. These equations are derived under the assumption that the input pump beam is perfectly steady and that cavity loss rates are constant. It is straightforward to include the modulation of cavity parameters in the equations; two examples are discussed below. The addition of noise to the equations, for instance, is useful for studying the effects of spontaneous emission noise and the sensitivity of the laser system to non-steady pumping. The second example, the forced periodic modulation of the pump, is a common technique in laser spectroscopy, where a particular frequency (usually at the frequency of relaxation oscillations) is amplified by the input modulation (Chakmakjian, et al., 1989; Hamilton, et al., 1987; Petersen, 1989; Kozlovsky, et al., 1989). We briefly present the changes in (3.25) necessary to apply these modulations; the analysis of the resulting equations remains an open problem.

The constant pump term γ in (3.25) does not multiply any of the time-dependent variables, so we can apply established techniques for including additive noise in our equations (Vemuri and Roy, 1989). We consider the two-mode case, first with white noise. Given two independent random numbers a and b at each time step t, uniformly distributed on [0,1], we use the Box-Mueller algorithm to generate independent gaussian numbers with variance $2D\Delta t$ (for an integration time step Δt):

$$q_1(t) = \sqrt{-4\,D\,\Delta t\,\ln(a)}\;\;\cos(2\pi b)$$

$$4.46$$

$$q_2(t) = \sqrt{-4\,D\,\Delta t\,\ln(a)}\;\;\sin(2\pi b)\,.$$

We then define the time-dependent pump term $P_j(t) = \gamma + q_j(t)$ (j=1,2), and put $P_j(t)$ into (3.25) in place of γ.

To add colored noise to γ, we need an additional differential equation for each noise term. We still generate q_j as above, with normal distributions, but we define $P_j(t) = \gamma + Q_j(t)$, where

$$\dot{Q}_j = -\lambda Q_j + \lambda q_j \qquad\qquad 4.47$$

$$Q_j(0) = q_j(0) \qquad\qquad j = 1, 2$$

and $1/\lambda$ is the correlation time of the colored noise. The noise term $Q_j(t)$ has zero mean and correlation function $\langle Q_j(t)Q_j(s)\rangle = D\lambda\exp(-\lambda|t-s|)$. The time-dependent pump term $P_j(t)$ is placed directly into (3.25).

The periodic modulation of the pump can be accomplished in the same way, where the time-dependent term $q_j(t)$ added to γ is simply a sine function with a selected frequency and amplitude.

CHAPTER V

CONCLUSIONS

The new model for intracavity frequency doubling in Chapter III exhibits many phenomena which have also been observed in experiments. The new set of rate equations derived in Chapter IV carries more information about individual modes and their frequency spacing, and reproduce at least one experimentally observed behavior which has not been reported in numerical solutions of other models. Our suggestions for future research highlight several unresolved issues about these two models, but the next steps in this research mostly center around modifications to the models.

The main loose end in all our rate equations is the calculation of the cross-saturation parameter β. We treat β as a free parameter in this thesis, either using previously published values, or making numerical data fit the character of experimental output. There are explicit formulae available to estimate β (e.g., Sargent, et al., 1974) and it is routinely estimated for other types of lasers (Yamada and Suematsu, 1981); the appropriate calculation needs to be carried out for the intracavity doubled Nd:YAG laser.

While our new model for intracavity doubling in Chapter III addresses the polarization states of longitudinal modes, it does not consider any possible effect of the polarization of the input pump beam. Laboratory tests show the pump beam from the diode laser to be nearly linearly polarized. This polarization may in fact have no influence on the polarization of cavity modes, but this effect has not yet been studied.

Even with the models in their current form, there is a need for more appropriate formats for the output. Our Poincaré maps of the gain variables, for instance, are essential to understanding the dynamics of the various models. However, these maps do not correspond to any directly measurable quantity in the laboratory. It would be very useful to compile a set of utility programs which process our current numerical output in a form more comparable to experimental data. The FFT's of total intensity output already serve this purpose; other examples include: return maps (plots of $I(t+\Delta t)$ versus $I(t)$); correlation functions; histograms of intensity values, intensity peaks, or peak-to-peak times; and estimates of Lyapunov exponents.

There are several straightforward variations to our models which bear further investigation. The addition of noise or pump modulation to the models is discussed in Chapter IV. The influence of asymmetries has not yet been addressed in depth. This is an especially important issue, for the following reason. In a laser with three oscillating modes, it is seldom the case that all three modes have the same magnitude. Quite the contrary, at a lower power level where only two modes oscillate, an increase in power past a certain threshold causes the third mode to appear only slightly at first; higher powers usually have several modes oscillating with vastly different relative magnitudes. This situation, for instance, can be modeled by assigning different gains and losses to each mode in the model.

Another interesting problem is to see how the numerical integrations match experimental output for cases of more than three modes. Some of our laboratory data, for instance, have six modes oscillating in one polarization direction and two modes in the orthogonal direction.

The complete analysis of the Chapter IV rate equations remains an open research topic. The steady state results illustrated in Fig. 4.3 suggest that the effect of mode spacing

on the linearized analysis may itself be a difficult analytical problem. There is much to be learned from a thorough series of numerical integrations of this model. Future work on these equations also needs to include the polarization states of the longitudinal modes which have not been accounted for yet in this particular model.

An unresolved issue in the analysis of our models concerns the Poincaré maps, upon which we rely to observe the intermittency route to chaos, for instance. We generate these maps numerically, but it remains to be seen if we can construct an appropriate analytic approximation to the true map (which requires integration of the coupled set of differential equations). The construction of an approximate map would serve as an important check for our numerical results.

The larger problem of characterizing intermittent flow through an invariant measure on the dynamical system is discussed in Appendix C. Several important issues arise, including: how to "best" approximate an appropriate invariant measure for the system, and how to infer estimates of the duration of laminar or turbulent behavior from such a measure. There is also an interesting aside to this problem: how to use a technique designed for approximating invariant measures (one of the cell mapping techniques, for instance) and use it to calculate other statistics for the flow, such as Lyapunov exponents. Some of this work has been accomplished already, but there may be room for improvement using new variations of cell mapping (Tongue and Gu, 1988).

The intracavity frequency doubled laser has been shown, in theory and experiment, to be a model system for studying a wide range of dynamical behavior. Analytical and numerical results demonstrate that our new model for intracavity doubling successfully predicts the stable and unstable configurations for several applications of the general model, and reproduces the experimental behavior of a one-, two- and three-mode Nd:YAG laser.

Comparable ranges of behavior can be observed, in both laboratory and numerical experiments, by the variation of a single control parameter. Overall, the intracavity doubled Nd:YAG laser is found to be a paradigm for investigations of nonlinear dynamics.

APPENDIX A

THE MAXWELL-BLOCH EQUATIONS

This appendix is a brief comment on the background of the Maxwell-Bloch equations. These semiclassical equations are a well-established standard for describing single-mode laser dynamics; details of their derivation can be found in (Haken, 1975; Sargent, et al., 1974; Arecchi, 1987) among others. The following description summarizes discussions found in (Roy, et al., 1989; Arecchi, 1987).

The derivation begins with the quantum form of the molecule, radiation and interaction Hamiltonians. Decay rates for the electric field, molecular polarization, and population inversion are introduced by including the interactions of the molecules and radiation with reservoirs. In the semiclassical approximation to these equations, the quantum operators are replaced by their classical expectation values (according to Ehrenfest's Theorem (Borowitz, 1967; Park, 1964)), and factored under assumptions of statistical independence.

The single-mode Maxwell-Bloch equations that result are (in their simplest form):

$$\dot{E} = -(i\omega_c + k)E + gP$$
$$\dot{P} = -(i\omega_0 + \gamma_\perp)P + gE\Delta \qquad\qquad A.1$$
$$\dot{\Delta} = -\gamma_\parallel(\Delta - \Delta_0) - 2g(E^*P + c.c.).$$

The time-dependent variables are electric field amplitude E with angular frequency ω_c, molecular polarization P, and population inversion Δ. Their respective decay rates are k,

$\gamma_\perp$ and $\gamma_\parallel$; g is proportional to the atomic dipole moment, ω_0 is the resonance frequency of the molecules, and Δ_0 is the equilibrium inversion in the absence of lasing.

Arecchi's classification of lasers depends on the relative time scales in (A.1). A class-C laser is a system for which the three decay rates are of similar orders of magnitude, and all three equations in (A.1) are necessary to describe the single-mode dynamics. In a class-B laser, the polarization decay $\gamma_\perp$ is very fast with respect to the other time scales, and P can be replaced by its steady state value. This **adiabatic elimination** of P implies that the polarization effectively responds instantaneously to any changes in the other variables, such that only two differential equations are necessary to describe the single-mode dynamics. This is a reasonable approximation for Nd:YAG and CO_2 lasers, for example. Finally, class-A lasers are those whose field variations are slow with respect to changes in polarization and inversion; both P and Δ can be adiabatically eliminated and replaced by their steady state values in the E-field equation. This class of lasers includes dye lasers and atomic gas lasers.

APPENDIX B

PARAMETER VALUES

In this appendix we identify the sources, or give sample calculations, for the parameter values used in our model equations. The parameter notations apply consistently to variables used throughout the thesis; the calculated values correspond to a 5.0 cm cavity with 98% reflection of the fundamental wavelength at the output mirror.

Some of the parameters of interest are physical constants:

$$\varepsilon_0 = 8.85 \times 10^{-12} \ C^2/N{\cdot}m^2 \qquad \text{permittivity}$$
$$h = 6.6 \times 10^{-34} \ J{\cdot}s \qquad \text{Planck's constant} \qquad B.1$$
$$\hbar = h/2\pi = 1.0 \times 10^{-34} \ J{\cdot}s$$
$$c = 3.0 \times 10^8 \ m/s \qquad \text{light speed .}$$

The next easiest parameters to get are physically measurable properties of the Nd:YAG crystal and cavity:

$$n = 1.8 \qquad \text{average refraction index}$$
$$\text{(Svelto, 1989)}$$

$$L = 5.0 \times 10^{-2} \ m \qquad \text{example cavity length}$$

$$l = \delta z = 5.0 \times 10^{-3} \ m \qquad \text{YAG crystal length}$$

$$\text{diam} = 3.0 \times 10^{-3} \ m \qquad \text{YAG diameter}$$

$N_o = 6.0 \times 10^{25} / m^3$ — number density of Nd^{+3} ions for a 1% concentration in YAG (Svelto, 1989)

$\tau_f = 0.24 \times 10^{-3}$ s — fluorescence or upper state lifetime (Baer, 1986)

$\Gamma = 1/\tau_f$ — upper state decay rate

$\rho = 5.0 \times 10^{11}$ s^{-1} — dipole decay or dephasing rate (Siegman, 1986)

$T = 0.02$ — transmission percentage of output mirror at fundamental frequency

The remaining parameters are combinations of the above quantities:

$$\bar{\omega} = \frac{2 \pi c}{\lambda} \approx 18.0 \times 10^{14} \text{ s}^{-1}$$ — fundamental frequency

$$\nu = \frac{\bar{\omega}}{2\pi} \approx 3.0 \times 10^{14} \text{ s}^{-1}$$ — fundamental frequency

$$\tau_d = \frac{2L}{cT} \approx 1.7 \times 10^{-8} \text{ s}$$ — cavity (field) decay time

$$\Gamma_L = 1/\tau_d$$ — cavity decay rate

$$d^2 = |\mu|^2 = \frac{3\Gamma\hbar\varepsilon_0 c^3}{16\pi^3\nu^3 n} \approx 8.0 \times 10^{-62} \text{ c}^2 \cdot m^2$$ — dipole moment

$$\tau_c = \frac{2L}{c} \approx 3.3 \times 10^{-10} \text{ s}$$ — cavity round trip time

$$\alpha = \frac{2\tau_c}{\tau_f} = 2T \approx 0.04 \qquad\qquad \text{intensity mode loss}$$

We also include a scaling between watts (W) and squared field (V^2/m^2) which was useful to change the units of d_{eff}^2, the measured KTP doubling coefficient, in (3.12.a):

$$W \mapsto \left(\frac{J}{s}\right)\left(\frac{1}{c}\right)\left(\frac{1}{\varepsilon_0}\right)\left(\frac{1}{D^3}\right)$$

$$\left(\frac{J}{s}\right)\left(\frac{s}{m}\right)\left(\frac{N\cdot m^2}{C^2}\right)\left(\frac{1}{m^3}\right) \overset{d}{=} \frac{V^2}{m^2} , \qquad\qquad \text{B.2}$$

where D is an appropriate atomic length, on the order of 1 Å.

The above expressions give measurable estimates for all the parameters we need except for the cross saturation term, β. Theoretically, β assumes values from 0 to 2 (Siegman, 1986) and the fact that experiments do not display bistable behavior indicates that $0 < \beta < 1$ (see Appendix E). The specific value of β depends on the degree of spatial overlap of modes in the gain medium, so that β is close to 1 for modes which are strongly correlated, and β is small for modes which are anticorrelated in the gain medium. The amount of overlap for two modes can be estimated by integrating the product of two sine functions, with the same frequencies, over the length of the gain medium (and scale the result to vary between 0 and 1). This is the closest approximation we have for β as of this writing.

APPENDIX C

INTERMITTENCY

Numerical integrations of the three-mode rate equations in Chapter II display an intermittency route to chaos. This appendix provides a brief overview of intermittency and its classification into three types in (Pomeau and Manneville, 1980; Berge, 1984); most of the following discussion is taken from these two sources. Extensive references about the theory of intermittency, and its observation in physical systems, appear in the groups of references entitled: Experiments Displaying Intermittency; Intermittency Theory; Entropies and Dimension with Intermittency; Resonances, Frobenius-Perron Operators and Power Spectra; and Scaling and Renormalization.

The theory of intermittency in nonlinear dynamical systems is not yet complete in many ways. For example, there do not appear to be any good algorithms for estimating the times of metastability and the transition times between metastable states. When the intermittency is not associated with a bifurcation from a nearby equilibrium, we are not aware of any useful estimates other than for linear systems. In this light, we also discuss a new way to characterize an intermittent system proposed by Evans Harrell which remains an open research topic.

Any regular time-dependent behavior (usually periodic) which is occasionally interrupted by irregular, turbulent behavior can be described as **intermittent**. We call the regular regimes of intermittent behavior **laminar** or **metastable** flow, and the irregular regimes **turbulent**. Intermittent behavior is easily visualized in turbulent flow in water or air. In the laser rate equations, a sample of intermittent flow appears in Fig. 2.16.

We let r_t be the transition value of some control parameter in a return map or system of equations where we observe stable, periodic observations for $r < r_t$, and we see apparently periodic behavior interrupted by turbulent bursts for $r > r_t$. It is important to note that neither the amplitude nor the duration of the turbulent behavior depend strongly on r, only the average duration of the laminar behavior. The classification of intermittent behavior is based on the linearized analysis of the fixed point in a Poincaré map as r passes through r_t. There are three classifications:

Type I. A real Floquet multiplier increases through +1.

Type II. Complex conjugate Floquet multipliers exit the unit circle.

Type III. A real Floquet multiplier decreases through - 1.

These classifications are based on strictly local phenomena, i.e., the linearized analysis of a limit cycle. At the onset of intermittent behavior, as r just surpasses r_t, the laminar flow resembles the previously stable limit cycle. Turbulent flow is observed when a trajectory leaves the neighborhood of the now unstable limit cycle to wander about in phase space. To observe intermittency (with recurring laminar behavior) there must be some global process of **reinjection** which drives a trajectory back to a neighborhood of the limit cycle in finite time. This reinjection process is unique to each dynamical system and is not accounted for in the Pomeau-Manneville classification. We now examine the three types of behavior in terms of their local bifurcations and estimates of the durations of laminar flow.

Type I Intermittency

We characterize the destabilization of periodic flow by approximating the first-return map locally, with a one-dimensional Taylor series. Suppose we have a multidimensional dynamical system and define a Poincaré map on a transversal in the neighborhood of a periodic orbit. This orbit is represented by a fixed point for the Poincaré map. Let u be an eigenvector of the map of the fixed point. Then multiplying u by the Floquet matrix is equivalent to multiplying by the parameter-dependent eigenvalue $\lambda(r)$:

$$u_{n+1} = \lambda(r)\, u_n \qquad\qquad C.1$$

where "λ passing through $+1$ at r_t" translates into

$$\lambda(r_t) = 1, \quad \text{and} \quad \frac{d\lambda(r_t)}{dr} \neq 0. \qquad\qquad C.2$$

We look at a representative coordinate y of u and approximate $y_{k+1} = f(y_k, r)$ near r_t and near the fixed point y^*, i.e., $y^* = f(y^*, r_t)$. Near r_t the first return map is nearly the identity, so we approximate it by

$$y_{k+1} = y_k + \varepsilon + y_k^2 + \text{ higher order terms,} \qquad\qquad C.3$$

where

$$\varepsilon = r - r_t \quad (\text{or } \frac{r - r_t}{r_t}).$$

Fixed points of (C.3) exist only for $\varepsilon < 0$: $y_\pm = \pm(-\varepsilon)^{1/2}$ (see Fig. C.1). The local quadratic in Fig. C.1(a) slides upward with increases in ε. We calculate
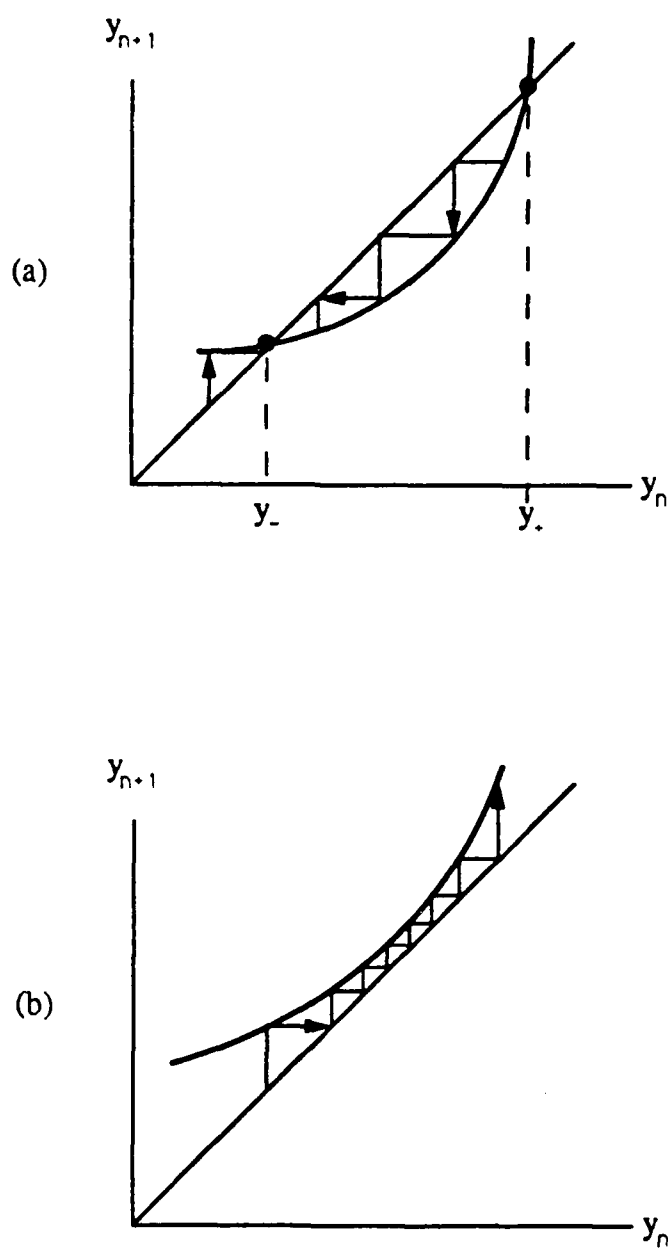
Fig. C.1 Local Approximation for (C.3). (a) The fixed point y. is stable;
y+ is unstable. (b) When ε > 0, there is no fixed point and a channel
forms where the flow is nearly the identity.

$f'(y_\pm) = 1 \pm 2(-\epsilon)^{1/2}$ and find that y_- is stable and y_+ is unstable. When $\epsilon > 0$, we see there is no fixed point (Fig. C.1(b)) and a local channel is formed for the flow. This channel is not merely an artifact of our approximation, it appears very clearly for the second (y) coordinate in the Lorenz equations (Pomeau and Manneville, 1980).

We can derive general scaling laws for the passage time through this channel, which corresponds to the duration of laminar flow, as follows. If $y_{k+1} \approx y_k$ then (C.3) implies that

$$\frac{dy}{dk} \approx \frac{y_{k+1} - y_k}{(k+1) - k} = y_{k+1} - y_k \qquad \text{C.4}$$

so in the narrow channel we have

$$\frac{dy}{dk} \approx \epsilon + y^2 \qquad \text{C.5}$$

which essential represents the coordinate distance traveled per iteration. The general solution to (C.5) is $y(k) = \epsilon^{1/2} \tan[\epsilon^{1/2} (k-k_0)]$, where k_0 is the iteration number referenced to the waist of the channel; we take $k_0 = 0$. This solution diverges for $k = \pm \frac{\pi}{2} \epsilon^{-1/2}$, so this defines the iteration limit at which the approximation (C.4) is no longer valid. It also indicates that the number of iterations needed to cross the channel is of order $\epsilon^{-1/2}$; this is an estimate of the average laminar duration for Type I intermittency. We note that the Lyapunov number associated with a trajectory is on the order of (1/correlation time), so for intermittent flow, the Lyapunov number should be $O(\epsilon^{-1/2})$; this is confirmed by numerical integration of the Lorenz model in (Pomeau and Manneville, 1980).

The above estimate for average laminar duration leads to a heuristic probability distribution for laminar flow duration (the analytic probability distribution remains an open

topic of research). Pomeau and Manneville point out that the duration of laminar regimes is bounded above by a term of $O(\epsilon^{-1/2})$ and there is a higher probability of reinjecting into the laminar regime for $y<y^*$ than $y>y^*$ (where the tendency is to exit the laminar regime). The heuristic distribution which results is shown in Fig. C.2.
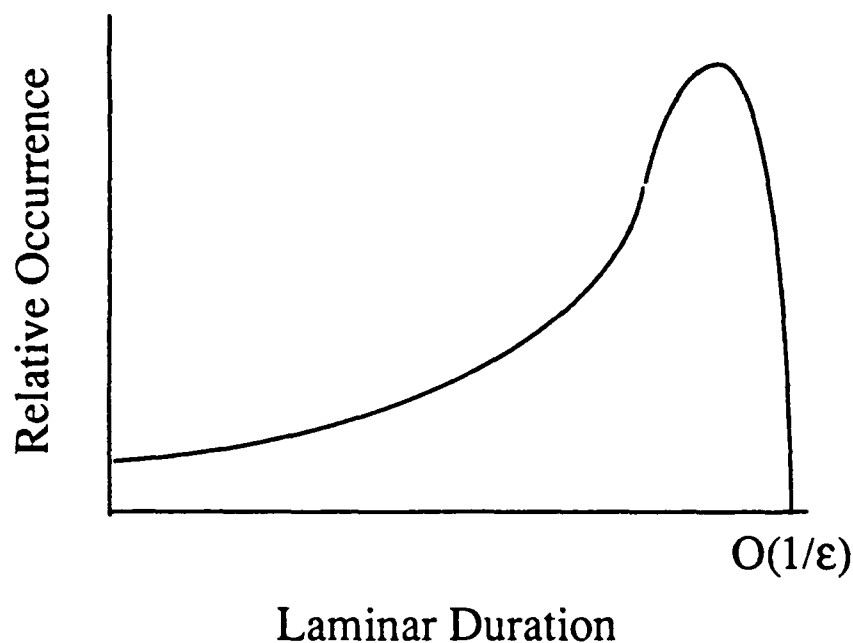
Fig. C.2 Heuristic Distribution of Laminar Durations for Type I Intermittency.

Type II Intermittency

For this type of intermittency, the flow near the fixed point of the first-return map is approximated by a relation similar to (C.3) (see Berge, et al., 1984, for details):

$$y_{n+1} = (1 + \epsilon) y_n + \mu y_n^3 + \text{higher order terms} . \qquad \text{C.6}$$

The estimate of average laminar duration which results is inconsistent with numerical experiments; Pomeau and Manneville admit there is less known analytically about the statistics of Type II intermittency than about the other two types. The best analytic treatment we found for this type of intermittency was (Argoul, et al., 1988), which concentrates on a specific three-dimensional model exhibiting Type II intermittency.

Type III Intermittency

In this type of intermittency, the Floquet multiplier decreases through -1, so the local linear approximation to the first-return map is:

$$y_{n+1} = - (1 + \varepsilon) y_n \ . \qquad \text{C.7}$$

This is different from the local flow for Type I intermittency where the fixed point disappears as ε increases through 0. Here, the fixed point still exists, but loses its stability. To see the bifurcation in this case, we use a local cubic approximation, because we eventually need to follow the 2-cycle fixed points (i.e., fixed points of the Poincaré map composed with itself):

$$y_{n+1} = - (1 + \varepsilon) y_n + \alpha y_n^2 + \beta y_n^3 \qquad \text{C.8}$$

so that

$$y_{n+2} \approx (1 + 2 \varepsilon) y_n + b y_n^3 \qquad \text{C.9}$$

where $b = -2 (\beta + \alpha^2)$. We note that the linear term here is approximately +1, and there is no quadratic term, within $O(\varepsilon)$. If $b < 0$, we get period doubling as ε increases through 0.

If b > 0, we get the inverse pitchfork illustrated by the laser rate equations in Chapter II. As before, we approximate the derivative of y near the fixed point:

$$y_{n+2} - y_n \approx \frac{dy}{dk} = y (2\epsilon + \beta y_n^2) \qquad \text{C.10}$$

and we scale y by $(2\epsilon/\beta)^{1/2}$ and scale k by $(1/\epsilon)$ to get

$$\frac{dy}{dk} = y (1 + y^2) . \qquad \text{C.11}$$

The scaling suggests that the average laminar duration is of order $(1/\epsilon)$, and that the average amplitude of fluctuations from the laminar behavior are of order $\epsilon^{1/2}$. There is no upper bound on laminar duration imposed by the approximation (C.10); is it characteristic of Type III intermittency that the distribution of laminar durations can have an infinite tail. The heuristic distribution of laminar durations proposed by Pomeau and Manneville is shown in Fig. C.3. We find in Chapter II that the statistics we gather from a numerical solution to the laser rate equations has the same features.
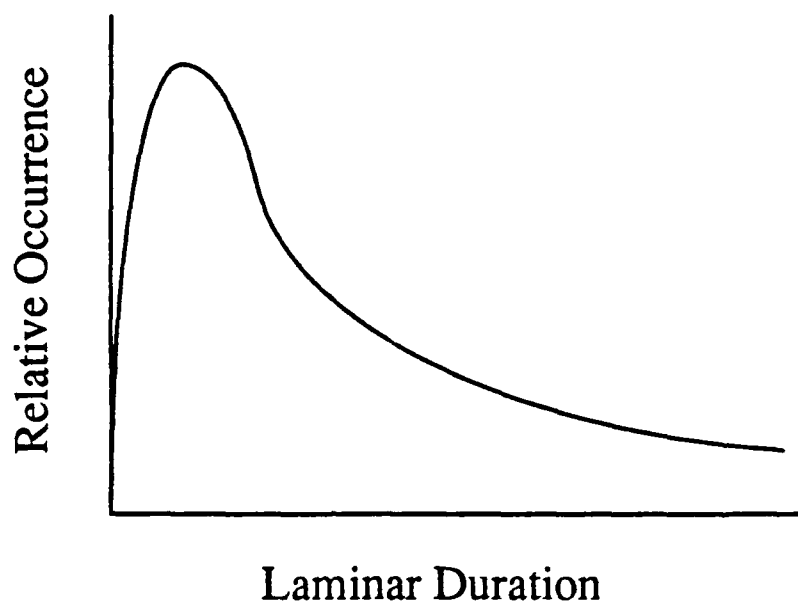
Fig. C.3 Heuristic Distribution of Laminar Durations for Type III Intermittency.

We emphasize above that the Pomeau-Manneville intermittency categories only consider local properties of the flow. Evans Harrell proposes that we attempt to characterize intermittency by estimating the time of laminar duration from an invariant measure of the flow in phase space. We illustrate this idea in Fig. C.4 with a sketch of the phase space for a metastable system, for instance, a driven pendulum with the equation: $x'' + \beta x' + \sin x = f \cos(\theta t)$. For certain parameter values, the chaotic flow of a single trajectory fills out a portion of the phase space. Intuitively, we expect a significant portion of the associated invariant measure to be supported in the periodic wells where laminar flow occurs; the time spent near the origin, switching from one well to the other, should be fairly short.

$$0 \leq \rho \leq 1$$

$$supp(d\mu)$$
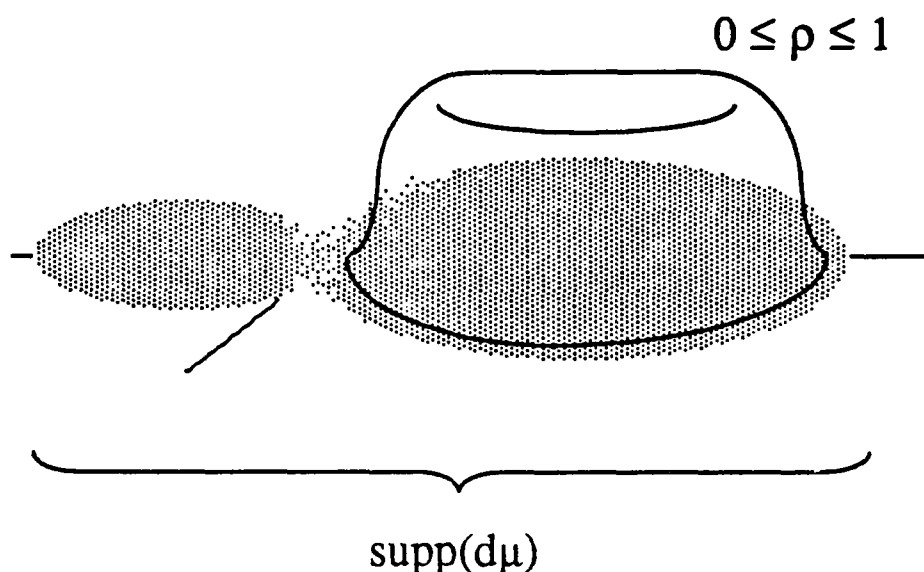
Fig. C.4 Sketch of an Invariant Measure for a Two-Well System.

More generally, suppose that we have the equations of motion for vectors x, in some manifold M, of the form

$$\frac{dx}{dt} = F(x) .$$

C.12

A nonautonomous equation (like the forced pendulum) can be converted to an autonomous system like (C.12) in a standard way by adding an additional dimension z, where $dz/dt = 1$. Let $\phi_t(x)$ be the solution operator such that $\frac{d}{dt} \phi_t(x) = F(\phi_t(x))$. While the solution operator moves individual solutions along flow vectors in the phase space M, the linear operator

$$\exp(t\, F \cdot \nabla)$$

C.13

describes the corresponding flow on an appropriate vector space of functions on the phase space, e.g., $L^p(M,d\mu)$ for some p. We observe, for example, that $(F \cdot \nabla)$ operating on the identity is zero, and $(F \cdot \nabla) \chi_S = 0$ for any invariant set S, since $\phi_t(S) = S$ and so $\exp(tF\cdot\nabla) \chi_S = \chi_S$.

Here is a possible approach to characterize intermittency. Suppose we identify the support of a suitable invariant measure $d\mu$ and let ρ be a smooth cut-off function which lies between 0 and 1 on a subset of that support. Suppose we also calculate $F\cdot\nabla\rho$ and find that

$$\| F\cdot\nabla\rho \|_{L^2(M,d\mu)} = \varepsilon \| \rho \|_{L^2(M,d\mu)} \qquad\qquad C.14$$

where ε is small. Then we expect that

$$\exp(tF\cdot\nabla) \rho \approx \rho + O(t \varepsilon \| \rho \|) \qquad\qquad C.15$$

i.e., the support of ρ is a metastable region of phase space with a characteristic time on the order of $1/\varepsilon$.

A key problem in using this operator is to define the measure $d\mu$ on M. We might to arrange, for instance, for $(iF\cdot\nabla)$ to be self-adjoint on $L^2(M,d\mu)$. Ideally, $d\mu$ would be a stationary measure generated by the dynamical system itself. Unfortunately, such measures are often concentrated on fractal sets, which makes differentiation as in (C.14) problematic. It may be preferable to use instead a Lebesgue absolutely continuous measure, such as the convolution of the fractal measure with a Gaussian. In analogy with the situation in quantum mechanics and Markov semigroups (Harrell, 1982 and 1988;

Davies, 1982) one might hope to relate the metastable times to a property of an eigenvalue of the linear operator iF·∇, such as a near degeneracy or a small imaginary part.

Estimating invariant measures can be a difficult problem; one approach to finding a measure is to approximate the Frobenius-Perron operator, whose domain is the set of measures on M (see, e.g., Li, 1976). An invariant measure of the system is a fixed point of the Frobenius-Perron operator, and an iterative method using this operator can be shown to converge to an invariant measure in certain cases. For many-dimensional systems (like our laser rate equations) the approximation to this operator has not been extensively studied.

Another finite approximation to an invariant measure can be found using the Cell-to-Cell mapping technique developed in (Hsu, 1980 through 1987). In this method, a bounded transversal of the flow is divided into a finite number of cells. By following the images of a sample of points in each cell, a probability matrix is constructed that maps a given discrete measure to its image under the Poincaré mapping. Iterating this matrix multiplication has also been shown to converge to an invariant measure on the transversal; this cell mapping method seems the most tractable technique we found for approximating invariant measures computationally.

APPENDIX D

JONES MATRICES

This appendix summarizes the fundamentals of the Jones matrix representation of electric field (E-field) propagation in a laser cavity. Jones matrices are used in Chapter III to describe the influence of intracavity optical elements on an E-field during a round trip through a laser cavity. A good source for more details of Jones matrices is the optics text by Hecht and Zajac (Hecht and Zajac, 1979); this appendix is an outline of section 8.12.2 of that text, written from the perspective of our intracavity doubled laser.

The Jones technique applies to polarized waves as they propagate along the z-axis of the laser cavity, with coordinates defined in Fig. D.1. A field vector E(t) with time-dependent scalar components

$$E(t) = \begin{bmatrix} E_x(t) \\ E_y(t) \end{bmatrix} \qquad \text{D.1}$$

completely defines the polarization state of the E-field (we are ignoring any spatial dependence on z in this discussion). To identify the time-dependent behavior of the amplitude and phase of each coordinate, we rewrite (D.1) as:

$$E(t) = \begin{bmatrix} E_{ox}(t)e^{i\varphi_x(t)} \\ E_{oy}(t)e^{i\varphi_y(t)} \end{bmatrix}. \qquad \text{D.2}$$
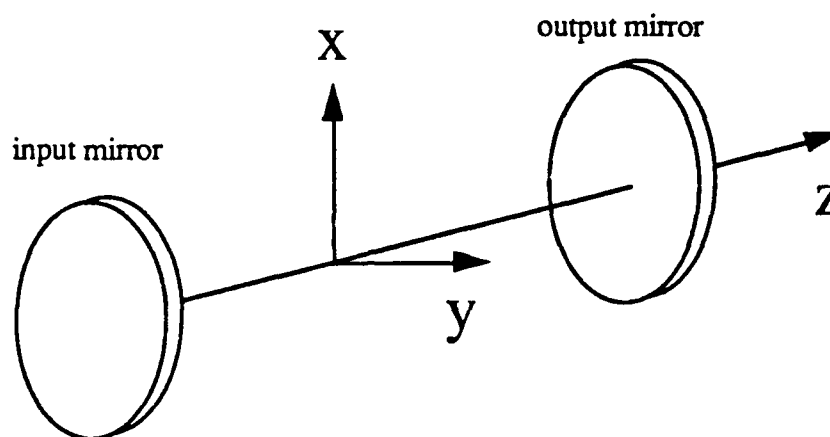
Fig. D.1. Definition of Axes in a Laser Cavity. The z-axis is often referred
to as the "optical" axis.

The following examples illustrate the form of (D.2) for specific polarization states. For instance, a linearly polarized E-field E_h which is polarized in the horizontal direction, and the field E_v polarized in the vertical direction, may be written as:

$$E_h(t) = E_0(t) e^{i\varphi(t)} \begin{bmatrix} 0 \\ 1 \end{bmatrix} \qquad E_v(t) = E_0(t) e^{i\varphi(t)} \begin{bmatrix} 1 \\ 0 \end{bmatrix}, \qquad \text{D.3}$$

while an arbitrary linearly polarized field may be written as:

$$E(t) = E_0(t) e^{i\varphi(t)} \begin{bmatrix} a \\ b \end{bmatrix} \frac{1}{(a^2+b^2)^{1/2}}, \qquad \text{D.4}$$

where a and b are constant real numbers. Notice that this is the form which we assume the E-fields take in Chapter III.

In circularly polarized E-fields, the amplitudes of the x and y components are equal, but the phase of one component differs from the other by $\pi/2$. Right-circular polarization, for example, is written as:

$$\mathbf{E}_r(t) \;=\; \begin{bmatrix} E_0(t)e^{i\varphi_x(t)} \\ E_0(t)e^{i[\varphi_x(t)-\pi/2]} \end{bmatrix}. \qquad\qquad D.5$$

We rewrite (D.5) in the normalized form of (D.3):

$$\mathbf{E}_r(t) \;=\; E_0(t)\, e^{i\varphi_x(t)} \begin{bmatrix} 1 \\ -i \end{bmatrix} \qquad\qquad D.6$$

and note that E-fields which are not linearly polarized have complex components when written in this normalized form. The most general, elliptical polarization has the form (D.2) where $E_{0x}(t)$ is not identically equal to $E_{0y}(t)$, and there is no fixed difference between $\varphi_x(t)$ and $\varphi_y(t)$.

The Jones technique uses these vectors to describe how an E-field propagates through a laser cavity. To describe the passage of an E-field through any optical element, we premultiply the vector by an appropriate matrix. (The method assumes all optical elements have uniform properties which are, in general not z-dependent.) Suppose, for example, the linearly polarized field in (D.4) encounters a birefringent crystal whose fast axis aligns with the x-axis of the cavity. Let $\hat{a}_x$ and $\hat{a}_y$ denote the normalized x and y components of E. The crystal introduces a relative phase delay δ in the y-component of the E-field. By convention, the phase shift is applied to an E-field by adding $\delta/2$ to the phase of the x-component, and subtracting $\delta/2$ from the phase of the y-component, so the matrix $C(\delta)$ for such a birefringent element is:

$$C(\delta) \ = \ \begin{bmatrix} e^{i\delta/2} & 0 \\ 0 & e^{-i\delta/2} \end{bmatrix} \qquad\qquad D.7$$

and passage through the crystal is described by premultiplication with $C(\delta)$:

$$C(\delta) \ E(t) \ = \ \begin{bmatrix} e^{i\delta/2} & 0 \\ 0 & e^{-i\delta/2} \end{bmatrix} E_0(t) \ e^{i\varphi(t)} \begin{bmatrix} a \\ b \end{bmatrix}$$

$$= \ E_0(t) \ e^{i\varphi(t)} \begin{bmatrix} a \ e^{i\delta/2} \\ b \ e^{-i\delta/2} \end{bmatrix}$$

$$= \ E_0(t) \ e^{i[\varphi(t)+\delta/2]} \begin{bmatrix} a \\ b \ e^{-i\delta} \end{bmatrix} . \qquad\qquad D.8$$

No matrix is necessary to account for an E-field's passage through free space (with no optical elements); the spatial dependence of the E-field is contained in the amplitude factor $E_0(t)$ and has simply been suppressed in this discussion. To describe the round trip of an E-field through a cavity with N elements, we begin at one end of the cavity, and premultiply by the appropriate matrix for each birefringent element; each matrix has the form (D.7). The fast and slow axes of adjacent birefringent elements are not generally parallel. However, the birefringent properties are defined along the direction of these axes, so the E-field vector must be expressed in terms of the fast and slow directions before multiplying with the birefringence matrix. This operation is accomplished by premultiplication with a rotation matrix whose angle is prescribed by the relative angle between the fast axes of the adjacent elements. The most general round trip matrix, then, includes a rotation matrix

$$R(\theta) = \begin{bmatrix} \cos\theta & -\sin\theta \\ \sin\theta & \cos\theta \end{bmatrix} \qquad \text{D.9}$$

between each pair of birefringent matrices (D.7). The general round trip matrix M is then constructed as shown in equation (3.4).

An E-field must replicate after each round trip through a laser cavity in order to sustain the lasing process. Thus, the eigenvectors of the associated round trip matrix completely describe the polarization state of a longitudinal mode in the laser. We use this polarization information in Chapter III to calculate the E-field produced in a frequency doubling crystal (see (3.10)).

APPENDIX E

ON THE UNIQUENESS OF STEADY STATE POINTS

We analyze the two-mode rate equations (2.10) by assuming symmetric parameters and linearizing about four steady state points. The first point considered is the "interior" steady state where both intensities I_1 and I_2 are positive. The approximate values for intensity and gain at this steady state (2.12) are accurate to within $O(\varepsilon)$ when we assume that the steady state in question has $I_1=I_2$. In this appendix we argue the uniqueness of this interior steady state point.

The four relations that must be satisfied for a steady state point of (2.10) are:

$$G_1 = \alpha + \varepsilon I_1 + 2\varepsilon I_2 \qquad\qquad \text{E.1.a}$$

$$\gamma = G_1 (1 + I_1 + \beta I_2) \qquad\qquad \text{E.1.b}$$

$$G_2 = \alpha + \varepsilon I_2 + 2\varepsilon I_1 \qquad\qquad \text{E.1.c}$$

$$\gamma = G_2 (1 + I_2 + \beta I_1) . \qquad\qquad \text{E.1.d}$$

We substitute the equations for G_1 and G_2 into (E.1.b and d) to get two quadratic expressions in I_1 and I_2:

$$\gamma = (1 + I_1 + \beta I_2)(\alpha + \varepsilon I_1 + 2\varepsilon I_2) \qquad\qquad \text{E.2.a}$$

$$\gamma = (1 + I_2 + \beta I_1)(\alpha + \varepsilon I_2 + 2\varepsilon I_1) . \qquad\qquad \text{E.2.b}$$

If we assume $I_1=I_2=I_s$ then (E.2) is simply a quadratic in I_s:

$$\gamma = (1 + [1+\beta] I_s)(\alpha + 3\epsilon I_s)$$

$$= \alpha + (3\epsilon + \alpha[1+\beta])I_s + 3\epsilon[1+\beta]I_s^2 \qquad \text{E.3}$$

with the (positive) solution:

$$I_s = \frac{-(3\epsilon+\alpha[1+\beta])}{6\epsilon[1+\beta]} + \frac{\sqrt{(3\epsilon+\alpha[1+\beta])^2 + 12\epsilon[1+\beta][\gamma-\alpha]}}{6\epsilon[1+\beta]}. \qquad \text{E.4}$$

Expanding the square root in terms of ϵ confirms the approximation in (2.12):

$$I_s = \frac{\gamma - \alpha}{\alpha[1+\beta]} + O(\epsilon). \qquad \text{E.5}$$

Now we look for a solution of (E.2) where $I_1 \neq I_2$. We do this graphically in Fig. E.1 (for a similar discussion, with two modes but no frequency doubling, see Sargent, et al., 1974; Siegman, 1986). We graph (E.2.a) as a solid line, and (E.2.b) as a dashed line, for different values of the cross saturation (the figure shows sketches redrawn from numerical graphs). Any intersection in the first quadrant represents an experimentally obtainable steady state solution of (2.10). We find the graphs of each function to be essentially linear; the reason is evident in (E.3). The quadratic term is multiplied by the
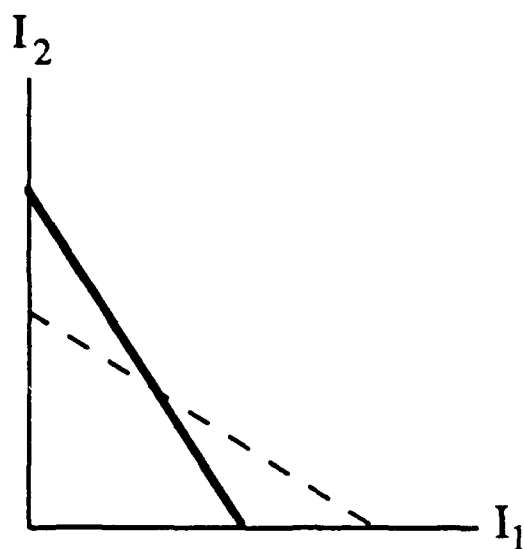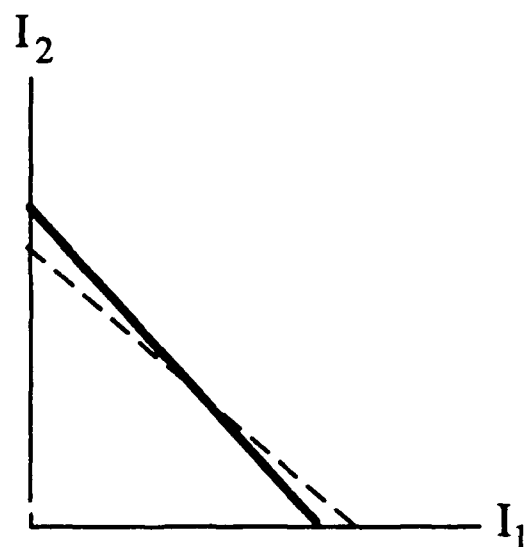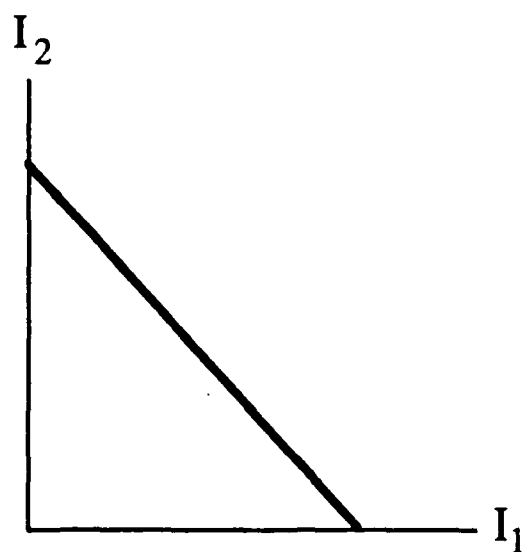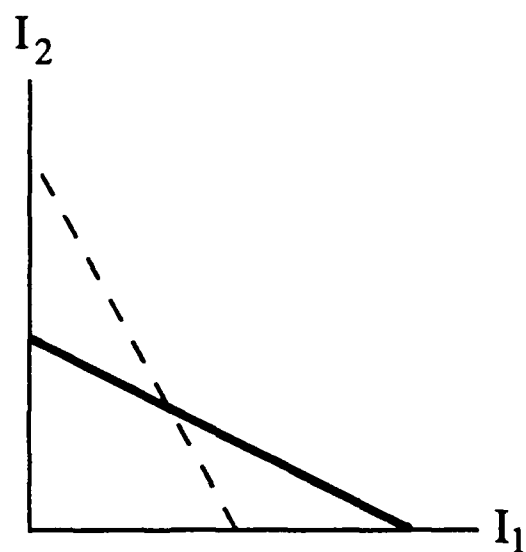
Fig. E.1 Quadratic Equations (E.2) Graphed for Selected Values of β. Solid lines are for (E.2.a); dashed lines are for (E.2.b). The intersection represents the interior steady state point. The lines coincide in (c).

small parameter ϵ, so (E.2.a), seen as a function of I_1, has a small second derivative: $6\epsilon[1+\beta]$. Thus, the curve of the quadratics is imperceptible, and the problem is essentially reduced to finding the intersection of two lines.

We see in Fig. E.1 that there is an obvious unique steady state point for β not close to 1. For $\beta\equiv 1$, there are an infinite number of solutions, i.e. $\beta\equiv 1$ renders (E.2.a) identical to (E.2.b). For $\beta \approx 1$, a numerical calculation is necessary to determine uniqueness of the solution of (E.2).

The sketches in Fig. E.1 also illustrate stability information about the four steady state points (Cases A through D for (2.10)). We find numerically that (for the parameters in Table 2) the interior steady state is a stable solution of (2.10) when $\beta<0.9$. For $\beta>1.1$, the interior steady state is unstable, and the equations are bistable. That is, there are basins

(a) $\beta = 0.666$ (b) $\beta = 2.0$
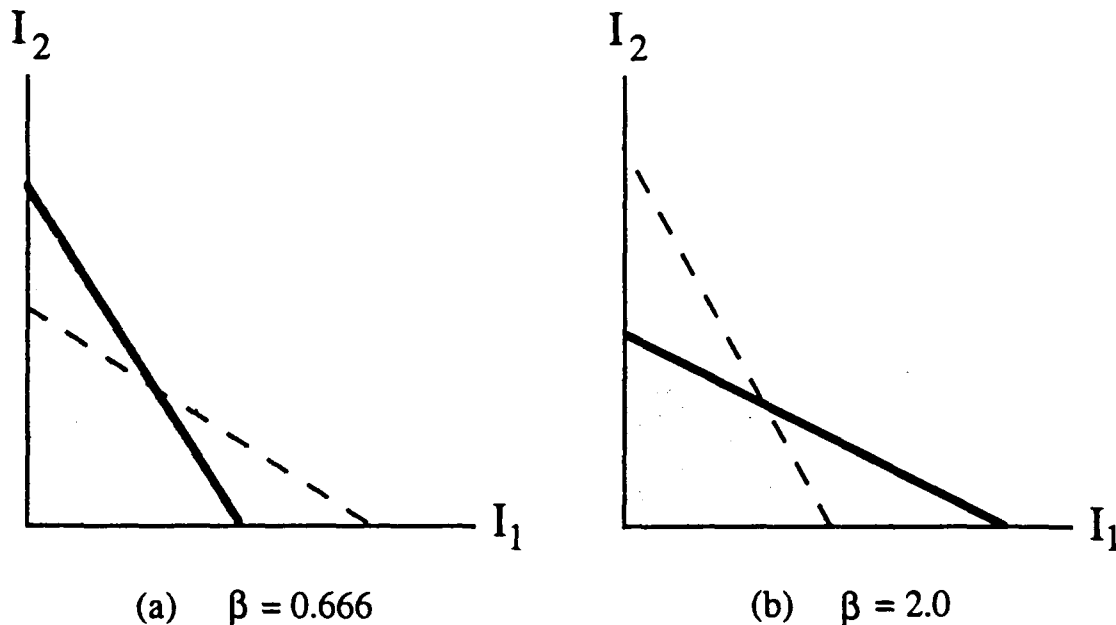
Fig. E.2   Intersection of Quadratics (E.2) Indicating Stability of Interior Steady State. An intersection inside the shaded triangle indicates weak coupling and stability (a); intersection outside the triangle indicates instability.

of attraction for both of the points where one intensity is positive and the other is zero. It is pointed out in both references above that the case of weak coupling (β<0.9) is seen graphically when the two lines intersect inside the triangle shown in Fig. E.2(a). The lines intersect outside the triangle for the case of strong coupling (β>1.1 in Fig. E.2(b)), indicating the instability of the interior steady state point.

For the more general equations (2.8) with asymmetric parameters, the graphical approach still shows the existence of a unique interior steady state point (for β not close to 1), but this point no longer has $I_1=I_2$. This steady state similarly is stable for small β and unstable for large β.

The results above further imply that models with three or more modes also have a unique interior steady state point. Since (E.3) is essentially linear, the problem of finding an interior steady state point for three modes, for example, is equivalent to finding the intersection of three planes. The quadratic formula applied to (2.26) shows the existence of such a solution; this solution is unique because the cross sections of the each pair of planes must look like Fig. E.1, so the three planes do not intersect in a line.

APPENDIX F

COMPUTER PROGRAMS

This appendix includes the main computer programs used to numerically integrate the various rate equations discussed in the thesis. A brief description of each program precedes its listing. We also include some general comments on our choices of integration routines, program parameters and initial conditions. All programs are written in Fortran 77 and run on the Georgia Institute of Technology Cyber 855 and Cyber 990 computers. Eigenvalue calculations are performed by the EISPACK routine RG.

Numerical integrations are performed with IMSL routine DGEAR, using the Adams integrator (METH=1) and the approximate Jacobian (MITER=2). We chose this integrator over the stiff Gear method (METH=1) and the Runge-Kutta integrator in the IMSL routine DVERK. We compared extensive calculations with DGEAR and DVERK and found that, with the same error tolerance (10^{-8} to 10^{-12}) DVERK generally takes 5 to 10 times longer to integrate the same two-mode equations (2.24). For example, with TOL=1.0×10^{-12}, DT=50 nsec and 5000 time steps, DGEAR ran the integration in 6 cp sec, while DVERK ran the problem in 43 cp sec.

The large difference in time scales in our equations (see τ_c and τ_f in Table 1) does not force us to use the stiff Gear integrator in DGEAR. The most efficient integrator for our equations is the DGEAR Adams method, with no analytic Jacobian calculated (i.e., MITER=2). We see no gain in speed or accuracy using the analytic Jacobian (MITER=1).

We run DGEAR with error tolerances from 10^{-5} to 10^{-8} and observe no difference in the numerical results. All numerical data presented in this thesis were run with TOL in this range of values. We also integrate with a small, regular time step, between 1 and 10

nanoseconds. We use a fixed time step to allow efficient fast Fourier transforms (FFT's) of numerical time histories which can be directly compared to experimental data.

The large number of variables in our rate equations make it difficult to numerically integrate from enough initial conditions to be sure we observe all possible numerical solutions. We generally choose initial conditions the following way. For the first integration of a new set of equations, say (2.24), we let the intensity variables be small ($I_j = 0.001$) and the gain variables be near their equilibrium values ($G_j = \alpha$). We then numerically integrate until we observed some limiting behavior such as a stable steady state or periodic cycle. These integrations usually require very small time steps since the intensity gradients are steep during the early transient times. We form a restart file with the values of intensity and gain at the end of each integration; the restart file serves as the initial condition for further integrations with different parameters.

POLYAG3 integrates rate equations (3.25) for the special case of three modes oscillating in the same polarization direction, i.e., N=3, P=0. ("YAG" in the program name indicates Nd:YAG rate equations, "POL" identifies our new model for polarization states, "3" indicates three parallel modes.) The program requires an input file of initial conditions, and keyboard input of: time step, dt; number of integration steps, nsteps; value for the doubling coefficient, g; and pump strength, p.

The output files are:

TAPE 4: Lists all parameter settings and contains digital time histories of the total fundamental and doubled intensities; is used to plot time histories like Fig. 3.17(a).

TAPE 8: Contains the values of intensities and gains at the end of the integration; is used as an initial condition for later integrations.

TAPE 9: (optional) Lists all parameter values and contains FFT of total intensity data; is used to make frequency plots like Fig. 3.17(c).

TAPE 10: (optional) Lists all parameter values and contains digital time histories of the intensity of each mode; is used to plot time histories like Fig. 3.17(b).

The program time t is expressed in nanoseconds.

```
              PROGRAM POLYG3(TAPE 3,TAPE 4,TAPE 8,TAPE 9,TAPE 10)
C
C       USAGE:
C        LGO,INITIALFILE(INPUT),OUTPUTFILE,RESTARTFILE(OUTPUT),
C                   FFTOUTPUTFILE,INTENSITIESOUTPUT
C       THIS VERSION INCLUDES SAME-POL'ZATION COUPLING. ALL 3
C        MODES SAME
C       OUTPUT TOTAL INTENSITIES,INDIVIDUAL INTENSITIES, FFT'S
C       THIS VERSION USES THE G-DEPENDENT LOSS-MODEL
C       USE IMSL ROUTINE DGEAR TO NUMERICALLY INTEGRATE
C       SIX 1ST-ORDER DIFF EQ'S DESCRIBING THE TIME-DEPENDENT
C       INTENSITIES AND GAINS FOR 3 MODES IN A ND:YAG LASER
C       WITH AN INTRA-CAVITY DOUBLING CRYSTAL.
C       OUR CAVITY IS ABOUT 3. CM AND OUTPUT COUPLER TRANSMITS
C       .005 OF THE FUNDAMENTAL FREQUENCY
C
C       REF: T. BAER, J. OPT. SOC. AM. B, VOL 3, NO 9, SEP 86,
C          1177.
C
          REAL I1,G1,I2,G2,I3,G3
          REAL WK(200000),ITOT(200000),IDUB(200000)
          INTEGER IWK(200000)
          COMPLEX X(200000)
          COMMON /LOGIC/ RISING,THRESH
          CHARACTER*1 ANS
  73    WRITE(*,2201)
  2201  FORMAT(/" INPUT DT IN NANOSECONDS AND NSTEPS")
        READ(*,2202) DT,NSTEPS
  2202  FORMAT(E11.4,/,I6)
        WRITE(*,2203) DT,NSTEPS
  2203  FORMAT(/" DT = ",E11.4,"    NSTEPS = ",I6," OK?")
        READ(*,700) ANS
  700   FORMAT(A1)
        IF(ANS.NE.'Y'.AND.ANS.NE.'Y') GOTO 73
C
C       SUBROUTINE KNOB SETS THE VALUE OF DOUBLING PARAM G
C       INTEG PERFORMS INTEGRATES THE EQUATIONS IN ROUTINE FCN
C
        CALL KNOB
        CALL INTEG(DT,NSTEPS,ITOT,IDUB,X,WK,IWK)
        END
C
        SUBROUTINE INTEG(DT,NSTEPS,ITOT,IDUB,X,WK,IWK)
C
C        MAIN INTEGRATION ROUTINE
C
        REAL I1,G1,I2,G2,I3,G3,ITOT(NSTEPS),IDUB(NSTEPS)
        COMPLEX X(NSTEPS)
        REAL WK(3*NSTEPS+200),H
        INTEGER IWK(3*NSTEPS+200)
```

```fortran
      REAL I1INIT,I2INIT,I1NEXT,I2NEXT,I3INIT,I3NEXT
      REAL Y(6)
      CHARACTER*1 ANS
      EXTERNAL FCN,FCNJ
C
C     THE VECTOR Y HOLDS THE INTENSITY AND GAIN VARIABLES
C
      EQUIVALENCE (Y(1),I1),(Y(2),G1),(Y(3),I2),(Y(4),G2),
     &            (Y(5),I3),(Y(6),G3)
      LOGICAL FIRST,FLAG,PEAKED,PASSED,RISING
      COMMON /LOGIC/ RISING,THRESH
C
      COMMON / /
     & TAUC,TAUF,EPS,A1,A2,A3,B,B12,B21,G10,G20,B13,B23,
     &           B31,B32,G30
      COMMON /DBAND/ NLC,NUC
      COMMON /GEAR/ DUMMY(48),SDUMMY(4),IDUMMY(38)
      COMMON /GJ/ G,SIG,ANGLE
C
C
C     OPEN(UNIT=3,FILE='YAGIN',STATUS='OLD')
C     OPEN(UNIT=4,FILE='YAGOUT')
      WRITE(*,'(" DO YOU WANT OUTPUT OF INDIVIDUAL
     & INTENSITIES?")')
      READ(*,700) ANS
  700 FORMAT(A1)
      FLAG=.FALSE.
      IF(ANS.EQ.'Y'.OR.ANS.EQ.'Y') FLAG=.TRUE.
C
      NWK=6
C          NWK: NUMBER OF DIFFL EQUATIONS
      TOL=1.E-5
C              ERROR TOLERANCE FOR INTEGRATOR
C
C     SET PARAMATER DEFAULTS
C
      TAUC=0.2
C              NANOSEC, CAVITY ROUND-TRIP TIME
      TAUF=0.24E6
C                  NANOSEC, FLUORESCENCE LIFETIME
      A1=0.010
C                  MODE-1 LOSSES
      A2=0.010
C                  MODE-2 LOSSES
      A3=0.010
C                    MODE-3 LOSSES
      EPS=5.E-5
C              1/W  NONLINEAR COUPLING COEFFICIENT
      B=1.
C            1/W  SATURATION PARAMETER
C     WRITE(*,'(" INPUT COMMON CROSS-SATURATION PARAM")')
```

```
C       READ(*,'(F20.18)') BIJ
C       SET BIJ LARGE ENOUGH TO ALLOW POSSIBILITY OF CHAOS
        BIJ=.6
C
        B12=BIJ
C                       1/W  CROSS-SATURATION PARAMETER
        B21=B12
C
        B13=BIJ
        B31=B13
C
        B23=BIJ
        B32=B23
C
C       G10=0.12
C               SMALL-SIGNAL GAIN
C       G20=0.12
C
C       G30=0.12
        WRITE(*,'(/," INPUT PUMP AS FRAC OF THRESHOLD
     &     (TH=1.)")')
        READ(*,'(F5.2)') P
        PUMP=P*A1
        G10=PUMP
        G20=PUMP
        G30=PUMP
C
        READ(3,101)
     &    TINIT,DTB,NSTEPSB,I1INIT,G1INIT,I2INIT,G2INIT,
     &            I3INIT,G3INIT
  101  FORMAT(E11.4,/,E11.4,
     &         /,I6,/,E20.14,/,E20.14,/,E20.14,/,E20.14,
     &         /,E20.14,/E20.14)
C
C
        T=TINIT
        Y(1)=I1INIT
        Y(2)=G1INIT
        Y(3)=I2INIT
        Y(4)=G2INIT
        Y(5)=I3INIT
        Y(6)=G3INIT
        TSTOP=T
C
C       OPEN(UNIT=9,FILE='FFTOUT')
        WRITE(9,201)
     &    TOL,TAUC,TAUF,A1,A2,A3,EPS,B,B12,B21,B13,B31,B23,
     &           B32,G10,G20,G30,DT,NSTEPS,G,P
        WRITE(4,201)
     &    TOL,TAUC,TAUF,A1,A2,A3 EPS,B,B12,B21,B13,B31,B23,
     &           B32,G10,G20,G30,DT,NSTEPS,G,P
```

```
      WRITE(10,201)
     &    TOL,TAUC,TAUF,A1,A2,A3,EPS,B,B12,B21,B13,B31,B23,
     &         B32,G10,G20,G30,DT,NSTEPS,G,P
 201  FORMAT("DGEAR INTEGRATION OF FREQUENCY-DOUBLED ND:YAG
     &    SYSTEM",//,
     &         "TOL = ",E11.4,/,
     &         "TAUC = ",E11.4," NSEC",/,"TAUF = ",E11.4,"
     &    NSEC",/,
     &         "ALPHA1 = ",E11.4,/,"ALPHA2 = ",E11.4,/,"ALPHA3
     &    = ",E11.4,
     &         /,"EPS = ",E11.4,
     &         " 1/W",//,"BETA = ",E16.9," 1/W",//,"BETA12 =
     &    ",E16.9," 1/W"
     &         ,/,"BETA21 = ",E16.9," 1/W",//,"BETA13 =
     &    ",E16.9,/,
     &         "BETA31 = ",E16.9,/,"BETA23 = ",E16.9,/,"BETA32
     &    = ",E16.9,
     &         /,"G10 = ",E11.4,/,"G20 = ",E11.4,/,"G30 = ",
     &         E11.4,/,"DT = ",E11.4," NSEC",/,"NSTEPS = ",I6,
     &         4X,"DOUBLING COEF  G = ",F9.5," PUMP = ",F5.2)
      WRITE(4,211)
      WRITE(10,219)
 219  FORMAT(//,"T (NANOSEC)",9X,"I1 (WATTS)",14X,"I2
     &    (WATTS)",
     &         14X,"I3 (WATTS)",/)
 211  FORMAT(//,"T (NANOSEC)",8X,"FUNDAMENTAL",14X," DOUBLED
     &    ",/,
     &              18X,"OUTPUT (WATTS)",10X,"OUTPUT (WATTS)",/)
C
      IF(FLAG) WRITE(10,105) T,Y(1),Y(3),Y(5)
      TOT=Y(1)+Y(3)+Y(5)
      DUB=EPS*(G*(I1*I1+I2*I2+I3*I3)
     &     +4.*G*(I1*I2+I2*I3+I3*I1))
      WRITE(4,105) T,TOT,DUB
C
 105  FORMAT(E11.4,4X,3(E20.14,4X))
C
      IND=1
CCCCCC
      TSTOP=0
      IFLAG=0
      FIRST=.TRUE.
      PASSED=.FALSE.
      RISING=.FALSE.
C
 298  CONTINUE
      NFFT=NSTEPS
      NRESET=0
      H=DT/2.
      METH=1
      MITER=2
```

```
C
C       METH=1:ADAMS,2:STIFF  MITER=1:USE FCNJ, 2:FCNJ IS DUMMY
        DO 100 J=1,NSTEPS
        T=TSTOP
        TSTOP=T+DT
        IFLAG=IFLAG+1
C
C
        CALL DGEAR (NWK,FCN,FCNJ,T,H,Y,TSTOP,TOL,METH,
     &              MITER,IND,IWK,WK,IER)
C
C       PRINT*, J,DUMMY(8),IDUMMY(6),IDUMMY(7)
C
        IF(IER.GT.130) THEN
            WRITE(*,113) J,IND,IER
            GO TO 123
  113   FORMAT(/," STEP ",I6,/," ERROR TERMINATION.  IND =
     &     ",I2,
     &           "  IER = ",I4,/)
        ENDIF
C
        ITOT(J)=Y(1)+Y(3)+Y(5)
        IDUB(J)=EPS*(G*(I1*I1+I2*I2+I3*I3)
     &          +4.*G*(I1*I2+I2*I3+I3*I1))
        IF(IFLAG.GE.10) THEN
            IF(FLAG) WRITE(10,105) T,I1,I2,I3
C           WRITE(*,105) T,I1,I2,I3
            WRITE(4,105) T,ITOT(J),IDUB(J)
C
            IFLAG=0
        ENDIF
C
C
  100   CONTINUE
        WRITE(*,'(" Y:",6(1X,E10.4))') (Y(KK),KK=1,6)
        WRITE(*,'(" INTEGRATION STEP ",I7," REACHED",/,
     &       .  " WANNA GO ON?")')
     & NSTEPS
        READ(*,'(A)') ANS
        IF(ANS.EQ.'Y'.OR.ANS.EQ.'Y') GOTO 298
  123   CONTINUE
        IF(NRESET.NE.0) PRINT*,' NUMBER OF RESETS = ',NRESET
CCCCCCCCCCCC
C       OPEN(UNIT=8,FILE='RESTART')
  717   WRITE(8,707) T,G,Y(1),Y(2),Y(3),Y(4),Y(5),Y(6)
  707   FORMAT(E11.4,20X,"RESTART TIME",/,E11.4,20X,"DOUBLING
     &     COEF",/,
     &           "0",20X,"PUT NSTEPS HERE
     &     (I6)",/,E20.14,20X,"I1",/,
     &
     &     E20.14,20X,"G1",/,E20.14,20X,"I2",/,E20.14,20X,"G2"
```

```
     &           ,/,E20.14,20X,"I3",/,E20.14,20X,"G3")
C
      WRITE(*,'(" WANNA DO FFT?")')
      READ(*,'(A)') ANS
      IF(ANS.EQ.'N'.OR.ANS.EQ.'N') GO TO 7777
C
C     FFT IS TAKEN ON LAST NSTEPS OF IDUB DATA
      LENX=INT(NFFT/2.)+1
      FNYQ=1./(2.*DT)
      DFREQ=FNYQ/FLOAT(LENX)
C     CALL FFTRC(ITOT,NFFT,X,IWK,WK)
C     WRITE(9,2901) DFREQ,FNYQ,"ITOT",LENX

C     WRITE(9,2902) (X(K)/NFFT, K=1,LENX)
 2901 FORMAT(//," DFREQ = ",E13.4,"     NYQUIST = ",E13.4,
     &          "     FFT FOR ",A4,/,I6," FOURIER
     &   COEFFICIENTS",//)
 2902 FORMAT(2(E13.6))
      CALL FFTRC(IDUB,NFFT,X,IWK,WK)
      WRITE(9,2901) DFREQ,FNYQ,"IDUB",LENX
      WRITE(9,2902) (X(K)/NFFT, K=1,2000)
C     CALL FFTRC(G1,NFFT,X,IWK,WK)
C     WRITE(9,2901) "G1",LENX
C     WRITE(9,2902) (X(K)/NFFT, K=1,LENX)
C     CALL FFTRC(I2,NSTEPS,X,IWK,WK)
C     WRITE(9,2901) DFREQ,FNYQ,"I2",LENX
C     WRITE(9,2902) (X(K)/NSTEPS, K=1,LENX)
C     CALL FFTRC(G2,NSTEPS,X,IWK,WK)
C     WRITE(9,2901) "G2",LENX
C     WRITE(9,2902) (X(K)/NSTEPS, K=1,LENX)
C
 7777 STOP
      END
C
      SUBROUTINE FCN(N,T,Y,YPRIME)
C
C       DIFFERENTIAL EQUATIONS INTEGRATED BY DGEAR
C       THESE EQUATIONS ARE FOR THREE MODES IN THE SAME
C       POLARIZATION DIRECTION
C
      REAL I1,G1,I2,G2,I3,G3
      LOGICAL RISING
      REAL Y(6),YPRIME(6)
C
      COMMON /LOGIC/ RISING,THRESH
      COMMON / /
     &   TAUC,TAUF,EPS,A1,A2,A3,B,B12,B21,G10,G20,B13,B23,
     &            B31,B32,G30
      COMMON /GJ/ G,SIG,ANGLE
      I1=Y(1)
      G1=Y(2)
```

```
          I2=Y(3)
          G2=Y(4)
          I3=Y(5)
          G3=Y(6)
C
          YPRIME(1)=((G1-A1-G*EPS*I1-2.*G*EPS*(I2+I3))*I1)/TAUC
          YPRIME(2)=(G10-(B*I1+B12*I2+B13*I3+1.)*G1)/TAUF
          YPRIME(3)=((G2-A2-G*EPS*I2-2.*G*EPS*(I1+I3))*I2)/TAUC
          YPRIME(4)=(G20-(B*I2+B21*I1+B23*I3+1.)*G2)/TAUF
          YPRIME(5)=((G3-A3-G*EPS*I3-2.*G*EPS*(I1+I2))*I3)/TAUC
          YPRIME(6)=(G30-(B*I3+B31*I1+B32*I2+1.)*G3)/TAUF
C
          RISING=.TRUE.
C         IF(YPRIME(2).LT.0) RISING=.FALSE.
          END
C
          SUBROUTINE FCNJ(N,X,Y,PD)
          REAL Y(6),PD(6,6)
          REAL I1,G1,I2,G2,I3,G3
C
C           DUMMY ROUTINE FOR MITER = 2
C
          END
C
C
          SUBROUTINE KNOB
C
          CHARACTER*1 ANS
          REAL NSQ1,NSQ2,NUM
          COMMON /GJ/ G,SIG,ANGLE
C
 1        CONTINUE
          WRITE(*,'(/" INPUT DOUBLING COEFFICIENT G  (F7.5)")')
          READ(*,'(F7.5)') G
          SIG=2.*(1.-G)
 15       WRITE(*,'(/" G = ",E10.4," SIG = ",E10.4)') G,SIG
          WRITE(*,'(/" ARE THESE SETTINGS OK?")')
          READ(*,'(A)') ANS
          IF(ANS.NE.'Y'.AND.ANS.NE.'Y') GOTO 1
C
          END
```

POLYAG2 integrates (3.25) for N=2 and P=1, i.e., with two modes in one polarization direction and a third mode in the orthogonal direction. The entire structure of the program is identical to that of POLYAG3, except for the specific equations in routine FCN, so only the program lines unique to POLYAG2 are listed here.

The program time t is expressed in nanoseconds.

```
          PROGRAM POLYG2(TAPE 3,TAPE 4,TAPE 8,TAPE 9,TAPE 10)
C
C       USAGE:
C       LGO,INITIALFILE(INPUT),OUTPUTFILE,RESTARTFILE(OUTPUT),
C                    FFTOUTPUTFILE,INTENSITIESOUTPUT
            O
            O
            O

 7777 STOP
          END
C
          SUBROUTINE FCN(N,T,Y,YPRIME)
          REAL I1,G1,I2,G2,I3,G3
          LOGICAL RISING
          REAL Y(6),YPRIME(6)
C
          COMMON /LOGIC/ RISING,THRESH
          COMMON / /
        &     TAUC,TAUF,EPS,A1,A2,A3,B,B12,B21,G10,G20,B13,B23,
        &              B31,B32,G30
          COMMON /GJ/ G,SIG,ANGLE
          I`=Y(1)
          G1=Y(2)
          I2=Y(3)
          G2=Y(4)
          I3=Y(5)
          G3=Y(6)
C
          YPRIME(1)=((G1-A1-G*EPS*I1-2.*G*EPS*I2-
        &     SIG*EPS*I3)*I1)/TAUC
          YPRIME(2)=(G10-(B*I1+B12*I2+B13*I3+1.)*G1)/TAUF
          YPRIME(3)=((G2-A2-G*EPS*I2-2.*G*EPS*I1-
        &     SIG*EPS*I3)*I2)/TAUC
          YPRIME(4)=(G20-(B*I2+B21*I1+B23*I3+1.)*G2)/TAUF
          YPRIME(5)=((G3-A3-G*EPS*I3-SIG*EPS*(I1+I2))*I3)/TAUC
          YPRIME(6)=(G30-(B*I3+B31*I1+B32*I2+1.)*G3)/TAUF
C
          RISING=.TRUE.
C         IF(YPRIME(2).LT.0) RISING=.FALSE.
          END
C
          SUBROUTINE FCNJ(N,X,Y,PD)
          REAL Y(6),PD(6,6)
          REAL I1,G1,I2,G2,I3,G3
C
C         DUMMY ROUTINE WHEN MITER = 2
          END
```

P3PK integrates the same equations as POLYAG3 with a different purpose. This program can output all gain and intensity variables at a fixed (input) transversal cross-section defined by a plane G_1 = constant. The output file TAPE 4 lists all parameter values and contains the values of G_2 and G_3 on the transversal; this output is used to plot numerical Poincaré maps like those in Fig. 3.17(e). Note the use of a refined time step in the integration routine INTEG to get more accurate output as the numerical trajectory passes through the transversal.

The program time t is expressed in nanoseconds.

```
            PROGRAM P3PK(TAPE 3,TAPE 4,TAPE 8,TAPE 9)
C
C       USAGE:
C       LGO,INITIALFILES(INPUT),OUTPUTFILE,RESTARTFILE(OUTPUT)
C            ***    FFTOUTPUTFILE,INTENSITIESOUTPUT *** NOT
C         USED HERE
C       THIS VERSION HAS 3 MODES IN SAME POLARIZATION DIRECTION
C       OUTPUT ONLY G2,G3, AT CROSSING OF POINCARE SECTION
C       USE IMSL ROUTINE DGEAR TO NUMERICALLY INTEGRATE
C       SIX 1ST-ORDER DIFF EQ'S DESCRIBING THE TIME-DEPENDENT
C       INTENSITIES AND GAINS FOR 3 MODES IN A ND:YAG LASER
C       WITH AN INTRA-CAVITY DOUBLING CRYSTAL.
C       OUR CAVITY IS ABOUT 3 CM. OUTPUT COUPLER TRANSMITS
C         0.005 FUNDAMENTAL FREQUENCY
C
C       REF: T. BAER, J. OPT. SOC. AM. B. VOL 3, NO 9, SEP 86,
C         1177.
C
        REAL NORM
        REAL X0(6),X1(6),Y0(6),Y1(6),YK(6),YKP1(6),Y(6)
        INTEGER IPVT(6)
        CHARACTER*1 ANS
        COMMON /GWORK/ NWK,TOL,DT,ANS
        COMMON / /
     &      TAUC,TAUF,EPS,A1,A2,A3,B,G10,G20,G30,G1,NCUTS
        COMMON /DBAND/ NLC,NUC
        COMMON /GEAR/ DUMMY(48),SDUMMY(4),IDUMMY(38)
        COMMON /REF/ SR,BR,THETA,XR(6)
        COMMON /LOGIC/ RISING,THRESH
        COMMON /GJ/ G,SIG,ANGLE
        EXTERNAL NORM
        PI=3.14159265359
   73   WRITE(*,2201)
 2201   FORMAT(/" INPUT DT (NANOSEC), AND NCUTS TO GENERATE")
        READ(*,'(E10.4,/,I5)') DT,NCUTS
C       DT=10.0
C       NCUTS=1
 2202   FORMAT(E11.4)
        WRITE(*,2203) DT,NCUTS
 2203   FORMAT(/" DT = ",E11.4," NCUTS = ",I5,"  OK?")
        READ(*,700) ANS
C       ANS='Y'
  700   FORMAT(A1)
        IF(ANS.NE.'Y'.AND.ANS.NE.'Y') GOTO 73
        WRITE(*,'(/" INPUT POINCARE-CUT THRESHOLD (E15.9)")')
        READ(*,'(E15.9)') THRESH
C         SET POINCARE CROSS-SECTION AT G1=THRESH
C       THRESH=.0165
        G1=THRESH
```

```
C
      NWK=6
C            NWK: NUMBER OF DIFFL EQUATIONS
      TOL=1.E-8
C
C     SET PARAMATER DEFAULTS USED IN THE PAPER
C
      TAUC=0.2
C               NANOSEC, CAVITY ROUND-TRIP TIME
      TAUF=0.24E6
C               NANOSEC, FLUORESCENCE LIFETIME
      A1=0.010
C               MODE-1 LOSSES
      A2=0.010
C               MODE-2 LOSSES
      A3=0.010
C
      EPS=5.E-5
C             1/W   NONLINEAR COUPLING COEFFICIENT
      B=1.
C          1/W   SATURATION PARAMETER
C     WRITE(*,'(" INPUT COMMON CROSS-SATURATION PARAM")')
C     READ(*,'(F20.18)') BIJ
C
C     G10=0.12
C             SMALL-SIGNAL GAIN
C     G20=0.12
C
C     G30=0.12
      WRITE(*,'(/," INPUT PUMP AS FRAC OF THRESHOLD (E.G.
     &          TH=1.)")')
      READ(*,'(F5.2)') P
      PUMP=P*A1
      G10=PUMP
      G20=PUMP
      G30=PUMP
      CALL READIN(3,X1,B1)
      BX=.6
      CALL KNOB
C     DANGLE=ANGLE*180./PI
C
      WRITE(4,201)
     &    TOL,TAUC,TAUF,A1,A2,A3,EPS,B,BX,BX,EX,BX,BX,
     &         BX,G10,G20,G30,DT,NCUTS,THRESH,G,P
 201  FORMAT("DGEAR INTEGRATION OF FREQUENCY-DOUBLED ND:YAG
     &    SYSTEM",//,
     &         "TOL = ",E11.4,/,
     &         "TAUC = ",E11.4," NSEC",/,"TAUF = ",E11.4,"
     &    NSEC",/,
     &         "ALPHA1 = ",E11.4,/,"ALPHA2 = ",E11.4,/,"ALPHA3
     &    = ",E11.4,
```

```
      &           /,"EPS = ",E11.4,
      &           " 1/W",/,"BETA = ",E16.9," 1/W",/,"BETA12 =
      &      ",E16.9," 1/W"
      &          ,/,"BETA21 = ",E16.9," 1/W",/,"BETA13 =
      &      ",E16.9,/,
      &          "BETA31 = ",E16.9,/,"BETA23 = ",E16.9,/,"BETA32
      &      = ",E16.9,
      &          /,"G10 = ",E11.4,/,"G20 = ",E11.4,/,"G30 = ",
      &          E11.4,/,"DT = ",E11.4," NSEC",/," NCUTS = ",I6,
      &          1X," POINCARE SECT AT = ",F8.5,
      &          " DOUBLING COEFF  G   = ",F9.4," RELATIVE PUMP
      &      = ",F5.2)
         WRITE(4,211)
  211  FORMAT(//," CUT-TO-CUT ",13X,"     G2      ",
      & 4X,"     G3  ",/," TIME (MICROSC)",10X,"    AT SLICE
      &      ",/)
CCCCCCCCCCCCCCCCCCCCC SET UP FOR G1=CONST
         YK(1)=X1(1)
         G1=X1(2)
         DO 15 K=2,5
   15    YK(K)=X1(K+1)
C
C        PASS CROSS-SATURATION TO ROUTINE INTEG VIA YK(6)
C
         YK(6)=BX
C
   75    DO 25 K=1,NCUTS
         CALL INTEG(YK,DELT)
         WRITE(4,'(1X,3(E14.7,2X))') DELT,YK(3),YK(5)
         WRITE(*,'(1X,3(E14.7,2X))') DELT,YK(3),YK(5)
         IF(ANS.EQ.'N'.OR.ANS.EQ.'N') GOTO 82
   25    CONTINUE
C
         WRITE(*,'(" Y:",6(1X,E10.4))') (YK(KK),KK=1,6)
         WRITE(*,'(/" WANNA DO MORE POINTS?")')
         READ(*,'(A)') ANS
         IF(ANS.EQ.'Y'.OR.ANS.EQ.'Y') THEN
            WRITE(*,'(/" INPUT # OF ADDITIONAL POINTS ")')
            READ(*,'(I5)') NCUTS
            GOTO 75
         ENDIF
   82    CALL ALLOUT(YK,G1)
         STOP
         END
C
         SUBROUTINE INTEG(Z,DELT)
C
         REAL I1,G1,I2,G2,I3,G3,ZIN(6),Z(6)
         REAL H,WK(1000),IPREV
         INTEGER IWK(1000)
         REAL Y(6),YSAV(6)
```

```
         CHARACTER*1 ANS
         LOGICAL FIRST,FLAG,PEAKED,PASSED,RISING
         EXTERNAL FCN,FCNJ
C
         COMMON /GWORK/ NWK,TOL,DT,ANS
         COMMON / /
     &    TAUC,TAUF,EPS,A1,A2,A3,B,G10,G20,G30,G1,NCUTS
         COMMON /PARAM/ B12,B21,B23,B32,B13,B31
         COMMON /DBAND/ NLC,NUC
         COMMON /GEAR/ DUMMY(48),SDUMMY(4),IDUMMY(38)
         COMMON /LOGIC/ RISING,THRESH
         COMMON /GJ/ G,SIG,ANGLE
C
 700     FORMAT(A1)
         DTSAV=DT
C
C        SAVE DT BECAUSE WE REFINE DT AS WE CROSS TRANSVERSAL
C        TO GET AN ACCURATE MAP
C
         BX=Z(6)
         Z(6)=BX
C
         B12=BX
C                     1/W   CROSS-SATURATION PARAMETER
         B21=B12
C
         B13=BX
         B31=B13
C
         B23=BX
         B32=B23
         Y(1)=Z(1)
         Y(2)=G1
         Y(3)=Z(2)
         Y(4)=Z(3)
         Y(5)=Z(4)
         Y(6)=Z(5)
C        WRITE(*,'(" Y:",6(1X,E10.4))') (Y(KK),KK=1,6)
C
C
 105     FORMAT(E11.4,4X,3(E20.14,4X))
C
         IND=1
         TSTOP=0
         NRESET=0
         IFLAG=0
         TCUT=TSTOP
         FIRST=.TRUE.
         PASSED=.FALSE.
         TLAST=0
         RISING=.FALSE.
```

```
C
       ICUT=0
       NITS=100000
  298  CONTINUE
  299  DO 100 J=1,NITS
       T=TSTOP
       TSTOP=T+DT
C
       H=DT/2.
C      WRITE(*,'(" J,T,TSTOP,DT",I4,3(2X,E13.5))')
      &    J,T,TSTOP,DT
       METH=1
       MITER=2
       DO 10 K=1,6
  10   YSAV(K)=Y(K)
C
       CALL DGEAR (NWK,FCN,FCNJ,T,H,Y,TSTOP,TOL,METH,
      &            MITER,IND,IWK,WK,IER)
C      WRITE(*,'(" Y:",6(1X,E10.4))') (Y(KK),KK=1,6)
C
C      PRINT*, J,DUMMY(8),IDUMMY(6),IDUMMY(7)
C
       IF(IER.GT.130) THEN
           WRITE(*,113) J,IND,IER
           GO TO 123
  113  FORMAT(/," STEP ",I6,/," ERROR TERMINATION.  IND =
      &    ",I2,
      &            "  IER = ",I4,/)
       ENDIF
C
C      OUPTUT ALL VARIABLES BUT G1 WHEN POINCARE SECTION IS
C        CROSSED WITH
C      G1 DECREASING
C
       IF(.NOT.RISING) THEN
           IF(.NOT.PASSED.AND.(Y(2).LT.THRESH)) THEN
             PASSED=.TRUE.
             TCUT=T-DT
             ICUT=ICUT+1
           IF((FIRST)) THEN
             FIRST=.FALSE.
             GO TO 537
           ENDIF
C          WRITE(4,3711) (Y(KK),KK=1,6)
C3711 FORMAT(6(2X,E15.9))
           TLAST=TCUT
       IF(ICUT.GE.1) THEN
           IF(IFLAG.GE.1) GOTO 123
           IFLAG=1
           TT=TLAST
C
```

```
C           REFINE DT TO GET GOOD DATA ON TRANSVERSAL
C
            DT=DT/10.
C           WRITE(*,'("##:",6(1X,E10.4))') (Y(KK),KK=1,6)
            DO 34 K=1,6
  34           Y(K)=YSAV(K)
C           WRITE(*,'(" Y:",6(1X,E10.4))') (Y(KK),KK=1,6)
            NSTEPS=200
            TSTOP=0.
C           DO 54 K=1,1000
C           WK(K)=0.
C54         IWK(K)=0
C
            IND=1
            PASSED=.FALSE.
            ICUT=ICUT-1
            GOTO 298
         ENDIF
 537     ENDIF
         ENDIF
         IF(RISING.AND.(Y(2).GT.THRESH)) PASSED=.FALSE.
C
 100     CONTINUE
         WRITE(*,'(" Y:",6(1X,E10.4))') (Y(KK),KK=1,6)
         WRITE(*,'(" INTEGRATION STEP ",I7," REACHED",/,
     &        " WITH ",I6," PEAKS IDENTIFIED.",/," WANNA GO
     &     ON?")')
     & NITS,ICUT
         READ(*,'(A)') ANS
         IF(ANS.EQ.'Y'.OR.ANS.EQ.'Y') GOTO 299
 123     CONTINUE
         IF(NRESET.NE.0) PRINT*,' NUMBER OF RESETS = ',NRESET
         DT=DTSAV
         DELT=(TCUT+TT)*1.E-3
C
         Z(1)=Y(1)
         Z(2)=Y(3)
         Z(3)=Y(4)
         Z(4)=Y(5)
         Z(5)=Y(6)
         G1=Y(2)
C        WRITE(*,'(/" Z = ",6(E10.3,1X))') (Z(KK),KK=1,6)
C
         END
C
C
         SUBROUTINE FCN(N,T,Y,YPRIME)
         REAL I1,G1,I2,G2,I3,G3
         LOGICAL RISING
         REAL Y(6),YPRIME(6)
C
```

```
      COMMON /LOGIC/ RISING,THRESH
C     COMMON / /
     &    TAUC,TAUF,EPS,A1,A2,A3,B,B12,B21,G10,G20,B13,B23,
C    &             B31,B32,G30
      COMMON /PARAM/ B12,B21,B23,B32,B13,B31
      COMMON / /
     &    TAUC,TAUF,EPS,A1,A2,A3,B,G10,G20,G30,G1,NCUTS
      COMMON /GJ/ G,SIG,ANGLE
      I1=Y(1)
      G1=Y(2)
      I2=Y(3)
      G2=Y(4)
      I3=Y(5)
      G3=Y(6)
C
      YPRIME(1)=((G1-A1-G*EPS*I1-2.*G*EPS*(I2+I3))*I1)/TAUC
      YPRIME(2)=(G10-(B*I1+B12*I2+B13*I3+1.)*G1)/TAUF
      YPRIME(3)=((G2-A2-G*EPS*I2-2.*G*EPS*(I1+I3))*I2)/TAUC
      YPRIME(4)=(G20-(B*I2+B21*I1+B23*I3+1.)*G2)/TAUF
      YPRIME(5)=((G3-A3-G*EPS*I3-2.*G*EPS*(I1+I2))*I3)/TAUC
      YPRIME(6)=(G30-(B*I3+B31*I1+B32*I2+1.)*G3)/TAUF
C
      RISING=.TRUE.
      IF(YPRIME(2).LT.0) RISING=.FALSE.
      END
C
      SUBROUTINE FCNJ(N,X,Y,PD)
      REAL Y(6),PD(6,6)
      REAL I1,G1,I2,G2,I3,G3
C
C
C        DUMMY ROUTINE WHEN MITER = 2
C
C
      END
C
      SUBROUTINE READIN(IFILE,Z,B)
C
      REAL Z(6),B,I1INIT,I2INIT,I3INIT
C
      READ(IFILE,101)
     &    TINIT,BX,NC,I1INIT,G1INIT,I2INIT,G2INIT,
     &             I3INIT,G3INIT
  101 FORMAT(E11.4,/,E11.4,/,I6,/
     &          ,E20.14,/,E20.14,/,E20.14,/,E20.14,
     &          /,E20.14,/E20.14)
C
C
      Z(1)=I1INIT
      Z(2)=G1INIT
      Z(3)=I2INIT
```

```fortran
        Z(4)=G2INIT
        Z(5)=I3INIT
        Z(6)=G3INIT
        B=BX
C
        END
C
        SUBROUTINE ALLOUT(Z,GG)
C
        REAL Z(6),GG
        COMMON /GJ/ G,SIG,ANGLE
C
C       OPEN(UNIT=8,FILE='RESTART')
  717   WRITE(8,707) T,G,Z(1),GG,Z(2),Z(3),Z(4),Z(5)
  707   FORMAT(E11.4,20X,"RESTART TIME",/,
     &  E11.4,20X,"DOUBLING COEFF  G  ",/,"
     &    0",/,E20.14,20X,"I1",/,
     &
     &    E20.14,20X,"G1",/,E20.14,20X,"I2",/,E20.14,20X,"G2"
     &      ,/,E20.14,20X,"I3",/,E20.14,20X,"G3")
C
        END
C
        SUBROUTINE KNOB
C
        CHARACTER*1 ANS
        REAL NSQ1,NSQ2,NUM
        COMMON /GJ/ G,SIG,ANGLE
C
C       MOST GENERAL MODEL ONLY NEEDS G... GET PARAMETER
C         DEPENDENCE ON G
C       ELSEWHERE
        WRITE(*,'(/" INPUT DOUBLING COEFFICIENT G [0,1]
     &    (F7.5)")')
        READ(*,'(F7.5)') G
        SIG=2.*(1.-G)
        WRITE(*,'(/" G = ",F7.5," IS THIS OK?")') G
C       WRITE(*,'(/" D = ",E10.4," SIG = ",E10.4)') G,SIG
C       WRITE(*,'(/" ARE THESE SETTINGS OK?")')
        READ(*,'(A)') ANS
        IF(ANS.NE.'Y'.AND.ANS.NE.'    ` GOTO 1
C
        END
```

HOMO2 integrates the Baer rate equations (2.24) to carry out the homotopic continuation technique described in Chapter II. Recall that the goal is to find unstable fixed points of a Poincaré map using a stable iterative method. The algorithm of HOMO2 is outlined here:

1. Set THRESH which defines the transversal G_1 = THRESH.

2. Input an initial guess for the fixed point $y_0 = (I_1(0), I_2(0), G_2(0), I_3(0), G_3(0))$.

3. Integrate (2.24) from y_0 until G_1 = THRESH and $dG_1/dt < 0$; this is the numerical Poincaré map $M(y_0)$.

4. Let $P(y_k) = M(y_k) - y_k$. Approximate $P'(y_k)$ by equation (2.35).

5. Solve for y_{k+1} by the approximate Newton's method:

   Solve $P'(y_k) z = P(y_k)$,

   let $y_{k+1} = y_k + z$.

6. Report $\| y_{k+1} - y_k \|$.

7. If norm is "small enough", stop; output y_{k+1}.

8. Set $y_k = y_{k+1}$.

9. To iterate with the same approximation to $P'(y)$, go to (5).

10. To recompute P', go to (4).

The program time t is expressed in nanoseconds.

```
            PROGRAM HOMO2(TAPE 3,TAPE 4,TAPE 8,TAPE 9)
C
C       USAGE:
C         LGO,INITIALFILES(INPUT),OUTPUTFILE,RESTARTFILE(OUTPUT),
C              ***    FFTOUTPUTFILE,INTENSITIESOUTPUT *** NOT USED
C         HERE
C       THIS VERSION HAS NO FUNCTION EN TO ACT AS ARC-LENGTH
C       OUTPUT ONLY G2,G3, AND ALL I'S AT CROSSING OF POINCARE
C         SECTION
C       USE IMSL ROUTINE DGEAR TO NUMERICALLY INTEGRATE
C       FOUR 1ST-ORDER DIFF EQ'S DESCRIBING THE TIME-DEPENDENT
C       INTENSITIES AND GAINS FOR TWO-MODES IN A ND:YAG LASER
C       WITH AN INTRA-CAVITY DOUBLING CRYSTAL.
C       REF: T. BAER, J. OPT. SOC. AM. B. VOL 3, NO 9, SEP 86,
C         1177.
C       DGEAR ROUTINE IS ADVERTISED TO BE VARIABLE ORDER ACCURACY.
C
            REAL NORM
            REAL X0(6),X1(6),Y0(6),Y1(6),YK(6),YKP1(6),Y(6)
            REAL PPRIM(6,6),PD(6,7),P(6),YKM1(6),TEMP(6)
            REAL LU(6,6),EQUIL(6),DEL(6),RHS(6)
            INTEGER IPVT(6)
            CHARACTER*1 ANS
            COMMON /GWORK/ NWK,TOL,DT
            COMMON / / TAUC,TAUF,EPS,A1,A2,A3,B,G10,G20,G30,G1,NCUTS
            COMMON /DBAND/ NLC,NUC
            COMMON /GEAR/ DUMMY(48),SDUMMY(4),IDUMMY(38)
            COMMON /REF/ SR,BR,THETA,XR(6)
            COMMON /LOGIC/ RISING,THRESH
            EXTERNAL NORM,EN
C73     WRITE(*,2201)
C2201 FORMAT(/" INPUT DT IN NANOSECONDS")
C       READ(*,2202) DT
            DT=1.0
            NCUTS=1
 2202 FORMAT(E11.4)
C       WRITE(*,2203) DT
C2203 FORMAT(/" DT = ",E11.4,"  OK?")
C       READ(*,700) ANS
            ANS='Y'
 700    FORMAT(A1)
C       IF(ANS.NE.'Y'.AND.ANS.NE.'Y') GOTO 73
C       WRITE(*,'(" INPUT CONVERGENCE TOLERANCE (E15.9)")')
C       READ(*,'(E15.9)') CTOL
C           SET POINCARE CROSS-SECTION AT G1=THRESH
            THRESH=.017
            G1=THRESH
C
            NWK=6
C             NWK: NUMBER OF DIFFL EQUATIONS
            TOL=1.E-8
```

```
C
C       SET PARAMATER DEFAULTS USED IN THE PAPER
C
        TAUC=0.5
C                 NANOSEC, CAVITY ROUND-TRIP TIME
        TAUF=0.24E6
C                   NANOSEC, FLUORESCENCE LIFETIME
        A1=0.015
C                     MODE-1 LOSSES
        A2=0.015
C                     MODE-2 LOSSES
        A3=0.015
C
        EPS=5.E-5
C                 1/W  NONLINEAR COUPLING COEFFICIENT
        B=1.
C               1/W  SATURATION PARAMETER
C       WRITE(*,'(" INPUT COMMON CROSS-SATURATION PARAM")')
C       READ(*,'(F20.18)') BIJ
C
        G10=0.12
C                 SMALL-SIGNAL GAIN
        G20=0.12
C
        G30=0.12
CCCCCCCCCCCCCCCCCCCCCC GET 2 INITIAL GUESSES FROM 'CONVERGED' I.C.
C       CALL READIN(30,X0,B0)
        CALL READIN(3,X1,B1)
CCCCCCCCCCCCCCCCCCCCCC SET UP FOR G1=CONST, .017 HERE
C       S0=B0
        S1=B1
C       S2=S1+(S1-S0)
C       WRITE(*,'(/" S0 = ",E20.14," S1 = ",E20.14,/," INPUT
C       S2:")')
C     &         S0,S1
        WRITE(*,'(/" S1 = ",E20.14,/," INPUT S2:")') S1
        READ(*,'(E20.14)')  S2
        WRITE(4,'(" LOOKING FOR INITIAL CONDITIONS FOR ",
     &    "CROSS-SATURATION = ",E20.14,/," ON POINCARE ",
     &    "SECTION  G1 = ",E20.14)') S2,G1
        WRITE(4,'(/" OUTPUT ARRAYS LIST I1,I2,G2,I3,G3,B ")')
        SR=S1
        XR(1)=X1(1)
        DO 10 J=2,5
 10     XR(J)=X1(J+1)
C       XR(6)=B1
        THETA=0.5
CCCCCCCCCCCCCCCCCCCCCC NOW, FUNCTION EN HAS BEEN SET, THRU COMMON C
        /REF/
        Y0(1)=X0(1)
        Y1(1)=X1(1)
```

```
        DO 20 J=2,5
        Y0(J)=X0(J+1)
 20     Y1(J)=X1(J+1)
        Y0(6)=S2
        Y1(6)=S2
        WRITE(4,'(" Y0 AND Y1:",/,6(E12.6,1X),/,6(E12.6,1X))')
     &          (Y0(J),J=1,6),(Y1(J),J=1,6)
        DO 30 J=1,6
        YKM1(J)=Y0(J)
 30     YK(J)=Y1(J)
CCCCCCCCCCCCCCCCCCC FILL AND INVERT THE PPRIM APPROXIMATRIX
C       WRITE(*,'(/" YK: ",6(E10.3,1X))') (YK(KK),KK=1,6)
        DFAC=.001
 22     CALL INTEG(YK,Y)
C       WRITE(*,'(" Y : ",6(E10.3,1X))') (Y(KK),KK=1,6)
        DO 40 J=1,5
        P(J)=YK(J)-Y(J)
 40     PD(J,1)=P(J)
C       PD(6,1)=EN(YK,S2)
C       P(6)=PD(6,1)
C
        DO 50 K=1,5
           DO 51 J=1,6
 51        TEMP(J)=YK(J)
           TEMP(K)=YK(K)*(1.-DFAC)
C       WRITE(*,'(/" YK: ",6(1X,E10.3))') (YK(KK),KK=1,6)
           CALL INTEG(TEMP,Y)
C       WRITE(*,'(" Y : ",6(1X,E10.3))') (Y(KK),KK=1,6)
           DO 52 J=1,5
 52        PD(J,K+1)=TEMP(J)-Y(J)
C          PD(6,K+1)=EN(TEMP,S2)
 50     CONTINUE
C
        DO 60 K=1,6
        DENOM=ABS(DFAC*YK(K))
        DO 60 J=1,6
 60     PPRIM(J,K)=(PD(J,1)-PD(J,K+1))/DENOM
CCCCCCCCCCCCCCCCCCCCCCCCCCCCCCCCCCCCCCC INVERT PPRIM
        CALL LUDATF (PPRIM,LU,5,6,0,D1,D2,IPVT,EQUIL,WA,IER)
        WRITE(*,'(" LUDATF IER = ",I4)') IER
C
C       GET RHS OF AX=B....
C       WRITE(*,'(" YK AND YKM1:",/,6(E12.6,1X),/,6(E12.6,1X))')
C    &          (YK(J),J=1,6),(YKM1(J),J=1,6)
 11     DO 70 J=1,6
 70     RHS(J)=P(J)*(-1.)
C
C       WRITE(*,'(" PPRIM:",/,
C    &          5(1X,E10.4))') ((PPRIM(II,JJ),JJ=1,5),II=1,5)
C       WRITE(*,'(" RHS",/, 5(1X,E10.4))') (RHS(KK),KK=1,5)
C       WRITE(*,'(" DH, P ",/,E20.14,/,5(1X,E10.4))') DH,
```

```
C     &                 (P(KK),KK=1,5)
C
C
      CALL LUELMF (LU,RHS,IPVT,5,6,DEL)
C     WRITE(*,'(" DEL",/, 5(1X,E10.4))') (DEL(KK),KK=1,5)
C
      DO 80 J=1,5
   80 YKP1(J)=YK(J)+DEL(J)
      YKP1(6)=YK(6)
C
      DH=NORM(YKP1,YK)
      WRITE(*,'(/," NORM(YKP1-YK) = ",E11.4,/," YKP1 : ",/,
     &          6(1X,E12.6))') DH,(YKP1(J),J=1,6)
      WRITE(4,'(/," NORM(YKP1-YK) = ",E11.4,/," YKP1 : ",/,
     &          6(1X,E12.6))') DH,(YKP1(J),J=1,6)
      DO 90 J=1,6
      YKM1(J)=YK(J)
   90 YK(J)=YKP1(J)
      WRITE(*,'(/," WANNA ITERATE WITH SAME PPRIM-INVERSE?")')
      READ(*,'(A)') ANS
      IF(ANS.EQ.'Y'.OR.ANS.EQ.'Y') THEN
         CALL INTEG(YK,Y)
         DO 95 J=1,5
   95    P(J)=YK(J)-Y(J)
C        P(6)=EN(YK,S2)
         GOTO 11
      ENDIF
      WRITE(*,'(/," WANNA MAKE A NEW INVERSE?")')
      READ(*,'(A)') ANS
      IF(ANS.EQ.'Y'.OR.ANS.EQ.'Y') THEN
         DFAC=0.001*AMIN1(1.,DH)
         WRITE(4,'(" RE-EVALUTATING PPRIM-INVERSE  DFAC = ",
     &             F10.7)') DFAC
         GOTO 22
      ENDIF
      CALL ALLOUT(YK,G1)
      STOP .
      END
C
      SUBROUTINE INTEG(ZIN,Z)
C
      REAL I1,G1,I2,G2,I3,G3,ZIN(6),Z(6)
      REAL H,WK(1000),IPREV
      INTEGER IWK(1000)
      REAL Y(6)
      CHARACTER*1 ANS
      LOGICAL FIRST,FLAG,PEAKED,PASSED,RISING
      EXTERNAL FCN,FCNJ
C
      COMMON /GWORK/ NWK,TOL,DT
      COMMON / / TAUC,TAUF,EPS,A1,A2,A3,B,G10,G20,G30,G1,NCUTS
```

```
         COMMON /PARAM/ B12,B21,B23,B32,B13,B31
         COMMON /DBAND/ NLC,NUC
         COMMON /GEAR/ DUMMY(48),SDUMMY(4),IDUMMY(38)
         COMMON /LOGIC/ RISING,THRESH
C
 700    FORMAT(A1)
C
        BX=ZIN(6)
        Z(6)=BX
C
        B12=BX
C                       1/W   CROSS-SATURATION PARAMETER
        B21=B12
C
        B13=BX
        B31=B13
C
        B23=BX
        B32=B23
        Y(1)=ZIN(1)
        Y(2)=G1
        Y(3)=ZIN(2)
        Y(4)=ZIN(3)
        Y(5)=ZIN(4)
        Y(6)=ZIN(5)
C       WRITE(*,'(" Y:",6(1X,E10.4))') (Y(KK),KK=1,6)
C
C       WRITE(*,201)
C         TOL,TAUC,TAUF,A1,A2,A3,EPS,B,B12,B21,B13,B31,B23,
C     &          B32,G10,G20,G30,DT,NCUTS,THRESH
 201    FORMAT("DGEAR INTEGRATION OF FREQUENCY-DOUBLED ND:YAG
     &   SYSTEM",//,
     &          "TOL = ",E11.4,/,
     &          "TAUC = ",E11.4," NSEC",/,"TAUF = ",E11.4,"
     &  NSEC",//,
     &          "ALPHA1 = ",E11.4,/,"ALPHA2 = ",E11.4,/,"ALPHA3 =
     &  ",E11.4,
     &          /,"EPS = ",E11.4,
     &          " 1/W",/,"BETA = ",E16.9," 1/W",/,"BETA12 =
     &  ",E16.9,"
     &  1/W"
     &          ,/,"BETA21 = ",E16.9," 1/W",/,"BETA13 = ",E16.9,/,
     &          "BETA31 = ",E16.9,/,"BETA23 = ",E16.9,/,"BETA32 =
     &  ",E16.9,
     &          /,"G10 = ",E11.4,/,"G20 = ",E11.4,/,"G30 = ",
     &          E11.4,/,"DT = ",E11.4," NSEC",/," NCUTS = ",I6,
     &          4X,"THRESHOLD FOR POINCARE SECTION = ",F10.5)
C       WRITE(4,211)
C       WRITE(10,219)
C219    FORMAT(//,"T (NANOSEC)",9X,"I1 (WATTS)",14X,"I2 (WATTS)",
C     &          14X,"I3 (WATTS)",/)
```

```
  211  FORMAT(//,"T (NANOSEC)",8X," CUT-TO-CUT ",13X,"     G2
     &  ",
     & 4X,"    G3  ",/,18X,"TIME (MICROSC)",10X,"  AT SLICE
     &  ",/)
C
  105  FORMAT(E11.4,4X,3(E20.14,4X))
C
       IND=1
       TSTOP=0
       NRESET=0
       IFLAG=0
       TCUT=TSTOP
       FIRST=.TRUE.
       PASSED=.FALSE.
       TLAST=0
       RISING=.FALSE.
C
       ICUT=0
       NSTEPS=50000
  299  DO 100 J=1,NSTEPS
       T=TSTCP
       TSTOP=T+DT
       IFLAG=IFLAG+1
C
       H=DT/2.
C      WRITE(*,'(" J,T,TSTOP,DT",I4,3(2X,E13.5))') J,T,TSTOP,DT
       METH=1
       MITER=1
C
       CALL DGEAR (NWK,FCN,FCNJ,T,H,Y,TSTOP,TOL,METH,
     &             MITER,IND,IWK,WK,IER)
C      WRITE(*,'(" Y:",6(1X,E10.4))') (Y(KK),KK=1,6)
C
C      PRINT*, J,DUMMY(8),IDUMMY(6),IDUMMY(7)
C
       IF(IER.GT.130) THEN
           WRITE(*,113) J,IND,IER
           GO TO 123
  113  FORMAT(/," STEP ",I6,/," ERROR TERMINATION.  IND = ",I2,
     &         "  IER = ",I4,/)
       ENDIF
C
C
C      OUPTUT ALL VARIABLES BUT G1 WHEN POINCARE SECTION IS
C        CROSSED
C        WITH
C      G1 DECREASING
C
       IF(.NOT.RISING) THEN
           IF(.NOT.PASSED.AND.(G1.LT.THRESH)) THEN
               PASSED=.TRUE.
```

```
                TCUT=T-DT
                ICUT=ICUT+1
           IF((FIRST)) THEN
                FIRST=.FALSE.
                GO TO 537
           ENDIF
           DELT=(TCUT-TLAST)*1.E-3
C          IF (.NOT.FIRST) WRITE(4,3711) (Y(KK),KK=1,6)
 3711 FORMAT(6(2X,E15.9))
           TLAST=TCUT
      IF(ICUT.GE.NCUTS) GO TO 123
  537 ENDIF
      ENDIF
      IF(RISING.AND.(G1.GT.THRESH)) PASSED=.FALSE.
C
  100 CONTINUE
      WRITE(*,'(" INTEGRATION STEP ",I7," REACHED",/,
     &      " WITH ",I6," PEAKS IDENTIFIED.",/," WANNA GO
     & ON?")')
     & NSTEPS,ICUT
      READ(*,'(A)') ANS
      IF(ANS.EQ.'Y'.OR.ANS.EQ.'Y') GO TO 299
  123 CONTINUE
      PRINT*,' NUMBER OF RESETS = ',NRESET
C
      Z(1)=Y(1)
      Z(2)=Y(3)
      Z(3)=Y(4)
      Z(4)=Y(5)
      Z(5)=Y(6)
C     WRITE(*,'(/" Z = ",6(E10.3,1X))') (Z(KK),KK=1,6)
C
      END
C
      SUBROUTINE FCN(N,T,Y,YPRIME)
      REAL I1,G1,I2,G2,I3,G3
      LOGICAL RISING
      REAL Y(6),YPRIME(6)
C
      COMMON /LOGIC/ RISING,THRESH
      COMMON /PARAM/ B12,B21,B23,B32,B13,B31
      COMMON / / TAUC,TAUF,EPS,A1,A2,A3,B,G10,G20,G30,G1,NCUTS
      I1=Y(1)
      G1=Y(2)
      I2=Y(3)
      G2=Y(4)
      I3=Y(5)
      G3=Y(6)
C
      YPRIME(1)=((G1-A1-EPS*I1-2.*EPS*(I2+I3))*I1)/TAUC
      YPRIME(2)=(G10-(B*I1+B12*I2+B13*I3+1.)*G1)/TAUF
```

```
            YPRIME(3)=((G2-A2-EPS*I2-2.*EPS*(I1+I3))*I2)/TAUC
            YPRIME(4)=(G20-(B*I2+B21*I1+B23*I3+1.)*G2)/TAUF
            YPRIME(5)=((G3-A3-EPS*I3-2.*EPS*(I1+I2))*I3)/TAUC
            YPRIME(6)=(G30-(B*I3+B31*I1+B32*I2+1.)*G3)/TAUF
C
            RISING=.TRUE.
            IF(YPRIME(2).LT.0) RISING=.FALSE.
            END
C
            SUBROUTINE FCNJ(N,X,Y,PD)
            REAL Y(6),PD(6,6)
            REAL I1,G1,I2,G2,I3,G3
C
C      ROUTINE FOR ANALYTIC JACOBIAN IS USED WHEN MITER=1
C
            COMMON /LOGIC/ RISING,THRESH
            COMMON /PARAM/ B12,B21,B23,B32,B13,B31
            COMMON / / TAUC,TAUF,EPS,A1,A2,A3,B,G10,G20,G30,G1,NCUTS
C
            I1=Y(1)
            G1=Y(2)
            I2=Y(3)
            G2=Y(4)
            I3=Y(5)
            G3=Y(6)
C
            SUMI=I1+I2+I3
C
            PD(1,1)=(G1-A1-2.*EPS*SUMI)/TAUC
            PD(1,2)=I1/TAUC
            PD(1,3)=-1.*(2.*EPS*I1)/TAUC
            PD(1,4)=0.
            PD(1,5)=-1.*2.*EPS*I1/TAUC
            PD(1,6)=0.
C
            PD(2,1)=-1.*B*G1/TAUF
            PD(2,2)=-1.*(B*I1+B12*I2+B13*I3+1.)/TAUF
            PD(2,3)=-1.*B12*G1/TAUF
            PD(2,4)=0.
            PD(2,5)=-1.*B13*G1/TAUF
            PD(2,6)=0.
C
            PD(3,1)=-1.*2.*EPS*I2/TAUC
            PD(3,2)=0.
            PD(3,3)=(G2-A2-2.*EPS*SUMI)/TAUC
            PD(3,4)=I2/TAUC
            PD(3,5)=-1.*2.*EPS*I2/TAUC
            PD(3,6)=0.
C
            PD(4,1)=-1.*B21*G2/TAUF
            PD(4,2)=0.
```

```fortran
      PD(4,3)=-1.*B*G2/TAUF
      PD(4,4)=-1.*(B*I2+B21*I1+B23*I3+1.)/TAUF
      PD(4,5)=-1.*B23*G2/TAUF
      PD(4,6)=0.
C
      PD(5,1)=-1.*2.*EPS*I3/TAUC
      PD(5,2)=0.
      PD(5,3)=-1.*2.*EPS*I3/TAUC
      PD(5,4)=0.
      PD(5,5)=(G3-A3-2.*EPS*SUMI)/TAUC
      PD(5,6)=I3/TAUC
C
      PD(6,1)=-1.*B31*G3/TAUF
      PD(6,2)=0.
      PD(6,3)=-1.*B32*G3/TAUF
      PD(6,4)=0.
      PD(6,5)=-1.*B*G3/TAUF
      PD(6,6)=-1.*(B*I3+B31*I1+B32*I2+1.)/TAUF
C
      END
C
      SUBROUTINE READIN(IFILE,Z,B)
C
      REAL Z(6),B,I1INIT,I2INIT,I3INIT
C
      READ(IFILE,101) TINIT,BX,NC,I1INIT,G1INIT,I2INIT,G2INIT,
     &            I3INIT,G3INIT
 101  FORMAT(E11.4,/,E11.4,/,I6,/,
     & E20.14,/,E20.14,/,E20.14,/,E20.14,
     &        /,E20.14,/E20.14)
C
C
      Z(1)=I1INIT
      Z(2)=G1INIT
      Z(3)=I2INIT
      Z(4)=G2INIT
      Z(5)=I3INIT
      Z(6)=G3INIT
      B=BX
C
      END
C
      SUBROUTINE ALLOUT(Z,GG)
C
      REAL Z(6),GG
C
C     OPEN(UNIT=8,FILE='RESTART')
 717  WRITE(8,707) T,DT,Z(6),Z(1),GG,Z(2),Z(3),Z(4),Z(5)
 707  FORMAT(E11.4,20X,"RESTART TIME",/,E11.4,20X,"DT  NSEC",/,
     &       E11.4,20X,"CROSS-SAT
     &  PARAMETER",/,E20.14,20X,"I1",/,
```

```
      &           E20.14,20X,"G1",/,E20.14,20X,"I2",/,E20.14,20X,"G2"
      &           ,/,E20.14,20X,"I3",/,E20.14,20X,"G3")
C
      END
C
      REAL FUNCTION EN(Z,S)
C
      REAL Z(6)
      COMMON /REF/ SR,BR,THETA,XR(6)
C
      SUM1=0.
      SUM2=0.
      DO 10 J=1,5
      SUM1=SUM1+(Z(J)-XR(J))*(Z(J)-XR(J))
   10 CONTINUE
      SUM2=(Z(6)-BR)*(Z(6)-BR)
      EN=THETA*SUM1 + (1.-THETA)*SUM2 - (S-SR)*(S-SR)
C
      END
C
      REAL FUNCTION NORM(A,B)
C
      REAL A(6),B(6)
C
      SUMSQ=0.
      DO 10 J=1,6
C     WRITE(*,'(" AJ AND BJ: ",2(2X,E12.6))') A(J),B(J)
      SUMSQ=SUMSQ + (A(J)-B(J))*(A(J)-B(J))
   10 CONTINUE
      NORM=SQRT(SUMSQ)
      WRITE(*,'(" NORM = ",E12.6)') NORM
      RETURN
      END
```

The last two program listings include the parameter definitions and differential equations (FCN) for the three-mode version of the new rate equations (4.36) in RAY3G, and the three-level model for two modes (4.45) in RAY2S. The program time is scaled so that $t_{program} = \gamma \cdot t_{actual}$.

```
            PROGRAM RAY3G(TAPE 3,TAPE 4,TAPE 8,TAPE 9,TAPE 10)
C
C       USAGE:
C         LGO,INITIALFILE(INPUT),OUTPUTFILE,RESTARTFILE(OUTPUT),
C                   FFTOUTPUTFILE,INTENSITIESOUTPUT
C       *** ASYMMETRIC VERSION ***
C       THREE LEVEL TEST MODEL
C       THIS VERSION USES THE FROM-SCRATCH EQUATIONS NEAR-RAYMER
C       THREE-MODES; FIRST-ORDER APPROX
C       THIS VERSION IGNORES THE FAST-OSCILLATIONS , EXP(I*DEL*T)
C       WITH SCALING TO HOPEFULLY REDUCE STIFFNESS IN INTEGRATOR
C       USE IMSL ROUTINE DGEAR TO NUMERICALLY INTEGRATE
C       11 1ST-ORDER DIFF EQ'S DESCRIBING THE TIME-DEPENDENT
C       INTENSITIES AND GAINS FOR TWO-MODES IN A ND:YAG LASER
C       WITH AN INTRA-CAVITY DOUBLING CRYSTAL.
C       REF: T. BAER, J. OPT. SOC. AM. B, VOL 3, NO 9, SEP 86,
1177.
C
        REAL B1R,B1I,B2R,B2I,W,WK(200000),I1(200000),I2(200000)
        REAL I3(200000)
        INTEGER IWK(200000)
        COMPLEX X(200000)
        COMMON /LOGIC/ RISING,THRESH
        CHARACTER*1 ANS
 73     WRITE(*,2201)
 2201   FORMAT(/" INPUT DT AND NSTEPS")
        READ(*,2202) DT,NSTEPS
 2202   FORMAT(E11.4,/,I6)
        WRITE(*,2203) DT,NSTEPS
 2203   FORMAT(/" DT = ",E11.4,"    NSTEPS = ",I6,"   OK?")
        READ(*,700) ANS
 700    FORMAT(A1)
        IF(ANS.NE.'Y'.AND.ANS.NE.'Y') GOTO 73
C
        CALL KNOB
        CALL INTEG(DT,NSTEPS,I1,I2,X,WK,IWK)
        END
C
        SUBROUTINE INTEG(DT,NSTEPS,I1,I2,X,WK,IWK)
C
        REAL B1R,B1I,B2R,B2I,W,I1(NSTEPS),I2(NSTEPS)
        COMPLEX X(NSTEPS)
        REAL WK(3*NSTEPS+200),H
        INTEGER IWK(3*NSTEPS+200)
        REAL Y(11)
        CHARACTER*1 ANS
        EXTERNAL FCN,FCNJ
        EQUIVALENCE (Y(1),B1),(Y(2),B2),(Y(3),B3),(Y(4),W),
     &      (Y(5),W11),(Y(6),W22),(Y(7),W33),(Y(8),S),
     &      (Y(9),S11),(Y(10),S22),(Y(11),S33)
        LOGICAL FIRST,FLAG,PEAKED,PASSED,RISING
```

```
      COMMON /LOGIC/ RISING,THRESH
C
      COMMON / / GAM1,GAM,A,B,DEL,EPS,P,W0,THETA,PHI,G0G
      COMMON /ASYM/
     &  GAM2,GAM3,THETA1,THETA2,THETA3,D12,D13,D21,D23,
     &             D31,D32,F1,F2,F3,Q1,Q2,EPS1,EPS2,EPS3
      COMMON /DBAND/ NLC,NUC
      COMMON /GEAR/ DUMMY(48),SDUMMY(4),IDUMMY(38)
      COMMON /GJ/ G,SIG,ANGLE
C
      WRITE(*,'(" DO YOU REALLY WANT OUTPUT TO TAPE 4 ?")')
      READ(*,700) ANS
 700  FORMAT(A1)
      FLAG=.FALSE.
      IF(ANS.EQ.'Y'.OR.ANS.EQ.'Y') FLAG=.TRUE.
C
      NWK=11
C           NWK: NUMBER OF DIFFL EQUATIONS
      TOL=1.E-3
C
C     SET PARAMATER DEFAULTS ...
C
      GAM2=6.E7
C              SEC-INVERSE, CAVITY DECAY RATE
      WRITE(*,'(/" INPUT RELATIVE LOSS FRACTION")')
      READ(*,'(F6.4)') FLOSS
      GAM1=FLOSS*GAM2
      GAM3=GAM1
C
      GAM=4.E3
      GAM0=2.E6
      G0G=GAM0/GAM
C              SEC-INVERSE, POPULATION DECAY RATE
      THETA1=GAM/(2.*GAM1)
      THETA2=GAM/(2.*GAM2)
      THETA3=GAM/(2.*GAM3)
C
      D12=GAM1/GAM2
      D13=GAM1/GAM3
      D21=GAM2/GAM1
      D23=GAM2/GAM3
      D31=GAM3/GAM1
      D32=GAM3/GAM2
C
      B=1.E12
C
      F1=B/GAM1
      F2=B/GAM2
      F3=B/GAM3
C
      Q1=.137
```

```
        Q2=.168
C       Q2=Q1
C
        A=1.E-5
C
        EPS=1.E-5
        WRITE(*,'(/" INPUT P ")')
        READ(*,'(E12.4)') P
        WRITE(*,'(/" INPUT EPS")')
        READ(*,'(E12.4)') EPS
        EPS1=EPS*GAM/(A*GAM1)
        EPS2=EPS*GAM/(A*GAM2)
        EPS3=EPS*GAM/(A*GAM3)
C
        DEL=1.9E10
C       DEL=DEL/100.
C
C       P=1000.0
C               PERCENTAGE ABOVE THRESHOLD
        XL=5.E-3
C               YAG CRYSTAL LENGTH
        XLL=5.E-2
C                CAVITY LENGTH
        W0=(1.+P)*GAM1/B
        P=W0
C
C       P=(1.+P)*XL/XLL
C       P=W0*XL/XLL
C
        THETA=GAM/(2.*GAM1)
C                 (2.*GAM1)
        PHI=DEL/GAM1
C
        READ(3,101) TINIT,DTB,NSTEPSB,B1NIT,B2NIT,B3NIT,WNIT,
     &   W11NIT,W22NIT,W33NIT,SNIT,S11NIT,S22NIT,S33NIT
 101  FORMAT(E11.4,/,E11.4,/,I6,11(/,E20.14))
C
C
        T=TINIT
        Y(1)=B1NIT
        Y(2)=B2NIT
        Y(3)=B3NIT
        Y(4)=WNIT
        Y(5)=W11NIT
        Y(6)=W22NIT
        Y(7)=W33NIT
        Y(8)=SNIT
        Y(9)=S11NIT
        Y(10)=S22NIT
        Y(11)=S33NIT
        TSTOP=T
```

```
C

      O
      O
      O

7777 STOP
     END
C
     SUBROUTINE FCN(N,T,Y,YPRIME)
     LOGICAL RISING
     REAL Y(11),YPRIME(11)
C
     COMMON / / GAM1,GAM,A,B,DEL,EPS,P,W0,THETA,PHI,G0G
     COMMON /ASYM/
    &   GAM2,GAM3,THETA1,THETA2,THETA3,D12,D13,D21,D23,
    &               D31,D32,F1,F2,F3,Q1,Q2,EPS1,EPS2,EPS3
     COMMON /LOGIC/ RISING,THRESH
     COMMON /GJ/ G,SIG,ANGLE
     B1=Y(1)
     B2=Y(2)
     B3=Y(3)
     W=Y(4)
     W11=Y(5)
     W22=Y(6)
     W33=Y(7)
     S=Y(8)
     S11=Y(9)
     S22=Y(10)
     S33=Y(11)
C
     TERM1=G*EPS1*B1/2. + (1.-G)*EPS1*(B2+B3)
     TERM2=G*EPS2*B2/2. + (1.-G)*EPS2*(B1+B3)
     TERM3=G*EPS3*B3/2. + (1.-G)*EPS3*(B1+B2)
C    ARG=DEL*T
C    SS=SIN(ARG)
C    CC=COS(ARG)
     YPRIME(1)=(B1*(W11-1.-TERM1 ) )/THETA1
     YPRIME(2)=(B2*(W22-1.-TERM2 ) )/THETA2
     YPRIME(3)=(B3*(W33-1.-TERM3 ) )/THETA3
     YPRIME(4)= F2*P   - W -D12*B1*W11 - B2*W22 - D32*B3*W33
    &        - W*(3. + G0G)/2. - S*(1. - G0G)/2.
     YPRIME(5)= F1*P/2. - W11 - (B1*(W11 - D21*W/8.)
    &                          +B2*((W11+D21*W22)/2. - Q1*D21*W)
    &                          +B3*((W11+D31*W33)/2. - Q2*D21*W))
    &        - W11*(3. + G0G)/2. - S11*(1. - G0G)/2.
     YPRIME(6)= F2*P/2. - W22 - (B1*((D12*W11+W22)/2. - Q1*W)
    &                          +B2*(W22 - W/8.)
    &                          +B3*((W22+D32*W33)/2. - Q1*W))
    &        - W22*(3. + G0G)/2. - S22*(1. - G0G)/2.
```

```fortran
      YPRIME(7)= F3*P/2. - W33 - (B1*((D13*W11+W33)/2. -       &
Q2*D23*W)
     &                              +B2*((D23*W22+W33)/2. - Q1*D23*W)
     &                              +B3*(W33 - D23*W/8.))
     &          - W33*(3. + G0G)/2. - S33*(1. - G0G)/2.
      YPRIME(8)= P - W*(1. - G0G)/2. - S*(1. + G0G)/2.
      YPRIME(9)= P/2. -W11*(1. - G0G)/2. - S11*(1. + G0G)/2.
      YPRIME(10)= P/2. -W22*(1. - G0G)/2. - S22*(1. + G0G)/2.
      YPRIME(11)= P/2. -W33*(1. - G0G)/2. - S33*(1. + G0G)/2.
C
C     RISING=.TRUE.
C     IF(YPRIME(2).LT.0) RISING=.FALSE.
      END
```

```fortran
      PROGRAM RAY2S(TAPE 3,TAPE 4,TAPE 8,TAPE 9,TAPE 10)
C
C     USAGE:
C       LGO,INITIALFILE(INPUT),OUTPUTFILE,RESTARTFILE(OUTPUT),
C                    FFTOUTPUTFILE,INTENSITIESOUTPUT
C     *** THREE LEVEL TEST MODEL
C     THIS VERSION USES THE FROM-SCRATCH EQUATIONS NEAR-RAYMER
C     TWO-MODES; EIGHT EQUATIONS
C     WITH SCALING TO HOPEFULLY REDUCE STIFFNESS IN INTEGRATOR
C     USE IMSL ROUTINE DGEAR TO NUMERICALLY INTEGRATE
C         1ST-ORDER DIFF EQ'S DESCRIBING THE TIME-DEPENDENT
C     INTENSITIES AND INVERSIONS FOR TWO-MODES IN A ND:YAG LASER
C     WITH AN INTRA-CAVITY DOUBLING CRYSTAL.
C     REF: T. BAER, J. OPT. SOC. AM. B, VOL 3, NO 9, SEP 86,
C        1177.
C
      REAL B1R,B1I,B2R,B2I,W,WK(200000),I1(200000),I2(200000)
      INTEGER IWK(200000)
      COMPLEX X(200000)
      COMMON /LOGIC/ RISING,THRESH
      CHARACTER*1 ANS
 73   WRITE(*,2201)
 2201 FORMAT(/" INPUT DT AND NSTEPS")
      READ(*,2202) DT,NSTEPS
 2202 FORMAT(E11.4,/,I6)
      WRITE(*,2203) DT,NSTEPS
 2203 FORMAT(/" DT = ",E11.4,"   NSTEPS = ",I6,"  OK?")
      READ(*,700) ANS
 700  FORMAT(A1)
      IF(ANS.NE.'Y'.AND.ANS.NE.'Y') GOTO 73
C
      CALL KNOB
      CALL INTEG(DT,NSTEPS,I1,I2,X,WK,IWK)
      END
C
      SUBROUTINE INTEG(DT,NSTEPS,I1,I2,X,WK,IWK)
C
      REAL B1R,B1I,B2R,B2I,W,I1(NSTEPS),I2(NSTEPS)
      COMPLEX X(NSTEPS)
      REAL WK(3*NSTEPS+200),H
      INTEGER IWK(3*NSTEPS+200)
      REAL Y(8)
      CHARACTER*1 ANS
      EXTERNAL FCN,FCNJ
      EQUIVALENCE (Y(1),B1),(Y(2),B2),(Y(3),W),(Y(4),W11),
     &  (Y(5),W22),(Y(6),S),(Y(7),S11),(Y(8),S22)
      LOGICAL FIRST,FLAG,PEAKED,PASSED,RISING
      COMMON /LOGIC/ RISING,THRESH
C
      COMMON / / GAM1,GAM,A,B,DEL,EPS,P,W0,THETA,PHI,G0G
```

```
        COMMON /DBAND/ NLC,NUC
        COMMON /GEAR/ DUMMY(48),SDUMMY(4),IDUMMY(38)
        COMMON /GJ/ G,SIG,ANGLE
C
C
C       OPEN(UNIT=3,FILE='YAGIN',STATUS='OLD')
C       OPEN(UNIT=4,FILE='YAGOUT')
        WRITE(*,'(" DO YOU WANT OUTPUT TO TAPE 4?")')
        READ(*,700) ANS
  700   FORMAT(A1)
        FLAG=.FALSE.
        IF(ANS.EQ.'Y'.OR.ANS.EQ.'Y') FLAG=.TRUE.
C
        NWK=8
C            NWK: NUMBER OF DIFFL EQUATIONS
        TOL=1.E-3
C
C       SET PARAMATER DEFAULTS ...
C
        GAM1=6.E7
C               SEC-INVERSE, CAVITY DECAY RATE (SCALED)
        GAM=4.E3
C               SEC-INVERSE, POPULATION DECAY RATE (SCALED)
        GAM0=2.E6
C
        G0G=GAM0/GAM
C
        B=1.E12
C
        A=1.E-5
C
        EPS=0
        WRITE(*,'(/" INPUT P ")')
        READ(*,'(E12.4)') P
        WRITE(*,'(/" INPUT EPS")')
        READ(*,'(E12.4)') EPS
C
        DEL=1.9E10
C       DEL=DEL/100.
C
C       P=2.00
C               PERCENTAGE ABOVE THRESHOLD
        W0=(1.+P)*GAM1/B
C
        THETA=GAM/GAM1
C
        PHI=DEL/GAM1
        READ(3,101)
     &    TINIT,DTB,NSTEPSB,B1NIT,B2NIT,WNIT,W11NIT,W22NIT,
     &    SNIT,S11NIT,S22NIT
  101   FORMAT(E11.4,/,E11.4,/,I6,8(/,E20.14))
```

```
C
C
      T=TINIT
      Y(1)=B1NIT
      Y(2)=B2NIT
      Y(3)=WNIT
      Y(4)=W11NIT
      Y(5)=W22NIT
      Y(6)=SNIT
      Y(7)=S11NIT
      Y(8)=S22NIT
      TSTOP=T
C

         O
         O
         O

 7777 STOP
      END
C
      SUBROUTINE FCN(N,T,Y,YPRIME)
      LOGICAL RISING
      REAL Y(8),YPRIME(8)
C
      COMMON / / GAM1,GAM,A,B,DEL,EPS,P,W0,THETA,PHI,G0G
      COMMON /LOGIC/ RISING,THRESH
      COMMON /GJ/ G,SIG,ANGLE
      B1=Y(1)
      B2=Y(2)
      W=Y(3)
      W11=Y(4)
      W22=Y(5)
      S=Y(6)
      S11=Y(7)
      S22=Y(8)
C
      TERM1=G*EPS*B1/2. + (1.-G)*EPS*B2
      TERM2=G*EPS*B2/2. + (1.-G)*EPS*B1
C     ARG=DEL*T
C     SS=SIN(ARG)
C     CC=COS(ARG)
C
C       THE FACTOR BELOW, OF 0.137, ASSUMES NEAREST-NEIGHBOR
C       MODE SPACING
C
      W1111 = W11 -W/8.
      W1122 = (W11 + W22)/2. - 0.137*W
      W2222 = W22 -W/8.
C
      YPRIME(1)=(2.*B1*(W11-1.-TERM1 ) )/THETA
```

```
        YPRIME(2)=(2.*B2*(W22-1.-TERM2 ) )/THETA
C       YPRIME(3)=(1.+P)  - W*(1. + B1 + B2)
        YPRIME(3)= P   - W -B1*W11 - B2*W22
     &                  - W*(3. + G0G)/2. - S*(1. - G0G)/2.
        YPRIME(4)= P/2. - W11 -B1*W1111 - B2*W1122
     &                  - W11*(3. + G0G)/2. - S11*(1. - G0G)/2.
        YPRIME(5)= P/2. - W22 -B1*W1122 -B2*W2222
     &                  -W22*(3. + G0G)/2. - S22*(1. - G0G)/2.
        YPRIME(6)= P   - W*(1. - G0G)/2. - S*(1. + G0G)/2.
        YPRIME(7)= P/2. - W11*(1. - G0G)/2. - S11*(1. + G0G)/2.
        YPRIME(8)= P/2. - W22*(1. - G0G)/2. - S22*(1. + G0G)/2.
C
C       RISING=.TRUE.
C       IF(YPRIME(2).LT.0) RISING=.FALSE.
        END
```

REFERENCES

PRIMARY WORKS CITED

F.T. Arecchi, in Instabilities and Chaos in Quantum Optics (Springer-Verlag, Berlin, 1987).

D.G. Aronson, E.J. Doedel and H.G. Othmer, "An analytical and Numerical Study of the Bifurcations in a System of Linearly-Coupled Oscillators", Physica 25D, 20 (1987).

T. Baer, "Large-Amplitude Fluctuations Due to Longitudinal Mode Coupling in Diode-Pumped Intracavity-Doubled Nd:YAG Lasers", J. Opt. Soc. Am. B3, 1175 (1986).

P. Berge, Y. Pomeau and C. Vidal, Order Within Chaos (John Wiley, New York, 1984).

S. Borowitz, Fundamentals of Quantum Mechanics (W.A. Benjamin, New York, 1967).

R.L. Byer, E.K. Gustafson and R. Trebino, ed., Tunable solid State Lasers for Remote Sensing, Proc. of the NASA Conf., Stanford Univ. (Springer-Verlag, Berlin, 1984).

R.L. Byer, "Diode Laser-Pumped Solid-State Lasers", Science 239, 742 (1988).

P.E. Chumbley, "Microlasers Offer New Reliability for R&D", Research & Development 31, 72 (1989).

S.-N. Chow and J.K. Hale, Methods of Bifurcation Theory (Springer-Verlag, New York, 1982).

D. Cook, "Printed Wiring Board Direct Imaging", Print. Circuit Fabr. (USA) 11, 50 (1988).

E.B. Davies, "Metastable States of Symmetric Markov Semigroups I", Proc. London Math. Soc. 45, 133 (1982).

E.B. Davies, "Metastable States of Symmetric Markov Semigroups II", J. London Math. Soc. 26, 541 (1982).

F. De Tomasi, D. Hennequin, B. Zambon and E. Arimondo, "Instabilities and Chaos in an Infrared Laser with Saturable Absorber: Experiments and Vibrorotational Model", J. Opt. Soc. Am. B6, 45 (1989).

V. Evtuhov and A.E. Siegman, "A 'Twisted-Mode' Technique for Obtaining Axially Uniform Energy Density in a Laser Cavity", Appl. Opt. 4, 142 (1965).

T.Y. Fan, C.E. Huang, B.Q. Hu, R.C. Eckardt, Y.X. Fan, R.L. Byer, and R.S. Feigelson, "Second Harmonic Generation and Accurate Index of Refraction Measurements in Flux-Grown KTiOPO4", Appl. Opt. 26, 2390 (1987).

T.Y. Fan and R.L. Byer, "Diode Laser-Pumped Solid-State Lasers", IEEE J. Quantum Electr. 24, 895 (1988).

B. Fitzpatric, J. Khurgin, P. Harnack, D. de Leeuw, "Low Threshold Visible Electron-Beam-Pumped-Lasers", International Electron Devices Meeting 1986, Technical Digest, 630 (1986).

E.S. Fry and S.W. Henderson, "Suppression of Spatial Hole Burning in Polarization Coupled Resonators", Appl. Opt. 25, 3017 (1986).

K. Fujii, "White Light Lasers -- New Aspects and Developments", Oyo Buturi (Japan) 55, 1124 (1986).

J. Guckenheimer, Dynamical Systems (Birkhauser, Boston, 1980).

H. Haken, "Analogy between Higher Instabilities in Fluids and Lasers", Phys. Lett. 53A, 77 (1975).

J.K. Hale, Ordinary Differential Equations (Wiley, New York, 1969).

J.K. Hale and N. Sternberg, "Onset of Chaos in Differential Delay Equations", J. Comput. Phys. 77, 221 (1988).

E.M. Harrell II, "Estimating Tunneling Phenomena", Int. J. Quantum Chem. 21, 199 (1982).

E.M. Harrell II, "General Bounds for the Eigenvalues of Schrödinger Operators", in Maximum Principles and Eigenvalue Problems in Partial Differential Equations, D.W. Schaefer, ed. (Wiley, New York, 1988).

E. Hecht and A. Zajac, Optics (Addison-Wesley, Reading, 1979).

H. Ito, H. Naito and H. Inaba, "Generalized Study on Angular Dependence of Induced Second-Order Nonlinear Optical Polarizations and Phase Matching in Biaxial Crystals", J. Appl. Phys. 46, 3992 (1975).

G.E. James, E.M. Harrell II and Rajarshi Roy, "Intermittency and Chaos in Intracavity Doubled Lasers", in Coherence and Quantum Optics VI, edited by J.H. Eberly, L. Mandel, and E. Wolf (Plenum, New York, in press).

G.E. James, E.M. Harrell II and Rajarshi Roy, "Intermittency and Chaos in Intracavity Doubled Lasers II", Phys. Rev. A 41, to be published (1990a).

G.E. James, E.M. Harrell II, C. Bracikowski, Rajarshi Roy and K. Wiesenfeld, "On the Elimination of Chaos in an Intracavity Doubled Nd:YAG Laser", Opt. Lett., to be published (1990b).

D.W. Jordan and P. Smith, Nonlinear Ordinary Differential Equations (2nd ed.) (Clarendon Press, Oxford, 1987).

H.B. Keller, in Applications of Bifurcation Theory, edited by P.H. Rabinowitz (Academic Press, NY, 1977).

C.J. Kennedy and J.D. Barry, "Stability of an Intracavity Frequency-Doubled Nd:YAG Laser", IEEE J. Quantum Electron. QE-10, 596 (1974).

J.T. Lin, "Progress Report: Diode Pumping and Frequency Conversion", Lasers & Optronics 8, 61 (1989).

P. Mandel and X.-G. Wu, "Second-Harmonic Generation in a Laser Cavity", J. Opt. Soc. Am B3, 940 (1986).

I. McMackin, C. Radzewicz, M. Beck and M.G. Raymer, "Instabilities and Chaos in a Multimode, Standing-Wave, CW Dye Laser", Phys. Rev. A 38, 820 (1988).

D.C. O'Shea, W.R. Callen and W.T. Rhodes, Introduction to Lasers and Their Applications (Addison-Wesley, Reading, 1978).

M. Oka and S. Kubota, "Stable Intracavity Doubling of Orthogonal Linearly Polarized Modes in Diode-Pumped Nd:YAG Lasers", Opt. Lett. 13, 805 (1988).

K. Otsuka and H. Iwasaki, "Stabilization of Oscillating Modes in a $LiNdP_4O_{12}$ Laser", IEEE J. Quantum Electron. QE-12, 214 (1976).

D. Park, Introduction to the Quantum Theory, 2nd ed. (McGraw-Hill, New York, 1964).

H.-O. Peitgen, in Order and Chaos, edited by H. Haken (Springer-Verlag, Berlin, 1982).

P.E. Perkins, T.S. Fahlen, "20-W Average-Power KTP Intracavity-Doubled Nd:YAG Laser", J. Opt. Soc. Am. B4, 1066 (1987).

Y. Pomeau and P. Manneville, "Intermittent Transition to Turbulence in Dissipative Dynamical Systems", Comm. Math. Phys. 74, 189 (1980).

R. Roy, A.W. Yu and S. Zhu, "Colored Noise in Dye Laser Fluctuations", in Noise in Nonlinear Dynamical Systems, edited by F. Moss and P.V.E. McClintock (Cambridge Univ. Press, New York, 1989).

M. Sargent III, M.O. Scully and W.E. Lamb, Jr., Laser Physics (Addison-Wesley, Reading, MA, 1974).

Y.R. Shen, The Principles of Nonlinear Optics (Wiley, New York, 1984).

L.P. Shil'nikov, "A Case of the Existence of a Denumerable Set of Periodic Motions", Soviet Math. Dokl. 6, 163 (1965).

L.P. Shil'nikov, "On the Generation of a Periodic Motion from Trajectories Doubly Asymptotic to an Equilibrium State of Saddle Type", Math. USSR Sbornik 6, 427 (1968).

L.P. Shil'nikov, "On a New Type of Bifurcation of Multidimensional Dynamical Systems", Soviet Math. Dokl. 10, 1368 (1969).

L.P. Shil'nikov, "A Contribution to the Problem of the Structure of an Extended Neighborhood of a Rough Equilibrium State of Saddle-Focus Type", Math. USSR Sbornik 10, 91 (1970).

A.E. Siegman, Lasers (University Science Books, Mill Valley, CA, 1986).

R.G. Smith, "Theory of Intracavity Optical Second-Harmonic Generation", IEEE J. Quantum Electron. QE-10, 596 (1974).

O. Svelto, Principles of Lasers, D.C. Hanna, Trans. (Plenum, New York, 1989).

M. Takashima, S. Fukuda, S. Okada, H. Nishiyama, K. Fujii, "High-Quality Full-color Direct Printing Based on Selective Exposures", Proc. S.I.D. 28, 303 (1987).

K. Wallmeroth and P. Peuser, "High-Power, CW Single-Frequency, TEM_{00} Diode-Laser-Pumped Nd:YAG Laser", Electron. Lett. 24, 1086 (1988).

L.T. Watson, "Solving Finite Difference Approximations to Nonlinear Two-Point Boundary Value Problems by a Homotopy Method", SIAM J. Sci. Stat. Comput. 1, 467 (1980).

X.-G. Wu and P. Mandel, "Intracavity Second-Harmonic Generation with a Periodic Perturbation", J. Opt. Soc. Am B3, 1678 (1985).

X.-G. Wu and P. Mandel, "Second-Harmonic Generation in a Multimode Laser Cavity", J. Opt. Soc. Am. B4, 1870 (1987).

M. Yamada and Y. Suematsu, "Analysis of Gain Suppression in Undoped Injection Lasers", J. Appl. Phys. 52, 2653 (1981).

J.Q. Yao and T.S. Fahlen, "Calculations of Optimum Phase Match Parameters for the Biaxial Crystal $KTiOPO_4$", J. Appl. Phys 55, 65 (1984).

EXPERIMENTS DISPLAYING INTERMITTENCY

D.J. Biswas, V. Dev and U.K. Chatterjee, "Experimental Observation of Oscillatory Instabilities and Chaos in a Gain-Modulated Single-Mode CW CO_2 Laser", Phys. Rev. A 35, 456 (1987).

E. B. un, B. Derighetti, M. Ravani, G. Broggi, P. Meier, R. Stopp and R. Badii, "Instabilities and Chaos for a Solid State NMR Laser with Injected Signals", Phys. Scr. (Sweden) T13, 119 (1986).

M. Dubois, M.A. Rubio and P. Berge, "Experimental Evidence of Intermittencies Associated with a Subharmonic Bifurcation", Phys. Rev. Lett. 51, 1446 (1983).

D.M. Heffernan, "Multistability, Intermittency and Remerging Feigenbaum Trees in an Externally Pumped Ring Cavity laser System", Phys. Lett. A (Netherlands) 108A, 413 (1985).

C. Jeffries and J. Perez, "Observation of a Pomeau-Manneville Intermittent Route to Chaos in a Nonlinear Oscillator", Phys. Rev A 26, 2117 (1982).

S.M.J. Kelly, "Mode-Locking Dynamics of a Laser Coupled to an Empty External Cavity", Opt. Comm. 70, 495 (1989).

W. Klische and C.O. Weiss, "Instabilities and Routes to Chaos in a Homogeneously Broadened One- and Two-Mode Ring Laser", Phys. Rev. A 31, 4049 (1985).

M. Le Berre, E. Ressayre and A. Tallet, "Type-I Intermittency Route to Chaos in a Saturable Ring-Cavity-Retarded Differential Difference System", J. Opt. Soc. Am. B5, 1051 (1988).

L.A. Melnikov, E.M. Rabinovich and V.V. Tuchin, "Quasi-Periodic Oscillations and Chaos in a Gas-Discharge Active Mode-Locked Laser", J. Opt. Soc. Am. B5, 1134 (1988).

C. Noldeke and H. Seifert, "Different Types of Intermittent Chaos in Josephson Junctions: Manifestation in the I-V Characteristics", Phys. Lett. A 109A, 401 (1985).

F. Papoff, D. Dangoisse, E. Poite-Hanoteau and P. Glorieux, "Chaotic Transients in a CO_2 Laser with Modulated Parameters: Critical Slowing-Down and Crisis-Induced Intermittency", Opt. Comm. 67, 358 (1988).

Spatio-Temporal Coherence and Chaos in Physical Systems: Conference Proceedings, Physica 23D, no. 1-3 (1986).

CHAOS IN LASERS (theory and experiment)

G.P. Agrawal, "Effect of Gain Nonlinearities on Period Doubling and Chaos in Directly Modulated Semiconductor Lasers", Appl. Phys. Lett. 49, 1013 (1986).

G. Ahlers and M. Lücke, "Some Properties of an Eight-Mode Lorenz Model for Convection in Binary Fluids", Phys. Rev. A 35, 470 (1987).

A. Ankiewicz and C. Pask, "Chaos in Optics: Field Fluctuations for a Nonlinear Optical Fibre Loop Closed by a Coupler", J. Aust. Math. Soc. Ser. B 29, 1 (1987).

J.C. Antoranz and M.G. Velarde, "Comment on 'Some Properties of an Eight-Mode Lorenz Model for Convection in Binary Fluids'", Phys. Rev. A 37, 1381 (1988).

J.C. Antoranz, L.L. Bonilla, J. Gea and M.G. Velarde, "Bistable Limit Cycles in a Model for a Laser with a Saturable Absorber", Phys. Rev. Lett. 49, 35 (1982).

F.T. Arecchi, G.L. Lippi, G.P. Puccioni and J.R. Tredicce, "Deterministic Chaos in Laser with Injected Signal", Opt. Comm. 51, 308 (1984).

L.G. Bezaeva, L.N. Kaptsov and I.Z. Sharipov, "Stochastic Regimes in a Nd:YAG Laser with Active Mode Locking", Kvantovaya Elektron. Moskva (USSR) 12, 1743 (1985).

D.J. Biswas, V. Dev and U.K. Chatterjee, "Experimental Observation of Instabilities and Chaos in the Secondary-Beat Frequency of a Multiple-Transverse-Mode CO_2 Laser", Phys. Rev. A 38, 555 (1988).

D. Dangoisse, P. Glorieux and D. Hennequin, "Laser Chaotic Attractors in Crisis", Phys. Rev. Lett. 57, 2657 (1986).

D. Dangoisse, P. Glorieux and D. Hennequin, "Coexisting Attractors and Crisis in CO_2 Lasers with Modulated Parameters", Ann. Telecomm. (France) 42, 328 (1987).

D. Dangoisse, A. Bekkali, F. Papoff and P. Glorieux, "Shilnikov Dynamics in a Passive Q-Switching Laser", Europhysics Lett. 6, 335 (1988).

M.V. Danileiko, A.L. Kravchuk, V.N. Nechiporenko, A.M. Tselinko and L.P. Yatsenko, "Dynamic Chaos in a Gas Ring Laser", Kvantovaya Elektron. Moskva (USSR) 13, 2147 (1986).

O.N. Evdokimova and L.N. Kaptsov, "Chaotic Regimes and Stability of Peak Output Radiation Power of a Nd:YAG Laser with Resonator Loss Modulation", Kvantovaya Elektron. Moskva (USSR) 14, 146 (1987).

P. Glorieux, "Chaos in CO_2 Lasers", J. Phys. Colloq. (France) 48, C7/433 (1987).

A.A. Hnilo, "Chaotic (as the Logistic Map) Laser Cavity", Opt. Commun. 53, 194 (1985).

Y. Hori, H. Serizawa and H. Sato, "Chaos in a Directly Modulated Semiconductor Laser", J. Opt. Soc. Am. B5, 1128 (1988).

W. Lauterborn and I. Eick, "Numerical Investigation of a Periodically Driven Laser with an Intracavity Saturable Absorber", J. Opt. Soc. Am. B5, 1089 (1988).

M. Le Berre, E. Ressayre, A. Tallet and H.M. Gibbs, "High-Dimension Chaotic Attractors of a Nonlinear Ring Cavity", Phys. Rev. Lett. 56, 274 (1986).

P. Mandel, "Periodic Loss Modulation in a Ring Laser", J. Opt. Soc. Am. B5, 1113 (1988).

T. Midavaine, D. Dangoisse and P. Glorieux, "Observation of Chaos in a Frequency-Modulated CO_2 Laser", Phys. Rev. Lett 55, 1989 (1985).

P.W. Milonni, J.R. Ackerhalt and M.-L. Shih, "Routes to Chaos in the Maxwell-bloch Equations", Opt. Comm. 53, 133 (1985).

T. Ming and S. Wang, "Simulation Studies of the Dynamic Behavior of Semiconductor Lasers with Auger Recombination", Appl. Phys. Lett. 50, 1861 (1987).

T. Ogawa and E. Hanamura, "Dynamical Properties of the Multimode Laser with Modulated Inversion", Opt. Commun. 61, 49 (1987).

G. Reiner, M.R. Belic and P. Meystre, "Optical Turbulence in Phase-Conjugate Resonators", J. Opt. Soc. Am. B5, 1193 (1988).

M.-L. Shih, P.W. Milonni and J.R. Ackerhalt, "Modeling Laser Instabilities and Chaos", J. Opt. Soc. Am. B2, 130 (1985).

M. Tachikawa, K. Tanii and T. Shimizu, "Laser Instability and Chaotic Pulsation in a CO_2 Laser with Intracavity Saturable Absorber", J. Opt. Soc. Am. B5, 1077 (1988).

M. Tachikawa, K. Tanii, F.-L. Hong, T. Tohei, M. Kajita and T. Shimuzu, "First Observation of Deterministic Chaos in Passive Q-Switching Pulsation", J. Phys. Colloq. 49, 413 (1988b).

J.R. Tredicce, F.T. Arecchi, G.P. Puccioni, A. Poggi and W. Gadomski, "Dynamic Behavior and Onset of Low-dimensional Chaos in a Modulated Homogeneously Broadened Single-Mode Laser: Experiments and Theory", Phys. Rev. A 34, 2073 (1986).

R. Vallee, C. Marriott, P. Dubois and C. Delisle, "Period-Doubling and Chaos in an Nth Order Nonlinear differential Equation", J. Phys. Colloq 49, 423 (1988).

C.O. Weiss, "Chaotic Laser Dynamics", Opt. Quantum Electron. 20, 1 (1988).

C.O. Weiss and J. Brock, "Evidence for Lorenz-Type Chaos in a Laser", Phys. Rev. Lett. 57, 2804 (1986).

MODULATED PARAMETERS

S.H. Chakmakjian, K. Koch, S. Papademetriou and C.R. Stroud, Jr., "Effects of Pump Modulation on a Four-Level Laser Amplifier", J. Opt. Soc. Am. B6, 1746 (1989).

M.W. Hamilton, K. Arnett, S.J. Smith, D.S. Elliott, M. Dziemballa and P. Zoller, "Saturation of an Optical Transition by a Phase-Diffusing Laser Field", Phys. Rev. A 36, 178 (1987).

K. Koch, S.H. Chakmakjian, S. Papademetriou and C.R. Stroud, Jr., "Modulation Mixing in a Multimode Dye Laser", Phys. Rev. A 39, 5744 (1989).

W.J. Kozlovsky, C.D. Nabors, R.C. Eckardt and R.L. Byer, "Monolithic MgO:LiNbO$_3$ Doubly Resonant Optical Parametric Oscillator Pumped by a Frequency-Doubled Diode-Laser-Pumped Nd:YAG Laser", Opt. Lett. 14, 66 (1989).

J.C. Petersen, "Infrared-Infrared Double-Resonance Spectra of $^{13}CH_3OH$ and $^{12}CH_3OH$", J. Opt. Soc. Am. B6, 350 (1989).

AVERAGE POWER OUTPUT OF STABLE VS. CHAOTIC INTENSITIES

P. Diament and M.C. Teich, "Relation between Radiation Statistics and Two-Quantum Photocurrent Spectra", J. Opt. Soc. Am. 59, 661 (1969).

M.C. Teich and P. Diament, "Two-Photon Counting Statistics for Laser and Chaotic Radiation", J. Appl. Phys. 40, 625 (1969).

M.C. Teich, R.L. Abrams and W.B. Gandrud, "Photon-Correlation Enhancement of SHG at 10.6 μm", Opt. Commun. 2, 206 (1970).

INTERMITTENCY THEORY

F. Argoul, A. Arneodo and P. Richetti, "A Three-Dimensional Dissipative Map Modeling Type-II Intermittency", J. Physique 49, 767 (1988).

R. Benzi, G. Paladin, G. Parisi and A. Vulpiani, "Characterization of Intermittency in Chaotic Systems", J. Phys. A 18, 2157 (1985).

J.P. Bouchaud, A. Georges and P. le Doussal, "Fluctuations of the Lyapunov Exponent and Intermittency in Dynamical and Disordered Systems: The Example of 1D Localization", in Advances in Nonlinear Dynamics and Stochastic Processes II edited by G. Paladin and A. Vulpiani (World Scientific, Singapore, 1986) p.141

G. Broggi, B. Derighetti, M. Ravani and R. Badii, "Characterization of Chaotic Systems at Transition Points through Dimension Spectra", Phys. Rev. A 39, 434 (1989).

H. Chate and P. Manneville, "Transition to Turbulence via Spatiotemporal Intermittency", Phys. Rev. Lett. 58, 112 (1987).

J. Dias De Deus and A. Noronha Da Costa, "Symbolic Approach to Intermittency", Phys. Lett. A (Netherlands) 120, 19 (1987).

J. Dias De Deus, R. Dilão and A. Noronha Da Costa, "Scaling Behaviour of Windows and Intermittency in One-Dimensional Maps", Phys. Lett. A 124, 433 (1987).

H. Fujisaka, "Theory of Diffusion and Intermittency in Chaotic Systems", Prog. Theor. Phys. (Japan) 71, 513 (1984).

H. Fujisaka and M. Inoue, "Theory of Diffusion and Intermittency in Chaotic Systems II. Physical Picture for Non-Perturbative Non-Diffusive Motion", Prog. Theor. Phys. (Japan) 74, 20 (1985).

H. Fujisaka, H. Ishii. M. Inoue and T. Yamada, "Intermittency Caused by Chaotic Modulation II: Lyapunov Exponent, Fractal Structure and Power Spectrum", Prog. Theor. Phys. (Japan) 76, 1198 (1986).

H. Fujisaka and M. Inoue, "Theory of Diffusion and Intermittency in Chaotic Systems III", Prog. Theor. Phys. (Japan) 78, 268 (1987).

C. Grebogi, E. Ott, F. Romeiras and J.A. Yorke, "Critical Exponents for Crisis-Induced Intermittency", Phys. Rev. A 36, 5365 (1987).

J.D. Keeler and J.D. Farmer, "Robust Space-Time Intermittency and 1/f Noise", Physica 23D, 413 (1986).

P.S. Landa and R.L. Stratonovich, "Theory of Intermittency", Radophys. Quantum Electron (USA)z (USSR) 30, 65 (1987).

G. Nicolis and C. Nicolis, "Master-Equation Approach to Deterministic Chaos", Phys. Rev. A 38, 427 (1988).

G. Paladin, L. Peliti and A. Vulpiani, "Intermittency as Multifractality in History Space", J. Phys. A 19, L991 (1986).

G. Paladin and A. Vulpiani, "Intermittency in Chaotic Systems", in Advances in Nonlinear Dynamics and Stochastic Processes II edited by G. Paladin and A. Vulpiani (World Scientific, Singapore, 1986) p. 127.

D. Ruelle, Elements of Differentiable Dynamics and Bifurcation Theory (Academic Press, Boston, 1989) pp. 64-68.

R.K. Tavakol and A.S. Tworkowski, "Fluid Intermittency in Low dimensional Deterministic Systems", Phys. Lett. A (Netherlands) 126, 318 (1988).

C. Tresser, P. Coullet and A. Arneodo, "On the Existence of Hysteresis in a Transition to Chaos After a Single Bifurcation", J. Phys. Lett. 41, L-243 (1980).

ENTROPIES AND DIMENSION WITH INTERMITTENCY

D. Auerbach, P. Cvitanovic, J.-P. Eckmann, G. Gunaratne and I. Procaccia, "Exploring Chaotic Motion through Periodic Orbits", Phys. Rev. Lett. 58, 2387 (1987).

A. Csordas and P. Szepfalusy, "Generalized Entropy Decay Rates of One-Dimensional Maps", Phys. Rev. A 38, 2582 (1988).

B. Dorizzi, B. Grammaticos, M. Le Berre, Y. Pomeau, E. Ressayre and A. Tallet, "Statistics and Dimension of Chaos in Differential Delay Systems", Phys. Rev. A 35, 328 (1987).

G. Paladin and A. Vulpiani, "Intermittency in Chaotic Systems and Renyi Entropies", J. Phys. A 19, L997 (1986).

INVARIANT MEASURES

P. Collet and J.-P. Echmann, "Measures invariant under Mappings of the Unit Interval", in Proceedings of the Fifth International School of Mathematical Physics and NATO Advanced Study Institute G. Velo and A.S. Wightman, ed., (Plenum, New York, 1985) p. 233.

J.-P. Eckmann and D. Ruelle, "Ergodic Theory of Chaos and Strange Attractors", Rev. Mod. Phys 57, 617 (1985).

CELL MAPPING TECHNIQUES

H.M. Chiu and C.S. Hsu "A Cell Mapping Method for Nonlinear Deterministic and Stochastic Systems II", Trans. ASME J. Appl. Mech. 53, 702 (1986).

C.S. Hsu, "A Theory of Cell-to-Cell Mapping Dynamical Systems", J. Appl. Mech. 47, 931 (1980).

C.S. Hsu, "A Generalized Theory of Cell-to-Cell Mapping for Nonlinear Dynamical Systems", J. Appl. Mech. 48, 634 (1981).

C.S. Hsu, "A Probabilistic Theory of Nonlinear Dynamical Systems Based on the Cell State Space Concept", J. Appl. Mech. 49, 895 (1982).

C.S. Hsu, R.S. Guttalu and W.H. Zhu, "A Method of Analyzing Generalized cell Mappings", J. Appl. Mech. 49, 885 (1982).

C.S. Hsu and M.C. Kim, "Statistics of Strange Attractors by Generalized Cell Mapping", J. Stat. Phys. 38, 735 (1985).

C.S. Hsu and H.M. Chiu, "A Cell Mapping Method for Nonlinear Deterministic and Stochastic Systems I", Trans. ASME J. Appl. Mech. 53, 695 (1986).

C.S. Hsu, Cell-to-Cell Mapping: A Method of Global Analysis for Nonlinear Systems (Springer-Verlag, New York, 1987).

C.S. Hsu and H.M. Chiu, "Global Analysis of a System with Multiple Responses Including a Strange Attractor", J. Sound and Vib. 114, 203 (1987).

M.C. Kim and C.S. Hsu, "Computation of the Largest Lyapunov Exponent by the Generalized Cell Mapping", J. Stat. Phys. 45, 49 (1986).

T.R. O'Bannon, "A Comparison of Interpolative Methods for Cell Mapping", M.S. Thesis in Mechanical Engineering, Georgia Institute of Technology, directed by B.H. Tongue (1988).

D.R. Smith, "Nonlinear System Characterization through Interpolated Cell Mapping", M.S. Thesis in Mechanical Engineering, Georgia Institute of Technology, directed by B.H. Tongue (1988).

J.-Q. Sun and C.S. Hsu, "First-Passage Time Probability of Nonlinear Stochastic Systems by Generalized Cell Mapping Method", J. Sound and Vib. 124, 233 (1988).

B.H. Tongue and K. Gu, "A Higher Order Method of Interpolated Cell Mapping", J. Sound and Vib. 125, 169 (1988).

LASERS WITH SATURABLE ABSORBERS

E. Arimondo, F. Casagrande, L.A. Lugiato and P. Glorieux, "Repetitive Passive Q-Switching and Bistability in Lasers with Saturable Absorbers", App. Phys. B 30, 57 (1983).

E. Arimondo, D. Dangoisse, C. Gabbanini, E. Menchi and F. Papoff, "Dynamic Behavior of Bistability in a Laser with a Saturable Absorber", J. Opt. Soc. Am. B4, 892 (1987).

E. Arimondo, "Dynamics of the Bistable Laser with Saturable Absorber", in Synergetics and Dynamic Instabilities (Soc. Italiana di Fisica, Bologna, 1988).

E. Arimondo, F. De Tomasi, B. Zambon, F. Papoff and D. Hennequin, "Generalized Optical Bistability and Chaos in a Laser with a Saturable Absorber", J. Physique 49, C2-123 (1988).

D. Hennequin, F. De Tomasi, B. Zambon and E. Arimondo, "Homoclinic Orbits and Cycles in the Instabilities of a Laser with a Saturable Absorber", Phys. Rev. A 37, 2243 (1988).

M. Tachikawa, K. Tanii and T. Shimizu, "Comprehensive Interpretation of Passive Q Switching and Optical Bistability in a CO_2 Laser with an Intracavity Saturable Absorber", J. Opt. Soc. Am. B4, 387 (1987).

RESONANCES, FROBENIUS-PERRON OPERATORS AND POWER SPECTRA

T. Adachi and T. Sunada, "Twisted Perron-Frobenius Theorem and L-Functions", J. Funct. Anal. 71, 1 (1987).

V. Baladi, J.-P. Eckmann and D. Ruelle, "Resonances for Intermittent Systems", Nonlinearity 2, 119 (1989).

P. Collet and P. Ferrero, "On the Lasota-Yorke Counter-Example", in Advances in Nonlinear Dynamics and Stochastic Processes II edited by G. Paladin and A. Vulpiani (World Scientific, Singapore, 1986) p. 77.

M. Dörfle, "Spectrum and Eigenfunctions of the Frobenius-Perron Operator of the Tent Map", J. Stat. Phys. 40, 93 (1985).

J.P. Eckmann, "Resonances in Dynamical Systems", in IXth International Congress on Mathematical Physics edited by B. Simon, A. Truman and I.M. Davies (Adam Hilger, Bristol, 1989) p. 192.

G. Gyorgyi and P. Szepfalusy, "Relaxation Processes in Chaotic States of One Dimensional Maps", Acta Phys. Hungarica 64, 33 (1988).

M. Iosifescu, "On Invariant Probability Densities of Piecewise Monotonic Transformations", in Transactions of the Tenth Prague conference on Information Theory, Statistical Decision Functions, Random Processes (Academia, Prague, 1988) p. 41.

Y. Jiang and H. Gang, "Exact Solutions of the Invariant Density for Piecewise Linear Approximation to Cubic Maps", J. Phys. A 21, 2717 (1988).

T. Kohda and K. M. Tao, "Time Series Analyses of 1/f Noise with Its Unbounded Invariant Density", Electron. and Comm. Japan 70, 53 (1987).

A. Lasota and J.A. Yorke, "Exact Dynamical Systems and the Frobenius-Perron Operator", Trans. of AMS 273, 375 (1982).

T.-Y. Li, "Finite Approximation for the Frobenius-Perron Operator: A Solution to Ulam's Conjecture", J. Approx. Theory 17, 177 (1976).

H. Mori, H. Okamoto, Byon Chol So and S. Kuroki, "Global Spectral Structures of Intermittent Chaos", Prog. Theor. Phys. (Japan) 76, 784 (1986).

K. Murao and T. Kohda, "Time Series Analyses of Periodic Chaos", Trans. Inst. Electron. & Commun. Eng. Japan E68, 405 (1985).

D. Ruelle, "Resonances of Chaotic Dynamical Systems", Phys. Rev. Lett. 56, 405 (1986).

SCALING AND RENORMALIZATION

R.M. Everson, "Scaling of Intermittency Period with Dimension of a Partition Boundary", Phys. Lett. A 122, 471 (1987).

M. Inoue, H. Fujisaka and O. Yamaki, "Scaling Behavior of Fluctuation Spectrum for Pure Intermittency Chaos", Phys. Lett. A 132, 403 (1988).

H. Ishii, H. Fujisaka and M. Inoue, "Breakdown of Chaos Symmetry and Intermittency in the Double-Well Potential System", Phys. Lett. A 116, 257 (1986).

P. Manneville, "Intermittency, Self-Similarity and 1/f Spectrum in Dissipative Dynamical Systems", Jour. Physique $\underline{41}$, 1235 (1980).

H.-C. Tseng, W.-Y. Lai, C.-K. Hu and W.-D. Chen, "Renormalization-Group method for Transitions to Chaos via Period Doubling and Intermittency in the Chaotic Region", Phys. Lett. A $\underline{134}$, 417 (1988).

S. Zaleski and P. Lallemand, "Scaling Laws and Intermittency in Phase Turbulence", J. Phys. Lett. $\underline{46}$, L-793 (1985).

LIST OF PUBLICATIONS

R.F. Fox, G.E. James and R. Roy, "Laser with a Fluctuating Pump: Intensity Correlations of a Dye Laser", Phys. Rev. Lett. 52, 1778 (1984).

R.F. Fox, G.E. James and R. Roy, "Stochastic Pump Effects in Lasers", Phys. Rev. A 30, 2482 (1984).

G.E. James, E.M. Harrell II and Rajarshi Roy, "Intermittency and Chaos in Intracavity Doubled Lasers", in Coherence and Quantum Optics VI, edited by J.H. Eberly, L. Mandel, and E. Wolf (Plenum, New York, in press).

G.E. James, E.M. Harrell II and Rajarshi Roy, "Intermittency and Chaos in Intracavity Doubled Lasers II", Phys. Rev. A 41, to be published (1990).

G.E. James, E.M. Harrell II, C. Bracikowski, Rajarshi Roy and K. Wiesenfeld, "On the Elimination of Chaos in an Intracavity Doubled Nd:YAG Laser", (submitted to Opt. Lett., 1990).

G.E. James, E.M. Harrell II, C. Bracikowski, K. Wiesenfeld and Rajarshi Roy, "Chaos in Intracavity Second Harmonic Generation", (submitted to The International Conference on Nonlinear Dynamics in Optical Systems, Oklahoma, June, 1990).

K. Wiesenfeld, C. Bracikowski, G.E. James and Rajarshi Roy, "Observation of Antiphase States in a Multimode Laser", (submitted to The International Conference on Nonlinear Dynamics in Optical Systems, Oklahoma, June, 1990).

VITA

Glenn Edward James was born in Paterson, New Jersey, on January 10, 1961. After graduating from high school in Center Line, Michigan (1978), he was accepted as a cadet at the United States Air Force Academy where he earned a B.S. in Mathematics (1982). His undergraduate schooling included one semester as an exchange student at the French Air Force Academy, the École de l'Air, in Salon-de-Provence, France. At his graduation from the U.S. Air Force Academy he was honored as the Outstanding Cadet in Academic Performance and the Outstanding Cadet in Mathematics, finishing second in a class of 808. He completed his M.S. in Applied Mathematics at the Georgia Institute of Technology in 1983, and moved to Albuquerque, New Mexico, to an assignment at the Air Force Weapons Laboratory. While in New Mexico, he married Patricia Ann Saucedo in 1987; soon afterward he returned to the Georgia Institute of Technology to pursue a Ph.D. in Mathematics.